ABSTRACT

Title of dissertation: Measurement of the Electric Form Factor of the Neutron at High Momentum Transfer

Jonathan Miller, Doctor of Philosophy, 2009

Dissertation directed by: Professor Elizabeth Beise
Department of Physics

The electric form factor of the neutron, G_E^n, provides key understanding of the structure of one of the basic building blocks of visible matter in the universe. Recent interest in this quantity is the result of the improved quality of data provided by double polarization experiments, which have substantially improved in the last decade.

This thesis presents precision measurements of G_E^n by the E02-013 collaboration at Q^2 of 1.7, 2.5, and 3.5 GeV^2. This measurement used a double polarization technique, a highly polarized ^{3}He target, a polarized electron beam, a large acceptance spectrometer to detect the scattered electrons, and a large neutron detector to detect the recoiling hadrons in the reaction $^3\vec{\mathrm{He}}(\vec{e}, e'n)$. These measurements will be compared to a variety of models of the nucleon's internal structure, as well as used to extract individual contributions of the up and down quarks to the nucleon form factors.

Measurement of the Electric Form Factor of the Neutron at High Momentum Transfer

by

Jonathan Miller

Dissertation submitted to the Faculty of the Graduate School of the
University of Maryland, College Park in partial fulfillment
of the requirements for the degree of
Doctor of Philosophy
2009

Advisory Committee:
Professor Elizabeth Beise, Chair/Advisor
Dr. Bogdan Wojtsekhowski
Professor Nick Hadley
Professor Michael Coplan
Professor Steve Wallace

Dedication

In memory of my father

Robert Lewis Miller

1957-2003

and to my mother

Jeanene K Priddy

Acknowledgments

Many people have inspired me, supported me, mentored me, advised me, influenced me, challenged me, befriended me, and otherwise helped me come to where I am today, successfully completing my graduate career. It has been a long career, totalling over seven years, and I am unable to thank everyone completely for their contribution. I also would like to thank those who caused me to enter the physics program, from former professors to my parents. In particular, I would like to thank Betsy Beise, Nick Chant, and Jim Kelly, without whom I would not be graduating.

Without Jim Kelly, I would have left graduate school years ago. He was my professor, mentor, adviser, and a friend. He believed in me, even when I was struggling to become a productive scientist. I very much wish that he could have been alive to see me become a productive experimentalist and the successful completion of my dissertation and defense.

I would like to thank my mentor at the Jefferson Lab, Bogdan Wojtsekhowski, for his invaluable direction over these last two years. Many of the ideas and techniques that I developed and that are found in the analysis presented in this thesis were formed in discussions with him or where suggested to me by him. His love of physics has been an inspiration to me.

From my candidacy, to my defense, my adviser Betsy Beise has supported, mentored, advised, and guided me. I would like to thank her for providing feed back so quickly as I struggled to write this thesis, and for her expert direction on scientific communication. I would also like to especially thank her for accepting me

as a student and for her patience as I worked towards graduation.

When I first entered into graduate school, Nick Chant was the chair of the physics graduate program. His advising, kindness, and support were crucial, both in the years before I joined a research group, and during the period of Jim Kelly's illness. I would also like to thank Jane Hessing. Without her ability to take care of almost any administrative issue, as well as timely and frequent reminders to take care of what was needed, I am sure I would have been unable to complete this program.

I would like to thank my committee members for reading this thesis and agreeing to be on my committee. Specifically Steve Wallace for providing detailed comments and for being a pleasure to TA for. And Nick Hadley for agreeing to be on my committee on short notice. In particular I would like to thank Mike Coplan for his advice, understanding, and detailed comments.

I came down to Newport News at the beginning of 2006 to become the expert of the Neutron Detector with no experience with no experience with how to do so. There are a number of people who worked with me on the neutron detector to get the software and hardware working so that the detector could begin taking data when the experiment started. These people were Rob Feuerbach, Shigey Tajima, Alex Camsonne, Igor Rachek, Albert Shahinyan, and Nerses Gevorgyan. I also would like to thank Bodo Reitz for taking a bit of time to direct me in 2005 when I joined the E02-013 experiment. I would also like to thank Rob Feuerbach for mentoring early in my E02-013 career.

I would like to thank Gordon Cates and Nilanga Liyanage, spokespeople of the

E02-013 experiment, for their support and for the opportunity to take part in this experiment. I would also like to thank the E02-013 collaboration for the opportunity in taking part in this experiment, for the work accomplished, and for the opportunity to present results. In particular, I thank Bob Michaels, Brad Sawatzky, and Steve Wood for the parts they played during the early part of E02-013.

There were many students contributed to this experiment. Thanks to Tim Ngo for working with me on the Neutron Arm geometry, to Aidan Kelleher for advice and for teaching me about the target. I would like to thank Ameya Kolarkar, Brandon Craver, and Sergey Abrahamyan for working with me on making this experiment a success and in working with me to get results. Also I thank Seamus Riordan for providing feedback on the Big Bite sections of this thesis and for his hard work in completing the analysis.

In Newport News there were many people who provided me friendship and support while I studied and worked there. These include my former roommates Alex Coppens, Aji Daniel, and Nuruzzaman. Also my friends Phil Carter, Fatiha Benmokhtar, John McNabb, Amrendra Narayan, Micah Veilleux, Megan Freind, Kalyan Allada, Chiranjib Dutta, and many more provided me with support, dinner partners, and at times an audience.

I thank the nuclear physics students here at University of Maryland for befriending someone who some had not met before the semester of my defense. I would particularly like to thank Tanya Horn for help with the University of Maryland computer systems at JLab, Jainglai Liu for taking time to answer ROOT questions when I joined the group, and especially Colleen Ellis for assistance with the ENP groups

printer's and for being friendly when I imposed upon her office. Thanks to Judy Myrick for taking care of me from far away as the secretary for the experimental nuclear physics group. She made sure that all the administrative things were cared for without my presence. I would also like to thank Herbert Breuer for guiding my investigation of nuclear instrumentation.

I spent more years down at Jefferson Lab than I did at the University of Maryland. I still needed to return to the University periodically, and I owe a lot to Buckley and Beth Hopper for the use of their guest room over the years. Also, during these long years they have provided friendship and a home away from home. They have helped me when I needed assistance with the necessities of living alone. Buckley has been my friend since we first entered the University of Maryland physics program, almost 7.5 years ago. Beth's parents also provided me with a family to share holidays with.

I would like to thank my friends at the University of Maryland for providing me with friendship and company and often a place to stay. In particular my former roommates: Greg Morrison, Tommy Willis, John Polastro, Scott Fletcher, Wayne Witzel, and my friends Ben Cooper, Andy York, Tracy Moore, Matt Reames, Margaret Cheung, and Chris Fleming.

There are many professors who I worked for and learned at the University of Maryland who took some personal time to advise me or instruct me. Just a few of these were Prof. Dorfman, Prof. Pati, Prof. Anderson, Prof. Greenberg, and Prof. Gates.

I have many professors at Gustavus Adolphus College to thank for teaching,

mentoring, and advising me before I enrolled in graduate school. I would particularly like to thank my mathematics adviser Jeff Rosof, and my physics adviser Paul Saulnier. I would also like to thank Chuck, DC Henry, Steve Melema, and Thomas Huber who invited the physics students into their homes and made the physics department more a group of friends than just a place to learn physics.

Thanks to my friends at Gustavus Adolphus College, Matt Miller, Jonathan Jennings, Stephen Bacques, Andrew Ohrt, Mike Bland, Mandy Havnen, for being my friends at Gustavus Adolphus College and entertaining me when on breaks from home work.

I have many relatives who have supported me, provided me with a place to stay and to holiday with, who have helped me move, and other necessities. In particular, I would like to thank my grandpa and grandma Priddy, my grandpa and grandma Miller, my aunt Diane and her family, and my uncle Ken and his family.

A heartfelt thank to my father, Robert, and mother, Jeanene for providing me an environment where education was valued. One of my earliest memories is going to a NASA museum, and how as a youngster I wore out many of the astrophysics books we had. I would particularly like to thank my mother for sending me care packages, providing me support, and giving me advice during my education. My dad was always interested in physics and collected many general physics books which provided inspiration for me to go into physics myself. I miss my father, and wish he was still with us.

Besides my parents, my siblings have also provided me with campionship during my childhood. Thanks to Ross Miller, for providing me with interesting educa-

tion in humanities in highschool, when the science classes were not as interesting.

Most especially, I would like to thank God for giving me the intelligence to become a scientist, and for giving me the insight necessary. Also I am thankful for my continued health, and for all the wonderful people I have met and interacted with during these years.

Table of Contents

List of Tables xii

List of Figures xvi

List of Abbreviations xxvi

1 Physics of the Nucleon 1
1.1 Introduction to the Nucleon . . . 1
1.2 QCD . . . 2
1.2.1 Perturbative QCD . . . 4
1.3 Nucleon Structure . . . 5
1.3.1 Partons . . . 6
1.3.2 The Constituent Quark Model . . . 8
1.3.3 Generalized Parton Distributions . . . 9
1.3.4 Vector meson dominance models . . . 10
1.3.5 Chiral effective field theory . . . 11
1.3.6 Dyson-Schwinger Equations . . . 12
1.4 Experimental Investigation . . . 13

2 Physics of Electron and Nucleon Scattering 14
2.1 Introduction to electron scattering . . . 14
2.2 Definition of kinematic variables . . . 15
2.2.1 Current operator . . . 16
2.2.2 Dirac and Pauli form factors . . . 16
2.3 Breit frame . . . 17
2.4 Quasi-elastic scattering . . . 19
2.4.1 Impulse approximation . . . 20
2.4.2 PWIA . . . 21
2.5 Polarization observables . . . 21
2.5.1 Recoil polarization . . . 23
2.5.2 Target polarization . . . 25
2.6 Cross section with unpolarized observables . . . 25
2.7 Cross section with polarized observables . . . 26

3 Form Factors 29
3.1 Models and fits . . . 29
3.1.1 Fits . . . 29
3.1.2 Vector meson dominance model . . . 30
3.1.3 Pion cloud and CQM . . . 30
3.1.4 Model of Generalized Parton Distributions . . . 31
3.1.5 pQCD predictions . . . 31
3.2 Measuring GEn via the Rosenbluth technique . . . 32
3.2.1 Elastic e-D scattering . . . 34

3.2.2 Quasi-elastic scattering and the Rosenbluth Technique 35
3.2.3 Difficulties with Rosenbluth method 36
3.3 Double polarization techniques 36
3.3.1 Quasi-elastic scattering and (e,e'n) 38
3.3.2 Recoil polarimetry 41
3.3.3 Polarized target measurement 43
3.3.4 Experiments with polarized deuterium 44
3.3.5 Experiments with polarized helium-3 45
3.4 Summary of past measurements 48
3.5 E02-013 at Jefferson Lab 49

4 G_E^n experiment E02-013 51
4.1 Experimental Overview 51
4.2 Principle and Experiment setup 52
4.3 The Electron Beam 57
4.4 The Helium-3 Target 60
4.4.1 Target System 63
4.4.2 Polarization 64
4.4.3 Polarization Measurement 68
4.5 Big Bite 73
4.5.1 The Big Bite Apparatus 73
4.5.2 The Big Bite Scintillators and Shower 75
4.5.3 The Wire Chambers and Tracking 76
4.5.4 Big Bite Electronics 79
4.6 Big Hand 82
4.6.1 Neutron Geometry 82
4.6.2 Veto and Marker Bars 83
4.6.3 Neutron Arm Electronics 84
4.7 Data Acquisition 86
4.7.1 Encoding and Decoding 88

5 Analysis 93
5.1 Event filtering and scintillator timing 94
5.2 Electron parameters 100
5.3 Hadron identification 104
5.4 Identification of the hadron charge 113
5.5 Dilution of the neutron sample by protons 119
5.5.1 Single Track Analysis and Background Correction 130
5.5.2 Nitrogen Dilution 135
5.5.3 RF correction 135
5.6 Asymmetry calculation 138
5.7 Corrections 143
5.7.1 FSI Corrections 143
5.7.2 Inelastic Contribution 146

6 Results and Discussion 149
6.1 Framework Formalism . . . 151
6.2 Results . . . 153
6.3 Pauli and Dirac Form Factors . . . 153
6.3.1 Flavor Form Factors . . . 154
6.4 GPD Models . . . 157
6.4.1 Impact Parameter Space . . . 158
6.4.2 Fit to our data . . . 159
6.4.3 Quark Orbital Angular Momentum . . . 161
6.4.4 Conclusions . . . 163

A Neutron Arm Analysis 165
A.1 Simulations . . . 166
A.2 Calibrations . . . 167
A.2.1 High Voltage Tune . . . 169
A.2.2 Time Offsets . . . 171
A.2.3 Amplitude Correction . . . 178
A.2.4 Energy Calibration . . . 183
A.2.5 Veto Calibration . . . 183
A.3 Neutron Software . . . 184
A.4 Veto Analysis . . . 188

B Error Analysis 194

C Calculations 206
C.1 Asymmetry Best Value . . . 206

D Jefferson Laboratory E02-013 Collaboration 208

List of Tables

1.1 The three light quarks and their respective charges. Other quarks are the c (charm), b (beauty), and t (top) quark, but they are too heavy to play a large role in the experiments described here. These three light quarks form the SU(3) group. 4

3.1 Double polarization experiments for measuring the electric form factor of the neutron that have been carried out to date [77]. 39

4.1 A table showing the running conditions, time, accumulated charge, and kinematics of the different measurements referred to here and elsewhere as kinematics or for short kin. Kinematic one includes both the commissioning time and the first measurement. The measurement of $Q^2 = 1.3$ and 1.7 GeV^2 provide a comparison of the polarized ^{3}He technique with previous recoil polarization data while the other two measurements extend the measured range of Q^2. Not shown is the periods for commisioning and kinematic 1 which won't be covered in this thesis. 54

4.2 A table of the beam polarization as measured by different means at different times. The Møller measurements were done in the Hall A Møller. The Mott measurements were done using the injector Mott measurement. Only selected Compton data is presented, and the Compton data isn't used in this analysis. 92

5.1 A table of the initial event selection for analysis. Sanity cut 1 is the requirement that Big Bite has a track, Sanity cut 2 is the requirement that at least one scintillator paddle in Big Bite has an event, Sanity cut 3 is that the coincidence time (L1A) was recorded. Sanity cut 4 is the requirment that there is a coincidence event. Negative is a requirement that only negative particles in the drift chambers can be considered as electrons. 104

5.2 A table of selection criteria used to determine which veto hits to consider when doing charge identification. The spatial cuts of Y1, Y2, and X determine which bars are to be included, events were only differentiated by time and amplitude within a veto detector which was within range of the hadron hit. The subscript V signifies veto, while C signifies the cluster in the neutron arm. 119

5.3 A table of the ratios for different criteria. Over the course of a kinematic setting, runs varied in rate. This had a small effect on the purity factor, the results presented in this table is for a normal run. . 126

5.4 The effective ratio of $\frac{Z}{N}$ for the target and cuts. The ratio for ^{3}He is from simulation. 126

5.5 Table of quasi-elastic event selection cuts. The Single QE cut is that there is one and only one hit in the associated region of time and $q_\perp < 0.15$. This is in addition to the region of time and $q_\perp$ which are selected as quasi-elastic event candidates. The vertical cut and horizontal cut are neutron arm fidicual cuts. 138

5.6 Determination of the physical asymmetry from the measured experimental asymmetry. A full discussion and analysis of errors is presented in Appendix B. Systematic uncertainties are listed second. . . 139

5.7 Expansion Coefficients in the determination of λ from the physical asymmetry. Uncertainty in λ calculated as discussed in Appendix B. . 142

5.8 Displayed is the calculated values for λ and Q^2, and the value of G_M^n as arrived at from a parameterization [59]. From this the value of G_E^n can be determined. Determination of uncertainty is discussed in Appendix B. 143

5.9 Shown are preliminary inelastic asymmetries and dilutions for the various kinematic [82]. The * row relates to an expanded selection of quasi-elastic events, with a maximum invariant mass of 1.15 GeV rather than the usual maximum of 1.05 GeV and a maximum missing mass of 2.2 GeV rather than 2 GeV (see Table 5.5). 148

6.1 Given here are previous fit parameters [59] and a new fit presented in this thesis. The fit only includes data from experiments using double polarization techniques. 151

6.2 Given here are the fit parameters from the previous work [45] and a new fit presented in this thesis. 161

6.3 Presented is a calculation of the quark orbital angular momentum using Ji's Sum Rule [54] in the framework of [45]. Compared is this previous work (**), with a new fit (*) using the form factor results presented in this thesis. 163

A.1 A table showing the proton and neutron efficiency as calculated using the Monte Carlo Simulation. 167

A.2 Table of the list of high voltage changes (HV) for the neutron arm in the E02-013 experiment. 192

A.3 A table showing the deadtime region for a set of veto detectors. This was selected as the maximum for that set of detectors. 193

A.4 A table of the correlation beetween hits in Veto plane 1 and Veto plane 2. The is for all events within a single run in kinematic 2A (3190). 193

B.1 A table showing the measurements and error calculations for the nitrogen dilution of the uncharged sample, for all three kinematics. $N_{^3He}$ is the number of background corrected counts for the selected ^3He runs, ρ_{N_2} is the nitrogen density, $Q_{^3He}$ is the total charge of the selected ^3He runs. This calculation is as described in section 5.5.2. Densities are determined by target measurements [62][57][81]. 200

B.2 A table of the errors for the calculation of A_{proton}. The calculation is calculated according to equation 5.54. The uncertainty in G_M^p and G_E^p is determined using a parameterization [59] and the propagation of the error is according to equation B.1. Parenthesis is used to identify the systematic uncertainty. 201

B.3 A table for all three kinematics showing the measurements for the charged and uncharged background and the uncertainty in the background ratio. 202

B.4 A table of the errors for the calculation of G_E^n. Uncertainty in the ratio of form factors was calculated from the physical asymmetry as expressed in section 5.6 and Table 5.8 and Table 5.7. The uncertainty in G_M^n is determined from a parameterization [59] and propagation of the error is according to equation B.1. 202

B.5 A table of the uncertainties that contribute to the physical asymmetry (A_{phys}). The contributions are calculated and contribute to the physical asymmetry precision as determined by equation B.1. This table shows the errors for $Q^2 = 2.5$ GeV^2. 203

B.6 A table of the uncertainties that contribute to the physical asymmetry (A_{phys}). The contributions are calculated and contribute to the physical asymmetry precision as determined by equation B.1. This table shows the errors for $Q^2 = 3.5$ GeV^2. 204

B.7 A table of the uncertainties that contribute to the physical asymmetry (A_{phys}). The contributions are calculated and contribute to the physical asymmetry precision as determined by equation B.1. This table shows the errors for $Q^2 = 1.7$ GeV^2. 205

List of Figures

1.1 Shown is a schematic of the DVCS process, in the framework of generalized parton distributions (GPDs). Here ξ is the skewness, x is the longitudinal momentum fraction, N is the nucleon, $\gamma*$ is the virtual photon, and γ is the detected photon. The skewness gives the longitudinal momentum asymmetry, as shown in the figure. 8

2.1 Feynman diagram for one interaction between an electron and a nucleon. The electron has four-momentum k^μ and the nucleon has four-momentum p^μ. 15

2.2 Feynman diagram for interaction between an electron and the nucleus. The electron has four-momentum k^μ and the ejected nucleon has momentum p_f^μ. 19

2.3 Polarization exchange in the one photon exchange approximation for polarized-electron, polarized nucleon scattering. θ and ϕ define the polarization of the recoiling nucleon. 22

3.1 Various fits discussed in the text. The points plotted are from [66], which was used to fit the pQCD curve. These data are only representative, see figure 3.2 for the full set. The Bijker curve is a representative Vector Meson Dominance model, the Guidal curve is a representative GPD based model, the Miller curves are from a CQM. 33

3.2 Previous G_E^n data from experiments involving polarization techniques. The curve is the Galster parametrization [40]. Herberg provided new calculations of the Ostrick data, while Golak provided a FSI corrected analysis of the Becker data. For references see Table 3.3. 37

4.1 Image of Jefferson Laboratory. Shown is the accelerator and the mounds over the three experimental halls. The mound to the left is Hall A. 53

4.2 General layout, not to scale, of the experiment. Shown is the beamline, the target, the Big Bite detector stack, and the Neutron Arm detector. Also shown are the two polarimeters in the hall before the target, and the approximate distances to the detectors. The components of the Big Bite (BB) detector stack are also shown and consist of the Big Bite dipole magnet, multi-wire drift chambers (MWDCs), pre-shower, shower, and timing plane. 55

4.3 Coordinate systems for Big Hand, Target, and Lab. The lab z is along the beam line while the target z is toward Big Bite. All coordinate systems are right handed. 56

4.4 Schematic of the accelerator as it existed in 2006. Shown are the three halls, injector, and LINACs. 57

4.5 Diagram of the ^{3}He nucleus. Shown is the most common state with the proton spins aligned anti-parallel. The neutron carries $\approx 86\%$ of the polarization of the nucleus while the protons carry $\approx 3\%$. 61

4.6 Picture of an empty ^{3}He cell. On top is the spherical pumping chamber, and below is the cylindrical target chamber. The beam passes through 40cm of target material [41]. 62

4.7 Measurement of the holding field as a function of position along the beamline in the target. The origin is the target center. 65

4.8 Magnet box for Target [57]. Shown is the coils that create the magnetic field. 66

4.9 Figure showing the polarization process [57]. Optical pumping excites the electron to an excited state, which can exchange (50%) to a state that decays to a spin state that is not optically pumped by the lasers. 67

4.10 In a traditionally polarized helium cell, one that contains only Rb and ^{3}He, the Rb exchanges spin in one of three ways. Spin is exchanged either by changing the spin of the He nucleus, or by just rotating the atoms it interacts with. This rotation is not useful for polarizing the He, so by adding K, which is likely to engage in "spin-rotation" with the Rb, but likely to engage in "spin-exchange" with He, the polarization efficiency of the cell is increased. Only the spin-exchange collision process causes polarization of the ^{3}He [57] [93]. 69

4.11 The coils used for the NMR measurement of target polarization. Shown is the holding field coils (iron box), the RF coils (which can be adjusted), and the pick-up coils. Two sets of pick-up coils are down at the target chamber, one more set is up above the pumping chamber. One of the RF coils could be adjusted, as could the pick-up coils, to maintain the transverse relationships needed for an NMR measurement. 70

4.12 Measured polarization in the ^{3}He cells during the experiment [56]. Shown is all cells, including Dolly, Edna, and Barbara used during Kinematics 2, 3, and 4. 73

4.13 Schematic of the Big Bite detector. Shown is the large dipole which provides a magnetic field integral of 1.2 T·m, the 15 planes in three chambers that made up the wire chamber, and the lead glass shower and preshower separated by a layer of plastic scintillator. 74

4.14 This diagram, which is not to scale, shows Big Bite, the location of the dipole, target, drift chambers, and shower, and the quantities known as the deflection angle (θ_{def}), θ_{tgt}, and the back and front tracks. Shown on the upper left is the coordinate system for the target coordinates. The shower is shown providing a fourth location for the particle, to anchor the track reconstruction. Big Bite detector coordinates have their origin at the center of the first plane. The z direction is perpendicular to the first chamber, and x is the magnetic dispersion direction. 78

4.15 Momentum resolution achieved with the latest optics model. Shown is the momentum resolution for all four kinematics. 80

4.16 Resolution of the carbon foils after vertex corrections. The foils should be 6.7 cm apart with the BeO foil at 0 cm. This histogram is of data from a foil target run in kinematic 3. These foils were used for the optics calibration. 80

4.17 The electronics schematic for Big Bite. Shown are the modules and the wire lengths. Two neighboring preshower blocks, and two neighboring sets of shower blocks, which have a summed amplitude that passes some threshold provides the trigger for the electron arm. . . . 81

4.18 Neutron Arm electronics schematics. Included in the schematic is the length of the cables. From the PMTs of the various tubes, the signal goes into both a TDC and a sum module with the non-summed output going to an ADC. The different summed signals are added together and sent to both an ADC and TDC, with an OR of the TDCs forming the trigger. 85

4.19 Neutron arm (NA) schematic for the sums. In front are the two veto planes. Shown is the relative offset. Additionally, color coded, the sums are shown. Each sum was made up of two neighboring color bands. Shown on top are the bars from Glasgow (GLA), in the front are four planes of bars from Carnegie Mellon University (CMU), and in the back are three planes of bars from University of Virginia (UVA). The colorless bars in the final plane are bars that were not connected to the electronics. The first two thin planes are the veto planes, the figure shows the vertical shift between the two planes. 87

4.20 Plot showing the reference time and coincidence counts in relation to the Big Bite trigger time [37]. Best coincident events are in the circled region. 89

5.1 The flowchart for the analysis. This is after the preliminary replay of events that is described in section 4.7. The resulting ROOT files contain the subset of events necessary to undertake the remaining analysis, also assigns charge, and identifies quasi-elastic event candidates. Two separate scripts are run as part of this process for each run before this post processing. This is to determine the RF correction (see section 5.5.3) and the hadron time-of-flight. 95

5.2 Flowchart for the event processing. Events in the analysis are ignored if no tracks or Big Bite scintillator hits exist, or if the event does not have a well defined trigger time as demonstrated by the existence of the Level 1 Accept (L1A) Time. The optics can be updated here if necessary, and the kinematics of the event are calculated to ease post processing. All event cuts are detailed in Table 5.1. 96

5.3 Flowchart associating clusters, both with each other and as quasi-elastic event candidates. Some clusters should be associated together, where some neutron detector did not fire to make the cluster continuous. Charged candidates are identified, and momentum is calculated for the hit. 97

5.4 Amplitude distribution for all events showing pions and electrons in Big Bite. In blue is the distribution after cuts have been applied to remove events which are lacking the information needed for analysis, shaded is the region selected. See Table 5.1 for cuts, in black is all events and in blue is with just the "sanity" cuts applied. This distribution is for $Q^2 = 3.5$ GeV^2. 98

5.5 Electron momentum for all tracks in Big Bite. In blue are just those tracks for which the preshower energy is greater than 450 channels, shaded is the selected momentum. See Table 5.1 for cuts, in black is all events and in blue is with the "sanity" and pre-shower energy cuts applied. This distribution is for $Q^2 = 3.5$ GeV^2. 101

5.6 X position (m) within the Big Bite scintillator detector. This is for before cuts (black), after electron and sanity cuts (blue), with the selected region of X shaded. Variation is due to the lack of calibration for the total shower in the Big Bite detector. See Table 5.1 for cuts, in black is all events and in blue is with the "sanity", pre-shower energy, and electron momentum cuts applied. This distribution is for $Q^2 = 3.5$ GeV^2. 102

5.7 Vertex, this shows the target z position reconstructed by the Big Bite wire chambers for all events with tracks (black). In blue is after cuts on particle ID. Shaded is the region selected as being within the target. See Table 5.1 for cuts, in black is all events and in blue is with the "sanity", pre-shower energy, Big Bite fidicual, and electron momentum cuts applied. This distribution is for $Q^2 = 3.5$ GeV^2. . . . 103

5.8 $q_\perp$ versus W for neutral particles in the various kinematics. Shown is the selection of quasi-elastic events in the square. As shown, at higher Q^2 the inelastic tail becomes stronger. 105

5.9 $q_\perp$ versus W for charged particles in the various kinematics. In the red box is the selection of quasi-elastic events. 106

5.10 $q_\parallel$ versus W for charged particles in kinematic 3. 107

5.11 Distribution of $q_\perp$ in the various kinematics. Shown in blue is the neutral spectrum, in black is the total spectrum (That passed the event based selection). The majority of neutral quasi-elastic events fall under 0.15 GeV. 108

5.12 ΔT (ns) for the various kinematics. In blue is the neutral time-of-flight spectrum, in black is the total time-of-flight spectrum. The photon peak is shown at ≈ -3ns. Quasi-elastic events are selected with time between -1 and 1 ns. 110

5.13 Missing mass (GeV) for the various kinematics. In blue is the neutral scaled up by a factor of 20 for $Q^2 = 3.5$ GeV^2 and 10 for $Q^2 = 2.5$ and 1.7 GeV^2, in black is the total spectrum. 111

5.14 ΔT (ns) for the various kinematics. In blue is the charged time-of-flight spectrum, in blue is the charged time-of-flight spectrum. The charged spectrum is scaled down to the neutral spectrum. 112

5.15 Shown in these figures is the time versus $q_\perp$ for various kinematics. Also shown is the box showing which cuts were used for identifying quasi-elastic clusters within the neutron arm. As is shown, the ability to select quasi-elastic clusters is much better for the lower kinematics. 114

5.16 Shown in these figures is the time versus invariant mass for various kinematics. Also shown is the box showing which cuts were used for identifying quasi-elastic clusters within the neutron arm. As is shown, the ability to select quasi-elastic clusters is much better for the lower kinematics. 115

5.17 Shown in these figures is the time versus missing mass for various kinematics. Also shown is the box showing which cuts were used for identifying quasi-elastic clusters within the neutron arm. As is shown, the ability to select quasi-elastic clusters is much better for the lower kinematics. 116

5.18 Shown in these figures is the invariant mass versus missing mass for various kinematics. Also shown is the box showing which cuts were used for identifying quasi-elastic clusters within the neutron arm. As is shown, the ability to select quasi-elastic clusters is much better for the lower kinematics. 117

5.19 Vertical position (m) within the Big Hand detector. This is for before cuts (black), after event selection cuts (blue), with the selected region of x shaded. In the vertical direction the neutron arm was segmented, giving the segmented structure observed. GLA bars are removed, as seen in the most negative region. See Table 5.5 for cuts.This distribution is for $Q^2 = 3.5$ GeV^2. 120

5.20 Horizontal position (m) within the Big Hand detector. This is for before cuts (black), after event selection cuts (blue), with the selected region of y shaded. In the horizontal direction the neutron arm was not entirely covered by the veto planes, giving the peaks on the two edges. See Table 5.5 for cuts.This distribution is for $Q^2 = 3.5$ GeV^2. . 120

5.21 Presented is the ratio of protons to neutrons within the target for nitrogen. Shown are two models, one a simple extension to the plane wave impulse approximation (in blue), and the other is a model by Udias (in black) [96]. Shown is the ratio for various cuts of $p_\perp$. A cut of 150 MeV was used in this experiment. This is for $Q^2 = 3.5$ GeV^2. . 122

5.22 Presented is the ratio of protons to neutrons within the target for ^{3}He. Shown are from cuts on $p_\perp$. The applied cut on $p_\perp$ was 0.15 GeV with $P_\parallel$ cuts of 400, 250, and 200 MeV for kinematics of $Q^2 =$ 3.5, 2.5, and 1.7 GeV^2. Shown is the ratio for various cuts of inverse distance. This study was done by Aidan Kelleher. 123

5.23 Shown in these figures is the measured uncharged to charged ratio, the uncharged to charged ratio within the model, and the fit line of the model in nitrogen. These are plotted against the natural dependence $\frac{\xi}{T}$. In green are the points of the model. 127

5.24 Shown in these figures is the measured uncharged to charged ratio, the uncharged to charged ratio within the model, and the fit line of the model in hydrogen. These are plotted against the natural dependence $\frac{\xi}{T}$. In green are the points of the model. 128

5.25 Shown in these figures is the measured uncharged to charged ratio, the uncharged to charged ratio within the model, and the fit line of the model in ^{3}He. These are plotted against the natural dependence $\frac{\xi}{T}$. In blue are the points of the model. 129

5.26 Plot $q_\perp$ for a region in time. This is 5 ns removed from the peak region. 131

5.27 Plot $q_\perp$ for a region in time. This is at the quasi-elastic region. 131

5.28 Plot of the ratio of uncharged to charged for the region of $q_\perp$ between 0.55 and 0.60 GeV. The region near 3 ns is removed due to the photon peak being there. Add axis information time (ns), update description (changed plot) 132

5.29 Plot of $q_\perp$ versus time-of-flight for events with only a single hit in the $|t| < 7$ and $q_\perp < 0.15$ region. The area in the spectrum of events coming from k photons via π_0 production was removed (between 2 and 4 ns). This is for run 4090. 132

5.30 Spectrum used to determine the RF correction. This is for run 3888. The peak location is determined from the Mid parameter, which is $t_{rfshift}$. 136

5.31 RF correction versus run number for $Q^2 = 2.5$ GeV^2. Note that since the plotted function is **Fmod** $\left(\frac{1}{0.499}\right)$ that the values of 2 ns and 0 ns are almost equivalent. Run 4146 with a shift of ≈ 1 ns demonstrates that the shift likely is not adequately determined for "junk" runs. . . 137

5.32 Shown is the run number versus raw asymmetry for $Q^2 = 2.5$ GeV^2. . 137

5.33 The four dominant lowest order diagrams in single nucleon scattering. Shown is (a) impulse approximation, (b) meson exchange currents, (c) isobar contributions, and (d) FSI [88]. 144

5.34 In nuclei with more than a single nucleon, the plane wave impulse approximation can be used to give the description of the interaction. Shown are the leading order diagrams for ^{3}He which is the PWIA diagram, single re-scattering diagram, and double re-scattering diagram [88]. 144

5.35 The asymmetry as a function of invariant mass. The plotted curve is the expected change due to the acceptance of the detectors. This shows that the invariant mass doesn't vary much over the region selected (see Table 5.5). 147

6.1 The electric form factor of the neutron with values presented for various experiments including the one presented in this thesis. Also included are representative models of the CQM [71], VMD [15][65], GPD [28][45], and diQuark variety [26]. In black is the traditional Galster parametrization. Circled is the measurement at $Q^2 = 1.3$ GeV^2 which is not included in this thesis. 150

6.2 Shown is the transverse density in the neutron. This is with the magnetic form factor described as a dipole, and the electric form factor described by the fits in Table 6.1. Here + is the previous fit and × is the new fit, the transverse density for these fits is almost identical. 153

6.3 The Dirac form factor, F_1^n, using measured values of G_E^n and the dipole approximation for G_M^n. Shown in black is the Galster parametrization. 154

6.4 The Pauli form factor, F_2^n, using measured values of G_E^n and the dipole approximation for G_M^n. Shown in black is the Galster parametrization. 155

6.5 Ratio of the down and up quark flavor Dirac form factors. The form factors not dependent on G_E^n are just dipole approximations. The black curve is for G_E^n in the Galster parametrization, the dotted curve is for $G_E^n = 0$. 156

6.6 Ratio of the down and up quark flavor Pauli form factors. The form factors not dependent on G_E^n are just dipole approximations. The dotted curve is for G_E^n in the Galster parametrization, the blue curve is for $G_E^n = 0$. 157

6.7 The combined form factors of the proton ($\frac{\mu G_E^p}{G_M^n}$) with values presented for various experiments. Included are the calculations of the electric form factor in the GPD framework with the fits as described in Table 6.2. 161

6.8 The electric form factor of the neutron with values presented for various experiments including those presented in this thesis. Included are the calculations of the electric form factor in the GPD framework with the fits as described in Table 6.2. 162

6.9 Shown are the upper bounds of the value for b. These bounds are determined by applying the condition in equation 6.17 [45]. The solid line is for the Up quark while the dotted is for the down quark. 162

A.1 Calibration of the mean time for plane 1 bar 20. This shows the difference between the time of flight and the expected time of flight peak for quasi-elastic protons between the BigBite scintillators and the front plane of the neutron arm. 175

A.2 Calibration of the horizontal position for plane 1 bar 20. This histogram shows the peak in the horizontal bars time difference, with coincidence with a hit in the "marker" counters. 176

A.3 Calibration of the mean time difference for plane 2 bar 12. This is the difference between neighboring bars in different planes. In particular, this is the difference between plane 1 bar 12 and plane 2 bar 12. . . . 179

A.4 Calibration of the relative horizontal position for plane 2 bar 12. This is the horizontal position (transformed to time) of the hits in plane 1 bar 12 and plane 2 bar 12 for events with well timed hits within the two bars. 180

A.5 Calibration summary plot for run 3975 after pass 3 calibration. In this plot, X is the result, + is the before calibration. On the x axis, 0 is for plane 1 and 1-6 show the differences between planes 1 and planes 2-7). At 7 on the x axis is the horizontal absolute position calibration for plane 1. 181

A.6 Calibration of the veto time for the left veto plane 1 bar 16. 185

A.7 Plot of X position in the veto subtracted by the X position in the neutron arm versus Δt. These are for quasi-elastic hits in the neutron arm. Plotted on the x axis is the time difference between the neutron arm and the veto arm. This identifies a region of 0.3-0.5 m to consider in the veto detector to identify charge hits. 189

A.8 Plotted is the time difference between the veto hit and the neutron arm hit for a single veto plane versus the amplitude in the veto bar. This figure shows all bars in the plane. The gate is seen to start arround 40 ns before the coincidence hit in the neutron arm. The deadtime of the various veto detectors is between 40 and 110 ns. During this dead time, the hits are identified as charged if the amplitude is above 200. For a region of $\pm$10 ns around 0, all events are identified as charged. 190

A.9 Plot showing the rate both with and without a 200 channel ADC cut for the veto detector L1-14. The ADC cut rate is in blue. The window between 300 and 350 ns was used to calculate the rate. This rate is in kHz. 190

A.10 Plot of hits within the Veto detector. Colors are given to show coincidence between the two separate halves of the V1 veto detector. . . . 191

B.1 The physical asymmetry as the accidental background ratio of charged to uncharged used in the calculation is changed. This figure shows that the dependence on this ratio is very small, with an estimated fractional uncertainty on the accidental background charge ratio of 20%. This esimated fractional uncertainty corresponds to a fractional uncertainty of less than 0.2%. Plotted is a linear fit, showing the small dependence. This is for an analysis of Kinematic 2(b). 196

List of Abbreviations

α	alpha
β	beta
γ	gamma
η	eta
λ	lambda

QED	quantum electro-dynamics
QCD	quantum chromo-dynamics
SRF	superconducting radio frequency
RF	radio frequency
RTD	resistive temperature device
CEBAF	continuous electron beam facility
EPR	electron paramagnetic resonance
BB	Big Bite
BH	Big Hand
NA	Neutron Arm
Rb	Rubidium
He	Helium
K	Potassium
SEOP	Spin Exchange Optical Pumping
NMR	nuclear magnetic resonance

Chapter 1

Physics of the Nucleon

1.1 Introduction to the Nucleon

In 1933 with the discovery that the magnetic moment of the proton (having mass M_N and charge e) was not simply that of a point particle, $\frac{e}{2M_N}$, nucleons were known to have internal structure [52]. This structure has been the object of interest to physicists for over 50 years. Nucleon structure may be examined with scattering experiments utilizing electromagnetic, hadronic or "weak" probes. The electromagnetic interaction, by scattering real or virtual photons from the nucleon, can be used to parametrize the unknown electromagnetic structure into effective form factors. One set of parametrizations for the electromagnetic form factors is the Sachs form factors, G_E and G_M, which relate to the charge and magnetic distributions of the nucleons. These form factors only depend on the square of the four-momentum transfer carried by the photon, Q^2.

However, the electromagnetic form factors provide more than just a relation to the charge and magnetization distributions of the nucleon. Any theory of the nucleon must explain the nucleon's structure, and the form factors provide an experimental test of this structure. The form factors are also important for the analysis of many other experiments, so having precise measurements can enable better determination of other quantities.

This thesis reports on a measurement of the neutron's electric (otherwise known as charge) form factor extracted from the asymmetry resulting from polarized electron scattering from a polarized ^{3}He target. The structure of this thesis is as follows. In Chapter 1, the nucleon structure is introduced and discussed within the framework of various models. In Chapter 2, the formalism required for describing the form factors and the discussion of the measurement is developed. In Chapter 3, previous measurements of the electric form factor are presented in addition to selected fits within the framework of the models discussed in Chapter 1. In Chapter 4, the experiment is introduced, along with a description of the experimental apparatus. In Chapter 5, the analysis is presented along with the experimental values for G_E^n. Finally, in Chapter 6 new results are discussed in the context of the presented models, the flavor form factors are decoupled, and the quark orbital angular momentum is presented. The remainder of this chapter will have a short introduction to quantum chromo-dynamics (QCD) presented in section 1.2 and an introduction to the various models of nucleon structure in section 1.3.

1.2 QCD

The ground state structure of the nucleon can be investigated using momentum transfer in an elastic scattering experiment, where the initial state of the nucleon is not changed. In electron scattering, the electromagnetic properties of the nucleon are probed, and they are characterized by the aforementioned form factors. These form factors express the difference between scattering from an object with internal

structure and scattering from a point particle.

In the very successful theory of the strong interaction, quantum chromo-dynamics (QCD), the nucleon is the lowest energy three-quark bound state. QCD is similar in structure to quantum electro-dynamics (QED), but where in QED the strength of interaction is governed by electric charge and the exchange particle is photon, in QCD the exchange particles are gluons and the interaction strength is due to color charge. The nucleons are then made up of these gluons and quarks, with the individual quarks being resolved in the Bjorken limit. The three lightest quarks are identified in Table 1.1.

The notion of valence versus "sea" quarks, where it is the valence quarks that define the electromagnetic attributes of the hadron, is useful. For the proton, the valence quarks are two up quarks and one down quark, for the neutron the valence quarks are two down quarks and one up quark.

Protons and neutrons, as has been implied here, share many similar properties. Models and theories have been developed to explain both proton and neutron properties together, in terms of their shared properties as nucleons. Similar properties are expected because both nucleons are made up of the same constituents, and have the same types of valence quarks. Both also have the same spin, are very close in mass, and are long lived. This allows one to discuss the two nucleons as two states of a single object, differentiated by the additional quantum number "isospin". When the next lightest quark, the strange quark (with strangeness charge -1), is included, an SU(3) symmetry group can be formed, although this symmetry is only approximate due to the larger mass of the strange quark.

The charge in QCD is color, with three colors instead of the single electromagnetic charge which is familiar from classical physics. A significant distinction of QCD is that, unlike the photon in QED, the exchange particles (gluons) hold the property of color themselves. As a result, the gluons can interact with each other, and a quark of a particular color will be "anti-screened", causing the force to increase as distance increases. This phenomenon results in confinement. The three color charges of the quark form a SU(3) group as well. This confinement and the creation of the QCD vacuum implies the existence of "sea quarks" ($\bar{u}u$, $\bar{d}d$, $\bar{s}s$) and gluons within the nucleon [46].

name	electric charge	isospin	strangeness	current quark mass [35]
u (up)	$+\frac{2}{3}$	$\frac{1}{2}$	0	1.5 to 4 MeV
d (down)	$-\frac{1}{3}$	$-\frac{1}{2}$	0	4 to 8 MeV
s (strange)	$-\frac{1}{3}$	0	-1	80 to 130 MeV

Table 1.1: The three light quarks and their respective charges. Other quarks are the c (charm), b (beauty), and t (top) quark, but they are too heavy to play a large role in the experiments described here. These three light quarks form the SU(3) group.

1.2.1 Perturbative QCD

Quantum electrodynamics is a highly successful and calculable theory, in part because it is perturbative. This is not the case for QCD. At large distances from the bare charge, the QED coupling is the familiar $\alpha(Q^2) \approx \frac{1}{137}$ while the QCD coupling, $\alpha_s(Q^2)$, is ≈ 1 at low momentum transfer making an expansion in $\alpha_s(Q^2)$ impossible. However, the coupling decreases with increasing Q^2, the theory is said

to be "asymptotically free". The renormalization scale, Λ, defines the energy at which the effective coupling becomes large. When Q^2 is well below this, quarks and gluons are bound into hadrons [46].

At sufficiently high momentum transfers ($Q^2 > \Lambda^2$), we would expect to be able to understand the nucleon structure using perturbative QCD. A virtual photon of high enough transferred momentum will see the nucleon as consisting of three massless quarks moving collinearly. In (quasi-)elastic scattering the momentum of the virtual photon is shared among the three quarks through two hard gluon exchanges, with each gluon's momentum being proportional to Q. This gives the dominant scaling of $1/Q^4$ for the helicity conserving form factor (known as $F_1(Q^2)$). This power counting is justified by QCD factorization theorems [12].

1.3 Nucleon Structure

When the transferred momentum is below the scale Λ, the QCD interaction is strong and quarks are confined. In this parameter space there is no clear way to calculate quantities using QCD analytically. There is much promise for future calculations using direct computational techniques such as Lattice QCD. In the meanwhile, various models have been developed to describe the dominant features of nucleon structure.

1.3.1 Partons

In deeply inelastic scattering (DIS), where the proton breaks up, the final state of the interaction cannot be described by a particle in a single final state. Because of this, a tensor $W^{\mu\nu}$ is used to parametrize the unknown final state. In the Bjorken limit ($Q^2 \to \infty$), apparent point particles known as quarks are resolved inside of the nucleon, each of which is carrying some fraction of the nucleon's four-momentum. The nature of the strong interaction is such that individual quarks are never seen; instead these "partons" exit the nucleon in jets of colorless hadrons; either qqq baryons or $q\bar{q}$ pairs (mesons). At lower momentum transfers where deep inelastic scattering is not applicable, mesons can also be produced through the production and decay of a nucleon excited state.

In the infinite momentum frame, where the momentum of the hadron is large and all masses can be neglected, and in the case that the invariant mass of the system is large, the response tensor $W^{\mu\nu}$ can be represented in terms of dimensionless structure functions. It is useful for these to be expressed in terms of Bjorken x, a dimensionless kinematic variable of the virtual photon. This variable gives the component (xE) of the initial energy/momentum carried by the resulting "parton". In the limit $x \to 1$, all of the momentum is being carried by the parton, and so the valence quarks dominate the interaction. As x approaches 0, the sea quarks dominate. The momentum which is not carried by the quarks and antiquarks is carried by the gluons [46].

The analysis of partons and the constituents of the nucleon is made more

complicated because many energetic terms must be included. This means that relativistic effects should be considered. However, this makes the interpretation of the wave function unclear, because a Lorentz boost mixes the momentum states. If QCD is quantized at a fixed light-cone time, τ, where $\tau = t + \frac{z}{c}$, the challenges of mixing due to Lorentz boosts is removed along with the complexity of the vacuum in relativistic quantum field theory. The following models and interpretations of nucleon structure are mostly considered in such a quantization. Further discussion on this is in Section 6.1 [19][20][21][64].

In elastic scattering, where the nucleon neither breaks up nor is excited, there is a single final state. The tensor $W_{\mu\nu}$ then can be reduced to a form factor. Obviously, a complete model of the internal structure of the nucleon must include a description of form factors. In the case of a spin-$\frac{1}{2}$ object like a nucleon, there are two independent form factors, which can be expressed in the form of Sachs electric and magnetic form factors (G_E and G_M) or as the Pauli and Dirac form factors, F_1 (chirality conserving) and F_2 (chirality-flip) (The relationship between these will be described in Chapter 2). In addition to elastic and deeply inelastic scattering other hard exclusive processes such as deeply virtual Compton scattering (DVCS), can also used to investigate nucleon structure (for a pictorial description see figure 1.1) [23] [46].

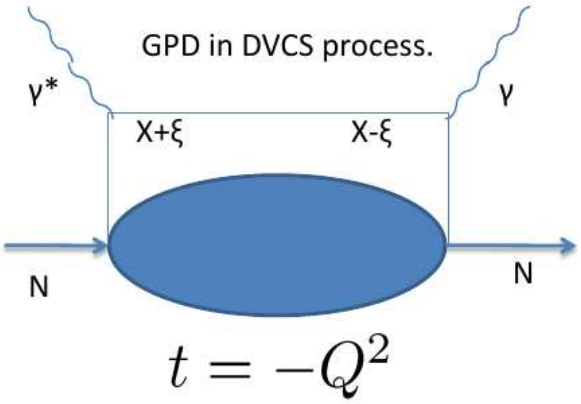

Figure 1.1: Shown is a schematic of the DVCS process, in the framework of generalized parton distributions (GPDs). Here ξ is the skewness, x is the longitudinal momentum fraction, N is the nucleon, $\gamma*$ is the virtual photon, and γ is the detected photon. The skewness gives the longitudinal momentum asymmetry, as shown in the figure.

1.3.2 The Constituent Quark Model

An early model of nucleon structure is the constituent quark model (CQM). In this case, the nucleon is a ground state of three massive quarks in a confining potential. The masses of these quarks are determined by SU(3) flavor symmetry and it is assumed that the mass of the hadron is held by just the valence quarks. While relativistic modifications of this model have had some descriptive success, the model does not satisfy the chiral symmetry of the QCD Lagrangian. Some modifications, such as goldstone-boson-exchange (GBE) where there is an additional quark-quark interaction, and the one-gluon exchange (OGE), provide a general fit to the data for the form factors and the radii of the nucleons.

The long distance behavior of hadronic wave functions should be able to be described by the exchange of the lightest of the $q\bar{q}$ states, the pions. As a result, pion signatures should be seen in the low momentum behavior of hadrons, and the

addition of this pion cloud to the constituent quark model is used to form a better model of the nucleon. An early model of this type is the cloudy bag model. Here the pion cloud interacts with the confined quarks such that chiral symmetry is restored. This cloudy bag model provides a good fit of low Q^2 nucleon form factors [76][69].

1.3.3 Generalized Parton Distributions

In a number of reactions, the scattering amplitudes factorize such that they can be described by a simple diagram known as the handbag diagram. Here there is one valence quark interacting with the virtual photon, with the rest of the structure contained within a generalized parton distribution (GPD). An appealing feature of GPDs is that, depending on the kinematic limit selected, they can be related to a wide variety of scattering processes, such as deeply inelastic scattering, deeply virtual Compton scattering, wide angle compton scattering, and elastic scattering [29] [45].

Currently, GPDs cannot be measured explicitly, and are instead expressed by models which are generally simple parametrizations constrained by the GPD relationship to the form factors, properties of the nucleon, and by the fact that the GPDs become parton densities in vanishing momentum transfer.

In this framework, hard exclusive reactions (like DVCS) result in an interaction between the probe and a single quark within the nucleon (see Figure 1.1). At leading order, the interaction that is described by the traditional form factors can also be described by four Generalized Parton Distributions (GPDs), these GPDs depend

on the longitudinal momentum fractions (light-cone and skewness), and the squared four-momentum transfer (Q^2) to the nucleon. The four GPDs are H^v and E^v, where v indicates either an up quark or a down quark. [1]

These GPDs depend on Bjorken x, momentum transfer Q^2, skewness (ξ), and a scale parameter μ. The following sum rules, which are independent of ξ, relate the GPDs and the form factors:

$$\int_{-1}^{1} dx H_v(x, \xi, Q^2) = F_1^v(Q^2) \ , \tag{1.1}$$

$$\int_{-1}^{1} dx E_v(x, \xi, Q^2) = F_2^v(Q^2) \ . \tag{1.2}$$

$F_{1,2}^v(Q^2)$ are the flavor form factors, which describe the distribution of that flavor of quark within the nucleon. These can be expressed in terms of the electromagnetic form factors as $F_1^u = 2F_1^p + F_1^n + F_1^s$ and $F_1^d = 2F_1^n + F_1^p + F_1^s$, where F_1^s is the strangeness form factor of the nucleon. It is assumed, here as in most analyses, that the strange form factor is negligible. Similar relationships exist for the Pauli form factor, F_2. The GPDs must still be modeled in order to predict form factors, and usually this is done using the sum rules [29][28][45].

1.3.4 Vector meson dominance models

Some of the earliest models coupled a virtual photon to the nucleon both through its internal structure and through exchange of intermediate vector mesons with a meson cloud. These vector mesons (the ρ^0, ω, and ϕ) have the same quantum

[1] There are other GPDs which aren't related to the electromagnetic form factors such as one to describe the polarized distribution.

numbers as the virtual photon and are the lightest hadrons in the time-like region ($Q^2 < 0$ in the standard definition), and so could potentially play a major role in nucleon structure at low Q^2. The form factors are commonly described by a dipole form, resulting from two nearby vector meson resonances (poles) that have opposite residue. This structure can be written in terms of a photon-meson coupling strength ($C_{\gamma V_i}$) and a meson-nucleon vertex ($F_{V_i N}$):

$$F^{iv,is} = \sum \frac{m_i C_{\gamma V_i}}{Q^2 + m_i^2} F_{V_i N}(Q^2). \tag{1.3}$$

These isovector and isoscalar form factors (F^{iv} and F^{is}) are then written as linear combinations of the electromagnetic form factors [76][77].

The internal structure coupling is sometimes identified with the three valence quarks. The initial models had only F_1 coupling with the internal structure, but some of those considered in this thesis include F_2 as well [15][65].

1.3.5 Chiral effective field theory

In chiral effective field theory, the electromagnetic form factors are computed using a chiral effective Lagrangian with pion, nucleon, and Δ fields. The short distance physics is determined by low-energy constants, which are fit using the measured nucleon charge radius and moments. While this technique has had some success at low Q^2, by about 0.4 GeV^2 the predictions break down, due to an increasing role of vector mesons. Since this thesis deals with G_E^n at intermediate Q^2, such models can not reliably provide a description of the discussed data. Thus, the focus will be on models that are more appropriate to the energy regime investigated

in this experiment [76].

1.3.6 Dyson-Schwinger Equations

As has been expressed earlier, there is a significant difference between the bare quark and the dressed (or "anti-screened") quark. All models of nucleon structure at intermediate Q^2 try to describe this difference. In a framework that uses Dyson-Schwinger equations, the primary cause of this parton behavior is a dense cloud of gluons which surround the quark at low momentum transfer ($Q^2 < M_N^2$). This is a manifestation of dynamical chiral symmetry breaking (DCSB), and becomes a source for the nucleon's mass [26].

Describing the relativistic region in a framework that is consistent with this low energy description is difficult. In terms of these DSE, the nucleon appears as a pole in a six-point Green's function. Here, the three dressed quarks are described in terms of a "bystander" quark and a diquark pseudoparticle in a single color-$\bar{3}$ channel. The binding depends on the exchange of the bystander quark and quarks in the diquark pseudoparticle. This framework combines the descriptions of mesons and nucleons. It is the observation of this diquark description of the nucleon which is used to truncate the DSE and allow calculations using DSE.

An interesting prediction of models in this framework is that the radius of the "dressed" u-quark in the neutron is greater than that of the d-quark [14] [83] [26]. Another is that since the up and down current quark masses are thought to be small, the dominant mechanism for the helicity flip behavior in QCD comes from

quark orbital angular momentum and an additional polarized gluon [26].

1.4 Experimental Investigation

These various models described above provide a description of the nucleon which is more complete than the simple constituent quark model or dynamical chiral symmetry breaking. Most of these models share, as part of their description, a non-zero current quark orbital angular momentum. In this regime, the constituents of the nucleus are dominated by the up and down quarks (with possibly a small strange quark component). The simplest probe available of this structure is the electron. The common experimental techniques used to study this behavior and to investigate the models are deep inelastic scattering (DIS), deeply virtual Compton scattering (DVCS), and (quasi-)elastic scattering. By expanding our knowledge of the nucleon form factors, the pieces needed to complete our picture of the neutron are brought together. The measurement described in this thesis is one important piece. The physics of electron scattering will be developed in the next section.

Chapter 2

Physics of Electron and Nucleon Scattering

2.1 Introduction to electron scattering

Scattering is the process in which a particle is deflected during an interaction. There are two main categories of scattering, elastic, where the particles are left intact and only the momentum changes, and inelastic, where the scattered particles are modified, excited, or destroyed. The differential scattering cross section is often written as the product of a cross section for scattering from a spin-0 point particle and a "form factor" which characterizes the structure of the target

$$\frac{d\sigma}{d\Omega} = \left(\frac{d\sigma}{d\Omega}\right)_{Mott} f_{rec}|F(q^2, \theta_e)|^2 \ . \tag{2.1}$$

Here F is the form factor, q is the momentum transfer, the Mott cross section is that of a spin-$\frac{1}{2}$ electron scattered from a point-like particle, and f_{rec} is a kinematic factor (to be defined later). For a spin $\frac{1}{2}$ particle, $F(q^2, \theta_e)$ can be expressed in terms of the form factors G_E and G_M, which will be developed later [46].

The neutron is known to have no net charge. With high energy electrons, distances smaller than the size of a nucleon can be probed, allowing the structure to be described at different scales. Nonetheless, the neutron electric form factor is small compared to the other nucleon form factors. Various models exist that provide detailed descriptions of the nucleon over different kinematic ranges; specific

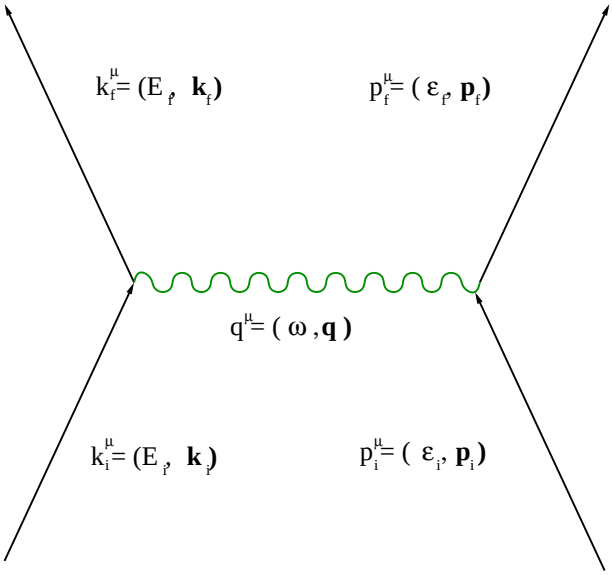

Figure 2.1: Feynman diagram for one interaction between an electron and a nucleon. The electron has four-momentum k^μ and the nucleon has four-momentum p^μ.

examples of models giving G_E^n at intermediate Q^2 will be given in more detail in section 3.1.

2.2 Definition of kinematic variables

The interactions of electrons and photons are well understood within the theory of quantum electrodynamics (QED). In this interaction, the properties of the incident and scattered electron and recoiling nucleon can be measured.

In the Feynman diagram in figure 2.1, the following kinematic variables are defined. The nucleon four-momentum is $p^\mu = (\epsilon, \mathbf{p})$, $k^\mu = (E, \mathbf{k})$ is the electron four-momentum, and $q^\mu = (\omega, \mathbf{q})$ is the virtual photon four-momentum. The four-momentum transferred to the nucleon is $q^2 = q_\mu q^\mu = \omega^2 - \mathbf{q}^2$, and is carried by the virtual photon. If evaluated in the laboratory frame, $\mathbf{p}_i = 0$ and $\epsilon_i = M_N$, where

M_N is the recoil nucleon mass. Since q^2 in electron scattering is space-like, Q^2 is best defined as $Q^2 = -q^2 = 4E_iE_f \sin^2 \frac{\theta_e}{2}$ (in the approximation $m_e = 0$), where θ_e is the angle the electron deviates from its initial direction. Q^2 is typically the quantity used to parametrize the form factors.

2.2.1 Current operator

The current of the electron in Figure 2.1 is arrived at from QED [46]

$$j^\mu(k_f, k_i) = \bar{u}(k_f)(-ie\gamma^\mu)u(k_i) \ . \tag{2.2}$$

Here γ^μ is the standard Dirac matrix and e is the electric charge. In this expression u is the Dirac spin $\frac{1}{2}$ spinor. For the spinor the following completeness relation holds

$$\sum_{s=1,2} u^{(s)}(p)\bar{u}^{(s)}(p) = \gamma^\mu p_\mu + m \ . \tag{2.3}$$

Similarly, the current for a structureless, spin $\frac{1}{2}$ charged particle can be expressed as

$$J^\mu(p_f, p_i) = \bar{u}(p_f)(-ie\gamma^\mu)u(p_i) \ . \tag{2.4}$$

These provide the invariant scattering amplitude $\mathcal{M}$ using the rules for Feynman diagrams. Following standard conventions, repeated indices are summed over

$$i\mathcal{M} = J^\mu(p_f, p_i)\frac{-ig_{\mu\nu}}{Q^2}j^\nu(k_f, k_i) \ . \tag{2.5}$$

2.2.2 Dirac and Pauli form factors

The vertex factor for the nucleon-photon interaction is not exactly known, but rather parametrized in terms of form factors. These form factors must be

functions of q^2 since it is the only independent Lorentz scalar at the nucleon vertex in elastic scattering. Generally, the form factors can be constructed with any Lorentz-invariant constituent; γ^μ, γ^5, or $\sigma^{\mu\nu}$. However, the choices of $i\sigma^{\mu\nu}q_\nu$ and γ^μ are made to conserve parity. Other possible forms are restricted due to current and parity conservation. The two terms, γ^μ and $i\sigma^{\mu\nu}q_\nu$, give a current of

$$J^\mu(p_f, p_i) = \bar{u}(p_f)[e(\gamma^\mu F_1(q^2) + \frac{i\sigma^{\mu\nu}q_\nu}{2M_N}F_2(q^2))]u(p_i) \ , \tag{2.6}$$

where F_1 and F_2 are known as the Dirac and Pauli form factors. They are normalized to give the proper charge and magnetic moment at $q^2 = 0$, so that

$$\begin{aligned} F_1^p(0) = 1, \ F_2^p(0) = \kappa_p \\ F_1^n(0) = 0, \ F_2^n(0) = \kappa_n \ . \end{aligned} \tag{2.7}$$

where κ is anomalous contribution to the nucleon's magnetic moment.

The Dirac and Pauli form factors are a parametrization of the electromagnetic structure in a different basis than the Sachs form factors. The Sachs form factors can be expressed in terms of F_1 and F_2 as [58]

$$G_E = F_1 - \tau F_2 \ , \ G_M = F_1 + F_2 \ , \tag{2.8}$$

where $\tau = \frac{Q^2}{4M_N^2}$.

2.3 Breit frame

As mentioned previously, the Sachs form factors can be related to the charge and magnetic moment distribution, in a particular reference frame called the Breit frame. No energy is transferred, only momentum ($\mathbf{p}_i = -\mathbf{p}_f$), therefore

$$Q^2 = \mathbf{q}_B^2 \ . \tag{2.9}$$

An important aspect of the Breit frame is that the Fourier transform of the electric form factor gives the charge density distribution, and that of the magnetic form factor gives the magnetic current density distribution.

The four components of the hadronic current in this frame are [46] [76]:

$$J^0 = ie2M_N\bar{u}_f(F_1 - \tau F_2)u_i = ie2M_N\bar{u}_f G_E u_i \ , \tag{2.10}$$

$$\overrightarrow{J} = -e\bar{u}_f(\overrightarrow{\sigma} \times \mathbf{q}_B)(F_1 + F_2)u_i = -e(\overrightarrow{\sigma} \times \mathbf{q}_B)\bar{u}_f G_M u_i \ . \tag{2.11}$$

Here $\overrightarrow{\sigma}$ is the Pauli spin matrices. Using this, Sachs [87] showed that G_E and G_M can be expressed as the Fourier transforms of the nucleon charge and magnetization densities

$$G_E(Q^2) = \frac{4\pi}{Q}\int r dr \rho_{ch}(r)\sin Qr \tag{2.12}$$

$$G_M(Q^2) = \frac{4\pi}{Q}\int r dr \mu\rho_{mag}(r)\sin Qr. \tag{2.13}$$

At low Q, equation 2.12 can be expanded such that

$$G_E(Q^2) = 1 - \frac{1}{6}Q^2\langle r_E^2\rangle + \frac{Q^4}{120}\langle r_E^4\rangle + ... \tag{2.14}$$

From this we can see a simple formula for the charge radius of the neutron. At very low momentum transfer, the slope of the form factor with respect to Q^2 defines the mean square radius of the distribution [60],

$$< r_n^2 >= -6\frac{d(G_E^n)}{dQ^2}\Big|_{Q^2\to 0}. \tag{2.15}$$

This is obviously only true in the non-relativistic limit. Recently, Miller *et al.* have developed a formalism that allows a representation of the transverse charge and magnetization densities that are not reference frame dependent [70].

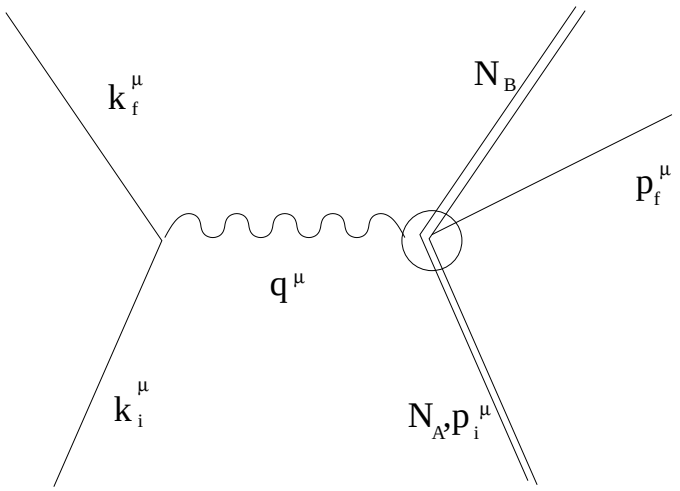

Figure 2.2: Feynman diagram for interaction between an electron and the nucleus. The electron has four-momentum k^μ and the ejected nucleon has momentum p_f^μ.

2.4 Quasi-elastic scattering

Rarely in scattering experiments is there an opportunity to scatter from a single nucleon. This is especially true of the neutron, which is short lived in its free state. There are many different approximations that can be used to put the nucleus in terms of elements that are better understood. Some of these are referenced in sections 5.5 and 5.7.1. While discussing all of them is out of the scope of this thesis, two which allow the final state nucleus to be understood in terms of a remainder nucleus and a scattered nucleon merit development. These are the impulse approximation (IA), and the plane wave impulse approximation (PWIA). Here and throughout much of this thesis, discussion will be formulated in terms of the one-photon exchange approximation.

2.4.1 Impulse approximation

In the impulse approximation the virtual (off-shell) photon interacts with a single nucleon. Afterward, the struck nucleon leaves the nucleus without any further interaction with the remaining "spectator" nucleons. This approximation can also be described as the assumption that the current of the nucleus is given by the sum of the currents of the individual nucleons, where the nucleons are treated as free particles [27].

The simplest nucleus that can be discussed in such terms is the deuteron. In the IA, the differential cross section for scattering from a neutron or proton embedded in the deuteron can be factorized. This allows the contributions of the neutron and proton to be separated. For an electron to scatter from a nucleon inside the deuteron, the contributions from the proton and the neutron can be separated

$$\frac{d\sigma_{ed}}{d\Omega} \approx \frac{d\sigma_{ep}}{d\Omega} + \frac{d\sigma_{en}}{d\Omega} \ . \tag{2.16}$$

This approximation, however, completely neglects nuclear binding and the inherent Fermi motion of the bound nucleons. It also neglects that the nucleon might re-scatter, the virtual photon might couple to a virtual meson exchanged between the nucleons, or the virtual photon might couple to an excited state of a nucleon (known as Isobar Configuration or IC). The quasi-elastically scattered nucleon interactions with the other "spectator" nucleons are known as final state interactions (FSI).

2.4.2 PWIA

A more detailed simple approximation is the Plane Wave Impulse Approximation (PWIA). This approximation is a quasi-free one, and is important in discussions of neutron double polarization experiments, where either the target or the recoiling nucleon is polarized. In PWIA the polarization of the recoiling nucleon or of the target is restricted to the scattering plane. The longitudinal component is parallel to the recoiling nucleon's momentum vector, and the transverse component is perpendicular [66]. In this approximation the initial and final state of the target nucleus are represented as products of plane waves for a nucleus and nucleon, where the nucleon is bound (with momentum $\mathbf{p}_i$). The nucleon absorbs the virtual photon, while the nucleus remains as a spectator. The nucleon then leaves the nucleus, which is assumed to be free after the absorption of the virtual photon, without any further interaction.

2.5 Polarization observables

A convenient coordinate system to work with observables when the beam, target, or recoiling nucleon are polarized is defined by [77]

$$\begin{aligned} \hat{z} &\parallel \mathbf{q}, \\ \hat{y} &\parallel \mathbf{k}_i \times \mathbf{k}_f, \\ \hat{x} &= \hat{y} \times \hat{z}. \end{aligned} \tag{2.17}$$

It is useful to refer to the polarization vector $\overrightarrow{P}$, which can serve as either the polarization of the nucleon inside the target in beam-target asymmetry mea-

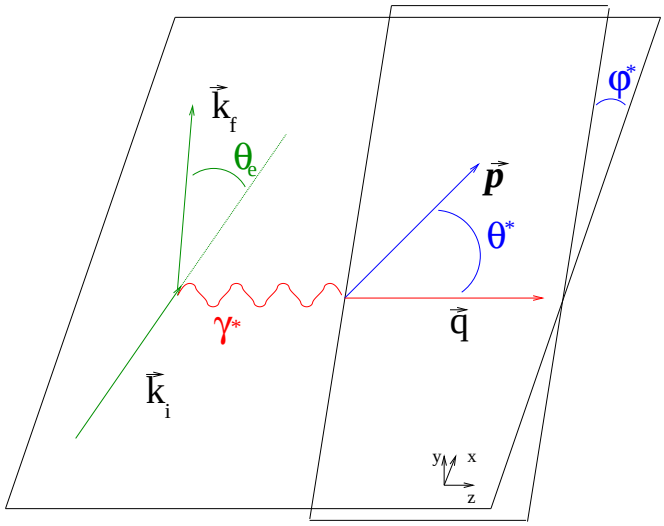

Figure 2.3: Polarization exchange in the one photon exchange approximation for polarized-electron, polarized nucleon scattering. θ and ϕ define the polarization of the recoiling nucleon.

surements, or the polarization of the ejected nucleon in beam-recoil polarization experiments.

$$\overrightarrow{P} = P(\sin\theta\cos\phi\hat{x} + \sin\theta\sin\phi\hat{y} + \cos\theta\hat{z}) \tag{2.18}$$

In the general case of parity conserving polarized scattering there are 18 independent response functions. Under the approximations of one photon exchange, PWIA, and parallel kinematics, only four terms survive. The cross sections of both a recoiling polarized nucleon and a polarized target share similar forms, and can be written in terms of products of kinematic quantities and response functions [58]. The kinematic variables (following the development in [58]) for these reduced terms are

$$V'_{TL} = (1-\tau)^{-1}\tan\frac{\theta_e}{2}\ , \tag{2.19}$$

$$V_T = \frac{1}{2(1-\tau)}\ , \tag{2.20}$$

$$V_L = \frac{1}{(1-\tau)^2} \ , \tag{2.21}$$

$$V'_{TT} = \sqrt{(1-\tau)^{-1} + \tan^2\frac{\theta_e}{2}}\tan\frac{\theta_e}{2} \ . \tag{2.22}$$

The response functions depend on the polarization of the recoiling nucleon and the target nucleus. These kinematic variables arise from the electron tensor in an alternate basis, where the coefficients refer to the nuclear response function with which the kinematic variable is associated ($_L$, $_{TL}$, $_T$ or $_{TT}$). The response functions arise from the nuclear response tensor ($W^{\mu\nu}$). The nuclear response tensor serves to parametrize the increased generality of the nucleus, where the same current doesn't exist in the initial and final states [46]. The four reduced response functions are $R'_{TT}(\hat{z})$, $R'_{LT}(\hat{x})$, R_L, and R_T, the first two of which reflect components associated with the polarized nature of the cross section. These subscripts $_L$ and $_T$ correspond to "longitudinal" and "transverse".

Two additional response functions exist for nuclei with more than one nucleon. These are R_{TT} and R_{TL} and only appear when the change in total angular momentum is greater than two units [31] [80].

2.5.1 Recoil polarization

From PWIA it can be shown that the unpolarized nuclear response tensor is symmetric, $W^{\mu\nu} = W^{\nu\mu}$. This means that the response tensor for recoil polarization is

$$W^{\mu\nu}(\hat{a}) = -W^{\nu\mu}(\hat{a}) = W^{\nu\mu}(-\hat{a}) \ . \tag{2.23}$$

In double-polarization experiments parallel kinematics are often used; under

these kinematics the nucleon's final momentum is parallel to the momentum transfer. Also, at the electron beam energies in the experiments described here, only the longitudinal component of the electron polarization is relevant.

In the laboratory reference frame there are two response functions that describe the polarization (in PWIA), $R'_{TT}(\hat{z})$ and $R'_{LT}(\hat{x})$. These are the longitudinal and transverse response functions from which the transverse (P_x) and longitudinal (P_z) components of recoil polarization arise [58].

The general form of the nuclear structure tensor, with a polarized target or recoiling nucleon, can be written as [76]:

$$W_{\mu\nu} = J_\mu J^*_\nu = W^0_{\mu\nu} + W_{\mu\nu}(\overrightarrow{P}_f) + W_{\mu\nu}(\overrightarrow{P}_i) + W_{\mu\nu}(\overrightarrow{P}_i, \overrightarrow{P}_f) \ . \tag{2.24}$$

In recoil polarization experiments, typically only the final nucleon polarization is measured, and $W_{\mu\nu}$ reduces to (in the Briet frame)

$$W_{\mu\nu} = \frac{1}{2} Tr F_\mu F^\dagger_\nu \overrightarrow{\sigma} \cdot \overrightarrow{P} \ . \tag{2.25}$$

Here $F_0 = 2M_N G_E$ and $F_j = iM_N G_M \vec{\sigma} \times \mathbf{q}_B \cdot \hat{j}$, where $j = x, y, z$. This gives $W_{\mu\nu}(P_x) \propto 2M_N G_E G_M$ and $W_{\mu\nu}(P_z) \propto G_M^2$.

As an example, this leads, after transformation back to the lab frame, to the following components of the recoil polarization of a free neutron [47][92]:

$$P_x = -P_e \frac{\sqrt{2\tau\epsilon(1-\epsilon)} G^n_E G^n_M}{\epsilon (G^n_E)^2 + \tau (G^n_M)^2} \ , \tag{2.26}$$

$$P_y = 0 \ , \tag{2.27}$$

$$P_z = P_e \frac{\tau\sqrt{1-\epsilon^2} (G^n_M)^2}{\epsilon (G^n_E)^2 + \tau (G^n_M)^2} \ , \tag{2.28}$$

where $\epsilon = [1 + 2(1+\tau)\tan^2 \frac{\theta_e}{2}]^{-1}$, and P_e is the polarization of the electron beam.

2.5.2 Target polarization

The arguments and results are similar for a polarized target, where the detected nucleon is either unpolarized or not detected. Once more, in parallel kinematics, the one photon interaction approximation, and PWIA, only the $\hat{x}$ and $\hat{z}$ components of the target polarization vector remain.

In the response function formulation, and with spin-$\frac{1}{2}$ nucleons, to within a multiplicative constant, the response functions are functions of the components $F_L = (1+\tau)G_E$ and $F_T = \sqrt{2\tau(1+\tau)}G_M$. The general expression for such a response function is

$$\sum_{j,j'} A_{j,j'}(k) F_j F_{j'} \tag{2.29}$$

where the $A_{j,j'}(k)$ has only two terms left for the polarized response, the F_T^2 and $F_L F_T$ terms. This formulation is developed in general for more complicated systems than elastic scattering with a polarized nucleon by Donnelly and Raskin [31] [80].

The response functions for the target are then [58]:

$$R_{LT}^T(\hat{x}) = 2\sqrt{\tau(1+\tau)}G_E G_M \ , \tag{2.30}$$

$$R_{TT}^T(\hat{z}) = 2\tau G_M^2 \ . \tag{2.31}$$

2.6 Cross section with unpolarized observables

The unpolarized differential cross section is dependent on the square of the scattering amplitude (spin averaged since it is unpolarized),

$$\frac{d\sigma}{d\Omega} = \frac{m_e^2}{4\pi^2}\frac{E_f}{E_i} f_{rec} \frac{1}{4}\sum |\mathcal{M}|^2, \tag{2.32}$$

where $f_{rec} = [1 + \frac{2E_i}{M} \sin^2 \frac{\theta_e}{2}]^{-1}$. It is useful to define the Mott cross section, which corresonds to a relativistic electron scattering from an unstructured target

$$\frac{d\sigma_{Mott}}{d\Omega} = \frac{\alpha^2 \cos^2 \frac{\theta_e}{2}}{4E_i^2 \sin^4 \frac{\theta_e}{2}}. \tag{2.33}$$

Here α is the fine structure constant.

Using the equations 2.2, 2.6, 2.32, and the Feynman rules the following relationship between the four-momenta, angles, and other elements of the electron and interacting fermion give the differential cross section. This relationship between the form factors and the cross section is also known as the Rosenbluth formula.

$$\frac{d\sigma}{d\Omega} = \left(\frac{\alpha^2}{4E^2 \sin^4 \frac{\theta_e}{2}} \right) \frac{E_f}{E_i} \left[\left(F_1^2 - \frac{q^2}{4M^2} F_2^2 \right) \cos^2 \frac{\theta_e}{2} - \frac{q^2}{2M^2} \left(F_1 + F_2 \right)^2 \sin^2 \frac{\theta_e}{2} \right] \tag{2.34}$$

Putting this in terms of the Sachs form factors gives [58]:

$$\frac{d\sigma}{d\Omega} = f_{rec} \left(\frac{d\sigma}{d\Omega} \right)_{Mott} [\frac{G_E^2 + \tau G_M^2}{1 + \tau} + 2\tau G_M^2 \tan^2 \frac{\theta_e}{2}]. \tag{2.35}$$

This is much simpler than equation 2.34 and readily suggests a method of measurement of the form factors. This method of measurement is known as the Rosenbluth Technique.

2.7 Cross section with polarized observables

The general form for the cross section when the beam of electrons is polarized and the polarization of the ejected particle is detected is:

$$\frac{d^6\sigma_{h,s}}{dE_f d\Omega_{k_f} d\epsilon_f d\Omega_{p_f}} = \sigma_{unpol} \frac{1}{2} (1 + \overrightarrow{P}_i \cdot \overrightarrow{\sigma} + h(A + \overrightarrow{P}_T \cdot \overrightarrow{\sigma})). \tag{2.36}$$

Here P_i is the induced polarization in the proton, h is the helicity of the incident electron, A is the beam analyzing power, s is the nucleon spin projection on σ, σ^{unpol} is the unpolarized cross section, and P_T is the polarization transfer coefficient [58]. In coplanar kinematics $A = 0$, $\mathbf{P}_i \cdot \overrightarrow{\sigma} = \mathbf{P}_i \cdot \hat{N}$, and $\mathbf{P}_T \cdot \hat{N} = 0$. Since $\mathbf{P}_i \cdot \hat{N} = 0$ in PWIA, two terms survive to provide the nucleon polarization, and from equations 2.26 and 2.28 an elegant measurement of G_E^n is possible.

This is similar in form to the cross section of polarized electrons on a polarized target where the recoil polarization is not measured:

$$\frac{d^6\sigma}{dE_f d\Omega_{k_f} d\epsilon_f d\Omega_{p_f}} = \sigma_{unpol}\frac{1}{2}(1 + \overrightarrow{P}_t \cdot \overrightarrow{A}_T + h(A + \overrightarrow{P}_t \cdot \overrightarrow{A}'_T)). \tag{2.37}$$

The new variables here are P_t which is the target polarization vector, A_T which is the target analyzing power, and A'_T which is the correlation vector [58].

Using a longitudinally polarized electron beam and a polarized target, the cross section can be written as:

$$\sigma^{pol} = \Sigma + h\Delta, \tag{2.38}$$

where Σ is the unpolarized cross section from equation 2.35, and Δ is the helicity dependent part [31]. Under the approximations of PWIA and one photon exchange, and in the case of parallel kinematics and relativistic electron beam, the cross section simplifies to [58]:

$$\sigma^{pol} = \sigma_{Mott} f_{rec}[V_L R_L + V_T R_T + h P_{target}(V'_T R'_{TT}(\hat{z}) + V'_{TL} R'_{TL}(\hat{x}))]. \tag{2.39}$$

Using equations 2.19, 2.22, 2.31, 2.30, Δ is given by

$$\Delta = -2\sigma_{Mott} f_{rec} \tan\frac{\theta_e}{2}\sqrt{\frac{\tau}{1+\tau}}(\sqrt{\tau(1+(1+\tau)\tan^2\frac{\theta_e}{2})}\cos\theta G_M^2 + G_E G_M \sin\theta\cos\phi). \tag{2.40}$$

Chapter 3

Form Factors

3.1 Models and fits

While the theory for strong interactions, QCD, is well known, because of confinement it is impossible to use perturbative techniques to do calculations at low Q^2. Since it is low Q^2 that is pertinent to the structure of hadrons, approximate models must be used to understand this physics. Understanding the form factors, especially G_E^n since it is relatively unknown, provides assistance in understanding nuclear structure. Models have been developed to describe the structure of hadrons, and data is needed to determine which models provide a better description.

There are a large number of models of nuclear form factors, a few classes of which will be discussed here. Although lattice QCD has the most long term promise for understanding the physics of strong interactions, since the comparison of the results with data will show the current limitation in computing power, comparisons with lattice QCD will not be included.

3.1.1 Fits

In the early studies of nucleon form factors, a phenomenological fit was performed to determine the behavior of G_E^n, based upon unpolarized data and the Rosenbluth technique. This fit of the data is known as the Galster parameterization

[40], and is

$$G_E^n(Q^2) = -\frac{\mu_n}{1+5.6\tau} G_D(Q^2), \tag{3.1}$$

where G_D is the dipole form factor

$$G_D = \frac{1}{(1+\frac{Q^2}{0.71})^2} \ . \tag{3.2}$$

The other three form factors (G_E^p, $\frac{G_M^p}{\mu_p}$, $\frac{G_M^n}{\mu_p}$) all show good agreement with G_D using data acquired from the Rosenbluth method. As new data have become available, this simple fit has been updated. See for example the fit by Kelly [59].

3.1.2 Vector meson dominance model

A representative vector dominance model which is in reasonable agreement with the low Q^2 data is one by Bijker *et al.* [15] This model has pQCD scaling relations built into it, and a phenomenological contribution attributed to the nucleon's qqq structure. The added term for F_2^V is $\frac{g(Q^2)}{1+\gamma Q^2}$ introduced to reflect pQCD. The intrinsic form factor used was $g(Q^2) = (1+\gamma Q^2)^{-2}$.

Another representative model, by Lomon *et al.*, also included meson pole terms and a term with pQCD behavior. This model also includes the additional vector mesons of ρ' and ω' compared to the previously described one, requiring a total of 14 free parameters [65].

3.1.3 Pion cloud and CQM

Miller, *et al.*, expanded the constituent quark model into the light-front cloudy bag model [69]. Here the three relativistic constituent quarks are surrounded by a

nonrelativistic cloud of pions. Poincaré invariance provides an additional constraint needed to fit the G_E^n data. This model has recently been expanded into the light front cloudy bag model, with the pion cloud contributing through a relativistic π-nucleon form factor. The corrected form factors are in terms of the form factors without relativistic effects, and the virtual pion four momentum. An additional parameter is introduced in the π-nucleon form factor, for the relativitistic correction [69].

3.1.4 Model of Generalized Parton Distributions

The interest in GPDs recently has led to several models being developed. Among these are models by Guidal *et al.* [45] [76] and Diehl *et al.* [28]. In these models, the GPD framework is used to describe observables that are independent of skewness ξ (see Figure 1.1). Guidal *et al.* parameterize the GPDs in the following way

$$H^q_{R2}(x,0,Q^2) = q_v(x)x^{\alpha'(1-x)Q^2} \ , \tag{3.3}$$

$$E^q_{R2}(x,0,Q^2) = \frac{\kappa^q}{N^q}(1-x)^{\eta^q} q_\nu(x)x^{\alpha'(1-x)Q^2} \ . \tag{3.4}$$

Here α' is the universal Regge slope, while the η^q govern the behavior for the helicity-flip GPDs as x approaches 1. This was added to produce a faster falloff at large Q^2 in the $x \to 1$ limit. The model by Diehl *et al.* is described in Section 6.4.2.

3.1.5 pQCD predictions

As stated in section 1.2.1, perturbative QCD gives the prediction that [12]

$$F_1 \propto \frac{1}{Q^4} \ . \tag{3.5}$$

This relationship is also expected to be relevant at moderate Q^2 when higher order QCD terms are included, which treat small-x partons better. The small quark masses mean that the dominant mechanism for helicity flip in QCD comes from the quark orbital angular momentum. Generalized power counting including this orbital angular momentum gives a scaling of

$$F_2 \propto \frac{1}{Q^6} \ . \tag{3.6}$$

This behavior depends on the leading order and next to leading order light-cone wave functions, the latter dominated by the probability amplitude for one quark to carry one unit of orbital angular momentum. It is suggested that the higher order resummation suppresses the low x contribution, providing an effective cut off for the integrals at $x \approx \ln^2(\Lambda^2/Q^2)$ [12].

$$\frac{F_2}{F_1} \propto \frac{\ln^2 \frac{Q^2}{\Lambda^2}}{Q^2} \ . \tag{3.7}$$

Here Λ is the QCD renormalization scale. While this scaling relation is accurate for the proton, a rough calculation of $Q^6 F_2(Q^2)$ gives about $\frac{1}{3}$ the value of experimental data for $Q^2 < 5$ GeV^2 [12]. This scaling, scaled to the previous measurement at $Q^2 = 1.5$ GeV^2, is presented in Figure 3.1 in addition to the other models just discussed.

3.2 Measuring GEn via the Rosenbluth technique

As mentioned earlier, equation 2.35 suggests one technique to determine the electric and magnetic form factors. By carrying out multiple measurements at dif-

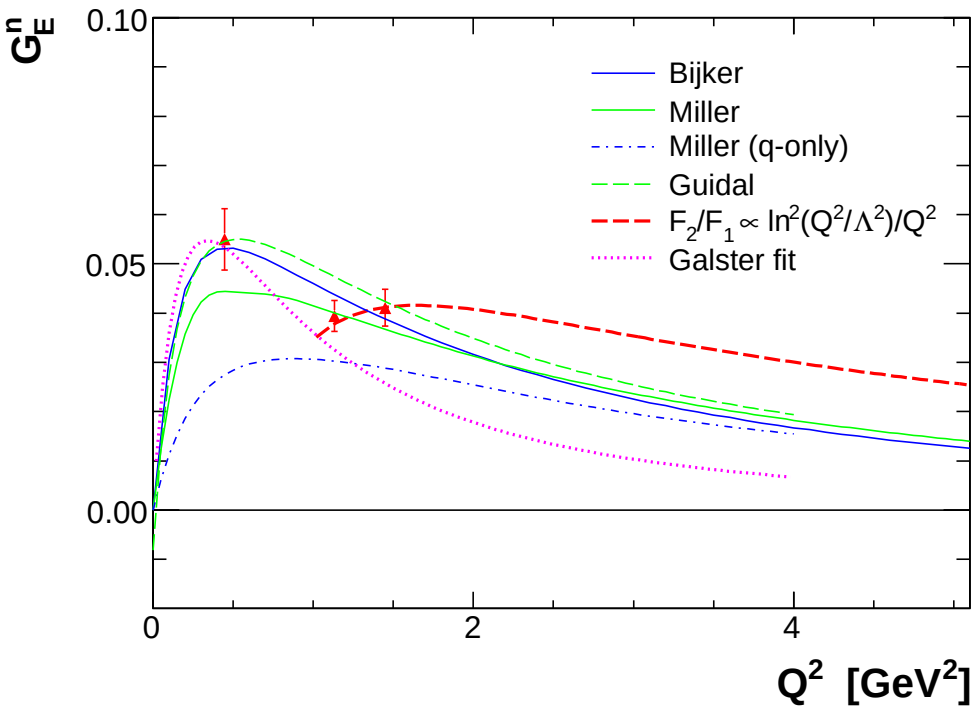

Figure 3.1: Various fits discussed in the text. The points plotted are from [66], which was used to fit the pQCD curve. These data are only representative, see figure 3.2 for the full set. The Bijker curve is a representative Vector Meson Dominance model, the Guidal curve is a representative GPD based model, the Miller curves are from a CQM.

ferent angles for a given Q^2 the two components of the cross section may be independently determined, allowing a separation of the electric and magnetic form factors. This technique is known as Rosenbluth separation. Experiments to measure the electric form factor of the neutron that use this Rosenbluth method fall into two categories: those in which the impulse approximation for quasi-elastic electron deuteron scattering with the Rosenbluth method is applied directly to the neutron component, and those where the Rosenbluth method is applied to the deuteron through elastic scattering, and an NN model is use to extract a value for G_E^n [58]. The latter is described first.

3.2.1 Elastic e-D scattering

The deuteron, containing two nucleons, is spin-1. Because of this, the equation for the elastic cross section has three form factors, the magnetic G_M, the charged G_C, and the quadrupole term G_Q [77]:

$$\frac{d\sigma}{d\Omega} = \frac{d\sigma_{Mott}}{d\Omega}[G_C^2 + \frac{8}{9}\tau^2 G_Q^2 + \frac{2}{3}\tau(1+\tau)G_M^2 + \frac{4}{3}\tau(1+\tau)^2 G_M^2 \tan^2\frac{\theta_e}{2}] \ . \qquad (3.8)$$

While the θ_e dependence allows G_M to be separated out, the charged and quadrupole terms cannot be separated using the Rosenbluth technique. In addition, it is the coherent sum of proton and neutron electric form factors which is extracted ($G_E^p + G_E^n$). Both of these complications add to the uncertainty in the determination of G_E^n. The electric form factors must be "unfolded" from G_C and G_Q using a model, which makes the results of this technique dependent on the model of the deuteron's wave function [76] [84]. The most recent extraction uses high precision data for G_C,

and the Arenhovel model of the deuteron [6] [36].

3.2.2 Quasi-elastic scattering and the Rosenbluth Technique

Recalling equation 2.16, a technique using quasi-elastic scattering from a nucleon rather than elastic scattering from a deuteron and the Rosenbluth formula (equation 2.35) directly presents itself. By subtracting the cross section of the proton from that of the deuteron, or by measuring the neutron in coincidence with the electron, at the quasi-elastic peak, the cross section of the neutron remains. Then the Rosenbluth formula can be used to arrive at a value for G_E^n.

Most commonly, the neutron is detected in coincidence with the scattered electron, to identify that the interaction was with the neutron. However, this technique has also been performed with anti-coincidence measurements, where "no proton" is required in coincidence with the electron [77]. Another technique is to measure the ratio of the neutron to proton production cross sections in the electro-disintegration the deuteron. This method has worked very well for the neutron magnetic form factor.

There have been some serious difficulties with these types of experiments. Among these are a heavy dependence on the proton form factors and the aforementioned problems with the Impulse Approximation (section 2.4.1). Additionally, coincidence and anti-coincidence experiments depend on the absolute detection efficiency, which is difficult to determine for neutrons [77].

3.2.3 Difficulties with Rosenbluth method

The uncertainties for these measurements based upon unpolarized quasi-elastic scattering from deuterium are too large to give a definitive nonzero measurement of G_E^n. The dependence on the proton form factors and the uncertainty directly from IA dominate the measurement.

The Rosenbluth technique has another inherent problem: the magnetic form factor is much larger than the electric form factor for the neutron, and the ratio $(\frac{G_E}{\tau G_M})^2$ becomes smaller as the transferred momentum increases. This means that the electric form factor is difficult to decouple from the magnetic form factor, since both the tangential and constant (relative to angle) portions of the cross section are proportional to G_M^2 [91].

3.3 Double polarization techniques

With the difficulties in measuring the electric form factor of the neutron using the Rosenbluth method, new techniques have been sought. Following the suggestion of Arnold, Carlson, and Gross [10] a technique using a longitudinally polarized beam and a recoil polarized neutron has been investigated. The most obvious reaction for such an experiment would be ${}^2H(\overrightarrow{e}, e'\overrightarrow{n})p$.

The most important advantage is that the measured term is proportional to $G_E^n G_M^n$ instead of $(G_E^n)^2$. Additionally, only one measurement is needed for a given Q^2 if all interesting components can be measured.

As mentioned earlier, polarized targets can allow the same physics to be ac-

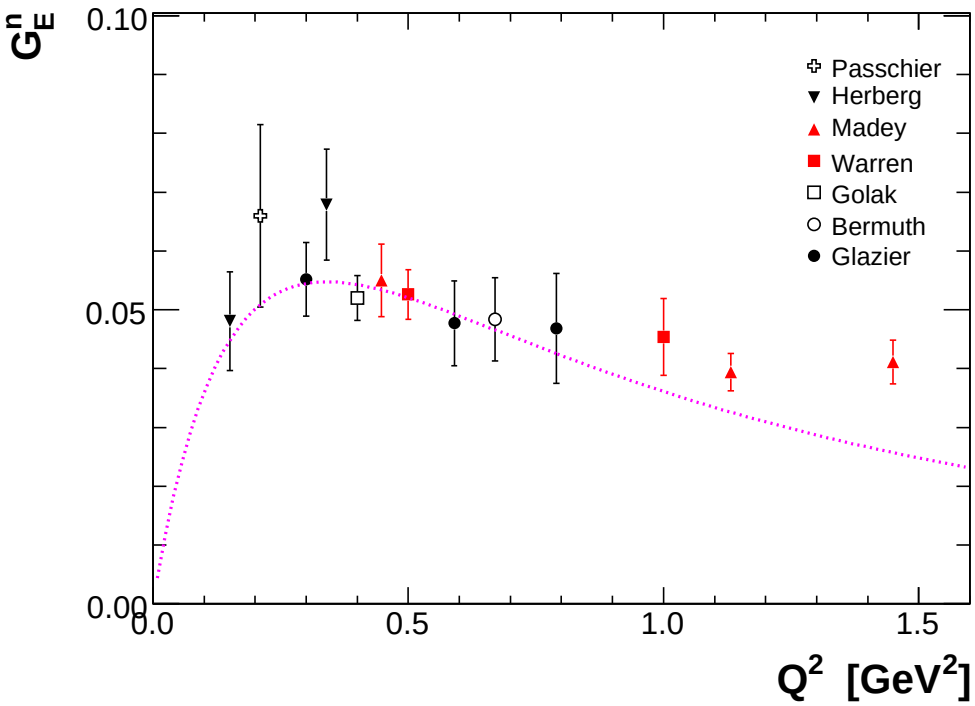

Figure 3.2: Previous G_E^n data from experiments involving polarization techniques. The curve is the Galster parametrization [40]. Herberg provided new calculations of the Ostrick data, while Golak provided a FSI corrected analysis of the Becker data. For references see Table 3.3.

cessed as detecting a polarized recoil neutron. Experiments have been carried out with either recoil polarization, where the polarized neutron is detected in a polarimeter, or with a polarized target, either polarized deuterium or polarized ^{3}He, with a detected unpolarized neutron [66]. Table 3.3 contains a summary of recent experiments using all of these techniques.

All experiments using the double polarization technique are dependent on a helicity dependent experimental asymmetry,

$$A_{exp} = \frac{N_+ - N_-}{N_+ + N_-} \ , \tag{3.9}$$

which can then be related to G_E^n. Here N_+ gives the number of events with helicity aligned with the nucleon polarization or with the beam direction and N_- gives the number of events with helicity with the opposite sign compared to nucleon polarization or against the beam direction.

3.3.1 Quasi-elastic scattering and (e,e'n)

For PWIA to be applicable, quasi-elastic events must be selected. Even though the cross section is not being measured, the process of selection of these events is important, as double polarization techniques depend on asymmetries, which are diluted by events which are not part of the desired asymmetry. Two useful quantities for selecting quasi-elastic events in coincidence experiments are the missing energy (defined by $E_m = m_f + m_B - m_{A+i}$ with A, B, i, and f as shown in figure 2.2) and the missing momentum (defined by $\mathbf{p}_m = \mathbf{p}_i - \mathbf{q}$).

In the experiments that have been carried out to date, the experimental trig-

Q^2	*Date*	*Reference*	*target*
0.16	1991	Jones-Woodward [55]	$^3\overrightarrow{\mathrm{He}}$
0.2	1992	Thompson [95]	$^3\mathrm{He}$
0.31	1994	Meyerhoff [68]	$^3\overrightarrow{\mathrm{He}}$
0.255	1994	Eden [34]	$^2\mathrm{H}$
0.15, .34	1999	Ostrick [74]	$^2\mathrm{H}$
0.4	1999	Becker [11]	$^3\overrightarrow{\mathrm{He}}$
0.21	1999	Passchier [75]	$^2\overrightarrow{\mathrm{H}}$
0.67	1999	Rohe [84]	$^3\overrightarrow{\mathrm{He}}$
0.45, 1.13, 1.45	2003	Madey [66]	$^2\mathrm{H}$
0.5, 1	2003	Warren [97]	$^2\overrightarrow{\mathrm{H}}$
0.3,0.6,0.8	2003	Glazier [43]	$^2\mathrm{H}$
0.67	2003	Bermuth [13]	$^3\overrightarrow{\mathrm{He}}$

Table 3.1: Double polarization experiments for measuring the electric form factor of the neutron that have been carried out to date [77].

ger was typically formed by coincidence between the scattered electron and recoiling neutron. The electrons were detected in a spectrometer or granulated calorimeter. The measured electron kinematics, in concert with large solid angle neutron detectors, allow for event-by-event reconstruction of the particle tracks. For the neutron detector, in higher Q^2 experiments a multi-plane neutron detector was used, with a layer or two of veto detectors in front. In other experiments, two separated layers of scintillator were used, with each layer having veto detectors in front.

Recoil polarimetry experiments required a different detection scheme in order to detect the polarization of the neutron, as it leaves the target. Polarimeters were set up to measure the "up-down" scattering asymmetry due to the transverse component of the recoil polarization. The polarimeters included a plastic or mineral oil scintillator which determined the neutron time of flight (TOF), and also served as a scatterer, with the polarized scattering exhibiting an asymmetry that was measured in a second set of scintillators. Since the spin vector of the neutron could have any combination of longitudinal and transverse polarizations, a dipole magnet was sometimes used to precess the neutron's spin vector.

These detectors provided scattering angles for both neutrons and electrons. The momentum of the particle(s) provides the needed fifth quantity to select quasi-free (e, n) scattering, and is determined by considering the time of flight (TOF) for the particle(s). A missing signal in the veto detectors along with the determination of the flight time of the particle from the target to the detector provided neutron detection. Additionally, pulse heights in the neutron detector scintillators can be used to filter out accidental and inelastic events. Quasi-elastic events can also be

selected by comparing the expected time of flight (from the electron energy and the angles) to the measured time of flight.

Other events, which dilute the quasi-elastic neutron events, were one of the main sources of uncertainty in these measurements. A major source of background is proton to neutron conversion in the shielding in front of the neutron detectors. This can be minimized with a tight time of flight cut at low hadron momentum. Good time resolution also allows removal of pion events, another source of dilution. Monte Carlo simulations have been used to determine the proper dilution factor from the uncertainties and to average out the theoretical asymmetries and the effects of finite acceptance.

3.3.2 Recoil polarimetry

Four experiments used recoil polarization techniques to measure G_E^n. These experiments were Madey *et al.* [66] in Hall C at Jefferson Lab, Glazier *et al.* [43] at the Mainz Micotron, Ostrick *et al.* [74] at the Mainz Microtron, and Eden *et al.* [34] at the MIT-Bates laboratory. The first three named experiments (Eden *et al.* was a proof of concept experiment) produced published data.

In these experiments, neutrons were produced through electrodisintegration of deuterons in an unpolarized liquid deuterium target using longitudinally polarized electrons. Contamination from hydrogen within such targets was found to be small [34] [66].

From equations 2.26 and 2.28 we can develop a relationship between the ratio

of the components of polarization (see discussion in section 2.5), and the ratio of the form factors

$$\frac{G_E}{G_M} = -\frac{P_x}{P_z}\frac{E_i + E_f}{2M}\tan\frac{\theta_e}{2} \ . \tag{3.10}$$

Here P_x and P_z are the x and z components of polarization. In order to determine the up-down asymmetry A_{meas} must be observed. It follows a sinusoidal dependence

$$A_{meas} = A_y |\overrightarrow{P}| \sin(\chi + \chi_0) \ . \tag{3.11}$$

Here A_y is the beam analyzing power, and χ is the spin precision angle, of the detected particle as it travels through a magnetic field.

$$\tan\chi_0 = \frac{P_x}{P_z} = -\frac{G_E}{G_M}\frac{\cos\frac{\theta_e}{2}}{\sqrt{\tau + \tau^2\sin^2\frac{\theta_e}{2}}} \ . \tag{3.12}$$

Using this spin precision technique removes the need for absolute calibration of the electron beam polarization and effective analyzing power [78].

Arenhovel [7] [8] showed that for a deuteron target, corrections due to meson exchange currents and isobar configurations are small, and these have little dependence on Q^2. It was found, however, that at lower values of Q^2, effects from final state interactions (FSI) can play a large role [74].

Ostrick *et al.* found at $Q^2 = 0.35$ GeV^2 that the neutron polarization was reduced by less than 4% due to FSI effects, but at $Q^2 = 0.12$ GeV^2 the transverse polarization is reduced by 50%. These final state interactions were calculated to mostly arise from $p - n$ charge exchange via pion exchange. A model was used to calculate the change to the polarization by FSI, and a correction was applied [74].

Glazier *et al.* found that at neutron energies of a few hundred MeV the scattering in the polarimeter was dominated by quasi-elastic scattering, which added

to the effective analyzing power of the polarimeter. This means that A_{meas}, the effective asymmetry, could not be computed accurately, and the statistical precision was not exactly known [43].

Madey *et al.* also used a cross ratio technique, which makes the neutron polarimeter results independent of any luminosity change based on beam helicity, as well as of the efficiencies and acceptances of the two halves of the polarimeter. This experiment used a different technique to account for FSI effects. By using possible G_E^n values in a simulation, the neutron polarization was calculated and then compared to experiment [66].

3.3.3 Polarized target measurement

To measure G_E^n using a polarized target, we measure the asymmetry A

$$A = \frac{\sigma_+ - \sigma_-}{\sigma_+ + \sigma_-} = \frac{\Delta}{\Sigma} \ , \tag{3.13}$$

where $\sigma_\pm$ are the cross sections (Equation 2.38) with electron helicity ± 1. If the polarization direction of the target is flipped, this changes the sign of the asymmetry. This asymmetry is not explicitly measured, but rather

$$A_{meas} = P_e P_t A \ , \tag{3.14}$$

where P_e is the polarization of the electron, P_t is the polarization of the target, and

$$A = -\frac{2\sqrt{\tau(1+\tau)}\left[\tan\frac{\theta_e}{2}\sin\theta\cos\phi G_E^n G_M^n + \sqrt{\tau[1+(1+\tau)\tan^2\frac{\theta_e}{2}]}\cos\theta(G_M^n)^2\right]}{(G_E^n)^2 + \tau[1+2(1+\tau)\tan^2\frac{\theta_e}{2}](G_M^n)^2} \ . \tag{3.15}$$

Here θ and ϕ are the angles defined in Figure 2.3. Setting the angles properly ($\theta = 90^\circ$ and $\phi = 0^\circ$) greatly simplifies things, giving the perpendicular asymmetry:

$$A_\perp = \frac{-2\sqrt{\tau(1+\tau)}\tan\frac{\theta_e}{2}\frac{G_E}{G_M}}{(\frac{G_E}{G_M})^2 + \tau[1 + 2(1+\tau)\tan^2\frac{\theta_e}{2}]}. \tag{3.16}$$

Since the ratio of $\frac{G_E}{G_M}$ is small, the perpendicular asymmetry is roughly proportional to the ratio $\frac{G_E}{G_M}$. The parallel asymmetry can be used to normalize the value, so that

$$G_E^n = \frac{a}{b} G_M^n \frac{(P_e P_t V)_\parallel A_\perp}{(P_e P_t V)_\perp A_\parallel} \ , \tag{3.17}$$

where $a = 2\sqrt{\tau(1+\tau)}\sqrt{\tau[1 + (1+\tau)\tan^2\frac{\theta_e}{2}]}$ and $b = 2\sqrt{\tau(1-\tau)}\tan\frac{\theta_e}{2}$.

3.3.4 Experiments with polarized deuterium

Two experiments used polarized deuterium targets to measure the value of G_E^n, one in Hall C at Jefferson Lab (Warren *et al.*[97]) and the other at NIKHEF in Amsterdam, the Netherlands (Passchier *et al.* [75]).

Under PWIA, for deuteron targets with polarization in the scattering plane and after proper averaging of the asymmetry (symmetrically around $\mathbf{q}$), the measured asymmetry is

$$A_{meas} = V \frac{P_e P_1^d A_{ed}^V}{1 + P_2^d A_d^T} \ , \tag{3.18}$$

where V is the dilution factor, P_1^d is the vector polarization, P_2^d is the tensor polarization, A_{ed}^V is the deuteron vector beam-target asymmetry, and A_d^T is the tensor deuteron target asymmetry. For most targets the tensor polarization is small, and that term can be ignored.

In these experiments data were compared to predictions by Arenhovel [7] [8] [9], which accounted for nuclear and FSI effects. This physics model is non-relativistic, and includes meson exchange, isobar configuration currents, and relativistic corrections. The comparison was done by simulating different observables, like $\mathbf{p}_m$, and plotting them versus the asymmetry, all using different values of G_E^n within the confines of the model [75] [97].

In the experiment performed by Warren *et al.*, polarized deuterated ammonia was used as the target. The ammonia granules were submerged in liquid helium and aligned with 5 T magnetic field resulting in a typical polarization of 24%. Good agreement with MC predictions showed that quasi-elastic scattering dominated the scattering reaction. This experiment had a narrow range of acceptance, so it was fairly insensitive to Q^2 dependence [97].

In the experiment performed by Passchier *et al.*, polarized electrons were injected into a recirculating storage ring, allowing for large beam currents. An atomic beam source injected a flux of polarized deuterium atoms into a cell in the storage ring with an electromagnet used to orient the polarization axis. This was created by deuteron atoms in two hyperfine states, with an electromagnet to orient the polarization axis [75].

3.3.5 Experiments with polarized helium-3

Another class of experiments to measure G_E^n have used $^3\overrightarrow{\mathrm{He}}$ as the target. Various experiments were carried out at the Mainz Microtron (MAMI) [11][84][13][68]

and at the MIT-Bates laboratory[55][95]. The results presented in [13] include those from the experiment reported in [84]. Additionally, experiment E02-013 is of this type and in early 2006 ran at Jefferson Lab in Hall A. The analysis of this experiment, with data up to $Q^2 = 3.5$ GeV^2, is being presented in this thesis.

Optical pumping techniques are used to polarize the ^{3}He either through metastability exchange where the ^{3}He is pumped directly, or through spin exchange. In the latter, the valence electron in rubidium is optically pumped and the polarization is transferred to the ^{3}He nucleus through collisions. The polarization process for ^{3}He generally does not take place in the target chamber, rather a pumping chamber is used and the polarized helium-3 diffuses into the target cell or is forced in with a compressor. The polarization vector inside of the ^{3}He target can then be measured with NMR.

One of the advantages of a polarized ^{3}He target is that in the ground state the spins of the protons are to a large extent aligned antiparallel to each other. This means that most of the spin of the helium nucleus is carried by the neutron; the polarization of the neutron is approximately 86% of the polarization of the nucleus [16]. Further details about polarized ^{3}He targets will be presented in section 4.4.

At low Q^2, the complications due to the nuclear wave function can be accounted for with calculations. However, at $Q^2 > 0.6$ GeV^2 this proves difficult, and extrapolation was used in these earlier experiments. Data for G_M^n is used, or a parametrization, in order to arrive at a value of G_E^n from the experimental asymmetry (equation 3.16). A Monte Carlo simulation was used to determine radiative loss and neutron energy loss before the detector, as well as other corrections.

It is possible to select the kinematics such that the measured asymmetry is expressed as:

$$A_{exp} = P_{beam} P_{target} D_{neutron} V_{other} A_{\perp}. \tag{3.19}$$

Here D accounts for dilution from sources related to the target (such as it not being a free neutron), and V is the dilution caused from other sources and from reactions other than quasi-elastic scattering. This formula assumes that the angles in equation 3.15 are exactly such that $A_{\parallel} = 0$; in practice this isn't possible.

The experiment performed by Becker *et al.* used circulated ^{3}He which was compressed into the target cell by a Toepler compressor. An experiment using deuterium provided a parallel measurement, using the same equipment, pointed to a significant role for FSI that decreases as Q^2 increases. The work by Golak *et al.* expanded upon the analysis of Becker *et al.* by summing the cross sections before forming asymmetries using Faddeev calculations. It was discovered that even at the quasi-elastic peak FSI effects played a significant role. Using theoretical ratios determined from models and comparing to experimental values, G_E^n was extracted from the FSI corrected results [11][44].

In the experiments performed by Rohe *et al.* and Bermuth *et al.*, the data were accumulated by rotating the target spin so that both $A_{\perp}$ and $A_{\parallel}$ could be measured. The measurement of both parallel and perpendicular asymmetries allowed the measurement of the target analyzing power (A_y) which provided a check on the understanding of FSI effects. These were compared to the calculation by Golak *et al.* and FSI effects caused a 3.4% decrease in the reported value of G_E^n. These FSI

effects are primarily caused by the photon coupling to one of the protons followed by charge exchange [13][84].

3.4 Summary of past measurements

These three different double polarization techniques have a variety of advantages over the Rosenbluth method, as described in this chapter. While models are used to make corrections, and for polarized deuterium for the measurement itself, the general method is model independent. The three different, independent, techniques used in double polarization measurements provides a check on the understanding of the different types of corrections required. The data from the double polarizations is presented in Figure 3.2 while the experiments are listed in Table 3.3.

Because $^3\overrightarrow{\text{He}}$ behaves similarly to a polarized neutron, and because of the low detection efficiency neutron polarimeters, polarized $^3\overrightarrow{\text{He}}$ experiments provide the best statistical precision for measuring G_E^n. FSI effects are taken into account by models for polarized deuterium and calculations for $^3\overrightarrow{\text{He}}$. Because of the robustness of the deuterium model, FSI effects have traditionally played less of a role in deuterium experiments compared to those using $^3\overrightarrow{\text{He}}$. For the discussion and calculation fo FSI effects in polarized ^{3}He for this experiment, at intermediate Q^2, please see the section 5.7.1.

The completed experiments provided precise enough data to clearly identify a small enhancement in G_E^n at $Q^2 = 0.4$ GeV^2. This enhancement is larger in value than the measurements from the Rosenbluth data. At the highest measured values

of G_E^n a noticeable difference between the Rosenbluth and polarized data is seen. This is speculated to be due to incomplete radiative corrections for the Rosenbluth data.

In the past decade, precise measurements of the neutron electric form factor have become possible and have provided precise knowledge of the structure of nucleons for Q^2 below 1.5 GeV^2. In this region, several models provide a good agreement with the data. The majority of the recent measurements have used the double polarization method, which has the advantage of having greater precision and less model dependence compared to the historic Rosenbluth method.

3.5 E02-013 at Jefferson Lab

As introduced, the physics of nucleons move from the bound behavior described by massive partons, into the behavior described by bare quarks in QCD. There is a complicated transitive region, in the models presented in Section 1.3, that starts at less than 1 GeV and continues to many GeV. The actual point where this behavior changes, and the description of the change, is unknown. In the experiment presented here, the key quantity G_E^n needed to understand nucleon stucture, and behavior such as quark orbital angular momentum, is measured at three separate points in the Q^2 region between 1 and 4 GeV^2.

In this experiment, E02-013, numerous improvements were made to increase the figure of merit (effective statistics) for a measurement in this region. Advances in both instrumentation and in the polarized ^{3}He target technology have been ac-

complished to improve this measurement. By injecting a small amount of potassium along with the rubidium, the polarization transfer efficiency from the optically pumped rubidium was improved to provide polarizations as high as 50% in the target chamber. The experimental apparatus and target will be explained in detail in Chapter 4. The value of the asymmetry will be analyzed as a function of $\mathbf{p}_{m,\perp}$, the perpendicular component of the missing momentum, to study FSI effects. A tight cut on $\mathbf{p}_{m,\perp}$ is needed to select low nucleon momenta in the ^{3}He wave function, but also will suppress dilution from proton polarization and FSI interactions. The high Q^2 at which this measurement is undertaken should suppress meson exchange currents. Additionally, meson exchange currents, delta isobar contributions, and finite acceptance effects should be suppressed by a tight cut on $\mathbf{p}_{m,\perp}$ [25]. This will be described in detail in Section 5.7.1.

Chapter 4

G_E^n experiment E02-013

Experiment E02-013 was carried out at Jefferson Lab from February 28 to May 11, 2006 to measure the electric form factor of the neutron. In this chapter the experiment setup and instrumentation needed to measure the interaction $^3\overrightarrow{\mathrm{He}}(\vec{e}, e'n)$ are described. First the experimental overview and relevant coordinate systems will be presented. Then a short summary of the beam and accelerator will be presented in section 4.3. The target and method of polarization is described in section 4.4. In section 4.5 the spectrometer (Big Bite) used to detect the electron and measure its momentum is portrayed. The neutron arm (Big Hand), used to detect the coincident hadron, is described in section 4.6. Finally, the data acquisition, software used for decoding and initial physics analysis, is presented in section 4.7.

4.1 Experimental Overview

During the running period of E02-013, data were collected in four kinematic settings which were spaced over six time intervals, not including the time spent on commissioning the apparatus. Three separate polarized ^{3}He target cells were used for the measured asymmetry. For calibration purposes, a foil target (containing six carbon foils and one BeO foil), a reference cell (providing an empty cell target, hydrogen target, and a nitrogen target), and a setting with no target cell were used.

Big Bite optics calibrations and beam spot check were acheived using the foil target. The nitrogen target is used to determine the contamination in scattering events from N_2 in the ^{3}He cells. The hydrogen target was used to calibrate the momentum and yields of the elastic events for Big Bite and Big Hand. Additionally, the nitrogen and hydrogen targets are used to determine the dilution of the neutral sample by protons empirically, which is an important correction for the physics asymmetry.

Data taking took place in this experiment for several different settings dependent on target, beam energy, neutron arm location, and electron scattering angle. These are described in Table 4.1. Kinematic 1 will not be presented in this thesis. Kinematic 2(a) used two different settings for the neutron arm threshold. This change in threshold creates a difference in the neutron and proton detection efficiencies which are a key component in the empirical measurement of the dilution of the neutral sample by protons. This difference in efficiencies is calculated using a Monte Carlo simulation.

4.2 Principle and Experiment setup

This experiment took place in Hall A of Jefferson Laboratory in Newport News, Virginia, USA. Jefferson Laboratory is the home of CEBAF, a continuous electron accelerator that can provide beam energies of 0.6 - 6 GeV [3] [63]. The three experimental halls, A, B, and C, can all receive beam simultaneously. Each hall contains various standard equipment detector systems that facilitate the types of experiments

Figure 4.1: Image of Jefferson Laboratory. Shown is the accelerator and the mounds over the three experimental halls. The mound to the left is Hall A.

Kinematics	2 (a)	3 (a)	2 (b)	3 (b)	4
Target Cell	Dolly	Edna	Edna	Edna	Edna
Beam E. (MeV)	2637	3291	2641	3290	2079
Q^2 GeV^2	2.5	3.5	2.5	3.5	1.7
BB Angle (°)	51.59	51.59	51.59	51.59	51.59
NA Distance (m)	10	10	10	10	8
Time Frame	3/09-3/24	3/24-4/17	4/17-4/24	4/24-5/02	5/02-5/09

Table 4.1: A table showing the running conditions, time, accumulated charge, and kinematics of the different measurements referred to here and elsewhere as kinematics or for short kin. Kinematic one includes both the commissioning time and the first measurement. The measurement of $Q^2 = 1.3$ and 1.7 GeV^2 provide a comparison of the polarized ^{3}He technique with previous recoil polarization data while the other two measurements extend the measured range of Q^2. Not shown is the periods for commisioning and kinematic 1 which won't be covered in this thesis.

the halls were designed to accomplish. While the beam was provided similarly to other experiments in Hall A, the equipment used to make this measurement was a custom installation that included a large momentum acceptance spectrometer, Big Bite, a high efficiency segmented neutron detector, Big Hand, and a polarized ^{3}He target, which serves as a source of highly polarized neutrons. A general layout of the apparatus is shown in Figure 4.2.

The requirements for Big Bite and Big Hand were developed using simulations. To match Big Hand to Big Bite, the required acceptance for elastics was simulated, and then expanded to insure the acceptance of all events with at least $\mathbf{p}_{m,\perp} = 150$ MeV. Because at $Q^2 = 3.5$ GeV^2 the desired hadron momentum is 2.6 GeV, the thresholds, shielding, and depth of the neutron arm were developed to maximize

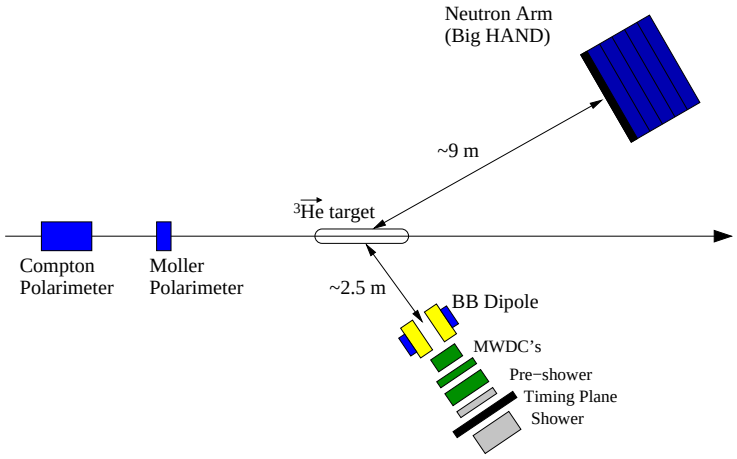

Figure 4.2: General layout, not to scale, of the experiment. Shown is the beamline, the target, the Big Bite detector stack, and the Neutron Arm detector. Also shown are the two polarimeters in the hall before the target, and the approximate distances to the detectors. The components of the Big Bite (BB) detector stack are also shown and consist of the Big Bite dipole magnet, multi-wire drift chambers (MWDCs), pre-shower, shower, and timing plane.

statistics. The desired Big Bite momentum resolution was 1-1.5% and the desired vertex resolution was 6 mm [25].

There were four major coordinate systems in this experiment: one for the lab, one for Big Bite, one for the target, and one for the Neutron Apparatus. In the hall system, the origin is at the center of the target, y is vertical with $+$ as "up", z is nominally along the direction of the beam, and x forms a right handed coordinate system. For the target coordinate system, the origin coincides with the hall origin, x is vertical with $+$ as "down", z is parallel to hall floor along the Big Bite central ray, and y completes the right-handed coordinate system. For the Big Bite detectors the origin is at the center of the first plane of the drift chambers. The $+z$ direction is defined in respect to the direction of particles perpendicular to the first drift chamber (and so is at a $\approx 10^\circ$ angle with the $x - z$ plane in the

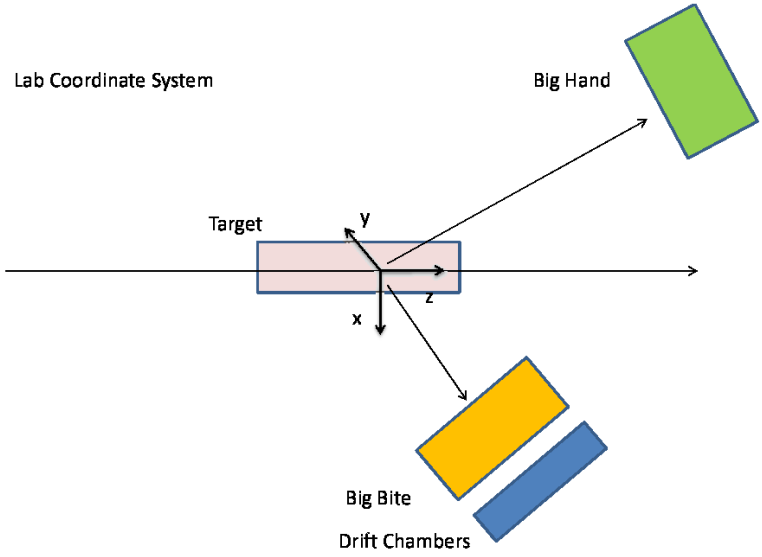

(a) Lab Coordinate System

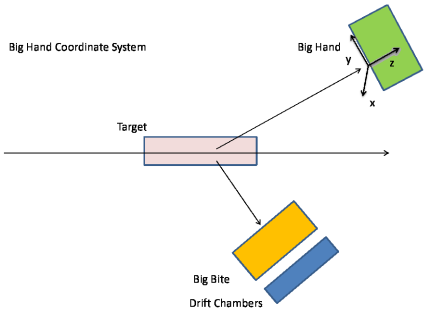

(b) Neutron Arm (NA) Coordinate System

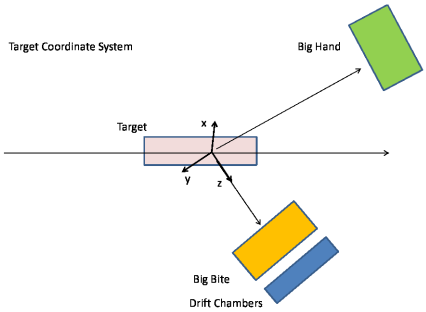

(c) Target Coordinate System

Figure 4.3: Coordinate systems for Big Hand, Target, and Lab. The lab z is along the beam line while the target z is toward Big Bite. All coordinate systems are right handed.

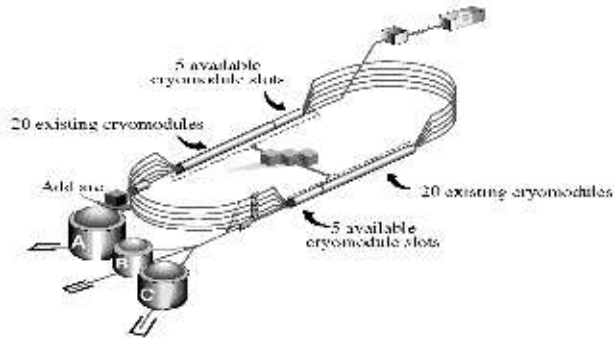

Figure 4.4: Schematic of the accelerator as it existed in 2006. Shown are the three halls, injector, and LINACs.

lab frame), while $+x$ is in the magnetic dispersion direction, and y completes the right-handed coordinate system. In Big Hand, the depth is z, the height is x, and the horizontal position is y. In this coordinate system positive x is associated with "down", positive z is associated with deeper into the Neutron Apparatus (NA), and positive y is away from the beam line. The origin was located in the center of the active area at the front of the shielding. Figure 4.3(c) shows the target, lab, and Neutron Arm coordinate systems and their relation to each other.

4.3 The Electron Beam

During 2006, the accelerator was capable of delivering beams with energy up to 5.7 GeV at currents of up to 150 μA semi-simultaneously to all three halls. The two main components of the accelerator are the injector and the two recirculated linear accelerators (LINACs). These delivered beams are not quite continuous, rather the beam was pulsed with 2 ns wide bunches at a rate of 499 MHz. Polarized electrons are produced from a strained GaAs photo-cathode via the photo-electric effect. A

maximum polarization of approximately 85% can be achieved. Inside the injector, the lasers for each hall are 120 degrees out of phase relative to each other. This allows for the energy and current to be determined for each hall semi-independently. After traveling through 18 superconducting radio frequency (SRF) cavities, the electrons are injected into the main accelerator at 23-68 MeV. After the initial acceleration, a prebuncher and chopper ensure that the three individual beams are separated in time and longitudinal spread. See Figure 4.4 for a schematic of the accelerator.

The polarization of the high energy beam as it enters Hall A can be measured with a Compton polarimeter. This is done by scattering electrons from polarized photons, and measuring the asymmetry in the cross section due to the beam helicity change. The scattering takes place when the electron beam interacts with a photon beam in a Fabry-Perot cavity (which enhances the yields). This method of measurement was used at the same time as data collection during kinematics two and three. On four separate occasions the beam polarization was measured by a Møller polarimeter in Hall A. This was done using magnetized foils which provide a target of polarized atomic electrons. The cross section was measured for two different orientations of the foil, in order to separate the longitudinal and transverse components of the beam polarization. At various times during the experiment both of these two methods along with a Mott polarimeter near the injector, were used to measure the polarization. This allowed for a good understanding of systematic errors for the beam polarization. An abridged summary of the beam polarization measurements is presented in Table 4.2.

The sign of the electron's helicity was put into the CODA [48] data stream with

a copy sent to the E02-013 trigger supervisor. The algorithm responsible produces helicity states (that last for a duration of 33.3 ms) in sets of four ($+--+$ or $-++-$). A 105 kHz clock was used to reconstruct the helicity if there was a problem with a missing helicity. After every transition there is a short unknown time during which the helicity is unknown (given by 0) in the data.

In the Hall A beamline before the target, a set of field coils move the beam to create a uniform pattern across a section of the target cell. This is done so that a small portion of the target is not overheated and the target cell is not compromised. The beam sweeps through its pattern at a rate of 17 to 24 kHz in a process known as rastering. The current used to do this is read into the data stream.

Beam position monitors (BPMs) are located upstream of the target (at 7.52 m and 1.29 m). The average position of the BPM is recorded at a rate of 1 Hz in EPICS. The fast rastering system is located 23 m upsteam of the BPMs. The BPMs were connected to an ADC for readout, such data could then be converted to a position for the beam. Harp scans in which a thin set of wires are swept through the beam, were carried out to provide absolute position information which could be used to calibrate the positions. The BPM and raster calibrations were carried out by Brandon Craver and discussed in greater detail in another thesis [81]. No scraping of the beam on the sides of the target was observed.

The two LINACs each accelerate the beam by up to 600 MeV during each pass. The beam can be bent and returned in RF cavities for up to five passes through the LINACs. The beam is accelerated in the east and west and bent 180 degrees in the arcs. See Figure 4.4 for details of the accelerator setup and beam cavities.

Because different electron energies need to travel through different magnetic fields to have the proper bend angle, the beam is split in a spreader and then recombined after traveling through the arc. Each cavity is also at 499 MHz to keep the beam properly bunched. The beam can be sent into the switch yard after any pass, where it is sent to hall A, B, or C. Beam energies were determined using the Tiefenbach method and recorded in EPICs. This method relates the beam energy to the current applied to one of the arc magnets [53].

4.4 The Helium-3 Target

Polarized targets and polarized ^{3}He have been used in previous experiments, as described in Section 3.3.3. To review and expand upon this description, polarized ^{3}He targets are one of the preferred methods of realizing a polarized neutron target. As described, nuclear targets are used rather than free neutrons as the latter only survives with a halflife of 885.7 ± 0.8 s [4]. For polarization experiments ^{3}He is ideal, because its polarization is almost entirely carried by the neutron [4]. Additionally, the relatively simple nature of the ^{3}He nucleus allows final state interactions to be understood. These final state interactions are thought to be small at high momentum transfer (see section 5.7.1). In polarized ^{3}He, the neutron carries $\approx 86\%$ of the spin of the nucleus (Figure 4.5) [4]. Most of the time, the spins of the protons are in opposite directions. About 3% of the time, the protons are polarized, and this proton asymmetry is corrected for when considering proton contamination of the neutral hadron candidates (see Section 5.5 and 5.6).

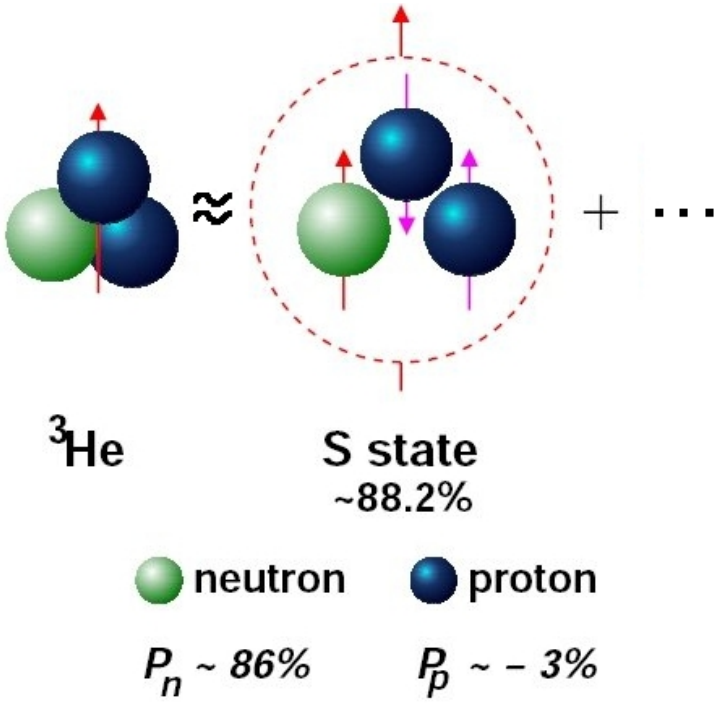

Figure 4.5: Diagram of the ^{3}He nucleus. Shown is the most common state with the proton spins aligned anti-parallel. The neutron carries $\approx 86\%$ of the polarization of the nucleus while the protons carry $\approx 3\%$.

The process of spin-exchange optical pumping (SEOP) was used to polarize the ^{3}He nucleus. In this process, alkali atoms are optically pumped and, through spin exchange, polarize the ^{3}He nucleus. An image of the target cell is provided in Figure 4.6. A unique feature of this target was the use of potassium (K) and rubidium (Rb) for the optical pumping, rather than the more traditional rubidium only. The process of SEOP will be described in Section 4.4.2.

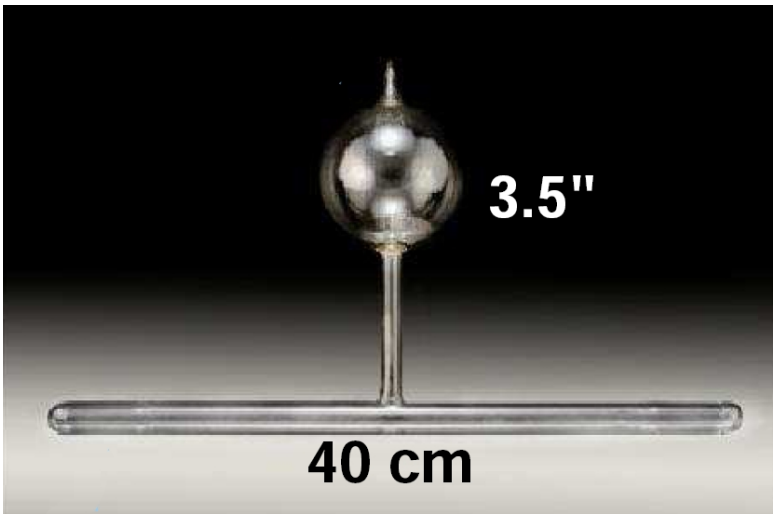

Figure 4.6: Picture of an empty ^{3}He cell. On top is the spherical pumping chamber, and below is the cylindrical target chamber. The beam passes through 40cm of target material [41].

4.4.1 Target System

The goal of the target system was to create a polarized ^{3}He target. To have a polarized target, a magnetic field is required to provide an axis with which to orient the target spin. To do this, the target system consists of a ladder holding the targets including a cell to hold the ^{3}He gas, a laser system to polarize the gas, and a system to create the uniform magnetic field.

The target ladder contained four different targets, and was enclosed in an iron box to provide a "constant" magnetic field in the target that is immune from interference due to the Big Bite dipole. The targets used were the $^3\overrightarrow{\text{He}}$, a set of optics (carbon and beryllium oxide) foils for calibration, and a reference cell (containing N_2 or H_2) targets. The reference cell was similar to the ^{3}He cell and approximately 40 cm in length.

An oven was used to keep the pumping chamber at a constant temperature of 240° C in order to maintain a sufficient density of potassium vapor for the spin exchange process.

The target cell was made from hand-blown glass, with two chambers, a pumping chamber and a target chamber, and a transfer tube between the two. The polarized gas in the heated top chamber would diffuse into the bottom target chamber where the polarized ^{3}He served as the target. The cell was constructed of alumine-silicate glass and was filled with 8 atm at room temperature of ^{3}He in addition to N_2 and sealed.

To optically pump the Rb, five 30 W lasers were used (totalling 150 W). In

order to decrease radiation damage and ease safety concerns, the lasers were not kept in the hall, rather they were kept in a shed. To pipe the light to the target, 75 m of optical fiber carried the laser light to the target where it was combined in the pumping chamber.

All components of the target system were held in an iron box, except the lasers. Around the target were coils to drive the RF field for the polarization measurements, sets of pickup coils to measure the NMR signals, and a coil to provide the excitation for the EPR measurement (see Figure 4.11). The magnitude of the field provided by the iron box was limited to 25 G in order to keep the beam from bending away from the beam dump. The iron box provided shielding from Big Bite, with eight coils arranged to create a "uniform" field in the target region (Figure 4.8). The holding field was not completely uniform, and since the experiment was very sensitive to polarization direction, this was measured using a custom built compass [61]. Figure 4.7 shows the relationship between position along the target and direction of the magnetic field.

4.4.2 Polarization

The ^{3}He target used in E02-013 was the first implementation of a hybrid target at Jefferson laboratory. The target's hybrid nature is due to containing two alkali metal vapors to reach a higher sustained polarization in less time than the previous mono-alkali targets. This target system was developed by Alan Gavalya and the polarized ^{3}He groups at the University of Virginia, the College of William

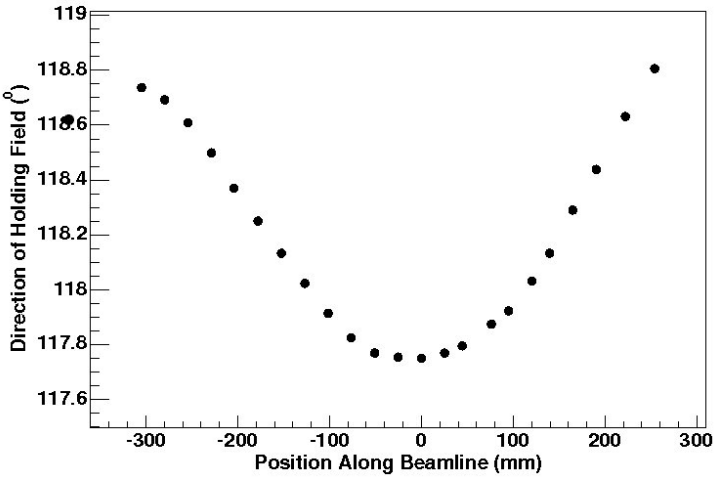

Figure 4.7: Measurement of the holding field as a function of position along the beamline in the target. The origin is the target center.

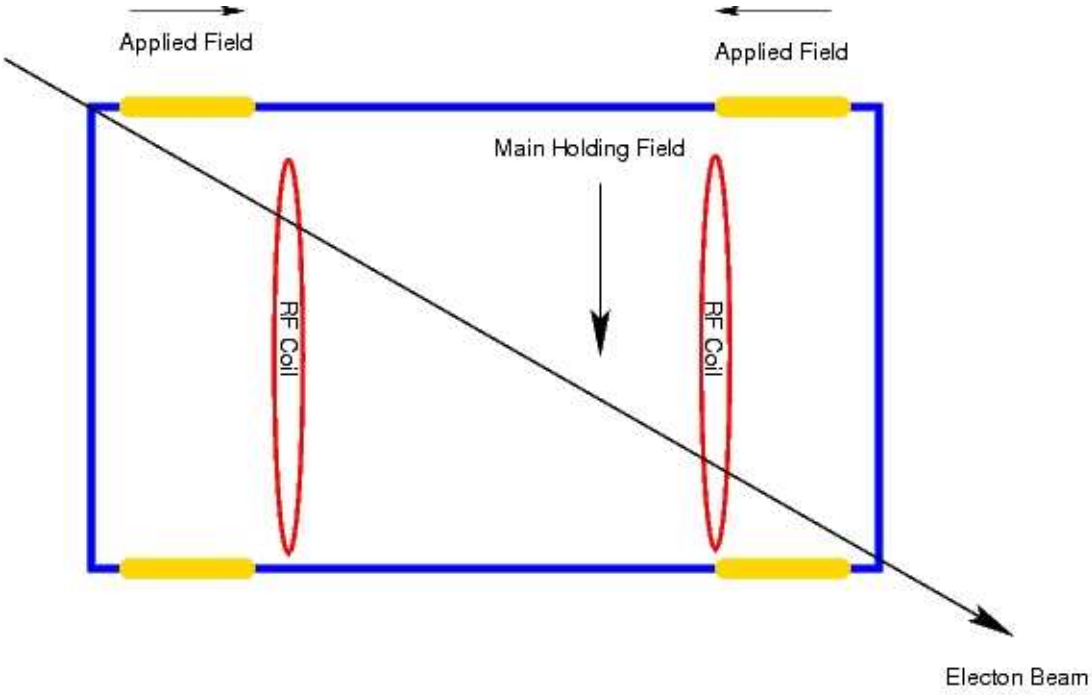

Figure 4.8: Magnet box for Target [57]. Shown is the coils that create the magnetic field.

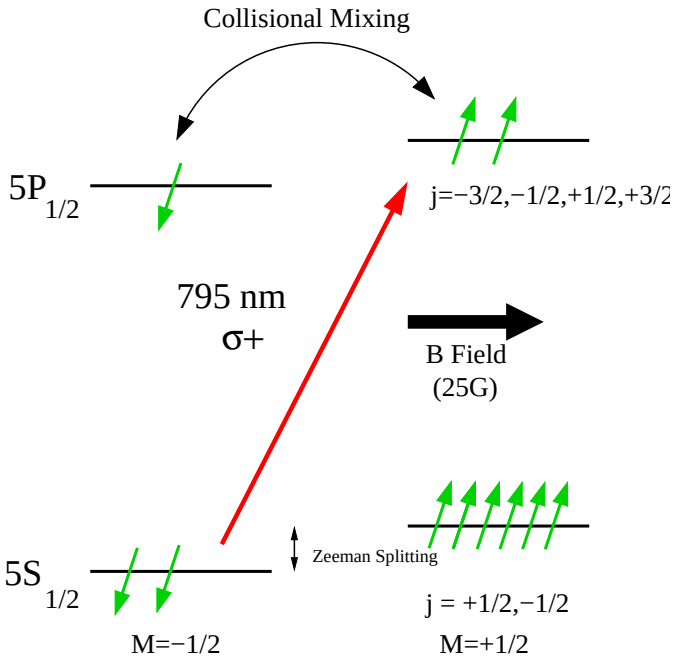

Figure 4.9: Figure showing the polarization process [57]. Optical pumping excites the electron to an excited state, which can exchange (50%) to a state that decays to a spin state that is not optically pumped by the lasers.

and Mary, the University of Kentucky, and the Hall A staff. By using a potassium and rubidium mixture in the cells, a polarization higher than 50% was acheived (see Figure 4.12).

In the process of spin exchange optical pumping (SEOP), rubidium is put in a magnetic field and exposed to the circularly polarized light, this pumps up the valence electron to a spin up sublevel in a P state. This excited state will either directly decay, or exchange spin through collision and then decay (see Figure 4.10). The photon released during decays can depolarize; the nitrogen in the cells (roughly 2% of ^{3}He volume) serves to quench this, allowing the transition back to a bound state through kinetic collisions rather than radiation. After decay there is a 50% chance to end in a spin state. This spin state is not excited by light from the

lasers and so becomes densely populated (see Figure 4.9). Angular momentum can be transferred from the polarized alkali valence electron to ^{3}He via the hyperfine interaction. A description of these processes is presented in Figure 4.10.

The spin exchange efficiency for K-^{3}He interaction is 10 times more efficient than Rb-^{3}He. Commercial lasers for optically pumping Rb are more readily available than those for potassium. Potassium (K) and other alkali metals have a high spin exchange cross section with rubidium and so the polarization of two such gases in a cell will be the same. This means that including the potassium into the cell enhances the transfer of polarization into the helium-3, decreasing the time to polarize the cell by a factor of two and causing a corresponding increase in sustained polarization in beam.

4.4.3 Polarization Measurement

The polarization of the target was measured by a combined use of EPR (electron paramagnetic resonance) and NMR (nuclear magnetic resonance) techniques. EPR provides an absolute measurement of ^{3}He polarization, while NMR provides a relative measurement. Both techniques cause depolarization of the target, but NMR disrupts the experiment less due to causing less depolarization. Because of this and because it could be carried out directly in the scattering chamber, NMR was done more frequently. These two techniques used two separate locations in the target cell. Due to using the alkali gases, EPR measured the polarization in the pumping chamber while NMR could be used to measure polarization in the target chamber.

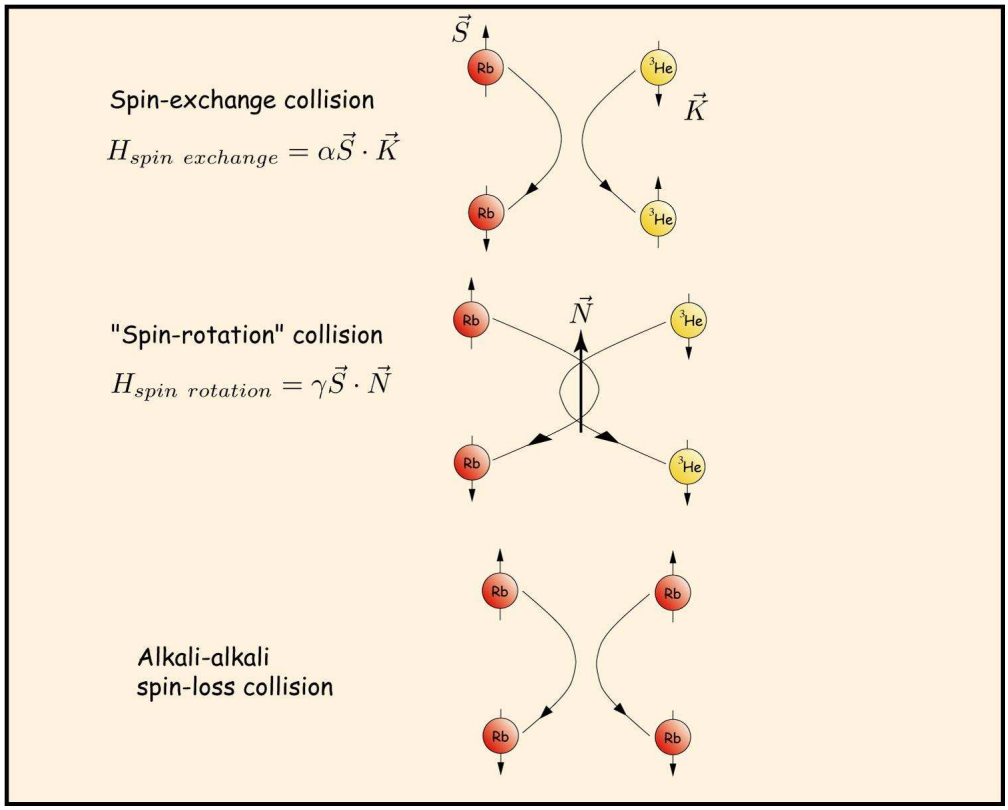

Figure 4.10: In a traditionally polarized helium cell, one that contains only Rb and ^{3}He, the Rb exchanges spin in one of three ways. Spin is exchanged either by changing the spin of the He nucleus, or by just rotating the atoms it interacts with. This rotation is not useful for polarizing the He, so by adding K, which is likely to engage in "spin-rotation" with the Rb, but likely to engage in "spin-exchange" with He, the polarization efficiency of the cell is increased. Only the spin-exchange collision process causes polarization of the ^{3}He [57] [93].

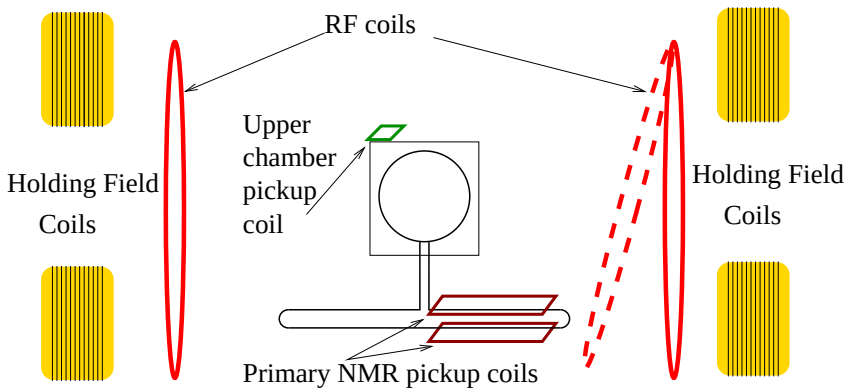

Figure 4.11: The coils used for the NMR measurement of target polarization. Shown is the holding field coils (iron box), the RF coils (which can be adjusted), and the pick-up coils. Two sets of pick-up coils are down at the target chamber, one more set is up above the pumping chamber. One of the RF coils could be adjusted, as could the pick-up coils, to maintain the transverse relationships needed for an NMR measurement.

The diffusion of polarized gas in the cell was modeled to relate the two techniques and properly calibrate the NMR signal.

To perform a NMR measurement, control of the magnetic field of the target is necessary. After an application of a radio frequency (RF) field, when resonance conditions are met, a signal is measured that is proportional to the polarization of the target.

The resonance was found using adiabatic fast passage (AFP). In adiabatic fast passage the magnetic field is changed with a perpendicular radio frequency field (91 kHz) held constant to find the resonance. At resonance, ^{3}He undergoes spin reversal. This spin reversal produces an EMF signal that was detected in a separate set of coils known as pick-up coils. See Figure 4.11 for a description of the coils involved in the NMR measurement.

This measurement technique switches the direction of the spins, so the mag-

netic holding field was swept back to give the original target polarization direction during each measurement. The depolarization caused by this process was found to be on the order of 1%. This measurement technique is relative due to the EMF signal depending on the magnetic flux through the coils, the amplification of the electronics, and the density of ^{3}He. The calibration of this measurement technique is presented in another thesis [56].

In an EPR measurement of the polarization of the ^{3}He, it is light from the polarization of the alkali metals in the cell that is measured. This is due to the alkali atoms being very sensitive magnetometers. This energy shift is due to the Zeeman effect. Obviously this means that there are two shifts in the Zeeman responses of the K and Rb, one due to spin exchange and another due to the magnetic field experienced by the metal including that of the polarized ^{3}He.

There are numerous magnetic fields which cause this shift, such as the holding field and interactions with the other atoms. However, these other shifts are not dependent on the polarization of the target, and by flipping the polarization the effect due to the polarized ^{3}He on the magnetic field creating slight differences in the K energy levels can be determined. For a spherical sample, combining shifts due to collision and the classical magnetic field, the following relationship for the signal shift is obtained [51]

$$\Delta\nu_{EPR} = \frac{8\pi}{3}\frac{d\nu_{EPR}(F,M)}{dB}\kappa_0\mu_{He}P_{He}\ . \tag{4.1}$$

Here B is the magnet field, P_{He} is the polarization of the ^{3}He, and κ_0 is a parameter. To flip the target polarization, the holding field is kept constant and the applied

RF field is swept (which is in resonance with the ^{3}He). The EPR resonance causes depolarization and the fluorescence caused by that repolarization can be tracked as a function of RF frequency. This decay is caused by a shift in electron energy levels in the potassium atoms.

To understand the two measurement techniques relative to one another, NMR measurements were performed both before and after each EPR measurement. The EPR measurements had the disadvantage of causing significant target depolarization. This is because the EPR transition causes the ^{3}He spins to be anti-aligned with that of the spin state the alkali is being pumped into. To minimize the depolarization, this transition was done twice for every EPR polarization measurement. The EPR measurement depends on κ_0, which is different for every alkali and noble gas combination and has temperature dependence [33] [85].

The measurements required to relate the absolute EPR measurements and the relative NMR measurements and the model used to relate the polarization at the different locations of the two measurements is presented in detail in another thesis [56]. The corrected polarization is shown in Figure 4.12. From equation 4.1 it is obvious that the target density needs to be known well. Resistive temperature devices (RTDs) were placed at eight locations on the cell to measure the temperature, from which the density was computed using the ideal gas law. These RTDs did not measure the internal temperature, and so a series of NMR measurements were carried out under various conditions to determine the true internal temperature [56].

Many corrections are needed to provide the needed polarization and direction of polarization to properly determine the physical asymmetry. The material

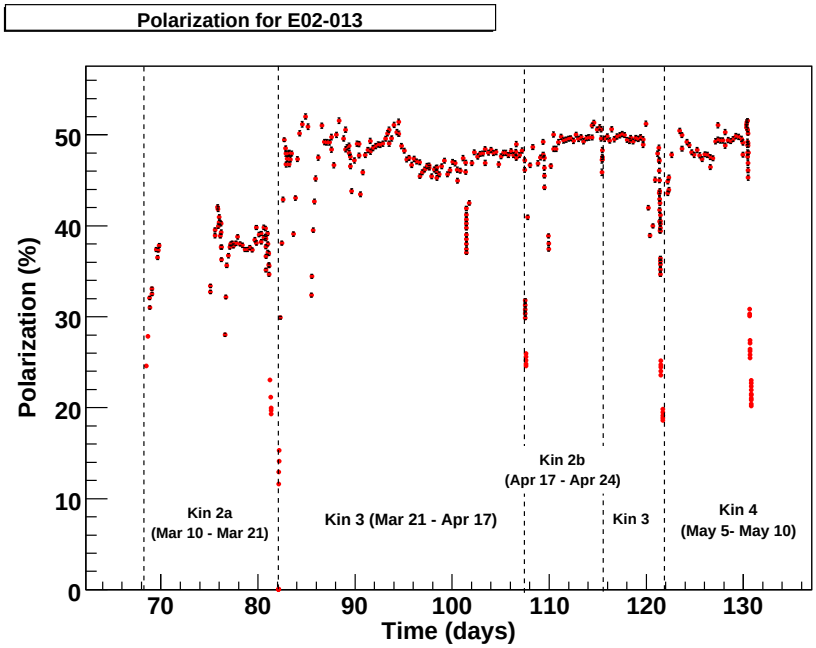

Figure 4.12: Measured polarization in the ^{3}He cells during the experiment [56]. Shown is all cells, including Dolly, Edna, and Barbara used during Kinematics 2, 3, and 4.

surrounding the helium-3 had to be understood to build a proper Monte Carlo simulation, while the unpolarized nitrogen within the cell caused a dilution in the asymmetry. Details of these corrections are presented in section 5.5.2.

4.5 Big Bite

4.5.1 The Big Bite Apparatus

Big Bite is the name of the electron spectrometer, and of the large 1.2 T dipole magnet that provides the magnetic field for the spectrometer. It consists of the large magnet, a plane of 13 scintillators, a calorimeter, and three multi-wire drift chambers (MWDC) containing a total of 15 wire planes. The calorimeter is

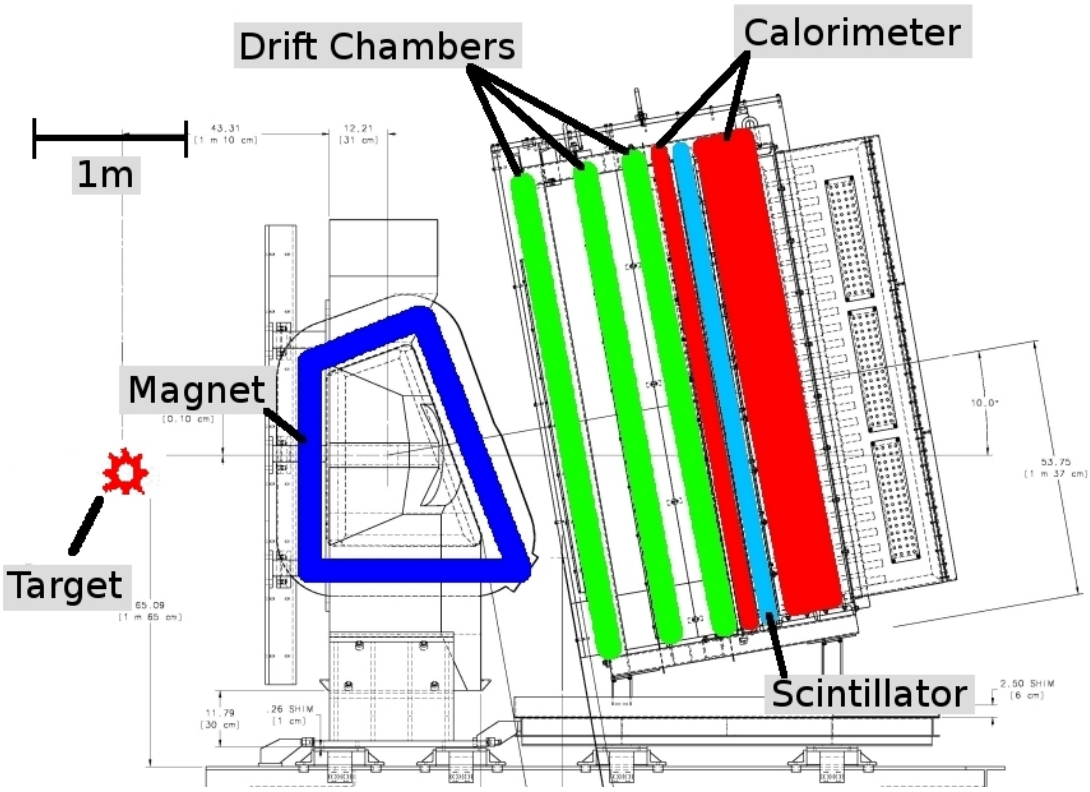

Figure 4.13: Schematic of the Big Bite detector. Shown is the large dipole which provides a magnetic field integral of 1.2 T·m, the 15 planes in three chambers that made up the wire chamber, and the lead glass shower and preshower separated by a layer of plastic scintillator.

split into a shower and preshower, and is constructed of 250 lead glass blocks. A schematic of the Big Bite detector is shown in Figure 4.13.

4.5.2 The Big Bite Scintillators and Shower

The Big Bite scintillators are located between the preshower and shower and provide the time of the event within Big Bite tracker. Each of the thirteen paddles has a photomultiplier tube on each end, with the signal split going to both a TDC via a discriminator and an ADC. The scintillators are used to calculate the time of the particle at the drift chambers, which are about 1 m away. The scintillator time, with resolution $\sigma = 300$ ps, is required for reconstructing the hadron time of flight due to its use in providing the reference time. These scintillators are 64 cm by 220 cm.

The front plane of the total shower, known as the pre-shower, is located 1 m behind the drift chambers. The preshower consists of 54 lead glass blocks in two columns of 27 rows. Behind the preshower, the shower consists of seven columns and 27 rows. Its lead glass blocks are 8.5 cm by 8.5 cm, while the preshower has lead glass blocks that are 35 cm by 8.5 cm. The total height of the structure was 230 cm. Each block is connected to a single photomultiplier tube, which collects the Cerenkov light. The signal is then sent to both an ADC and summation module, with the summed signals going both to an ADC and a TDC. The sum of the shower and preshower gives a signal roughly proportional to the energy of the particle. The total shower provides the trigger for Big Bite. A final set of information provided by

the total shower is the rough location of the particle. This aids track reconstruction in the multi-wire drift chambers and reduces the the search space by a factor of 10. The energy resolution provided by the total shower is approximately $\sigma_{\frac{dE}{E}} = 10\%$.

4.5.3 The Wire Chambers and Tracking

The drift chambers were constructed by the University of Virginia for this experiment in order to reconstruct the trajectory of the electron as it travels through the detector. To do this, the planes which make up the drift chambers were constructed with three different orientations, known as U, X, and V. The chambers were roughly 35 cm apart. In the Big Bite detector coordinate system, the X plane has wires running parallel to the y axis, while the U and V wires are rotated by $\pm 30^{\circ}$ with respect to that axis. The sense wires were 1 cm apart from each other within the plane. Cathode planes were placed 3 mm above and below each wire plane and field shaping wires were placed between each pair of sense wires to create a roughly symmetric potential around the sensing wires.

Charged particles which pass through the chamber release electrons by ionizing the gas within the chamber. This gas is a 50% argon and 50% ethane mixture that had been bubbled through ethyl alcohol and is kept slightly above atmospheric pressure. Since a voltage difference exists between the sense wires, the field shaping wires, and the cathode planes, the charges are attracted to the detector wires and interact with them forming a signal which is then detected in a TDC (after amplification and discrimination). The time it takes to drift to the wire can be determined

and used to calculate the distance between the wire and the particle track. Each plane was set at a different voltage to create the desired field surrounding the sensing wires.

The detector determines more than just the track that the particle traveled, it is also determines the particle momentum and its point of origin within the target. An effective bend plane model was used to determine this, where the interaction of the magnet is treated as occurring at the magnetic mid-plane. If we assume that there is only dispersion along Big Bite detector x, then the complete track between the target and the total shower can be reconstructed. By finding the point in the magnetic mid-plane that the observed track (back track) in the drift chambers points to, and assuming that dispersion happens only in the x (Big Bite) direction, the origin of the track along the beam (forward track) can be determined (V_0). All coordinates in this section are in the Big Bite detector coordinate system unless otherwise indicated.

In this model, the vertex is (after corrections $c_{x'}$, c_y, $c_{y'}$, and c_x)

$$V_{LAB} = c_0 V_0 + c_{x_0} x_0 + c_{x'_0} x'_0 + c_{y_0} y_0 + c_{y'_0} y'_0 + f(x_{bend}, y_{bend}) \ . \tag{4.2}$$

Here the V is the z vertex location in the lab coordinate system, and $f(x_{bend}, y_{bend})$ is a parameter to determine deviations outside of this model. The x_0 and y_0 describe the location of the intersection of the track with the plane $z = 0$ in the detector coordinate system. The variables $\Theta_{tgt} = x'_0$ and $\Phi_{tgt} = y'_0$ describe the track between the bend plane and the target and are found by $x'_0 = \frac{dx}{dz}$ and $y'_0 = \frac{dy}{dz}$ in the detector coordinate system. The bend coordinates (x_{bend}, y_{bend}) are the detector coordinates

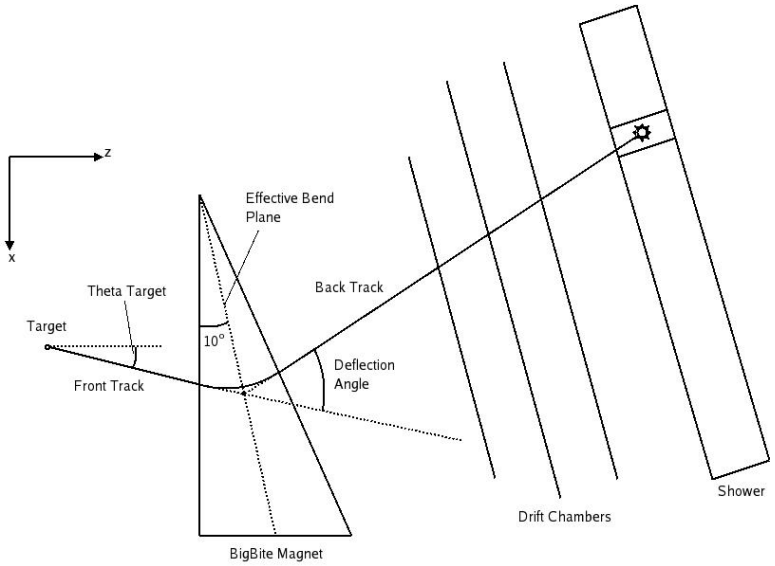

Figure 4.14: This diagram, which is not to scale, shows Big Bite, the location of the dipole, target, drift chambers, and shower, and the quantities known as the deflection angle (θ_{def}), θ_{tgt}, and the back and front tracks. Shown on the upper left is the coordinate system for the target coordinates. The shower is shown providing a fourth location for the particle, to anchor the track reconstruction. Big Bite detector coordinates have their origin at the center of the first plane. The z direction is perpendicular to the first chamber, and x is the magnetic dispersion direction.

where the track intersects the bend plane. A diagram of the effective bend plane model is in Figure 4.14. A histogram showing the foil target vertex reconstruction is shown in Figure 4.16. This shows that the position along the target is reconstructed properly.

The momentum can also be determined, as

$$p_{BB} = \frac{c_0(x_{bend}, y_{bend}) + c_x x_{bend}}{\theta_{def}} + c_\theta \theta_{tgt} + c_y y + c_{y'} y' + f(x_{bend}, y_{bend}) \ . \tag{4.3}$$

This θ_{def} is the deflection angle, and defined using the vectors $\vec{x}_f$ and $\vec{x}_b$ which describe the tracks the particle takes between the target and the magnetic mid-plane and between the magnetic mid-plane and the wire chambers, and is defined to be

$$\theta_{def} = \cos^{-1}\left(\frac{\vec{x}_f \cdot \vec{x}_b}{|\vec{x}_f||\vec{x}_b|}\right) \ . \tag{4.4}$$

The energy for the electron in elastic events can also be determined as

$$E_{elastic} = \frac{m_p E_e}{m_p + E_e\,(1 - \cos\theta_e)} \ , \tag{4.5}$$

where m_p is the mass of the proton and E_e is the energy of the electron, and θ_e is the electron scattering angle. The momentum calibration was done using hydrogen data. The momentum resolution is demonstrated in Figure 4.15.

4.5.4 Big Bite Electronics

Signals from each wire in the multi-wire drift chamber travel through an amplifier and discriminator before terminating at a LeCroy 1877 multi-hit TDC running in common-stop mode. Information is read out from these after each trigger. The

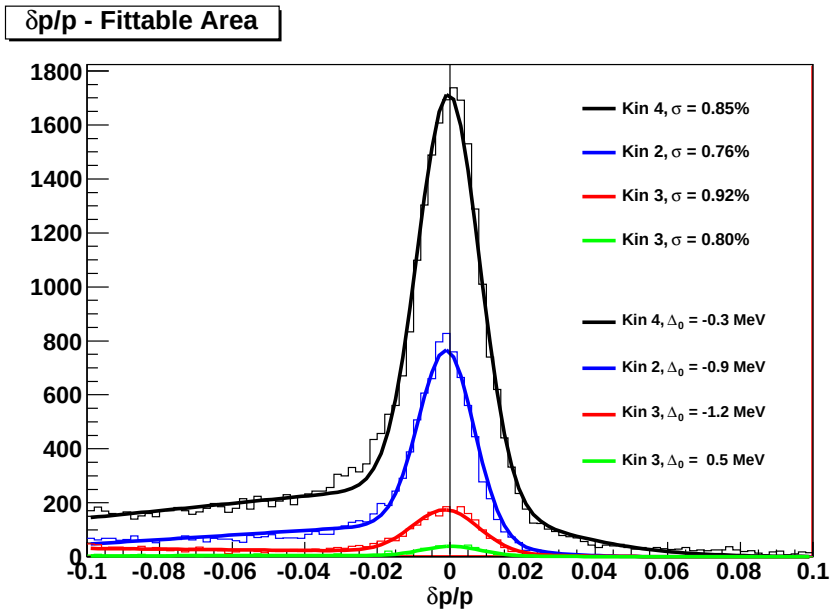

Figure 4.15: Momentum resolution achieved with the latest optics model. Shown is the momentum resolution for all four kinematics.

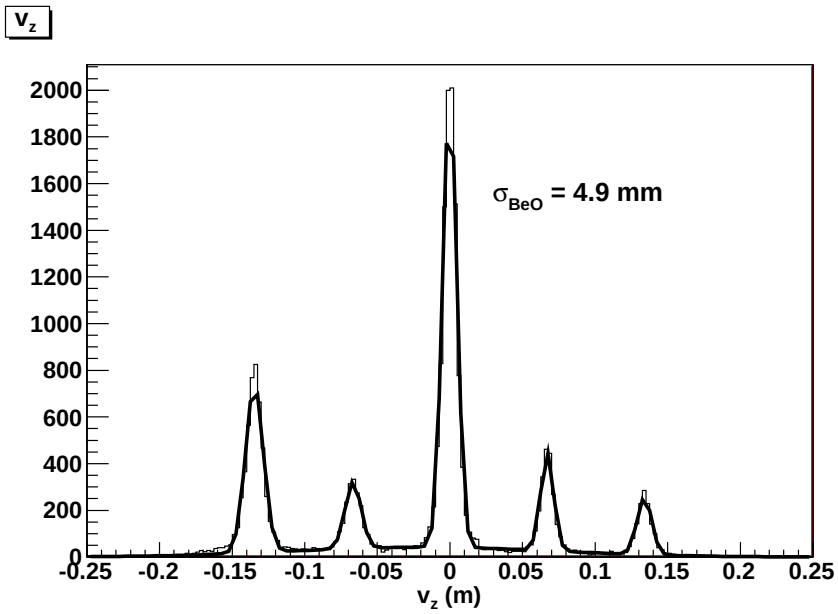

Figure 4.16: Resolution of the carbon foils after vertex corrections. The foils should be 6.7 cm apart with the BeO foil at 0 cm. This histogram is of data from a foil target run in kinematic 3. These foils were used for the optics calibration.

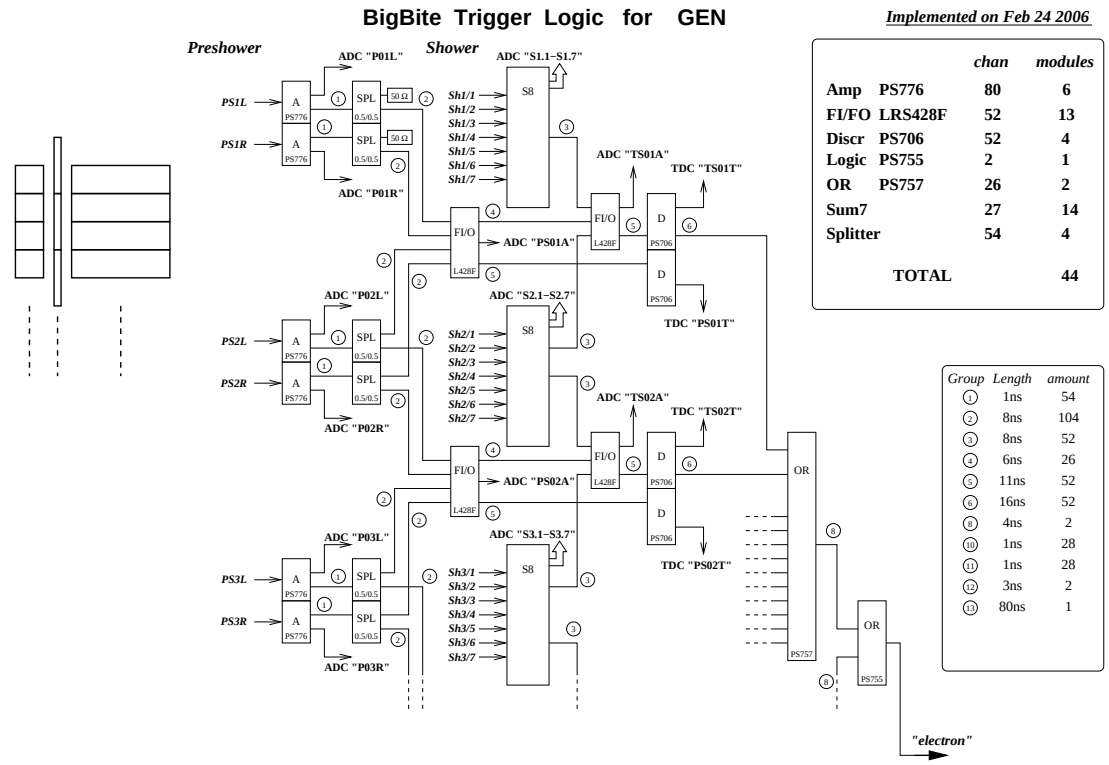

Figure 4.17: The electronics schematic for Big Bite. Shown are the modules and the wire lengths. Two neighboring preshower blocks, and two neighboring sets of shower blocks, which have a summed amplitude that passes some threshold provides the trigger for the electron arm.

scintillators have their signal split between a LeCroy 1881 ADC and a discriminator, with the discriminated signal terminating on a CAEN 775 TDC. The shower and preshower have all their signals (individual and summed) put into a LeCroy 1881 ADC, with the sums also having the signal discriminated and put into a LeCroy 1877 TDC.

The sums of the preshower and shower that are over some predefined threshold provide the Big Bite trigger.

4.6 Big Hand

While the subject of Big Hand is a major component of this thesis, the calibration and detailed analysis of the neutron arm's behavior is not needed directly for the analysis. As a result, the geometry was described in detail in a document put together by Tim Ngo [73] and the software, detector description, analysis, and calibration are presented in Appendix A. Neutron detection took place through hadronic interaction in iron converter layers in front of neutron detector counters organized in seven planes behind two veto layers and lead shielding. Discussion of neutron detection is also the subject of Chapter 5 and Appendix A.

4.6.1 Neutron Geometry

The neutron apparatus (NA), sometimes referred to as Big Hand, is a large hadron detector, designed to match Big Bite's acceptance at the highest kinematic with $Q^2 = 3.5$ GeV^2. The dimensions of Big Hand are $4.2\times2.0\times6.2$ m^3 and it has a 100 msr solid angle at a distance of 8 meters. The neutron detector is made up of 244 neutron bars in seven planes and 192 segmented, single sided veto bars in two planes. These counters were provided by University of Virginia (UVA), University of Glasgow (GLA), and Carnegie Mellon University (CMU). For the UVA counters PMT type XP 2282B were used, for the CMU counters PMT type XP 2262B, while for the GLA EMI 5" were used [98]. In order to properly identify quasi-elastic events at the highest kinematic, a time resolution of 0.3 ns was desired, which corresponds to neutron momentum resolution of 250 MeV/c at a hadron momentum

of 2.58 GeV [25]. The scintillation material in the counters was the standard organic plastic scintillation material [1]. To increase the detection efficiency of neutrons, a thin (one inch) layer of iron was placed in front of each counter to cause some portion of the incident neutrons to undergo hadronic interactions. A high degree of segmentation was important so that the vertical (X) position of the incident particle could be measured with the required resolution. This allows the selection of quasi-elastic events for which it is necessary to have a good measurement of momentum perpendicular to the virtual photon. Four "marker" counters were included for calibration purposes.

4.6.2 Veto and Marker Bars

The veto counters were divided into two so that they would provide the needed time resolution without problems with attenuation. The two veto planes were offset from each other both horizontally and vertically, for complete coverage of the active area of the neutron bars. This, in addition to the height of veto bars (11 cm) compared to the neutron bars (15 cm for CMU bars), meant that multiple veto bars could possibly fire to define the charge for an event within the neutron bars.

The marker counters were included late in the construction to calibrate the horizontal position reconstruction of the neutron detectors. These are long vertical scintillators placed before the first plane of the neutron detector, but after the shielding and veto detectors. They were placed within two constructed channels, with the same amount of space between the top marker bars and the bottom marker

bars for each channel [72]. Even with two marker bars to cover the whole height of the neutron arm, most coincident hits between a marker bar and a neutron bar were only measured in a single PMT in the marker bar. Using these marker bars assisted in the time offset calibration of the neutron arm.

4.6.3 Neutron Arm Electronics

The initial discriminators, amplifiers, and summing modules, were all placed in an electronics hut behind the neutron detector. The ADCs and TDCs were put behind shielding some 100 meters away, where the signals were discriminated again to provide a good signal. Signals from the detectors were combined into sums. This was done to increase the neutron detection efficiency at $Q^2 = 2.5$ GeV^2. Figure 4.19 shows the neutron bars and veto bars, a sum is made up of the left or right PMTs for two neighboring color coded sections.

The ADCs used for the detectors within the neutron arm were all Lecroy 1881, while the TDCs used for the veto detectors and sums were LeCroy 1877 TDCs. The F1 TDCs were specially developed electronics for Jefferson Lab and were used for the neutron counters. These TDCs were used in a common-stop mode and provided a resolution of 118 ps. The F1 TDC required that a reference signal be used, this was a delayed signal from the trigger and the F1 TDC signals could be reconstructed relative to it. Summing modules, amplifiers, fan in/out modules, discriminators, ADCs, TDCs are all presented in Figure 4.18 (and logic). This gives the NA side of the trigger as arising from any sum channel being past threshold on the left or

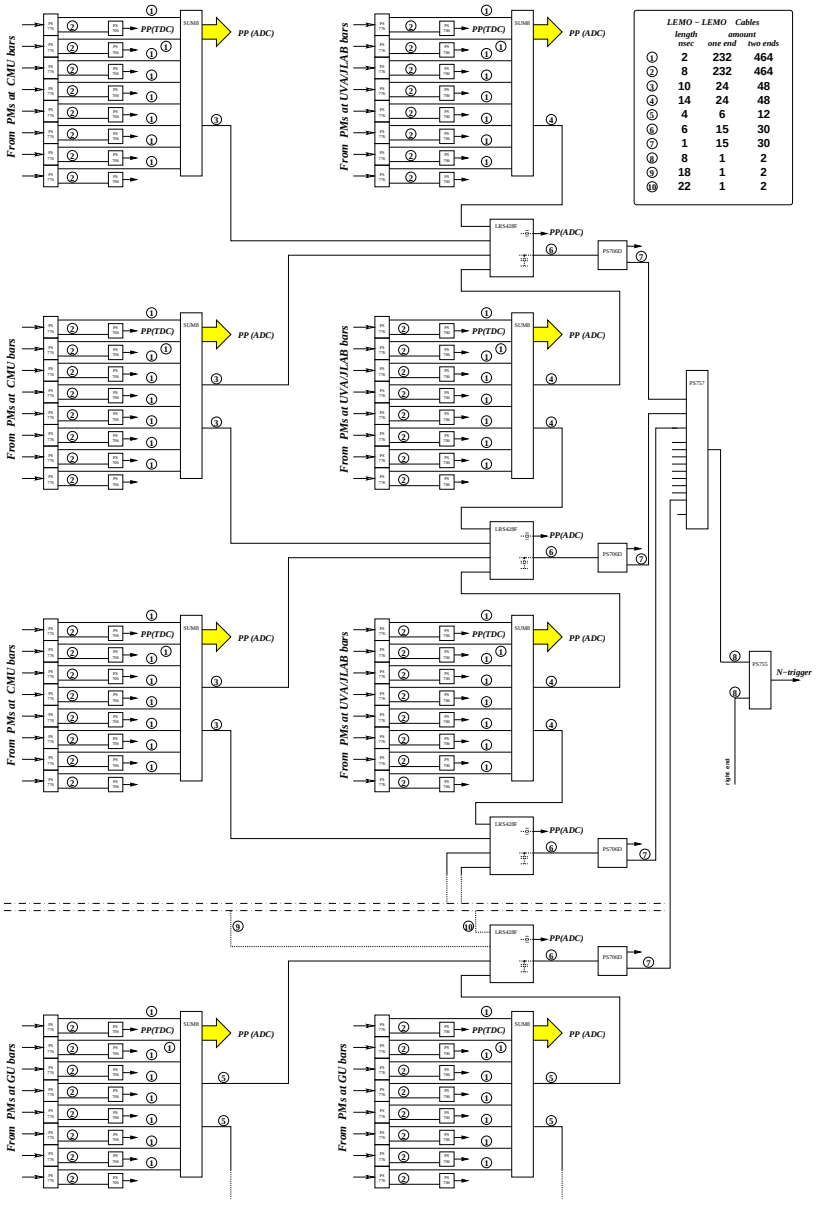

Figure 4.18: Neutron Arm electronics schematics. Included in the schematic is the length of the cables. From the PMTs of the various tubes, the signal goes into both a TDC and a sum module with the non-summed output going to an ADC. The different summed signals are added together and sent to both an ADC and TDC, with an OR of the TDCs forming the trigger.

right.

4.7 Data Acquisition

Six triggers were used in this experiment. These were the neutron arm trigger (1) known as T1, the Big Bite trigger (2) known as T2, the coincidence trigger (3) known as T3, the 8.5 Hz pulser (7), the 105 kHz helicity synchronization signal (8), and the 30 Hz helicity quad duration signal (9).

The T3 trigger was formed by coincidence between the neutron arm and Big Bite. This coincidence was formed between any single sum channel on the neutron arm (left or right) and detection beyond a certain threshold in the preshower and shower. In Figure 4.2 the grouping of neutron bars is presented. Two neighboring colors would be linked together to form one sum, with the left and right PMTs being considered separately. This was done to increase neutron detection efficiency at a higher threshold [79].

The time of the BigBite Shower signal was used for the time of the T2 trigger. The Big Bite scintillator time associated with this was then sent to the neutron arm to provide both the coincidence for the trigger and the reference time of the neutron arm events.

The neutron detector real time was recorded relative to a readout time or reference time. Thus the neutron arm recorded time was given as $t_{recorded} = t_{real} - t_{readout}$. The Big Bite trigger time relative to this same read out time was also recorded as $t_{L1A} = t_{readout} - t_{trig}$ known as the level one accept time and recorded

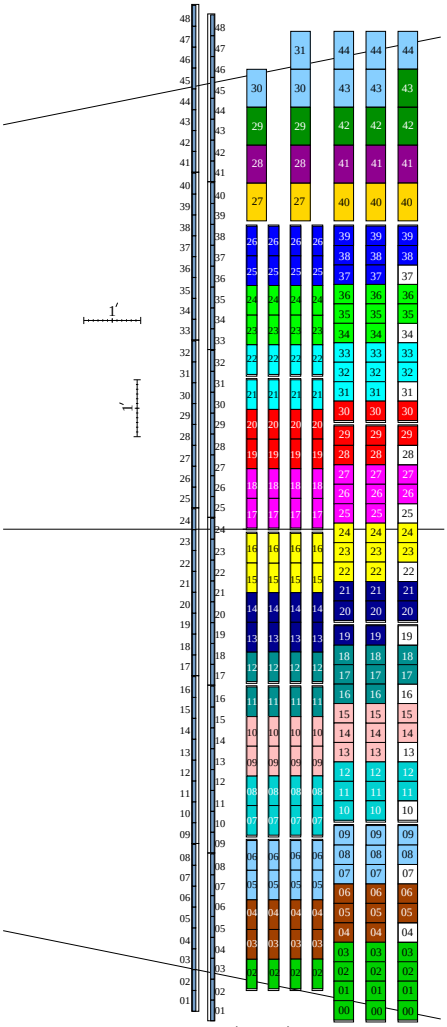

Figure 4.19: Neutron arm (NA) schematic for the sums. In front are the two veto planes. Shown is the relative offset. Additionally, color coded, the sums are shown. Each sum was made up of two neighboring color bands. Shown on top are the bars from Glasgow (GLA), in the front are four planes of bars from Carnegie Mellon University (CMU), and in the back are three planes of bars from University of Virginia (UVA). The colorless bars in the final plane are bars that were not connected to the electronics. The first two thin planes are the veto planes, the figure shows the vertical shift between the two planes.

in the TDC. The neutron arm time relative to the Big Bite trigger time is then $t_{real} = t_{recorded} + t_{L1A}$.

A trigger from both detectors, Big Hand and Big Bite, created a T3, the coincidence trigger. The $t_{readout}$ time was based on this T3 time. The T1 came 35 ns later than the T2 trigger due to delays added in. If the T1 came too early, $t_{readout}$ and T3 were based on on the T2 trigger. If the T2 trigger came very early, then the Big Bite readout was determined by $t_{readout}$ and not the T2 trigger. This is known as forced retiming. A plot showing the data with the different types of events is shown in Figure 4.20.

Both detectors provided information at each coincidence event. Single trigger events were also taken but prescaled to provide a minimum number of events in the experiment. All three multi-wire drift chambers provide TDC information, the scintillators provided both ADC and TDC, and the preshower and shower provided ADC information (with the preshower and shower sums providing TDC in addition to ADC information). All the neutron arm detectors provided both TDC and ADC information, with the neutron detectors also grouped into sums which provided ADC and TDC information as well. The neutron arm reference time was recorded in both the Neutron Arm TDCs and the Big Bite TDCs.

4.7.1 Encoding and Decoding

There are two main data acquisition systems. One is EPICS, which provides updates occasionally (no more often then every few ms) and provides information

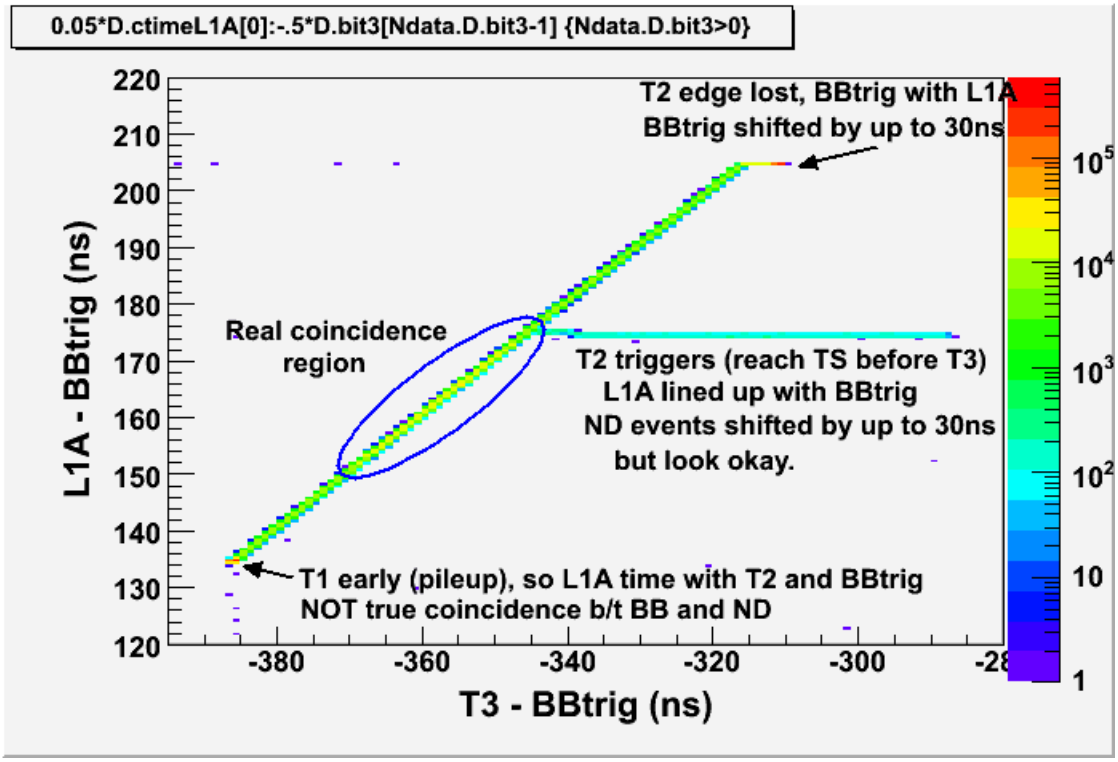

Figure 4.20: Plot showing the reference time and coincidence counts in relation to the Big Bite trigger time [37]. Best coincident events are in the circled region.

about the target, accelerator, electronics, and scalars. This is included in the data stream with the events from the detectors. The events from the detectors are acquired using CODA, which can monitor, acquire, record, and decode data taken during experiments [48]. Some target information was stored separately.

To do the analysis and turn the raw data into usable information, a modification of the ROOT software package called the Hall A Analyzer was used [5]. This package has features which make it easier to deal with large amounts of data and to make histograms and graphs. Special classes for the analysis of the different detectors have been developed for the analysis of the neutron arm data and for tracking and momentum reconstruction in Big Bite and are discussed in other sections. The library which contains these classes is the AGen library. The E02-013 experiment used a modification of this Hall A Analyzer. This was done so that in the decoding and initial calculation of physics quantities, Big Bite tracking code could take advantage of other detectors. The scalar data was put in separate trees in this initial decoding and analysis of the data. During the initial decoding and analysis steps, the first 1000 events of a run were discarded (due to being helicity diagnostic events) as were non-coincidence events. During decoding and processing, the data is put into trees, which is a data format commonly used in ROOT and are referred to as root files [86].

These root files were then processed an additional time and then the quasi-elastic events were selected using the Big Bite preshower, the reconstructed momentum, the reconstructed vertex hit location, and the hit locations and times of the coincident hadron and electron. This post processing and analysis is described in

Chapter 5, with the final value of G_E^n calculated for the kinematics $Q^2 = 3.5$, 2.5, and 1.5 GeV^2.

Date	Method	Polarization	Statistical	Systematic
March 30, 2006	Mott	83.32 %	1.45	1.00
March 30, 2006	Mott	81.62 %	1.45	0.98
April 13, 2006	Mott	84.12 %	1.11	1.01
April 13, 2006	Mott	83.25 %	1.11	1.00
Average	Mott	83.08 %	0.65	1.00
February 28, 2006	Møller	88.8 %	0.2	3.0
February 28, 2006	Møller	86.8 %	0.2	3.0
March 4, 2006	Møller	88.2 %	0.14	3.0
March 9, 2006	Møller	86.5 %	0.15	3.0
March 25, 2006	Møller	82.2 %	0.3	3.0
Average	Møller	86.5 %	0.09	3.0
April 18, 2006	Compton	82.92 %	2.31	2.40
April 20, 2006	Compton	85.63 %	3.87	1.55
April 22, 2006	Compton	86.47 %	1.63	3.55
April 24, 2006	Compton	82.65 %	1.64	3.20

Table 4.2: A table of the beam polarization as measured by different means at different times. The Møller measurements were done in the Hall A Møller. The Mott measurements were done using the injector Mott measurement. Only selected Compton data is presented, and the Compton data isn't used in this analysis.

Chapter 5

Analysis

In experiment E02-013 the electric form factor of the neutron was measured at four kinematic points. Three of these kinematic points are presented in this thesis, with the fourth still to be analyzed by another collaborator. The analysis procedure, excluding the initial decoding and analysis steps, is shown in flow charts in Figures 5.1, 5.2, and 5.3. The initial decoding and analysis passes provide the electron arm physics information, as described in section 4.7, in addition to neutron arm cluster information. The first step of this procedure is the event based filtering, as described in Table 5.1, which uses the time-of-flight of the electron, momentum, invariant mass of the recoiling hadron, and transferred momentum vectors which were already calculated from the electron arm (in section 5.1 and 5.2) information to select hadron event candidates. Next, hadrons are identified using the transferred momentum vectors and the constructed time-of-flight of the hadron, which is discussed in more detail in section 5.3. A charge is assigned to these hadrons as described in section 5.4. Next, various dilutions of the asymmetry (section 3.3), and corrections to it, are described and calculated in section 5.5. The neutron physical asymmetry determined from the neutral quasi-elastic events is then calculated in section 5.6, using the Table 5.5. In this section preliminary results for the electric form factor are also presented with corrections. The final state interaction corrections which

will be included in the final value of G_E^n are discussed in section 5.7. Discussion of error propagation can be found in Appendix B.

Electron event selection in the Big Bite spectrometer was achieved by means of the shower detector and scattering angle. Selection of events from within the target and by a coarse cut on transferred momentum were made using the multi-wire drift chamber (MWDC). Hadron identification was achieved using the location and time of the hit in the neutron detectors, and by using the veto detectors to differentiate the protons from the neutrons. Finally missing mass, missing momentum, and invariant mass were used to select the quasi-elastic process.

5.1 Event filtering and scintillator timing

The total shower detector, as described in section 4.5.2, is divided into two parts, called the shower and the pre-shower, separated by a plane of scintillator detectors. Using only the pre-shower amplitude, pions and electrons could be identified and clearly differentiated, (as shown in Figure 5.4). For any selection based on preshower energy which doesn't remove an unreasonable portion of electrons, some portion of pions will still exist in the selected sample. These pions will create a dilution of the (e,e'h) interaction. An emperical study was done to determine the contamination of the neutral hadron candidate sample by $(ep, e'\pi^0 n)$ events. This contamination was shown to be less than 2% [2].

While the total shower was the hardware trigger for the electron arm, the time based on the calorimeter alone would not provide the needed resolution for the

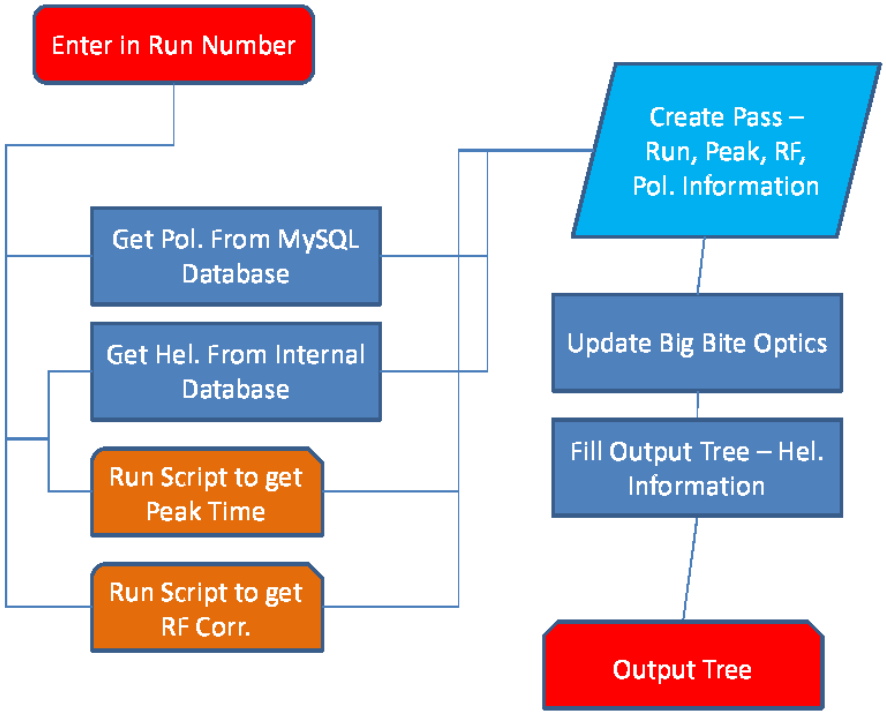

Figure 5.1: The flowchart for the analysis. This is after the preliminary replay of events that is described in section 4.7. The resulting ROOT files contain the subset of events necessary to undertake the remaining analysis, also assigns charge, and identifies quasi-elastic event candidates. Two separate scripts are run as part of this process for each run before this post processing. This is to determine the RF correction (see section 5.5.3) and the hadron time-of-flight.

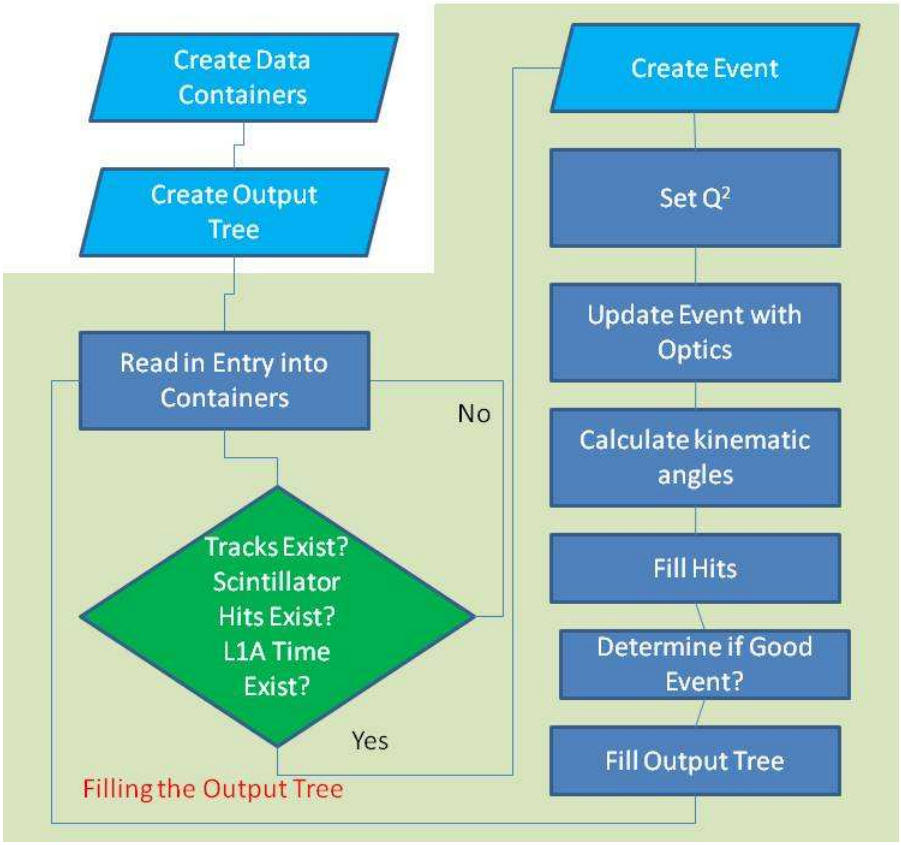

Figure 5.2: Flowchart for the event processing. Events in the analysis are ignored if no tracks or Big Bite scintillator hits exist, or if the event does not have a well defined trigger time as demonstrated by the existence of the Level 1 Accept (L1A) Time. The optics can be updated here if necessary, and the kinematics of the event are calculated to ease post processing. All event cuts are detailed in Table 5.1.

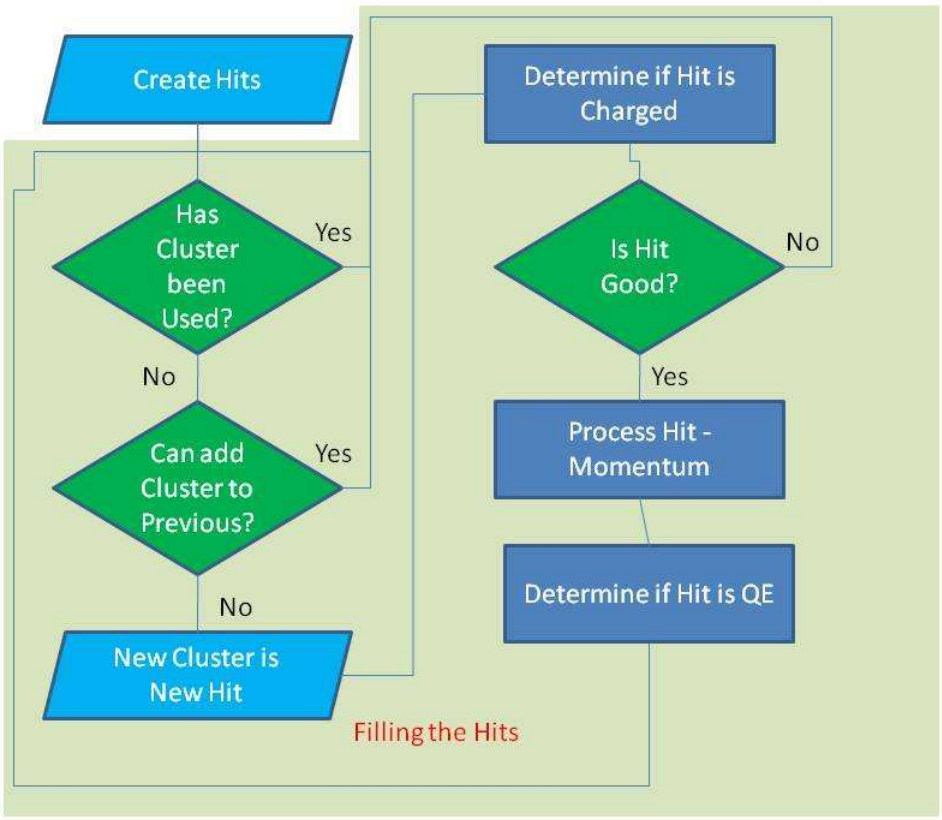

Figure 5.3: Flowchart associating clusters, both with each other and as quasi-elastic event candidates. Some clusters should be associated together, where some neutron detector did not fire to make the cluster continuous. Charged candidates are identified, and momentum is calculated for the hit.

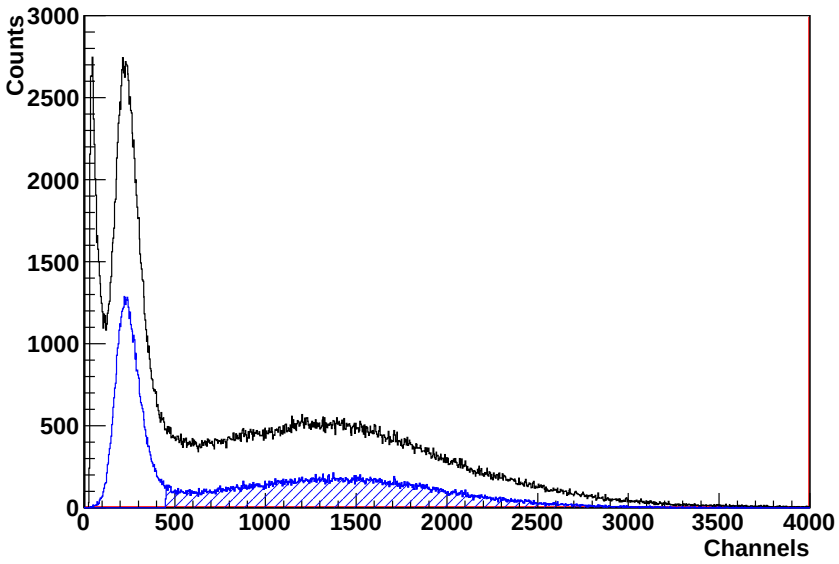

Figure 5.4: Amplitude distribution for all events showing pions and electrons in Big Bite. In blue is the distribution after cuts have been applied to remove events which are lacking the information needed for analysis, shaded is the region selected. See Table 5.1 for cuts, in black is all events and in blue is with just the "sanity" cuts applied. This distribution is for $Q^2 = 3.5$ GeV^2.

event. This function is provided by the plane of scintillators directly behind the pre-shower, which served as the primary time reference for both the electron and neutron arms. The path length for the electron was emperically determined using the optics with respect to this plane. This reference time was corrected for the variations in path length coming from differences in vertex location and corrections for vertical and horizontal position in the scintillator stack.

The time of the event within the electron arm, t_e, can be presented as the time in the scintillator t_s, with corrections for the vertical path length t_x, the horizontal path length t_y, and the difference between the scintillator plane and the wire chamber t_c.

$$t_e = t_s - t_x - t_y - t_c \tag{5.1}$$

$$t_x = \frac{1}{c} 1.2 |P_{x,BB} + 0.25| \tag{5.2}$$

$$t_y = \frac{1}{c} \frac{[2.2532 \sin(-\theta_{BB}) + Y_{BB} \cos(-\theta_{BB})]}{\sin[\tan^{-1}(P_{y,BB}) - \theta_{BB}]} - 2.2 \tag{5.3}$$

$$t_c = \frac{1}{c} \left(L_{D2S} (1 + P_{x,BB}^2 + P_{y,BB}^2 \right)^2 \tag{5.4}$$

Here, $L_{D2S} = 0.95$ m is the time from the detector to the scintillator, $P_{x,BB}$ is the track slope $\tan\Theta = \frac{dx}{dz}$ in Big Bite detector coordinates, $P_{y,BB}$ is the track slope $\tan\Phi = \frac{dy}{dz}$ in Big Bite detector coordinates, Y_{BB} is the reconstructed horizontal position vector y in Big Bite detector coordinates, and $\theta_{BB} = 51.59°$ is the central angle at which the detector was placed for the Q^2 of 1.7, 2.5, and 3.5 GeV^2. The other constants were empirically determined using the optics data.

5.2 Electron parameters

Quasi-elastic (from ^{3}He) and elastic events (from hydrogen) were selected using the momentum of the electron as measured by the Big Bite spectrometer in addition to deposited energy in the preshower (see Figure 5.5). Additional event selection was performed by removing events that were reconstructed to start from outside of the target (see Figure 5.7), or that travelled through a region of Big Bite where the magnetic field is not well understood (see Figure 5.6). Among the quantities computed from the identified electron tracks are the invariant mass of the hadron, the transferred momentum of the virtual photon, the electron momentum, and the electron scattering angle.

The transferred momentum, $\vec{q}$, calculated from the beam energy and scattered electron momentum, was used in the identification of quasi-elastic hits within the neutron arm. The transferred momentum is entirely independent of the neutron arm time-of-flight. The parallel and perpendicular components of transferred momentum with respect to the hadron momentum vector can be defined as

$$q_{\parallel} = \vec{q} \cdot \hat{p}_h \ , \tag{5.5}$$

$$q_{\perp} = \vec{q} \times \hat{p}_h \ . \tag{5.6}$$

Here $\hat{p}_h$ is the unit vector of the hadron momentum as determined by the neutron arm. This is determined purely from the hit location (x, y, and z) in the neutron arm, and is independent of time-of-flight.

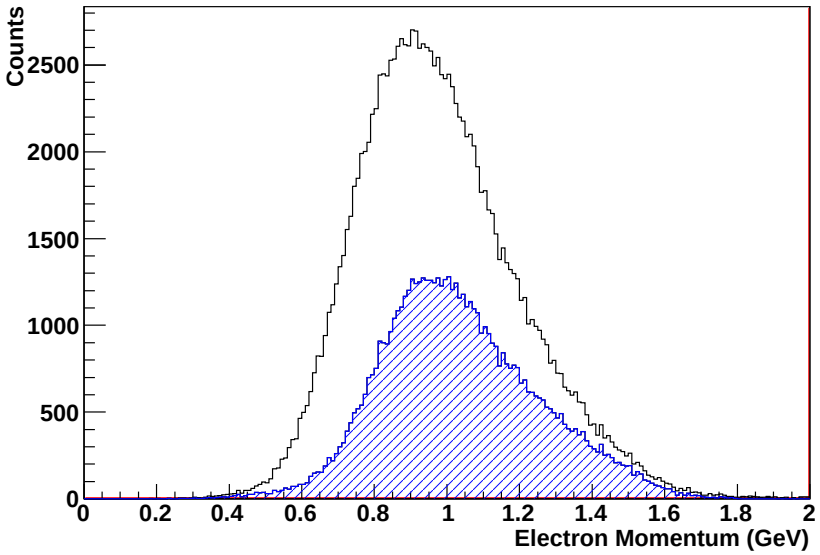

Figure 5.5: Electron momentum for all tracks in Big Bite. In blue are just those tracks for which the preshower energy is greater than 450 channels, shaded is the selected momentum. See Table 5.1 for cuts, in black is all events and in blue is with the "sanity" and pre-shower energy cuts applied. This distribution is for $Q^2 = 3.5$ GeV^2.

The invariant mass of the hadron is

$$W^2 = 2\omega M_N + M_N^2 - Q^2 \tag{5.7}$$

Here M_N is the nucleon mass, Q^2 is the transferred four-momentum squared, and ω is the virtual photon energy (see section 2.2).

The invariant mass and perpendicular transferred momentum ($q_\perp$) are the two time-of-flight independent variables which are used for quasi-elastic event selection. The selection of quasi-elastic events are shown for $Q^2 = 2.5$ GeV^2 in Figure 5.8(a) and 5.9(a). Both of these figures include fidicual cuts in the neutron arm. The final quasi-elastic neutral candidates selection for kinematic 2 as well as the overall spectrum is presented in perpendicular transferred momentum is presented in Figure

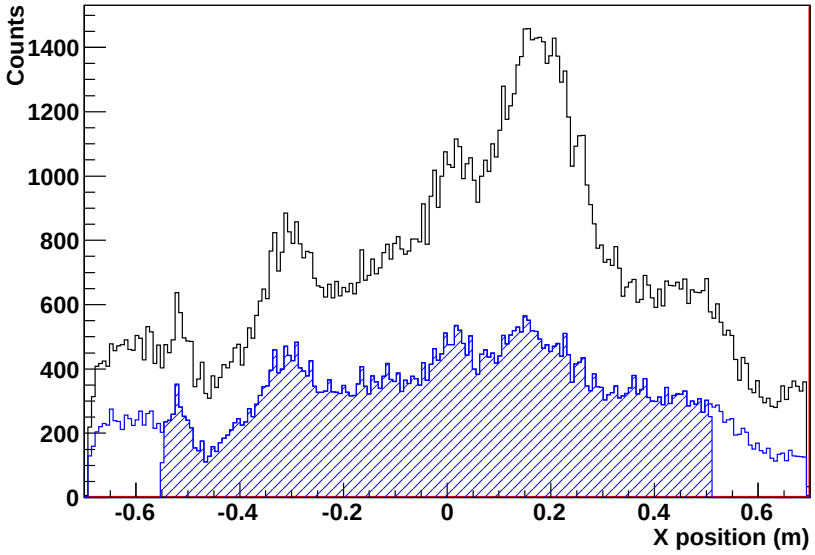

Figure 5.6: X position (m) within the Big Bite scintillator detector. This is for before cuts (black), after electron and sanity cuts (blue), with the selected region of X shaded. Variation is due to the lack of calibration for the total shower in the Big Bite detector. See Table 5.1 for cuts, in black is all events and in blue is with the "sanity", pre-shower energy, and electron momentum cuts applied. This distribution is for $Q^2 = 3.5$ GeV^2.

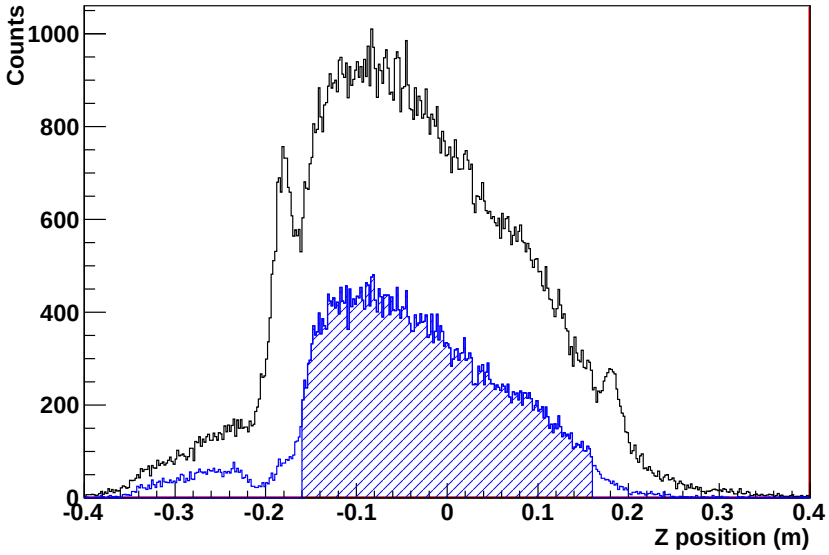

Figure 5.7: Vertex, this shows the target z position reconstructed by the Big Bite wire chambers for all events with tracks (black). In blue is after cuts on particle ID. Shaded is the region selected as being within the target. See Table 5.1 for cuts, in black is all events and in blue is with the "sanity", pre-shower energy, Big Bite fidicual, and electron momentum cuts applied. This distribution is for $Q^2 = 3.5$ GeV^2.

name	$Q^2 = 2.5$ GeV^2	$Q^2 = 3.5$ GeV^2	$Q^2 = 1.7$ GeV^2
W (GeV)	$\lvert W - 0.95\rvert < 0.6$	$\lvert W - 0.95\rvert < 0.6$	$\lvert W - 0.95\rvert < 0.6$
E. E. (Ch)	$E_{ps} > 450$	$E_{ps} > 450$	$E_{ps} > 450$
E. Mom.(GeV)	$\lvert p_e - 1.1\rvert < 0.9$	$\lvert p_e - 1.1\rvert < 0.9$	$\lvert p_e - 1.1\rvert < 0.9$
Vertex (m)	$\lvert V_{tgt}\rvert < 0.16$	$\lvert V_{tgt}\rvert < 0.16$	$\lvert V_{tgt}\rvert < 0.16$
X Fid. (m)	$-0.4 < X_{BB} < 0.45$	$-0.4 < X_{BB} < 0.45$	$-0.4 < X_{BB} < 0.45$
Sanity 1	$N_{Tracks} > 0$	$N_{Tracks} > 0$	$N_{Tracks} > 0$
Sanity 2	$N_{Paddles} \geq 0$	$N_{Paddles} \geq 0$	$N_{Paddles} \geq 0$
Sanity 3 (Ch)	$t_{L1A} < 4000$	$t_{L1A} < 4000$	$t_{L1A} < 4000$
Sanity 4	$N_{Type3} > 0$	$N_{Type3} > 0$	$N_{Type3} > 0$
Negative	$P_{x,BB} - 0.3X_{BB} < 0$	$P_{x,BB} - 0.3X_{BB} < 0$	$P_{x,BB} - 0.3X_{BB} < 0$

Table 5.1: A table of the initial event selection for analysis. Sanity cut 1 is the requirement that Big Bite has a track, Sanity cut 2 is the requirement that at least one scintillator paddle in Big Bite has an event, Sanity cut 3 is that the coincidence time (L1A) was recorded. Sanity cut 4 is the requirment that there is a coincidence event. Negative is a requirement that only negative particles in the drift chambers can be considered as electrons.

5.11(a). The expected invariant mass is about 0.94 GeV, the mass of a nucleon.

5.3 Hadron identification

Once electron events are selected and the invariant mass and the direction and magnitude of $\vec{q}$ are determined from information from the Big Bite spectrometer, the neutron arm is used to determine the three-momentum and charge of the hadron. Hits in the neutron arm were joined together into clusters as described in Appendix A. Typically, multiple bars recorded hits in the same event in the neutron apparatus due to particles with high energy traveling deep into the neutron apparatus, and to the segmented nature of the neutron apparatus.

The time of the counter with the earliest hit (of those nearby in time and space) was used as the time of the cluster. This time, the time of the electron

in the Big Bite scintillator, and the relevant path lengths allow the calculation of the momentum of the particle, assuming it is a hadron. Only those hits where the calculated velocity is less than c are included in the analysis.

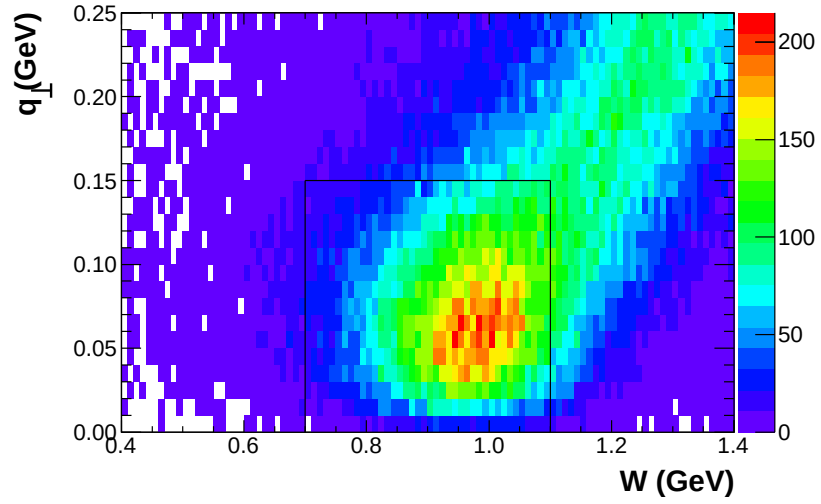

(a) $Q^2 = 2.5$ GeV^2 $q_\perp$

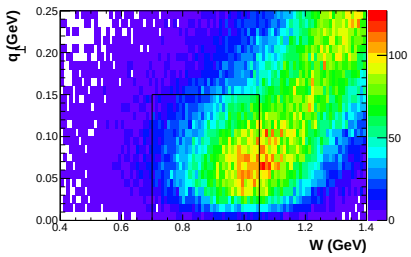

(b) $Q^2 = 3.5$ GeV^2 $q_\perp$

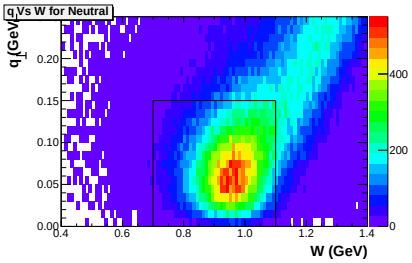

(c) $Q^2 = 1.7$ GeV^2 $q_\perp$

Figure 5.8: $q_\perp$ versus W for neutral particles in the various kinematics. Shown is the selection of quasi-elastic events in the square. As shown, at higher Q^2 the inelastic tail becomes stronger.

The clusters were combined if they were nearby in time and space. The time and position of only the first hits were used to determine whether the later cluster(s) should be considered part of the earlier cluster. Multiple clusters in a single event were considered as a single cluster if δX (vertical position) and δZ (depth) were within 0.4 m, and δY (horizontal position) was within 0.2 m. Additionally, the time

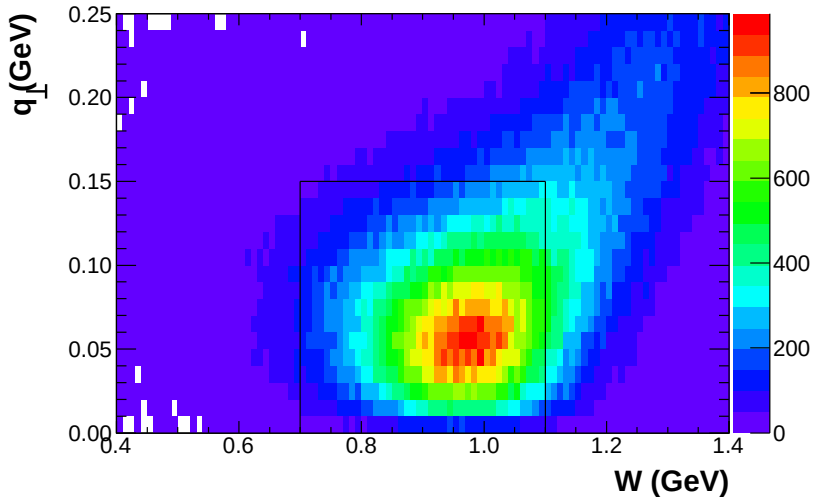

(a) $Q^2 = 2.5$ GeV^2 $q_\perp$

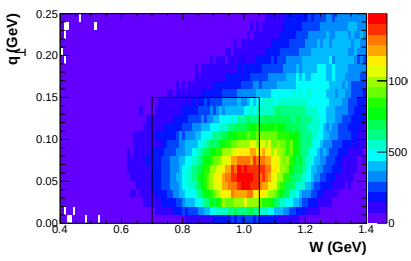

(b) $Q^2 = 3.5$ GeV^2 $q_\perp$

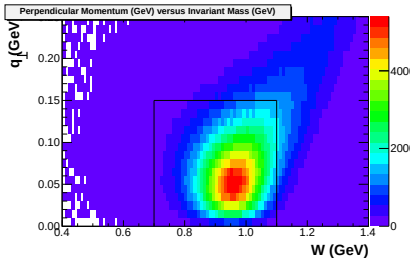

(c) $Q^2 = 1.7$ GeV^2 $q_\perp$

Figure 5.9: $q_\perp$ versus W for charged particles in the various kinematics. In the red box is the selection of quasi-elastic events.

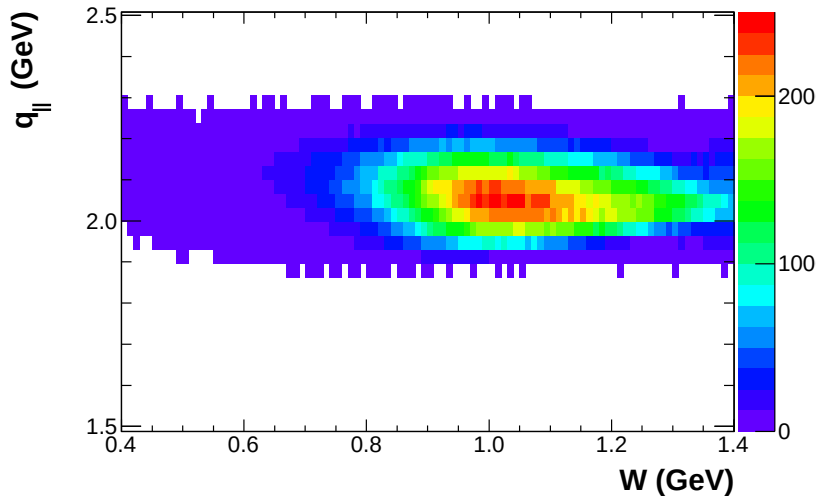

(a) $Q^2 = 2.5$ GeV^2 $q_{||}$

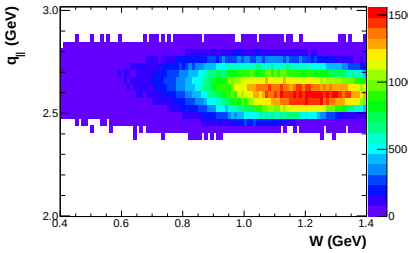

(b) $Q^2 = 3.5$ GeV^2 $q_{||}$

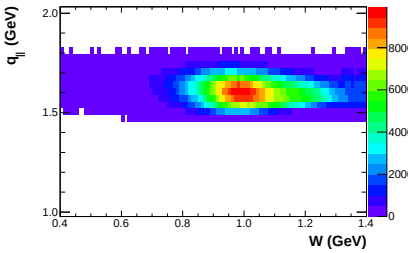

(c) $Q^2 = 1.7$ GeV^2 $q_{||}$

Figure 5.10: $q_{||}$ versus W for charged particles in kinematic 3.

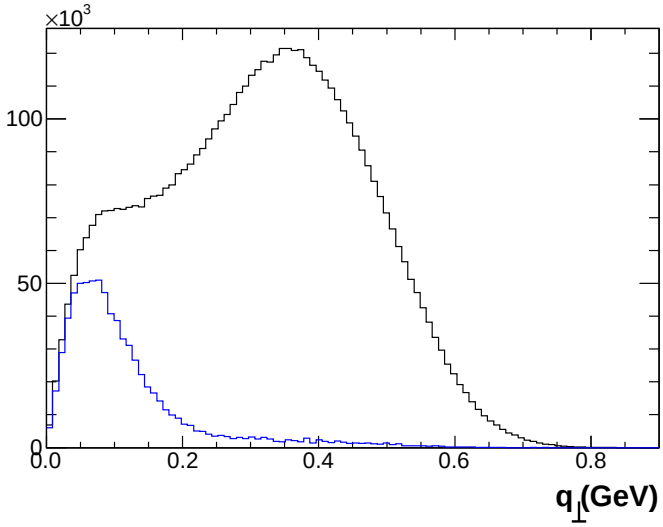

(a) $Q^2 = 2.5$ GeV^2 $q_\perp$

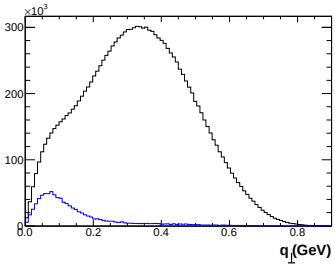

(b) $Q^2 = 3.5$ GeV^2 $q_\perp$

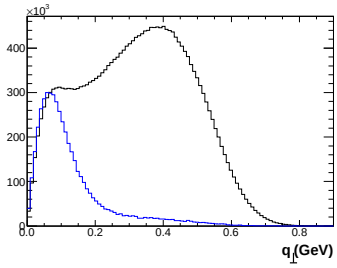

(c) $Q^2 = 1.7$ GeV^2 $q_\perp$

Figure 5.11: Distribution of $q_\perp$ in the various kinematics. Shown in blue is the neutral spectrum, in black is the total spectrum (That passed the event based selection). The majority of neutral quasi-elastic events fall under 0.15 GeV.

difference had to be within 10 ns. See Appendix A for more discussion of clusters and neutron arm software.

The expected time for hadron events within the neutron arm T_h is given by

$$T_h = \frac{\sqrt{L_{NA}^2 + Z_{tgt}^2 - 2L_{NA}Z_{tgt}\hat{p}_h \cdot \hat{z}}}{c\frac{q}{\sqrt{m_h^2+q^2}}} \ . \tag{5.8}$$

Here L_{NA} is the path measured from the center of the target to the neutron arm hit, Z_{tgt} is position of the interaction in the target as reconstructed by Big Bite, $\vec{p}_h$ is the hadron momentum vector (in the laboratory coordinate system). Since at this point the charge of the hadron is unknown, its mass is nominally set to the nucleon mass $m_N = 0.939$ GeV.

This is compared to the actual time-of-flight which is constructed from the measured location of the time-of-flight peak measured using the neutron arm and Big Bite scintillators. This actual time is constructed as

$$T_{TOF} = t_{NA} - t_e + t_{rf} + t_{L1A} - t_{peak} \ . \tag{5.9}$$

Here, the t_{NA} is the time measured in the neutron arm, t_{rf} is the correction that can be done using the beam information (to be discussed in section 5.5.3), t_{L1A} is the level 1 accept time (see section 4.7), and t_{peak} is the peak location in the total time-of-flight spectrum. To select quasi-elastic events, the expected time-of-flight is compared to the actual time-of-flight, giving ΔT. The time-of-flight spectrum for total events and quasi-elastic neutral candidates in kinematic 2 is shown in Figure 5.12(a).

From the time-of-flight, the hadron velocity, β, and momentum, p_h, can be

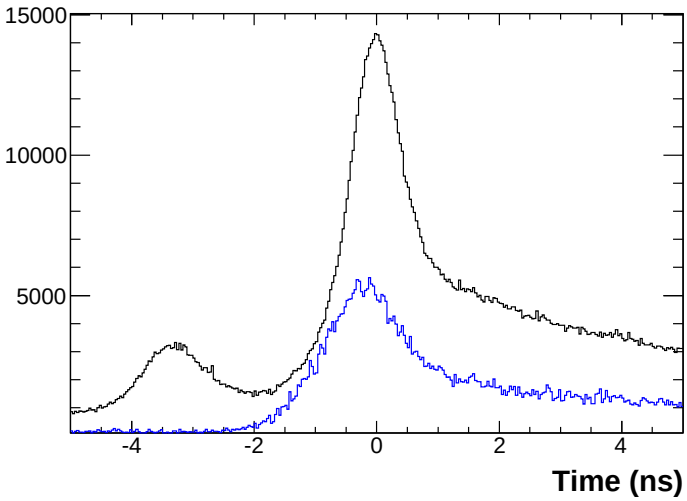

(a) $Q^2 = 2.5$ GeV^2 time

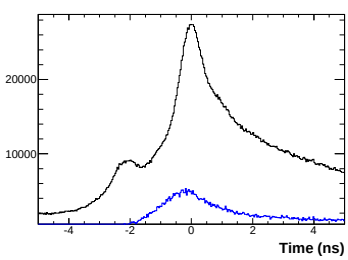

(b) $Q^2 = 3.5$ GeV^2 time

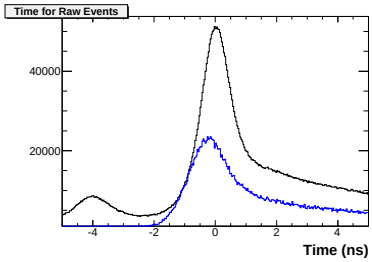

(c) $Q^2 = 1.7$ GeV^2 time

Figure 5.12: ΔT (ns) for the various kinematics. In blue is the neutral time-of-flight spectrum, in black is the total time-of-flight spectrum. The photon peak is shown at ≈ -3ns. Quasi-elastic events are selected with time between -1 and 1 ns.

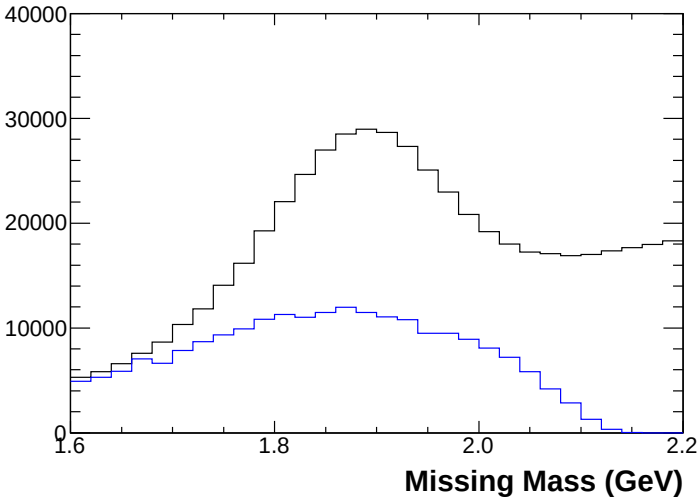

(a) $Q^2 = 2.5$ GeV^2 missing mass

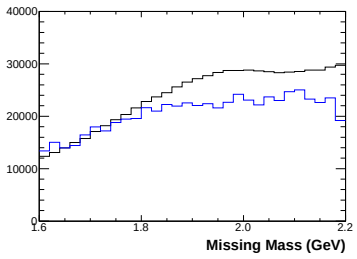

(b) $Q^2 = 3.5$ GeV^2 missing mass

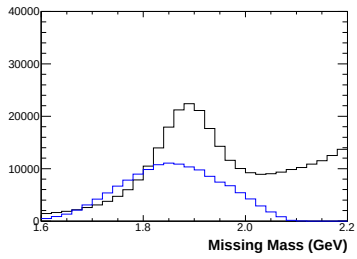

(c) $Q^2 = 1.7$ GeV^2 missing mass

Figure 5.13: Missing mass (GeV) for the various kinematics. In blue is the neutral scaled up by a factor of 20 for $Q^2 = 3.5$ GeV^2 and 10 for $Q^2 = 2.5$ and 1.7 GeV^2, in black is the total spectrum.

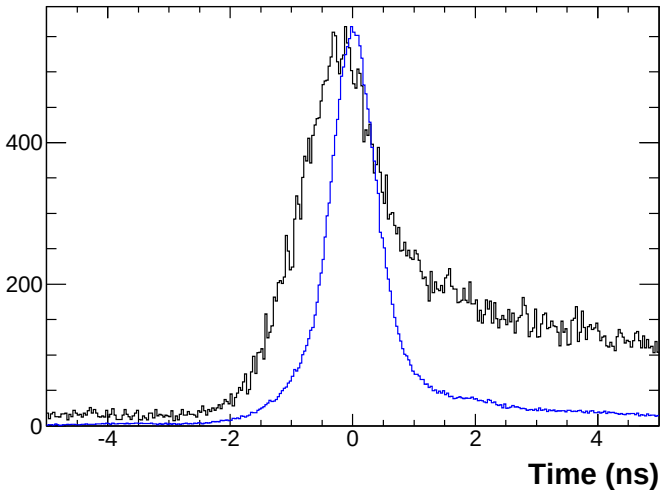

(a) $Q^2 = 2.5$ GeV^2 time

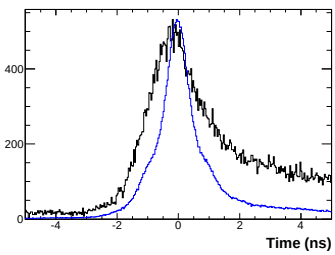

(b) $Q^2 = 3.5$ GeV^2 time

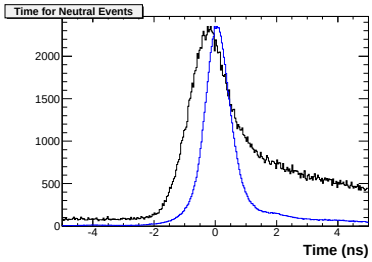

(c) $Q^2 = 1.7$ GeV^2 time

Figure 5.14: ΔT (ns) for the various kinematics. In blue is the charged time-of-flight spectrum, in blue is the charged time-of-flight spectrum. The charged spectrum is scaled down to the neutral spectrum.

constructed (all in laboratory coordinates):

$$\beta = \frac{\sqrt{L_{NA}^2 + V_{tgt}^2 - 2L_{NA}V_{tgt}\hat{p}_h \cdot \hat{z}}}{cT_{TOF}} \ , \tag{5.10}$$

$$p_h = \frac{m_h}{\sqrt{1-\beta^2}} \ . \tag{5.11}$$

Also calculated is the unit vector relating this hit and the central location in the target. Additionally, the perpendicular and parallel momenta can be calculated:

$$p_{h,\parallel} = \vec{p}_h \cdot \hat{q} \tag{5.12}$$

$$p_{h,\perp} = \vec{p}_h \times \hat{q} \ . \tag{5.13}$$

An additional quantity used to select quasi-elastic events which is dependent on hadron identification is the missing mass. This is defined as

$$M_{miss}^2 = (\mathbf{P}_i + \mathbf{q} - \mathbf{p}_h)^2 = (E_{He} + E_q - E_p)^2 - (\vec{q} - \vec{p}_h)^2 \ , \tag{5.14}$$

where $\mathbf{P}_i$ is the initial ^{3}He momentum four-vector, $\mathbf{q}$ is the transferred momentum four-vector and $\mathbf{p}_h$ is the nucleon four-vector.

The selection of quasi-elastic neutral events using time, invariant mass, and $q_\perp$ is demonstrated in Figures 5.15(a) and 5.16(a). The inelastic contribution becomes larger at higher Q^2 and so more aggressive cuts in invariant mass must be used.

5.4 Identification of the hadron charge

While a particle can be determined to be a recoil hadron candidate by hit location and time-of-flight, it is not easy to differentiate between protons and neutrons using only this information from within the neutron counters. For the purpose

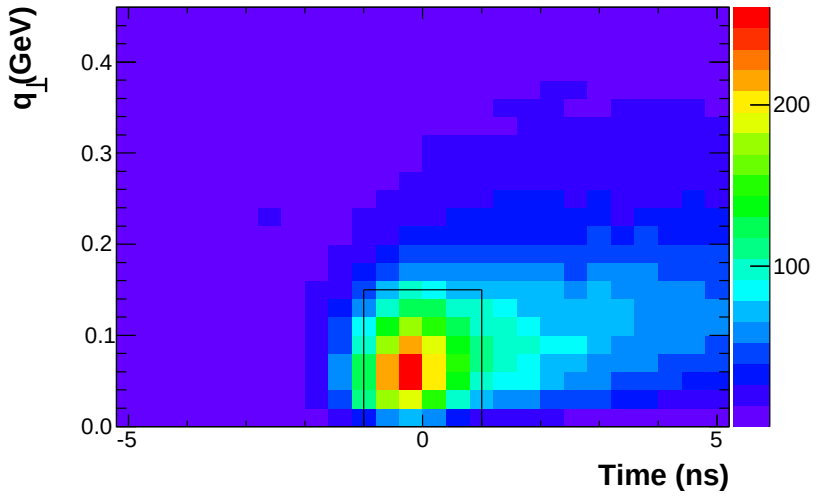

(a) $Q^2 = 2.5$ GeV^2 time versus $q_\perp$

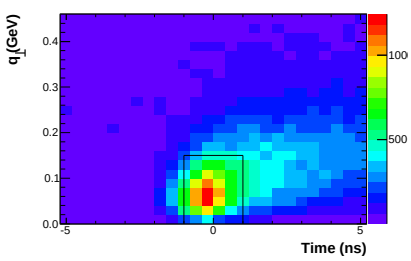

(b) $Q^2 = 3.5$ GeV^2 time versus $q_\perp$

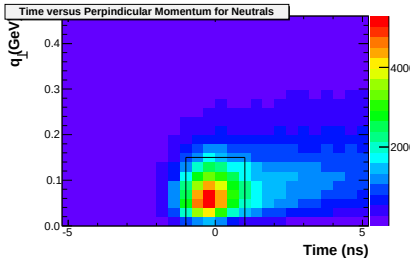

(c) $Q^2 = 1.7$ GeV^2 time versus $q_\perp$

Figure 5.15: Shown in these figures is the time versus $q_\perp$ for various kinematics. Also shown is the box showing which cuts were used for identifying quasi-elastic clusters within the neutron arm. As is shown, the ability to select quasi-elastic clusters is much better for the lower kinematics.

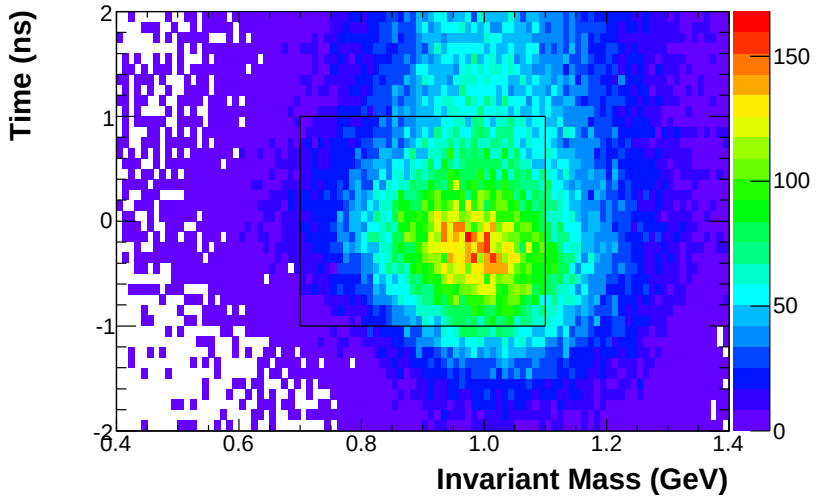

(a) $Q^2 = 2.5$ GeV^2 time versus invariant mass

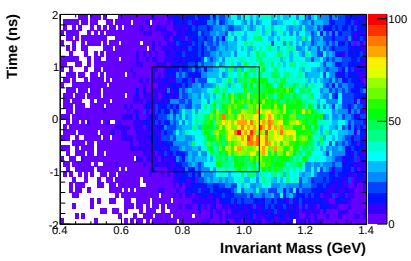

(b) $Q^2 = 3.5$ GeV^2 time versus invariant mass

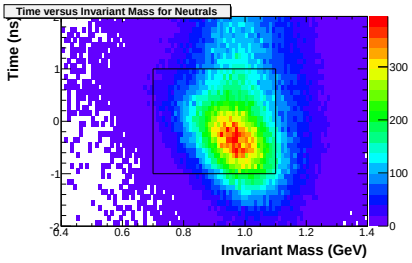

(c) $Q^2 = 1.7$ GeV^2 time versus invariant mass

Figure 5.16: Shown in these figures is the time versus invariant mass for various kinematics. Also shown is the box showing which cuts were used for identifying quasi-elastic clusters within the neutron arm. As is shown, the ability to select quasi-elastic clusters is much better for the lower kinematics.

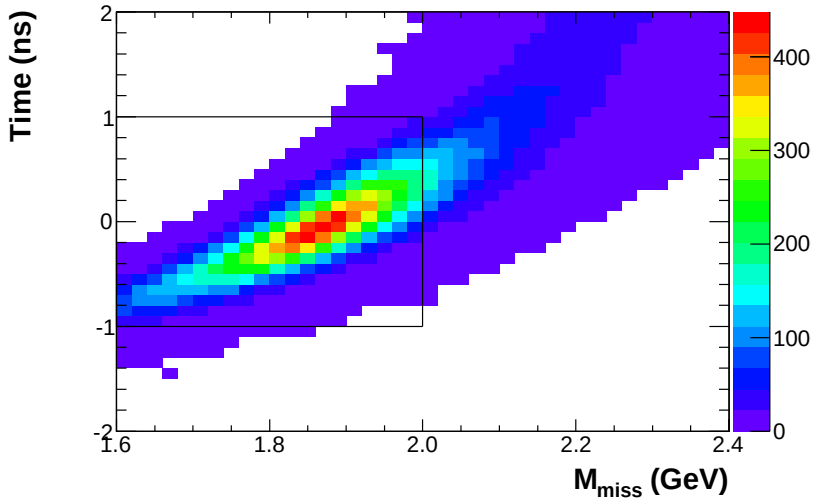

(a) $Q^2 = 2.5$ GeV^2 invariant mass versus missing mass

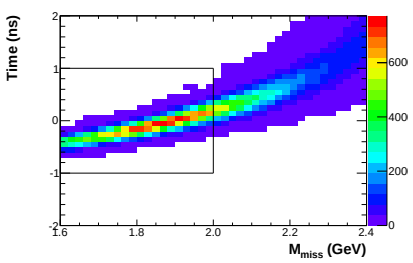

(b) $Q^2 = 3.5$ GeV^2 invariant mass versus missing mass

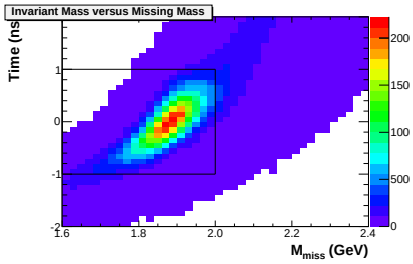

(c) $Q^2 = 1.7$ GeV^2 invariant mass versus missing mass

Figure 5.17: Shown in these figures is the time versus missing mass for various kinematics. Also shown is the box showing which cuts were used for identifying quasi-elastic clusters within the neutron arm. As is shown, the ability to select quasi-elastic clusters is much better for the lower kinematics.

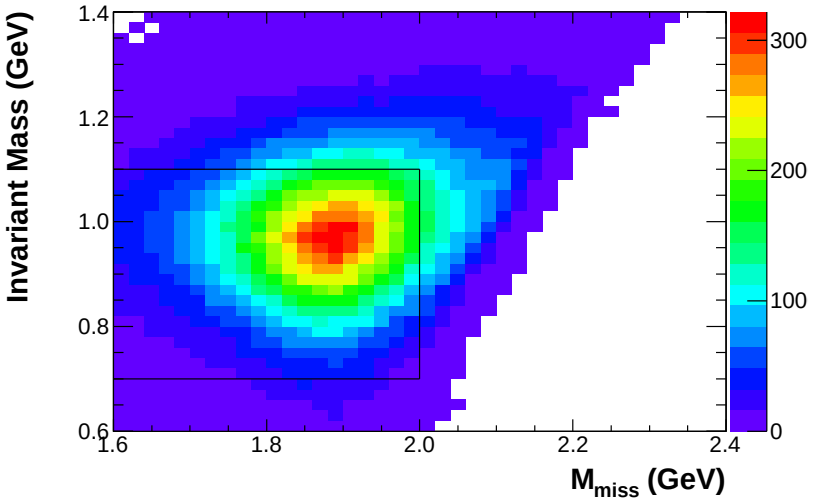

(a) $Q^2 = 2.5$ GeV^2 invariant mass versus missing mass

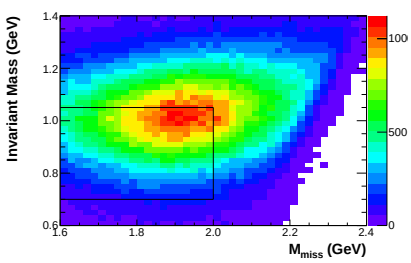

(b) $Q^2 = 3.5$ GeV^2 invariant mass versus missing mass

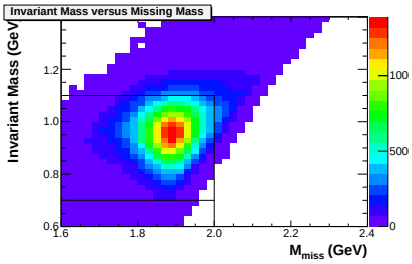

(c) $Q^2 = 1.7$ GeV^2 invariant mass versus missing mass

Figure 5.18: Shown in these figures is the invariant mass versus missing mass for various kinematics. Also shown is the box showing which cuts were used for identifying quasi-elastic clusters within the neutron arm. As is shown, the ability to select quasi-elastic clusters is much better for the lower kinematics.

of charge identification, two layers of veto counters were positioned in front of the neutron counters but behind some of the lead shielding (see section 4.6.1).

The charge of these hadrons was determined by an analysis of hits in the veto in a neighborhood around the hadron hit position in the neutron counters. The veto detectors were segmented vertically similarly to the neutron detectors. Due to scattering in the shielding and detectors, the relevant veto hit position could be greater than a few centimeters away from the identified hadron hit location. The factors used to select relevant veto detectors are listed in Table 5.4.

Determination of whether the hadron is charged or not was accomplished using the time between the neutron bar hit and the veto hit and the segmentation of the detectors. This segmentation defined the x and y position of each veto hit. The individual veto detectors had high rates (1 MHz) and high dead-time (up to 110 ns). This indicates that there exists a large number of possible hits where an earlier accidental hit masked the hit from the quasi-elastic event candidate. For coincident events, the hit in the veto bars varied in veto amplitude in addition to time, the veto amplitude was used in addition to time when selecting veto hits to associate to quasi-elastic events.

While it would be nice to have a detector with uniform neutron detection efficiency, this was not the case for Big Hand. The GLA detectors did not have the resolution to identify quasi-elastic neutrons as the rest of the neutron arm could, and the horizontal edges were not adequently covered by the veto detectors. Two additional cuts, on the neutron arm's x and y fidicual regions were used to select the region of the detector that had a high neutron detection efficiency. This selection is

name	$Q^2 = 2.5$ GeV^2	$Q^2 = 3.5$ GeV^2	$Q^2 = 1.7$ GeV^2
Amplitude	$A_V < 200$	$A_V < 200$	$A_V < 200$
Spatial (m)	$\|X_V - X_C\| < 0.3$	$\|X_V - X_C\| < 0.3$	$\|X_V - X_C\| < 0.3$
Time (ns)	$\|T_V - T_C\| < 10$	$\|T_V - T_C\| < 10$	$\|T_V - T_C\| < 10$
Y1 Cut (m)	$Y_C < 0.076 \& Y_V < 0$	$Y_C < 0.076 \& Y_V < 0$	$Y_C < 0.076 \& Y_V < 0$
Y2 Cut (m)	$Y_C > -0.774 \& Y_V > 0$	$Y_C > -0.774 \& Y_V > 0$	$Y_C > -0.774 \& Y_V > 0$

Table 5.2: A table of selection criteria used to determine which veto hits to consider when doing charge identification. The spatial cuts of Y1, Y2, and X determine which bars are to be included, events were only differentiated by time and amplitude within a veto detector which was within range of the hadron hit. The subscript V signifies veto, while C signifies the cluster in the neutron arm.

shown in Figures 5.19 and 5.20.

The area of the veto used to determine the charge of the hadron is determined by looking at the coincidence between the hadron hit and the veto hit, see Appendix A.4 for more details.

5.5 Dilution of the neutron sample by protons

Between the target and the veto detectors, there were several centimeters of lead and other material [73]. Hadrons that leave the target could be observed as if they were in the other isospin state, through hadronic interactions. This would create a dilution in the neutral candidate sample due to quasi-elastic events still being detected as hadrons, but with the wrong charge. This is especially important in the case of protons observed as neutrons, which creates a significant dilution (see Table 5.5) in the neutron sample. This conversion can be understood, and accounted for, using the ratios of observed protons and neutrons for different targets. The three targets used were hydrogen, which is a single proton, ^{3}He, which is the target of

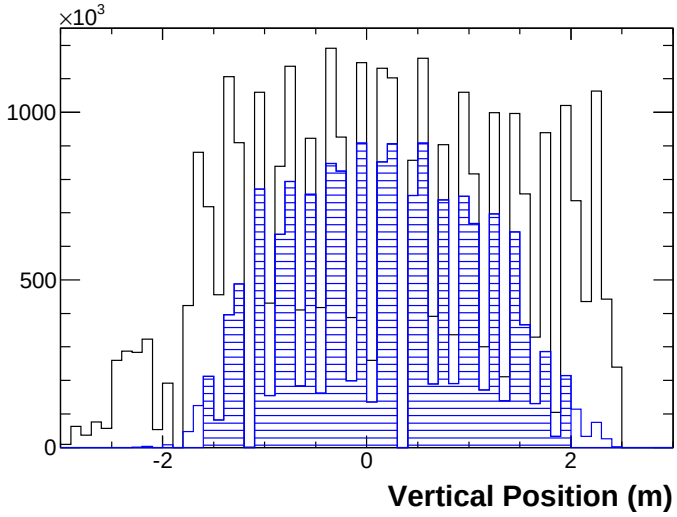

Figure 5.19: Vertical position (m) within the Big Hand detector. This is for before cuts (black), after event selection cuts (blue), with the selected region of x shaded. In the vertical direction the neutron arm was segmented, giving the segmented structure observed. GLA bars are removed, as seen in the most negative region. See Table 5.5 for cuts.This distribution is for $Q^2 = 3.5$ GeV^2.

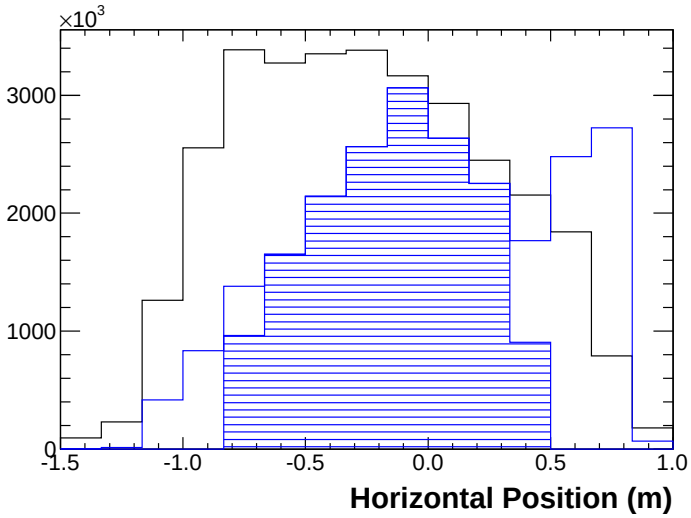

Figure 5.20: Horizontal position (m) within the Big Hand detector. This is for before cuts (black), after event selection cuts (blue), with the selected region of y shaded. In the horizontal direction the neutron arm was not entirely covered by the veto planes, giving the peaks on the two edges. See Table 5.5 for cuts.This distribution is for $Q^2 = 3.5$ GeV^2.

interest, and nitrogen, which has equal numbers of protons and neutrons. These ratios are referred to as R_{tgt},

$$R_{tgt} = \frac{f_n}{f_p} \ . \tag{5.15}$$

Here the subscript tgt stands for target, and is replaced by N for nitrogen, H for hydrogen, and He for ^{3}He. The fraction $f_{p(n)}$ is that of protons(neutrons) to the total number of hadrons.

The purity factor, D_n, is the ratio of observed neutrons to the neutrons knocked out of the target at the interaction point with the electron beam. Similarly, D_p is the ratio of observed protons to those starting from the target. For the observed R_{tgt}, the $f_{p(n)}$ are observed fractions. However, as mentioned, it is possible that interactions between the target and detector can cause a conversion in the observed iso-spin state. To account for this, the ratio can be expressed in terms of mixing coefficients. These provide the numbers of observed $N^{p(n)}$ resulting from an initial target population $N_{p(n)}$. Expressed in this manner

$$R_{tgt} = \frac{N_n^n + N_p^n}{N_p^p + N_n^p} = \frac{\sigma_n \nu_n^n + \frac{Z_{tgt}}{N_{tgt}} \sigma_p \nu_p^n}{\sigma_n \nu_n^p + \frac{Z_{tgt}}{N_{tgt}} \sigma_p \nu_p^p} \ . \tag{5.16}$$

As an example, N_p^n is the number of observed neutrons from initial protons. The above can be presented more compactly as:

$$R_{tgt} = \frac{\frac{\sigma_n}{\sigma_p}\frac{\nu_n^n}{\nu_p^p} + \frac{Z_{tgt}}{N_{tgt}}\frac{\nu_p^n}{\nu_p^p}}{\frac{\sigma_n}{\sigma_p}\frac{\nu_n^p}{\nu_p^p} + \frac{Z_{tgt}}{N_{tgt}}} \ . \tag{5.17}$$

Here $\sigma_{p(n)}$ are the single nucleon cross sections, ν are the mixing coefficients, and $\frac{Z_{tgt}}{N_{tgt}}$ is the ratio of protons to neutrons (unique for each target, and may be dependent on perpendicular and parallel missing momentum) within the target. Obviously

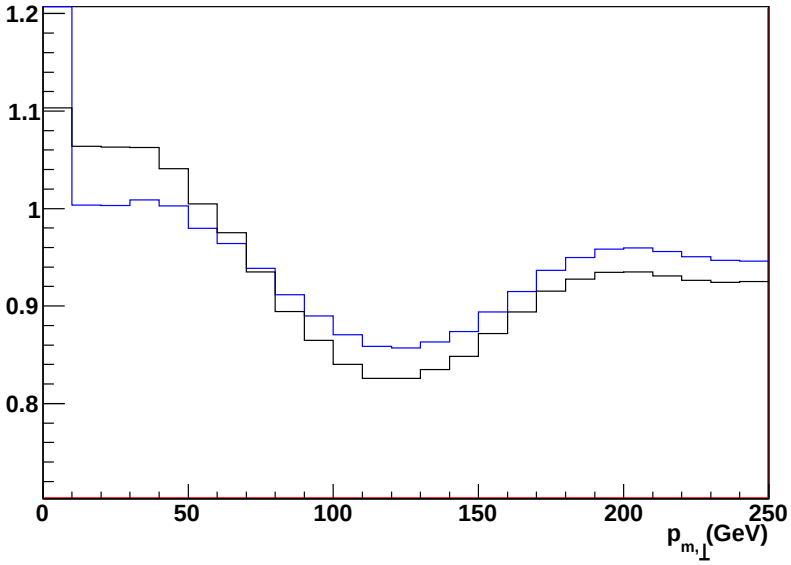

Figure 5.21: Presented is the ratio of protons to neutrons within the target for nitrogen. Shown are two models, one a simple extension to the plane wave impulse approximation (in blue), and the other is a model by Udias (in black) [96]. Shown is the ratio for various cuts of $p_\perp$. A cut of 150 MeV was used in this experiment. This is for $Q^2 = 3.5$ GeV^2.

$N_{tgt} = 0$ for hydrogen, $\frac{Z_N}{N_N} \approx 1$ for nitrogen, and $\frac{Z_{He3}}{N_{He3}} \approx 2$ for the ^{3}He. In particular models [96][90], the ratio was investigated for the applied cuts and kinematics (see Figure 5.21 and 5.22). This provided values for these two coefficients (see Table 5.5). In terms of these mixing coefficients, the purity factor is then

$$D_n = \frac{N_n^n}{N_n^n + N_p^n} = \frac{\frac{\sigma_n}{\sigma_p}\frac{\nu_n^n}{\nu_p^p}}{\frac{Z_{tgt}}{N_{tgt}}\frac{\nu_p^n}{\nu_p^p} + \frac{\sigma_n}{\sigma_p}\frac{\nu_n^n}{\nu_p^p}} \ . \tag{5.18}$$

Using this information, it is possible to solve for the mixing ratios from the ratios of hydrogen (H_2), ^{3}He, and nitrogen (N_2)

$$\frac{\nu_p^n}{\nu_p^p} = R_H \ , \tag{5.19}$$

$$\frac{\nu_n^p}{\nu_p^p} = \frac{\sigma_p}{\sigma_n}\left[\frac{R_{He}\frac{Z_{He3}}{N_{He3}} - \frac{Z_N}{N_N}R_N + \left(\frac{Z_N}{N_N} - \frac{Z_{He3}}{N_{He3}}\right)R_H}{R_N - R_{He}}\right] \ , \tag{5.20}$$

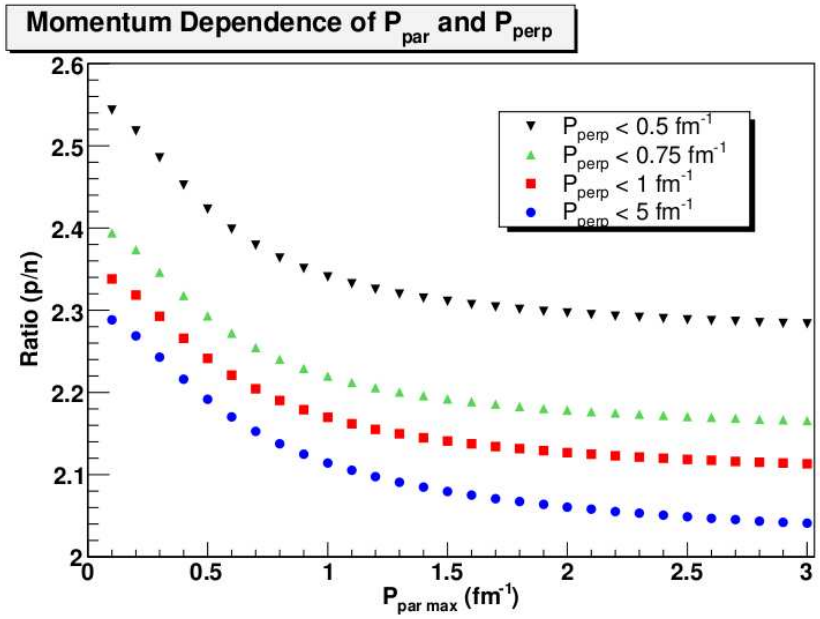

Figure 5.22: Presented is the ratio of protons to neutrons within the target for ^{3}He. Shown are from cuts on $p_\perp$. The applied cut on $p_\perp$ was 0.15 GeV with $P_\parallel$ cuts of 400, 250, and 200 MeV for kinematics of $Q^2 = 3.5$, 2.5, and 1.7 GeV^2. Shown is the ratio for various cuts of inverse distance. This study was done by Aidan Kelleher.

$$\frac{\nu_n^n}{\nu_p^p} = \frac{\sigma_p}{\sigma_n}\left[R_N\left(\frac{Z_{He3}}{N_{He3}} - \frac{Z_N}{N_N}\right)\frac{R_{He} - R_H}{R_N - R_{He}} - \frac{Z_N}{N_N}R_H\right] . \tag{5.21}$$

Therefore the dilution due to the proton to neutron conversion in the sample,

$$D_n = \frac{R_{He}[(\frac{Z_{He3}}{N_{He3}} - \frac{Z_N}{N_N})R_N + \frac{Z_N}{N_N}R_H] - \frac{Z_{He3}}{N_{He3}}R_N R_H}{R_{He}\left(\frac{Z_{He3}}{N_{He3}} - \frac{Z_N}{N_N}\right)(R_N - R_H)} . \tag{5.22}$$

This accounts for mixing due to conversions in the air and other material between the target and the veto detectors. However, there are additional considerations due to the veto detectors before the final dilution factor, due to protons observed as neutrons, can be determined.

As mentioned in section 5.4, the veto detector efficiency was related to large dead-time in the veto detector TDCs and high rate within the veto detectors. The dead-time could be as high as 110 ns for some paddles, while the rate in the indi-

vidual veto detectors was on the order of 1 MHz. Additionally, the hydrogen and nitrogen data were acquired at different rates from the ^{3}He data. Because of this, it is desirable to account for the rate dependence in the charge identification. This is complicated for a couple of different reasons. First, the veto was segmented into left and right and into two planes, which made the veto difficult to model. Also, because of the high activity in the veto, every event had multiple random hits within the veto planes.

The observed protons and neutrons detected in the veto can be represented in the following equations, where the $f_{p(n)}$ stands for the fraction of protons(neutrons) incident on the veto detectors over the total number of hadrons incident on the veto detectors; which is equivalent to the fraction when there is no deadtime. In these equations r represents the rate in the detectors.

$$N_n^p(r) + N_p^p(r) = f_p T(r) + f_n T(r) P_{busy}^{veto}(r) \tag{5.23}$$

$$N_n^n(r) + N_p^n(r) = f_n T(r)(1 - P_{busy}^{veto}(r)) \tag{5.24}$$

A charged hit is determined by a hit in the proper range of either veto plane (see Table 5.4). So the rate dependent number of observed neutrons is the rate dependent total number of hadrons, $T(r)$, incident on the neutron detector multiplied by the fraction, f_n, of the number of neutrons to hadrons multiplied by the probability that there was no accidental background hit in the veto detector to make it appear charged $(1 - P_{busy}^{veto})$. The rate dependent number of observed protons is the total number of hadrons multiplied by the fraction of protons over hadrons, f_p, plus

the fraction of neutrons misidentified by the accidental background.

These probabilities can be determined by modeling them using the Poisson distribution, and then adding up all the probabilities for each hadron event. This gives real numbers for everything but the fractions incident on the veto detectors. The observed ratios, at a given frequency, are

$$R_{tgt}(r) = \frac{N_n^n(r) + N_p^n(r)}{N_n^p(r) + N_p^p(r)} \ . \tag{5.25}$$

Using this formula twice, once for the observed rate r and once for the desired rate d, gives a formula to relate every observed ratio $R_{tgt}(r)$ to a desired ratio $R_{tgt}(d)$:

$$R_{tgt}(r) = \frac{R_{tgt}(d)T(d)[F^r(\beta)]}{R_{tgt}(d)T(d)[T(r) - F^r(\beta)] + [F^d(\beta) - R_{tgt}(d)(T(d) - F^d(\beta))]T(r)} \ . \tag{5.26}$$

The fitting parameter β accounts for correlations in hits in different veto bars in a given event. The function F depends on β and ξ, where ξ is the total rate dependent probability for veto detectors to be busy in an event:

$$F^r(\beta) = \sum_0^{T(r)} P_{busy}(\beta, r) \ . \tag{5.27}$$

here ξ is a useful quantity to define for the calculation and fit of

$$F^r(1) = \xi(r) = \sum_0^{T(r)} P_{busy}(\beta = 1, r) \ , \tag{5.28}$$

which is just $F^r(\beta)$ assuming no correlation between veto hits. The probability of an accidental hit, $P_{busy}(\beta)$ with r being the rate and τ being the dead-time (or busy time) of the bar, in a given event is

$$P_{busy}(\beta, r) = (e^{-\sum r\tau})^\beta \ . \tag{5.29}$$

The functional form of $F^r(\beta)$ can be approximated by assuming that the rate r multiplied by the deadtime τ_d is approximately the same for all bars, so the quantity $A = e^{-\sum r\tau_d}$ is the same for each bar. This is a good assumption, since the rate multiplied by dead-time is the same order of magnitude for all veto bars. From this,

$$F^r(1) = \xi(r) \approx T(r)A(r) \ . \tag{5.30}$$

Therefore a good approximation for $F(\xi, \beta)$ is

$$F^r(\beta) \approx T(r) \left(\frac{\xi(r)}{T(r)} \right)^{\beta} \ . \tag{5.31}$$

This allows the ratio at a specific rate of the different targets to be calculated using the fractions of uncharged and charged particles incident on the veto. Using these ratios in equation 5.22 gives the rate independent dilution correction for proton to neutron conversion:

$Q^2 =$	Ratio for ^{3}He	Ratio for Hydrogen	Ratio for Nitrogen	Purity Factor
2.5 GeV^2	0.105 ± 0.001	0.020 ± 0.002	0.195 ± 0.010	0.806 ± 0.028
3.5 GeV^2	0.077 ± 0.001	0.015 ± 0.002	0.106 ± 0.024	0.885 ± 0.053
1.7 GeV^2	0.107 ± 0.001	0.035 ± 0.001	0.191 ± 0.008	0.697 ± 0.019

Table 5.3: A table of the ratios for different criteria. Over the course of a kinematic setting, runs varied in rate. This had a small effect on the purity factor, the results presented in this table is for a normal run.

$Q^2 =$	Helium Ratio	Nitrogen Ratio
2.5 GeV^2	2.15	1.1
3.5 GeV^2	2.31	1.07
1.7 GeV^2	2.15	0.9

Table 5.4: The effective ratio of $\frac{Z}{N}$ for the target and cuts. The ratio for ^{3}He is from simulation.

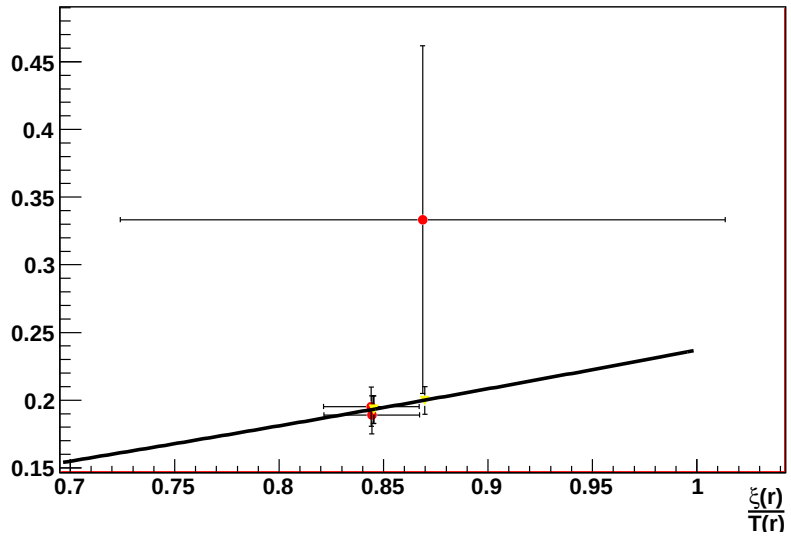

(a) uncharged to charged ratio for $Q^2 = 2.5$ GeV^2

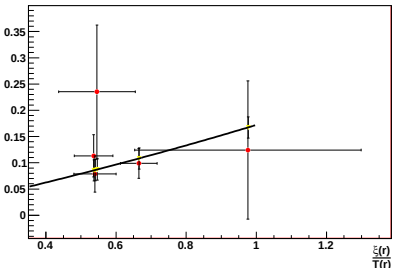

(b) uncharged to charged ratio for $Q^2 = 3.5$ GeV^2

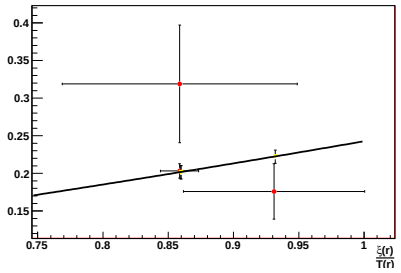

(c) uncharged to charged ratio for $Q^2 = 1.7$ GeV^2

Figure 5.23: Shown in these figures is the measured uncharged to charged ratio, the uncharged to charged ratio within the model, and the fit line of the model in nitrogen. These are plotted against the natural dependence $\frac{\xi}{T}$. In green are the points of the model.

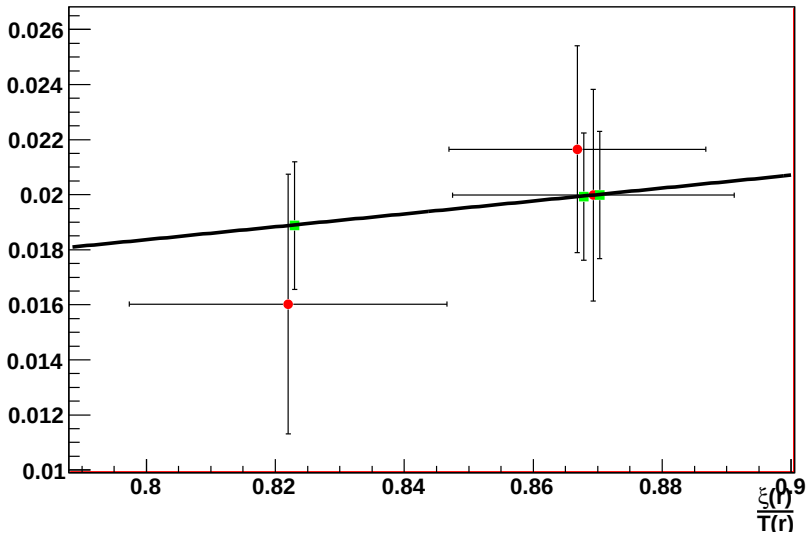

(a) uncharged to charged ratio for $Q^2 = 2.5$ GeV^2

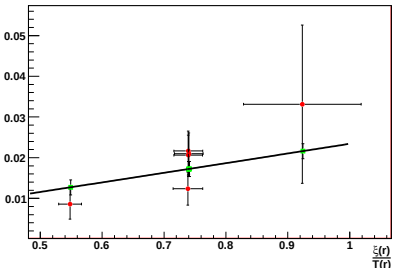

(b) uncharged to charged ratio for $Q^2 = 3.5$ GeV^2

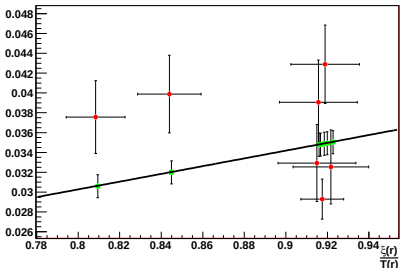

(c) uncharged to charged ratio for $Q^2 = 1.7$ GeV^2

Figure 5.24: Shown in these figures is the measured uncharged to charged ratio, the uncharged to charged ratio within the model, and the fit line of the model in hydrogen. These are plotted against the natural dependence $\frac{\xi}{T}$. In green are the points of the model.

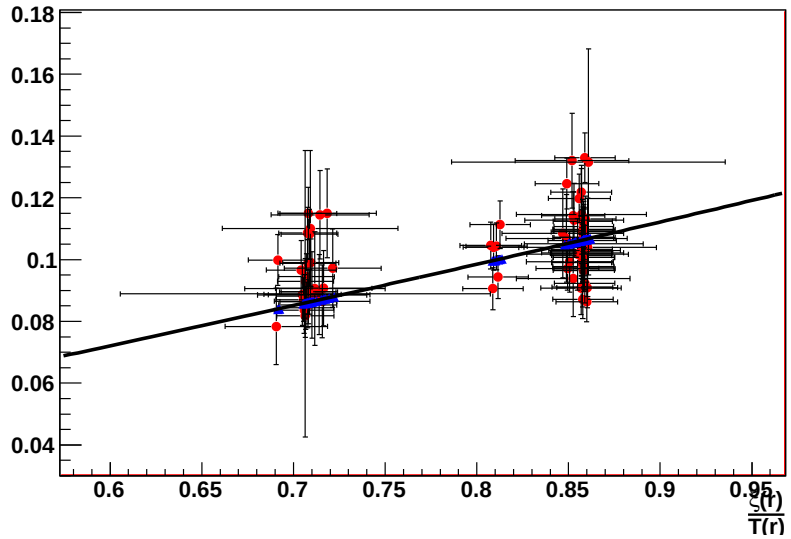

(a) uncharged to charged ratio for $Q^2 = 2.5$ GeV^2

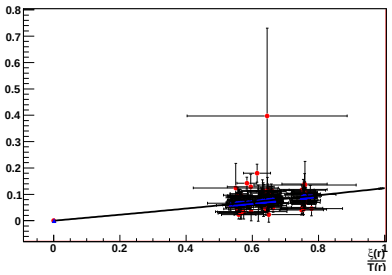

(b) uncharged to charged ratio for $Q^2 = 3.5$ GeV^2

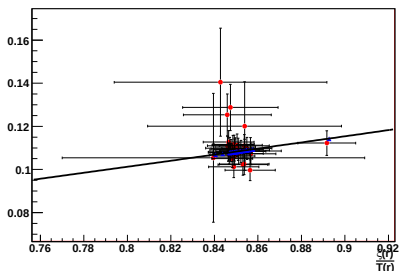

(c) uncharged to charged ratio for $Q^2 = 1.7$ GeV^2

Figure 5.25: Shown in these figures is the measured uncharged to charged ratio, the uncharged to charged ratio within the model, and the fit line of the model in ^{3}He. These are plotted against the natural dependence $\frac{\xi}{T}$. In blue are the points of the model.

$$D_n = \frac{R_{He}(d)[(\frac{Z_{He3}}{N_{He3}} - \frac{Z_N}{N_N})R_N(d) + \frac{Z_N}{N_N}R_H(d)] - \frac{Z_{He3}}{N_{He3}}R_N(d)R_H(d)}{R_{He}(d)\left(\frac{Z_{He3}}{N_{He3}} - \frac{Z_N}{N_N}\right)(R_N(d) - R_H(d))} \ . \qquad (5.32)$$

5.5.1 Single Track Analysis and Background Correction

For approximately 10% of the detected events, the hadron interacted in the lead resulting in multiple events in the neutron apparatus or an accidental background hit that could not be differentiated from the hadron. If there were two or more hits in the region of parameter space used to select quasi-elastic events (hereafter known as the quasi-elastic region), the charge becomes impossible to determine since just one "hit" in the veto detectors associated with the quasi-elastic region will often set all hits in the quasi-elastic region as charged.

By restricting the analysis to only those events which have a single hit identified as quasi-elastic, the problem of charge identity and multiple hits in the quasi-elastic region is solved. Using this single track analysis (SQE), however, causes the determination of the background to become more complicated.

When multi-hit events are eliminated, the spectrum far from the quasi-elastic hit is clean (see Figure 5.29). Using the perpendicular transferred momentum, $q_\perp$, the distance far from the quasi-elastic hit can be parametrized in the same variable which is used to select quasi-elastic events. In this band of $q_\perp$, the ratio of charged to uncharged background is relatively constant (see Figure 5.28). This gives the ratio of charged to uncharged for the background which is unrelated to the quasi-elastic events. The only determination that is made in this region is the charge ratio of the

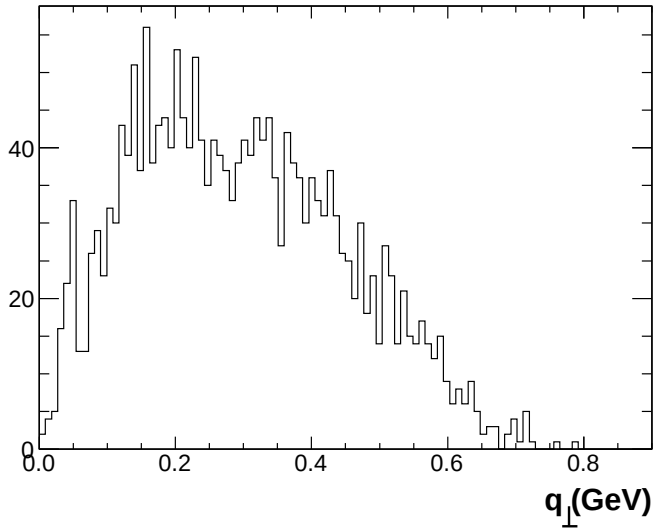

Figure 5.26: Plot $q_\perp$ for a region in time. This is 5 ns removed from the peak region.

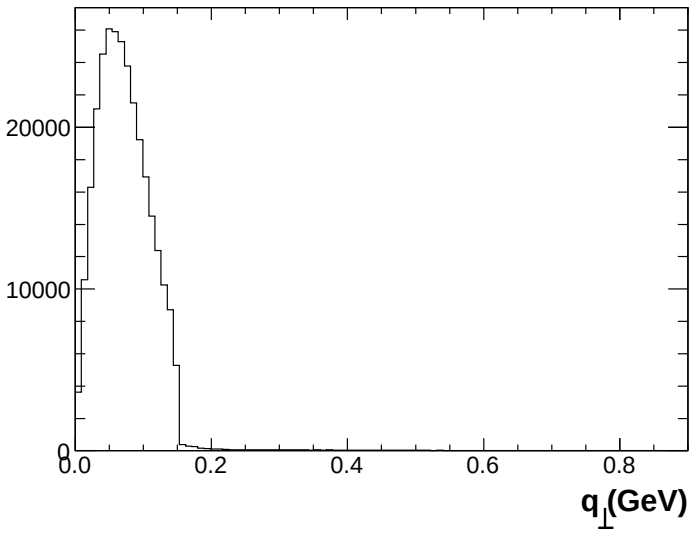

Figure 5.27: Plot $q_\perp$ for a region in time. This is at the quasi-elastic region.

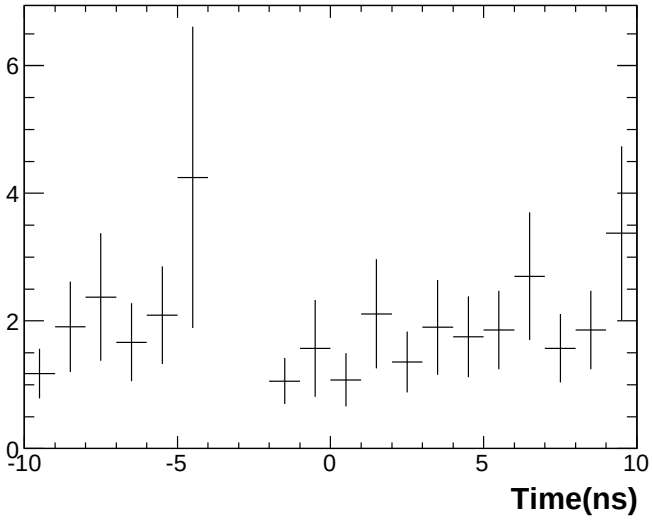

Figure 5.28: Plot of the ratio of uncharged to charged for the region of $q_\perp$ between 0.55 and 0.60 GeV. The region near 3 ns is removed due to the photon peak being there. Add axis information time (ns), update description (changed plot)

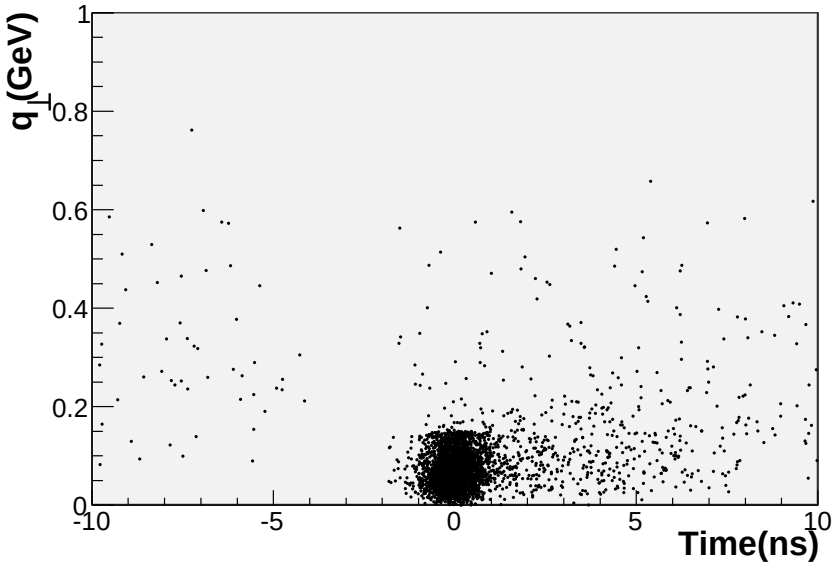

Figure 5.29: Plot of $q_\perp$ versus time-of-flight for events with only a single hit in the $|t| < 7$ and $q_\perp < 0.15$ region. The area in the spectrum of events coming from k photons via π_0 production was removed (between 2 and 4 ns). This is for run 4090.

background. The total background count is determined via a different mechanism.

Since it is required that every hit in the quasi-elastic region is either a single quasi-elastic hit, or a single background hit, the total number of counts (and events) is:

$$N_{SQE}^{A+B} = N_{back}^{A} + N_{QE}^{A} + N_{back}^{B} + N_{QE}^{B} \ , \tag{5.33}$$

where A and B are two regions within the SQE region. The SQE region is chosen so as to include all of the quasi-elastic events within it. It is useful to define region B as being a region where $N_{QE}^{B} = 0$.

This is a lot simpler than that of the full events, which can be expressed as the following:

$$N_{full}^{A+B} = N_{back}^{A} + N_{QE}^{A} + N_{QE}^{A}|_{back} + N_{back}^{A}|_{back} + N_{back}^{B}|_{back} + N_{QE}^{B}|_{back} + N_{QE}^{A}|_{QE} + N_{back}^{A}|_{QE} + N_{back}^{B} + N_{back}^{B}|_{QE} \ ,$$

here $|_{back}$ is the number of hits which also have at least one background hit, $|_{QE}$ is the number of hits with at least one QE hit. Another class of hits are $N_{QE}^{A}|_{QE}$ which are the number of QE hits with at least one other QE hit; these would be from fragmentation caused by interaction between the target and the final hit location in the neutron arm. Here A is the SQE region with the quasi-elastic hits within it and B is a region in the SQE region without any quasi-elastic hits.

If the region is restricted to being outside the QE region, the expression is left as:

$$N_{full}^{B} = N_{back}^{B} + N_{back}^{B}|_{back} + N_{back}^{B}|_{QE} \ . \tag{5.34}$$

Obviously it is just desired to remove the N_{back}^{B} from the QE sample in region A.

Since equation 5.33 is true for SQE analysis, outside of the QE region the expression for the counts is

$$N^B_{SQE} = N^B_{back} \ , \tag{5.35}$$

due to $N^B_{back}|_{back}$ and $N^B_{back}|_{QE}$ events not occuring because only one hit can occur in the SQE region. Once the regions A and B are scaled to be the same size, the number of quasi-elastic events in SQE analysis can be determined

$$N_{QE} = N_{A,SQE} - N_{B,SQE} \ , \tag{5.36}$$

here B is a sub region of the SQE region where the QE events don't reside, and A is the sub region of the SQE region where QE events do reside.

For times earlier than the quasi-elastic window, as described above, the hits are all background, coming from an accidental coincidence between the electron and hadron (see Figure 5.29). This is in the -4 ns to -13 ns window. Using the counts (scaled properly) from this background region provides the background in single quasi-elastic hit analysis. The same area in $q_\perp$ is used to make scaling easier. To determine the neutral accidental background, the earlier determined background ratio term is used:

$$N_{neut,back} = N_{back} f_{back} \ , \tag{5.37}$$

here f is the fraction of neutrals to hadrons in the background.

These background counts, neutral or charged, are used to determine the accidental background dilution and asymmetry used in the determination of the physical asymmetry. The neutral background dilution of a sample (N) can be expressed as

$$D_{back} = 1 - \frac{N_{neut,back}}{N} \ . \tag{5.38}$$

Similarly the background asymmetry can be defined in the standard way

$$A_{back} = \frac{N^{+}_{back} - N^{-}_{back}}{P_{^3He} N} \ . \tag{5.39}$$

5.5.2 Nitrogen Dilution

The ^{3}He inside the target cell is diluted by unpolarized nitrogen, used as a buffer gas to decrease interactions between the polarized ^{3}He and glass cell walls and to aid in the polarization process (Section 4.4.2). This contamination creates a dilution of the ^{3}He asymmetry, and is measured by looking at events which appear to be quasi-elastic in a N_2 target and scaling by the relative densities and total charge on target. This dilution factor is

$$D_{N_2} = 1 - \frac{N_{N_2} - N_{back,N_2}}{N - N_{back}} \frac{Q_{^3He} \rho_{^3He}}{Q_{N_2} \rho_{N_2}} \ . \tag{5.40}$$

The values used to calculate this dilution factor are provided in Table B.1.

5.5.3 RF correction

While the timing of the coincidence event relative to the beam crossing cannot be determined absolutely, it can be determined up to an arbitrary constant. Event by event variations about this constant can be determined from the 499 MHz RF signal, which can be used to improve the hadron time-of-flight measurement between the target and detectors.

The signal from the RF is put into the F1 TDC, which wraps (starts counting again at 0) at $W = 65526$ channels, and has $t_{res} = 0.1183$ ns resolution. The RF signal repeats in a $T_{win} = 2$ ns window. In the following formula t_{RF} = RF

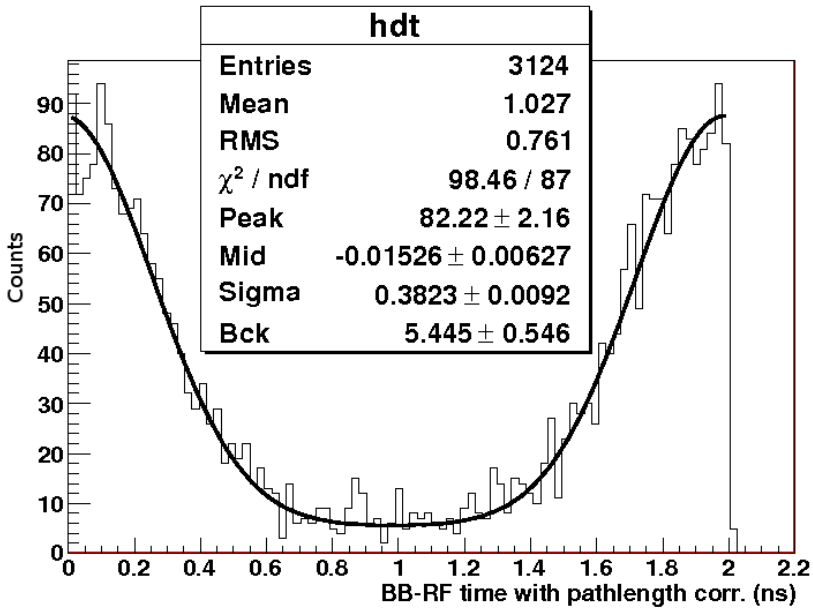

Figure 5.30: Spectrum used to determine the RF correction. This is for run 3888. The peak location is determined from the Mid parameter, which is $t_{rfshift}$.

time, t_{ref} = reference time, t_{L1A} = level 1 accept time, and the aforementioned time-of-flight (equation 5.9).

The RF correction is calculated using the following formula

$$RF_{corr} = \frac{V_{tgt}}{c} + t_{res}\left(t_{RF} - t_{ref} - \left(\left[\frac{t_{RF} - t_{ref}}{0.5W}\right] \textbf{ Fmod } 1\right)W\right) \ , \tag{5.41}$$

$$t_{rf} = \left[(t_e - t_{L1A} - RF_{corr} - t_{rfshift}) \textbf{ Fmod } \left(\frac{1}{0.499}\right) + \frac{2}{0.499}\right] \textbf{ Fmod } \left(\frac{1}{0.499}\right) . \tag{5.42}$$

This t_{rf} is the shift used for correcting the time-of-flight in equation 5.9. The $t_{rfshift}$ is the peak location shown in Figure 5.30. This shift is plotted versus run number in Figure 5.31. This correction is due time of the scattering within the target.

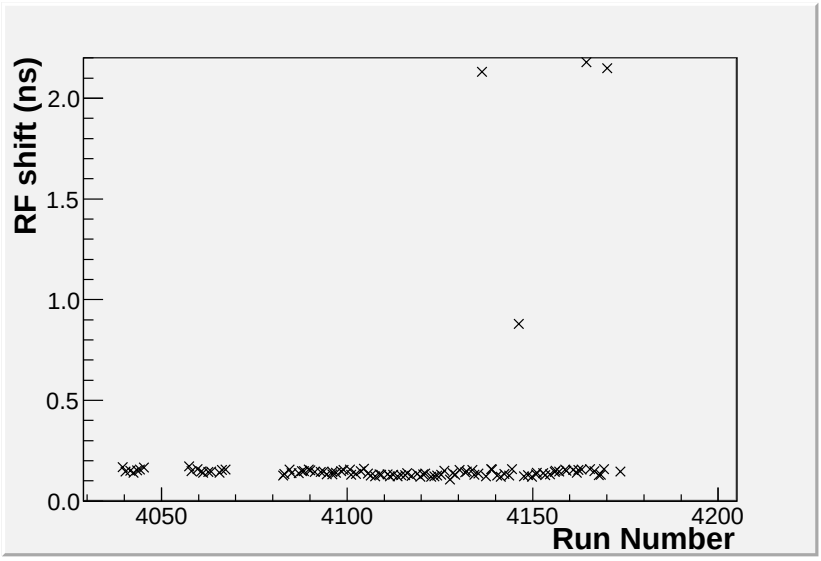

Figure 5.31: RF correction versus run number for $Q^2 = 2.5$ GeV^2. Note that since the plotted function is **Fmod** $\left(\frac{1}{0.499}\right)$ that the values of 2 ns and 0 ns are almost equivalent. Run 4146 with a shift of ≈ 1 ns demonstrates that the shift likely is not adequately determined for "junk" runs.

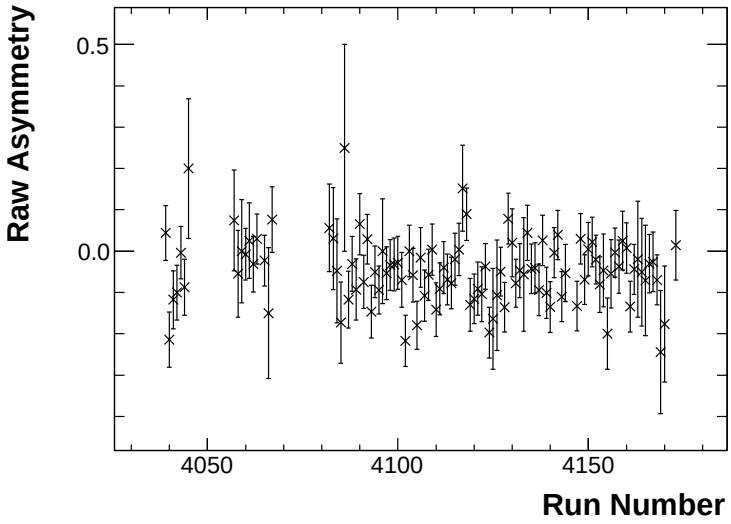

Figure 5.32: Shown is the run number versus raw asymmetry for $Q^2 = 2.5$ GeV^2.

Name	$Q^2 = 2.5$ GeV^2	$Q^2 = 3.5$ GeV^2	$Q^2 = 1.7$ GeV^2
Time (ns)	$\|t\| < 1$	$\|t\| < 1$	$\|t\| < 1$
Invariant Mass (GeV)	$\|W - 0.9\| < 0.2$	$\|W - 0.875\| < 0.175$	$\|W - 0.9\| < 0.2$
Q Perp (GeV)	$q_\perp < 0.15$	$q_\perp < 0.15$	$q_\perp < 0.15$
SQE region B (ns)	$\|t - 8.5\| < 4.5$	$\|t - 8.5\| < 4.5$	$\|t - 8.5\| < 4.5$
Missing Mass (GeV)	$M_{miss} < 2$	$M_{miss} < 2$	$M_{miss} < 2$
Vertical Cut (m)	$\|X - 0.2\| < 1.7$	$\|X - 0.2\| < 1.7$	$\|X - 0.2\| < 1.7$
Horizontal Cut (m)	$\|Y + 0.183\| < 0.6$	$\|Y + 0.183\| < 0.6$	$\|Y + 0.183\| < 0.6$

Table 5.5: Table of quasi-elastic event selection cuts. The Single QE cut is that there is one and only one hit in the associated region of time and $q_\perp < 0.15$. This is in addition to the region of time and $q_\perp$ which are selected as quasi-elastic event candidates. The vertical cut and horizontal cut are neutron arm fidicual cuts.

5.6 Asymmetry calculation

After the selection of quasi-elastic neutron events (Table 5.5), the measured asymmetry is corrected to give the physical asymmetry, which gives G_E^n as presented in section 3.3.3. This is the general expression, as mentioned in the previous sections there are corrections which need to be done for nitrogen dilution in the target cell (section 5.5.2), proton to neutron coversion between the target and scintillator bars (section 5.5), accidental background asymmetry and dilution (section 5.5.1), neutron polarization in the nucleus [39], beam polarization (section 4.3), target polarization (section 4.4), and final state interactions (section 5.7.1). The corrected expression is

$$A_{Phys} = \frac{A_{sum} - A_{proton} - A_{back}}{P_{^3He} P_{beam} P_n D_{N_2} D_n D_{FSI} D_{back}} \ . \tag{5.43}$$

Since the proton contamination of the neutron sample (D_n), proton asymmetry (A_{proton}), nitrogen dilution (D_{N_2}) , background asymmetry (A_{back}), and background dilution (D_{back}) all depend on similar quantities, corrections need to be applied as presented in sections 5.7 and 5.5. The nitrogen dilution is corrected for the

background dilution and the proton contamination dilution is corrected for both the nitrogen dilution and the background dilution.

The physical asymmetry, corrected for the discussed dilutions and asymmetries, is presented in Table 5.6. The dilutions can be expressed in terms of those due to polarization (P), those due to theoretical calculations like FSI (D_{fsi}) and neutron polarization (P_n), and experimental corrections not due to polarization (V). Expressed this way

$$P = P_{^3He} P_{beam} \tag{5.44}$$

and

$$V = D_n D_{N_2} D_{back} \ . \tag{5.45}$$

$Q^2 =$	1.7 GeV^2	2.5 GeV^2	3.5 GeV^2
A_{meas}	-0.0569 ± 0.0031	-0.0446 ± 0.0055	-0.0358 ± 0.0081
N	105529	32990	15319
P_{nucl}	0.488 ± 0.02	0.436 ± 0.02	0.477 ± 0.02
P_{beam}	0.835 ± 0.03	0.835 ± 0.03	0.835 ± 0.03
P_n	0.86 ± 0.02	0.86 ± 0.02	0.86 ± 0.02
D_{back}	0.9697 ± 0.0002	0.9790 ± 0.0003	0.9731 ± 0.0005
A_{back}	0.00004 ± 0.0000003	0.0013 ± 0.00002	-0.0013 ± 0.00003
D_n	$0.696 \pm 0.019 \pm 0.035$	$0.806 \pm 0.023 \pm 0.040$	$0.885 \pm 0.053 \pm 0.044$
A_{proton}	-0.0054 ± 0.0007	-0.0031 ± 0.0005	-0.0018 ± 0.0003
D_{N_2}	$0.947 \pm 0.002 \pm (0.005)$	$0.949 \pm 0.004 \pm (0.005)$	$0.978 \pm 0.005 \pm (0.002)$
P	0.408	0.364	0.398
V	0.640	0.749	0.842
A_{phys}	$-0.254 \pm 0.015 \pm 0.027$	$-0.191 \pm 0.024 \pm 0.022$	$-0.126 \pm 0.030 \pm 0.013$

Table 5.6: Determination of the physical asymmetry from the measured experimental asymmetry. A full discussion and analysis of errors is presented in Appendix B. Systematic uncertainties are listed second.

At times during the measurements at $Q^2 = 2.5$ and 3.5 GeV^2, the target cell and beam were changed. This meant that the P_{beam}, $P_{^3He}$, and D_n could

change during the run. To account for this, the target polarization corrected the asymmetry on a run by run basis. Using standard error analysis (and Appendix B), the summation was

$$A_{sum} = \frac{\sum A_i \frac{1}{\sigma_i^2}}{\sum \frac{1}{\sigma_i^2}} \ , \tag{5.46}$$

$$\sigma_{sum} = \frac{1}{\sqrt{\sum \frac{1}{\sigma_i^2}}} \ , \tag{5.47}$$

where the above equation was used for statistical uncertainties and the A_i are the measured asymmetries for each run. After this summation, the physical asymmetry is calculated using

$$A_{Phys} = \frac{A_{sum} - A_{proton} - A_{back}}{P_{beam} P_n D_{N_2} D_n D_{FSI} D_{back}} \ . \tag{5.48}$$

Many runs were taken over the course of a measurement at a given Q^2. The stability of the asymmetry over the course of the run, for a given running condition, was stable as shown in Figure 5.32.

While the other asymmetries and dilutions can be corrected for without using acceptance information, the FSI dilution and proton asymmetry require knowledge of the kinematics to be properly applied.

The framework using knowledge of the kinematics to determine the ratio of the electric and magnetic form factors, and so determine G_E^n, is based on equation 3.15. This provides the relationship between kinematic variables, the asymmetry, and the form factor ratio. The relation between the physical asymmetry and the ratio, λ, can be expressed as:

$$A = \frac{B\lambda + C}{\lambda^2 + D} \ , \tag{5.49}$$

where $\lambda = \frac{G_E}{G_M}$ is the form factor ratio, and B, C, and D are the following kinematic

quantities

$$B = -2\sqrt{\tau(1+\tau)}\tan(\frac{\theta_e}{2})\sin\theta\cos\phi \ , \tag{5.50}$$

$$C = -2\tau\sqrt{1+\tau+(1+\tau)^2\tan^2(\frac{\theta_e}{2})}\tan(\theta_e)\cos\theta \ , \tag{5.51}$$

$$D = -\tau + 2\tau(1+\tau)\tan^2(\frac{\theta_e}{2}) \ . \tag{5.52}$$

and the quantities τ, θ_e, θ, and ϕ were defined in section 4.4.2. These quantities can be averaged from all events, and are used in the determination of the proton asymmetry correction, the determination of Q^2, and the determination of λ from the physical asymmetry.

The dilution corrections are presented explicitly in section 5.5. The asymmetry corrections will be presented explicitly here. To make the best use of the good proton form factor measurements [76], values for the proton form factor ratio were used to determine the A_{proton}. The equations 5.50, 5.51, and 5.52 were used to calculate the proton physical asymmetry

$$A_{phys,proton} = \frac{(B\lambda_{proton} + C)}{\lambda^2_{proton} + D} \ . \tag{5.53}$$

This can then be corrected for the nitrogen dilution of the charged events (D_{ch,N_2}), the proton polarization (P_p), background dilution (D_{back}), and the beam polarization (P_{beam}) to give the proton asymmetry correction

$$A_{proton} = \frac{1 - D_N}{D_{back}D_{N_2}} P_{beam}P_p A_{phys,proton} \ . \tag{5.54}$$

By using the plot of this ratio at different values of the physical asymmetry, the error and value for the ratio can be determined. However, if instead of being

plotted, λ is solved for, an inversion must be used. This can be done using the following method [38]. Using equation 5.50, 5.51 and 5.52, we can express 5.49 as:

$$\frac{\Delta(\theta,\phi)}{\Sigma(\theta,\phi)} = A_{phys} = \frac{B\lambda + C}{D + \lambda^2} = \frac{C}{D} + \frac{B}{D}\lambda - \frac{C}{D^2}\lambda^2 - \frac{B}{D^2}\lambda^3 + \frac{C}{D^3}\lambda^4 + \frac{B}{D^3}\lambda^5 \ . \quad (5.55)$$

$Q^2 =$	1.7 GeV^2	2.5 GeV^2	3.5 GeV^2
A_{phys}	$-0.254 \pm 0.015 \pm 0.027$	$-0.191 \pm 0.024 \pm 0.022$	$-0.125 \pm 0.030 \pm 0.013$
T0	-0.0693	-0.0129	0.0433
T1	0.9877	0.8350	0.7112
T2	0.0863	0.0115	-0.0223
T3	-1.2175	-0.6804	-0.3842
T4	-0.1091	-0.0102	0.0116
T5	1.5253	0.5630	0.2107
λ	$-0.199 \pm 0.018 \pm 0.033$	$-0.222 \pm 0.033 \pm 0.029$	$-0.243 \pm 0.046 \pm 00.020$

Table 5.7: Expansion Coefficients in the determination of λ from the physical asymmetry. Uncertainty in λ calculated as discussed in Appendix B.

These expansion coefficients can be expressed as $T_0 = \frac{C}{D}$, $T_1 = \frac{B}{D}$, $T_2 = \frac{C}{D^2}$, $T_3 = \frac{B}{D^2}$, $T_4 = \frac{C}{D^3}$, and $T_5 = \frac{B}{D^3}$. In this expansion, these provide all the acceptance and kinematic information for a given event. This allows the expression of A_{phys} as a polynomial in λ with coefficients being equal to the averaged T_n values. For specific averaged values, λ can be solved for giving the ratio of the electric and magnetic form factors for that specific kinematic. To first order, this λ is

$$\lambda_0 = \frac{A_{phys} - \langle T_0 \rangle}{\langle T_1 \rangle} \ . \quad (5.56)$$

Using these terms, the value for Q^2 was also corrected for finite acceptance:

$$Q^2 = \frac{\sum T_{1,i} Q_i^2}{T_1} \ . \quad (5.57)$$

The value for λ,

$$\lambda = \frac{G_E^n}{G_M^n} \ , \quad (5.58)$$

provides the electric form factor of the neutron as a ratio to the magnetic form factor. Using this corrected value for Q^2 and using the value of the magnetic form factor as determined from a common parameterization [59], the value of the electric form factor was determined. This calculation is presented in Table 5.8. The calculation of the uncertainty is presented in appendix B.

The results and discussion of them in relation to previous measurements and selected models are presented in Chapter 6.

$Q^2 =$	1.7 GeV^2	2.5 GeV^2	3.5 GeV^2
λ	$-0.199 \pm 0.018 \pm 0.033$	$-0.222 \pm 0.033 \pm 0.029$	$-0.243 \pm 0.046 \pm 0.020$
Q^2	1.73 (GeV^2)	2.49 (GeV^2)	3.48 (GeV^2)
G_M^n	-0.164 ± 0.003	-0.0954 ± 0.0019	-0.0556 ± 0.0011
G_E^n	$0.033 \pm 0.003 \pm 0.005$	$0.021 \pm 0.003 \pm 0.003$	$0.014 \pm 0.003 \pm 0.001$

Table 5.8: Displayed is the calculated values for λ and Q^2, and the value of G_M^n as arrived at from a parameterization [59]. From this the value of G_E^n can be determined. Determination of uncertainty is discussed in Appendix B.

5.7 Corrections

5.7.1 FSI Corrections

As mentioned previously, in section 3.5, to first order there are four types of interactions at lower momentum transfer. Shown in Figure 5.33, these are the impulse approximation (IA), isobar current (IC), meson exchange currents (MEC), and final state interactions (FSI). As has already been argued, meson exchange currents and isobar currents are small for $Q^2 > 1$ GeV^2. This is due to their scaling as $\frac{1}{Q^4}$. This leaves just final state interactions as a necessary correction

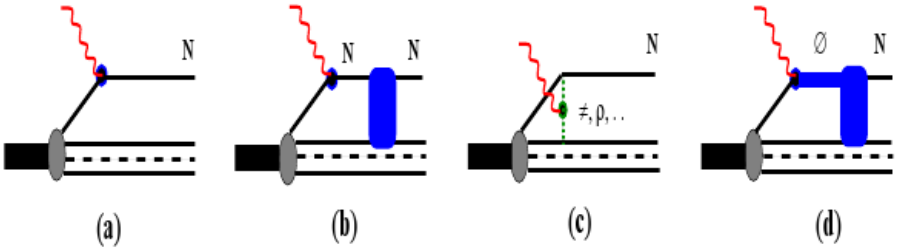

Figure 5.33: The four dominant lowest order diagrams in single nucleon scattering. Shown is (a) impulse approximation, (b) meson exchange currents, (c) isobar contributions, and (d) FSI [88].

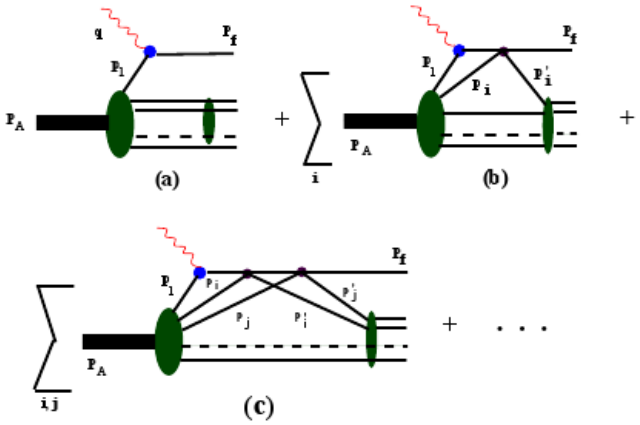

Figure 5.34: In nuclei with more than a single nucleon, the plane wave impulse approximation can be used to give the description of the interaction. Shown are the leading order diagrams for ^{3}He which is the PWIA diagram, single re-scattering diagram, and double re-scattering diagram [88].

to the physical asymmetry, which was arrived at from the impulse approximation. The final state interactions are based on nucleon-nucleon cross sections, which are flat above 2 GeV [88]. To lowest order, these FSI will be either single or double re-scattering between the spectator hadrons and the detected hadron (see Figure 5.34).

There are two similar approximations made in computing the effects of these FSI. These are the Glauber approximation and the generalized eikonal approximation (GEA). In the Glauber approximation the incident particle's energy is assumed to be much larger than that of the potential, and is large enough so that the wavelength of the incident particle is smaller than the potential width. This means that the Glauber approximation truncates the terms after double scattering due to the spectator hadrons being considered at rest. In the generalized eikonal approximation, the high momentum particle can not interact with a slow hadron a second time after interacting with another bound hadron.

The eikonal approximation reduces to the Glauber approximation in the limit of zero longitudinal momentum transfer, $\Delta = \frac{q_0}{|q|}(E_s - m) \rightarrow 0$. Here q is transfered momentum, the subscript s refers to spectator, and m is the recoiling nucleon mass. This is due to the Glauber approximation assuming that all nucleons are stationary while the GEA allows for nonzero initial momentum of the recoiling nucleon [88].

5.7.2 Inelastic Contribution

The inelastic contribution to the quasi-elastic asymmetry is the final correction to be developed. This contribution can be limited by removing some of the quasi-elastic region which is closest to the delta resonance (at $W = 1.2$ GeV). The observed width of the quasi-elastic peak in the invariant mass spectrum is increased due to the motion of the nucleon within ^{3}He and due to the resolution of the detectors. The inelastic resonance width is similarly increased. This inelastic contribution increases the tail in the quasi-elastic sample towards greater invariant mass as demonstrated in Figures 5.10(a), 5.9(a), 5.8(a), and 5.16(a) for $Q^2 = 2.5$ GeV^2.

The inelastic contribution will be deconvoluted using a Monte Carlo (MC). This Monte Carlo is described in section A.1 and simulates the quasi-elastic and inelastic spectrum near the quasi-elastic spectrum. Using the inelastic counts under the quasi-elastic peak and the inelastic asymmetry from the simulation, the measured quasi-elastic asymmetry can have the contribution from inelastic events removed [82]. This Monte Carlo is being analyzed by another collaborator. When this is completed, the invariant mass cuts in Table 5.5 can be widened to 1.2 GeV.

The contribution of the inelastic sample can be empirically estimated by considering the asymmetry as a function of invariant mass. This shows the asymmetry both in the inelastic region, the quasi-elastic region, and the region with a significant inelastic contribution to the quasi-elastic events. This is demonstrated in Figure 5.35.

Preliminary values for the inelastic asymmetry contribution and dilution are

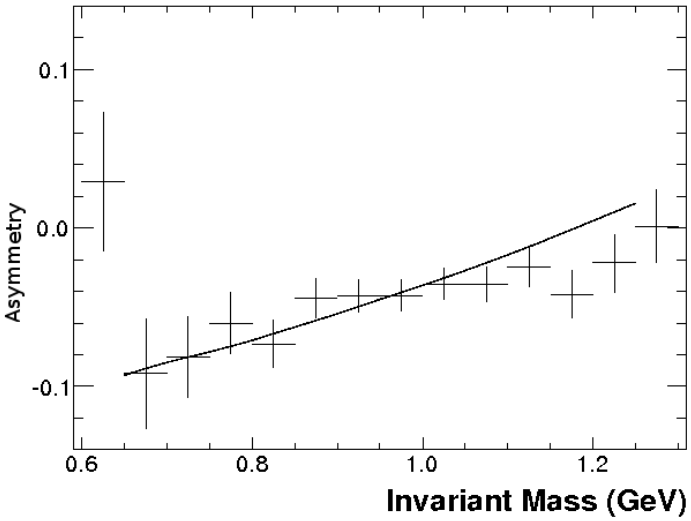

Figure 5.35: The asymmetry as a function of invariant mass. The plotted curve is the expected change due to the acceptance of the detectors. This shows that the invariant mass doesn't vary much over the region selected (see Table 5.5).

presented in Table 5.9. The presented values are calculated in the framework of a separate analysis with a different set of cuts and charge selection [81]. These are not included in the analysis presented here, but give an estimate of the contribution in the quasi-elastic event sample. The correction to the physical asymmetry due to the inelastic asymmetry and dilution is

$$A_{corr} = \frac{A_{phys} - A_{inelas}}{D_{inelas}} \ . \tag{5.59}$$

As seen, with the cuts presented in Table 5.5 the contribution of the inelastic events is small. Effects due to two photon exchange are also expected to be small, with less than a 5% suppression [17]. The likeliest source of a change in the results presented in Table 5.8 is due to increased theoretical understanding of ^{3}He nucleus. The results presented and discussed in Chapter 6 will be based on the results presented in Table 5.8.

Q^2	D_{inelas}	A_{inelas}	A_{phys}
1.7 GeV^2	0.9839	-0.0038	-0.254
2.5 GeV^2	0.9834	-0.0030	-0.191
3.5 GeV^2	0.9726	-0.0050	-0.125
3.5 GeV^{2*}	0.905	-0.0143	-

Table 5.9: Shown are preliminary inelastic asymmetries and dilutions for the various kinematic [82]. The * row relates to an expanded selection of quasi-elastic events, with a maximum invariant mass of 1.15 GeV rather than the usual maximum of 1.05 GeV and a maximum missing mass of 2.2 GeV rather than 2 GeV (see Table 5.5).

Chapter 6

Results and Discussion

The results presented in Table 5.8 are shown in Figure 6.1 along with selected theoretical curves and previous measurements using polarized techniques. Several models, including ones in the GPD, VMD, diQuark, and CQM frameworks, show agreement with the new measurements presented in this thesis. Further analysis of the $Q^2 = 1.3$ GeV^2 point, and the measurement near 1.5 GeV^2 at Mainz, will hopefully shed light on the possible discrepancy of the measurements near 1.5 GeV^2.

The form factors provide inputs for interpolations, including that by Guidal *et. al.* This model, which will be described below, can be refit using the new data for the electric form factor of the neutron in addition to other form factor data (in section 6.4.2). Within the GPD framework, the quark orbital angular momentum can be calculated using Ji's Sum Rule [54]. This is done in section 6.4.3.

It is common in the literature to use $t = -Q^2 = -\Delta^2$ rather than Q^2 when talking about fits and models. This practice will be followed in this chapter. Additionally, unless otherwise mentioned, the QCD scale evolution parameter is $\mu^2 = 1$ GeV^2.

The form factors have been fit many times [18] [59] [76]. For the magnetic form factors, the simplest fit is proportional to the dipole form factor (equation 3.2). As described in section 3.1.1 the electric form factor of the neutron has long

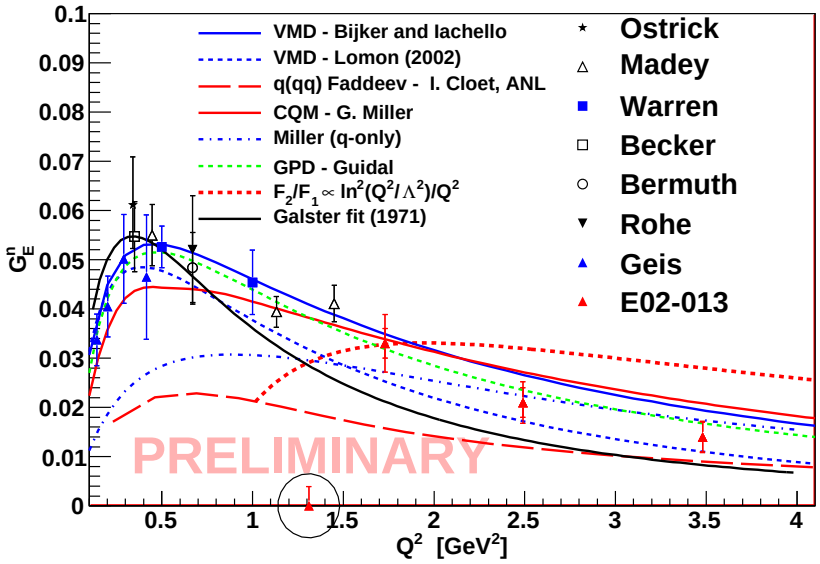

Figure 6.1: The electric form factor of the neutron with values presented for various experiments including the one presented in this thesis. Also included are representative models of the CQM [71], VMD [15][65], GPD [28][45], and diQuark variety [26]. In black is the traditional Galster parametrization. Circled is the measurement at $Q^2 = 1.3$ GeV^2 which is not included in this thesis.

been parametrized by the Galster fit. This fit was recently modified [59] to

$$G_E^n = \frac{A\tau}{1 + B\tau} G_D \ . \tag{6.1}$$

Parameter	Previous Work[59]	This Work
A	1.7	1.4 ± 0.1
B	3.6	1.6 ± 0.5

Table 6.1: Given here are previous fit parameters [59] and a new fit presented in this thesis. The fit only includes data from experiments using double polarization techniques.

6.1 Framework Formalism

As noted in section 1.3, QCD cannot be solved analytically in the regime where the quarks can be described as confined. The theory is also difficult to discuss analytically since Lorentz boosts of such a wavefunction is as complicated as solving the theory. By putting the problem into the Light Front gauge, a simpler description can be discussed. In Light Front Quantization, QCD is quantized at a fixed light front time $\tau = t + \frac{z}{c}$ giving the following quantities of

$$P^{\pm} = P^0 \pm P^Z \tag{6.2}$$

and $\vec{P}^{\perp}$ as the new four-momentum. Here P^+ is the longitudinal momentum and $\vec{P}^{\perp}$ is the transverse momentum. The wavefunctions of this formulation describe the nucleon in an arbitrary moving frame. To describe the quarks and gluons within the nucleon

$$p_i^+ = x_i P^+ \ , \tag{6.3}$$

and

$$\vec{p}_i^{\perp} = x_i P^{\perp} + \vec{k}_i^{\perp} \ , \tag{6.4}$$

are used where $x_i = \frac{p_i^+}{P^+}$ and $\vec{k}_i^{\perp}$ represent the relative momentum coordinates. The parton model is an approximation in a general reference frame, but is exact in the Light Front quantization. The transferred momentum in this frame is $q^+ = 0$, $q^- = \frac{2q\cdot P}{P^+}$ and $\vec{q}^{\perp}$. Obviously $Q^2 = -t = \vec{q}_{\perp}^2$ and is often referred to as $\Delta_{\perp}^2$.

In non-relativistic physics the natural framework for discussion of quantities is the center of mass; in the relativistic framework of light front QCD the natural framework is the center of transverse momentum, $\vec{R}^{\perp}$ [22]. The obvious, parton, definition is

$$\vec{R}^{\perp} = \sum_i x_i \vec{r}_i^{\perp} \ . \tag{6.5}$$

The conjugate position to the momentum $\vec{k}_i^{\perp}$ is $\vec{b}_i^{\perp}$. It is in terms of this position that the distribution of the quarks can be described. Obviously $\sum_i \vec{b}_i^{\perp} = 0$. In this mixed reference frame with longitudinal momentum and transverse position, the GPDs have a density interpretation. The probability to find a quark with x and $\vec{b}^{\perp}$ minus the probability to find an antiquark is given by

$$q_v(x, \vec{b}^{\perp}) = \int \frac{d^2\Delta}{4\pi^2} e^{-\vec{b}^{\perp}\dot{\Delta}} H_v^q(x, t = -\Delta^2) \ . \tag{6.6}$$

Using equations 1.1, 1.2 and 6.6, the parton charge density in this mixed reference frame is [70]

$$\rho_0(b) = \sum_q e_q \int dx q(x, \vec{b}) = \int \frac{d^2q}{4\pi^2} F_1(Q^2 = \Delta^2) e^{i\Delta\dot{b}} \ . \tag{6.7}$$

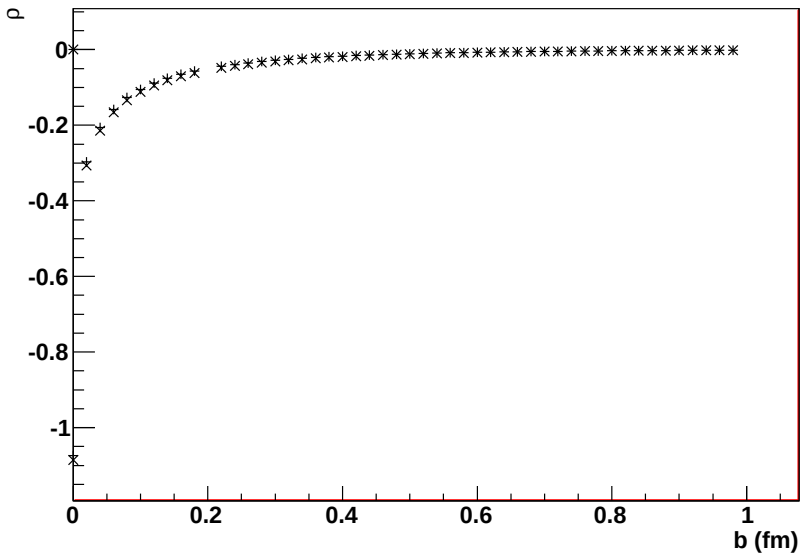

Figure 6.2: Shown is the transverse density in the neutron. This is with the magnetic form factor described as a dipole, and the electric form factor described by the fits in Table 6.1. Here + is the previous fit and × is the new fit, the transverse density for these fits is almost identical.

This integral can also be expressed in terms of the Sachs form factors

$$\rho(\vec{b}) = \int_0^\infty \frac{dQQ}{2\pi} J_0(Qb) \frac{G_E(Q^2) + \tau G_M(Q^2)}{1+\tau} \ . \tag{6.8}$$

Using the dipole parametrization of the magnetic form factor, and the electric form factor parametrized in equation 6.1, the transverse density in this mixed frame is shown in Figure 6.2.

6.2 Results

6.3 Pauli and Dirac Form Factors

As presented in equation 2.8, the Pauli and Dirac form factors can be related to the Sachs electromagnetic form factors. To calculate F_1^n and F_2^n, only G_E^n needs

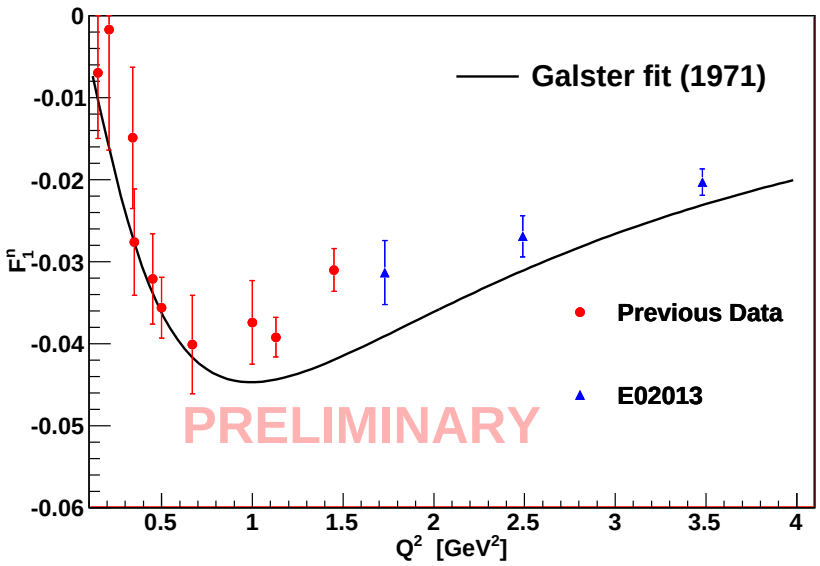

Figure 6.3: The Dirac form factor, F_1^n, using measured values of G_E^n and the dipole approximation for G_M^n. Shown in black is the Galster parametrization.

to be determined due to knowing G_M^n at $Q^2 < 4$ GeV^2. As can be seen in equation 2.8, F_1 has a stronger dependence on the electric form factor than does F_2. Using a dipole approximation for G_M^n

$$G_M^n = \mu_n G_D \ , \tag{6.9}$$

it is possible to determine the Pauli and Dirac form factors using only electric form factor data. These are shown in figures 6.3 and 6.4.

-

6.3.1 Flavor Form Factors

If the following assumptions are made, the flavor form factors can be deconvoluted from the nucleon form factors. These flavor form factors are the form factors of a flavor within the nucleon, not of a specific quark. Assuming that Iso-spin sym-

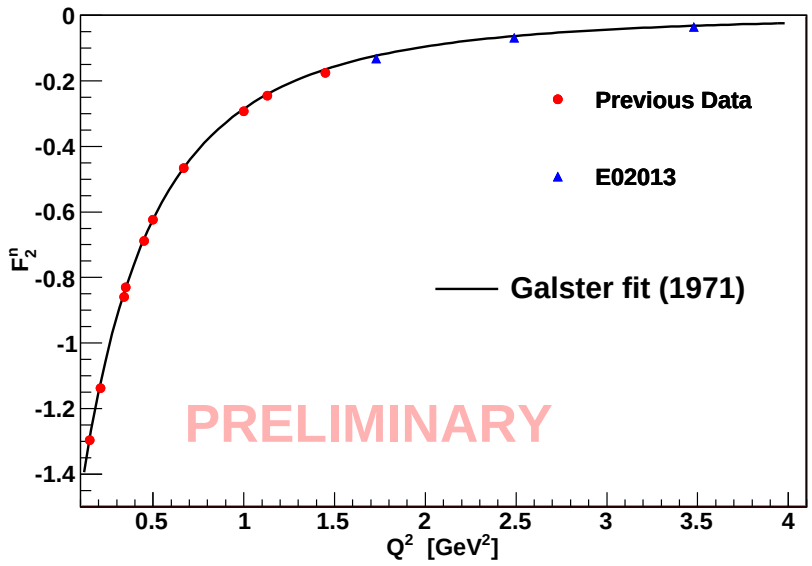

Figure 6.4: The Pauli form factor, F_2^n, using measured values of G_E^n and the dipole approximation for G_M^n. Shown in black is the Galster parametrization.

metry is conserved at $Q^2 > 0$, the neutron can be considered to be a proton in which the down quarks switch places with the up quarks. For the proton, since the charge of the proton is defined to be 1 (see equation 2.7), the equation for the proton form factors in terms of the flavor form factors is

$$F_{1,2}^p = \frac{2}{3}F_{1,2}^u - \frac{1}{3}F_{1,2}^d \ . \tag{6.10}$$

The formula for the neutron is similar,

$$F_{1,2}^n = -\frac{1}{3}F_{1,2}^u + \frac{2}{3}F_{1,2}^d \ . \tag{6.11}$$

For both the magnetic form factors of the neutron and proton, the dipole approximation is used. For the electric form factor of the proton, a modified dipole is used [76]

$$G_E^p = (1.06 + 0.14t)G_D \ . \tag{6.12}$$

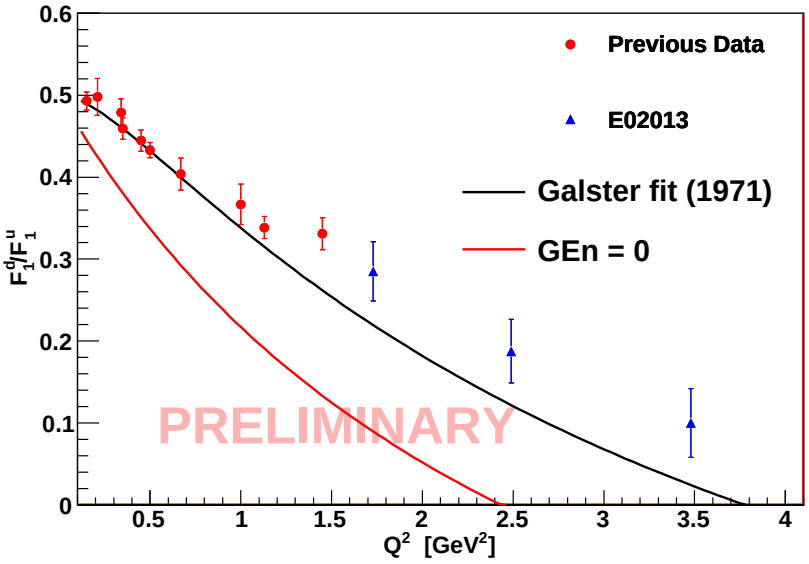

Figure 6.5: Ratio of the down and up quark flavor Dirac form factors. The form factors not dependent on G_E^n are just dipole approximations. The black curve is for G_E^n in the Galster parametrization, the dotted curve is for $G_E^n = 0$.

This allows the Pauli and Dirac form factors for both the proton and the neutron to be calculated, and the flavor form factors deconvoluted, with uncertainties assumed to be coming only from the neutron electric form factor data. Theorists predict the strange form factor is not different from 0 for these nucleons. There are no data available beyond $Q^2 = 1$ GeV^2. There are many theoretical estimates, the majority of which predicts a strange contribution that is negligible relative to the contributions of the up and down quarks. It is therefore ignored in this deconvolution.

The deconvolution into the flavor form factors is presented in Figures 6.5 and 6.6.

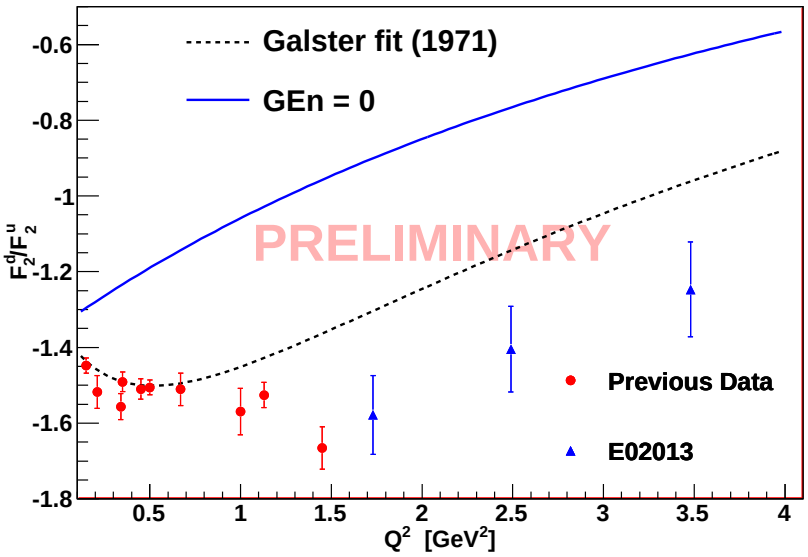

Figure 6.6: Ratio of the down and up quark flavor Pauli form factors. The form factors not dependent on G_E^n are just dipole approximations. The dotted curve is for G_E^n in the Galster parametrization, the blue curve is for $G_E^n = 0$.

6.4 GPD Models

Generalized parton distributions are a popular new framework in which to consider nuclear interactions and structure. These were discussed earlier in sections 3.1.4 and 1.3.3. The GPDs parametrize the non-forward pieces of the light-front operators. They have the advantage in being able to describe, in part, elastic processes, Deep Inelastic Electron Scattering, Deeply Virtual Compton Scattering, and physical properties like quark orbital angular momentum. In terms of the nucleon form factors, the GPDs give the quark contribution at a given x to the flavor form factors:

$$F_1^q(t) = \int_0^1 dx H^q(x,\xi,t) \tag{6.13}$$

$$F_2^q(t) = \int_0^1 dx E^q(x,\xi,t) \ . \tag{6.14}$$

There are two other GPDs, which are related to the pseudoscalar and axial form factors. These are not really affected by electric form factor measurements, and are more difficult to constrain by experiments.

6.4.1 Impact Parameter Space

Because GPDs divide the momentum into longitudinal and transverse components, t can be transformed (similar to a Fourier transform) into position space to provide a description of the nucleon in terms of an impact parameter. This impact parameter is the distance from the center of momentum of the nucleon. From this, the distribution of the flavor can be determined for different longitudinal momentum fractions (x). The impact parameter space versions of the GPDs are:

$$H^q(x,\vec{b}) = \int \frac{d^2\vec{\Delta}}{(2\pi)^2} e^{-i\vec{b}\cdot\vec{\Delta}} H^q(x,-\vec{\Delta}^2) \tag{6.15}$$

$$E^q(x,\vec{b}) = \int \frac{d^2\vec{\Delta}}{(2\pi)^2} e^{-i\vec{b}\cdot\vec{\Delta}} E^q(x,-\vec{\Delta}^2)\ . \tag{6.16}$$

This $H^q(x,\vec{b})$ is equivalent to $q(x,\vec{b})$ the distribution of partons as a function of the transverse position $\vec{b}$ from the center of momentum and light-cone momentum fraction x.

Because the impact parameter space corresponds to locations within the hadron, the density interpretation of GPDs is used to create conditions that must be satisfied by the GPDs. For example, giving a relation between the impact parameter and the longitudinal momentum fraction, any nucleon is going to have the allowed region of impact parameter space go to 0 as the longitudinal momentum fraction goes to 1

[45] [24]. It has been shown that H and E in impact parameter space satisfy [45]

$$\frac{1}{2}|\nabla_{\vec{b}} E^q(x,\vec{b})| \leq H^q(x,\vec{b}) \ . \tag{6.17}$$

This requirement provides an important constraint to possible GPDs.

The probability interpretation of $E^q(x,\vec{b})$ is in the transverse basis rather than the longitudinal basis. The distribution is then

$$q_v^X(x,\vec{b}) = q_v(x,\vec{b}) - \frac{b^y}{m}\frac{\partial}{\partial \vec{b}^2} E_v^q(x,\vec{b}) \ . \tag{6.18}$$

where $q_v^X(x,\vec{b})$ is the probability to find an unpolarized quark with momentum fraction x and impact parameter $\vec{b}$ in a proton polarized in the x-direction minus the probability to find an antiquark.

6.4.2 Fit to our data

As mentioned previously (section 3.1.4), many of the models in the GPD framework [28][45] have parameters which are dependent on the nucleon form factors. Since 2005, new data on the nucleon form factors, in particular the neutron electric form factor presented in this thesis. This allows for new fits.

The models for the helicity conserving GPD take the form of

$$H = q_v(x) e^{f_q(x)t} \tag{6.19}$$

where $q_v(x)$ is the quark density function. This function is acquired from global fits to DIS data and other data, the fits used by these models were the MRST2002 (Guidal *et al.*[45]) and the CRET (Diehl *et al.*[28]). New data are also available for these fits [67].

The form of $f_q(x)$ is another parameter. Diehl, *et al.* fit the nucleon data and use the Regge phenomenology to get a class of fits. Guidal, *et al.* use Regge phenomenology, which shows behavior that is close to correct both as $x \to 1$ and $x \to 0$. Guidal *et al.* use

$$f_q(x) = \alpha' ln\left(\frac{1}{x}\right) \tag{6.20}$$

while Diehl *et al.* use

$$f_q(x) = \alpha'(1-x)^2 ln\left(\frac{1}{x}\right) + A_q(1-x)^2 + B_q(1-x)^3 \ . \tag{6.21}$$

Diehl *et al.* argue that expecting $f_q(x)$ to be described at high t by α does not work, since Regge phenomenology does not apply at that regime.

The helicity flip GPD has an additional component meant to change its behavior as a function of t compared to H. It should drop as $\frac{1}{t}$ or faster, and so Guidal *et al.* solve this by putting in a term $(1-x)^{\eta_q}$. This gives the E GPD as

$$E = N_{\eta_q} q_v(x)\,(1-x)^{\eta_q}\, e^{f_q(x)t} \tag{6.22}$$

where N_{η_q} is a normalization constant to account for the added term.

Diehl *et al.* use a different profile function,

$$g_q(x) = \alpha'(1-x)^2 ln\left(\frac{1}{x}\right) + C_q(1-x)^2 + D_q(1-x)^3 \tag{6.23}$$

which gives the E GPD as

$$E = \frac{\Gamma\left(2-\alpha+\beta_q\right)}{\Gamma\left(1-\alpha\right)\Gamma\left(1+\beta_q\right)} \kappa_q x^{-\alpha}\,(1-x)^{\beta_q}\, e^{t g_q(x)} \ . \tag{6.24}$$

The previous fit of Guidal *et al.* and a new fit using the measurement of the electric form factor of the neutron presented in this thesis are presented in Table

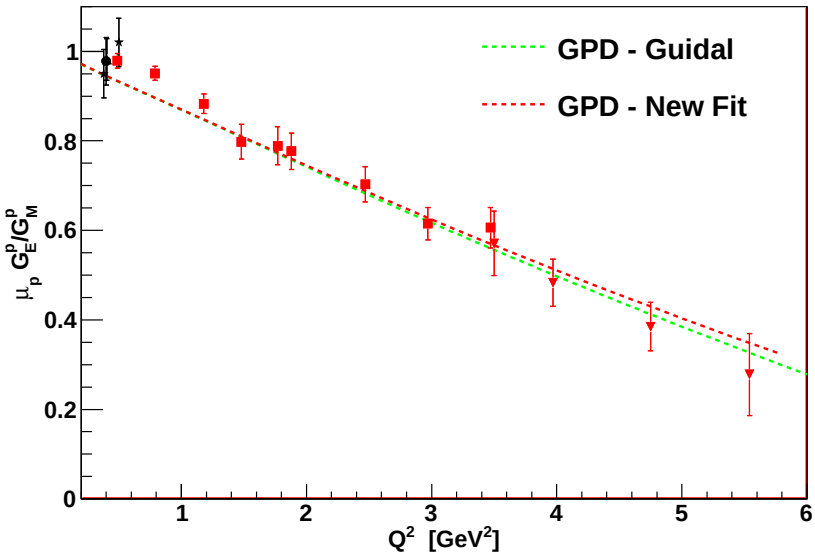

Figure 6.7: The combined form factors of the proton ($\frac{\mu G_E^p}{G_M^n}$) with values presented for various experiments. Included are the calculations of the electric form factor in the GPD framework with the fits as described in Table 6.2.

6.2. In figures 6.7, 6.8, and 6.9 the success of the new fit is demonstrated. This new fit uses the MRST2008 NNLO fit for the valence quark densities [67].

Parameter	Previous Work [45]	This Work
η_u	1.34	1.68
η_d	1.34	0.60

Table 6.2: Given here are the fit parameters from the previous work [45] and a new fit presented in this thesis.

6.4.3 Quark Orbital Angular Momentum

The quark orbital angular momentum can be calculated in the GPD framework using Ji's Sum Rule [54]:

$$2J^q = \Delta q + 2L^q = \int_{-1}^{1} x dx [H^q(x,0,0) + E^q(x,0,0)] \ . \tag{6.25}$$

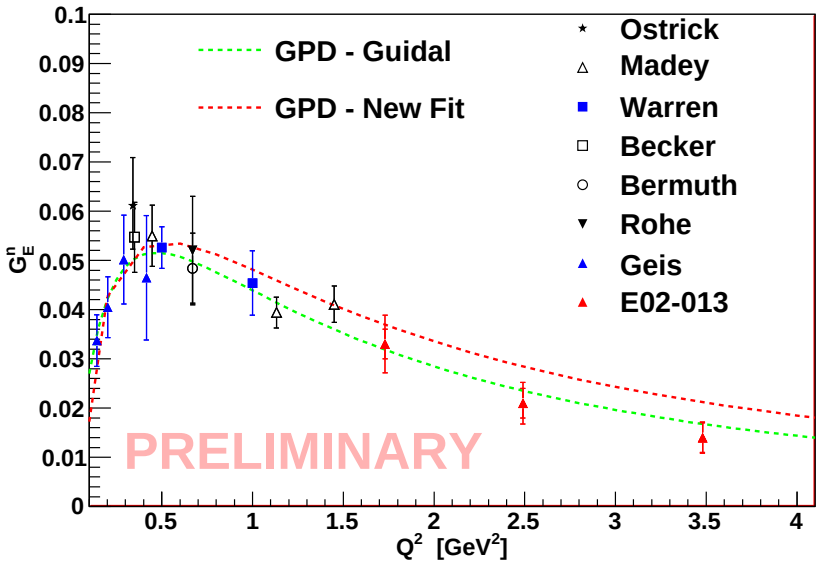

Figure 6.8: The electric form factor of the neutron with values presented for various experiments including those presented in this thesis. Included are the calculations of the electric form factor in the GPD framework with the fits as described in Table 6.2.

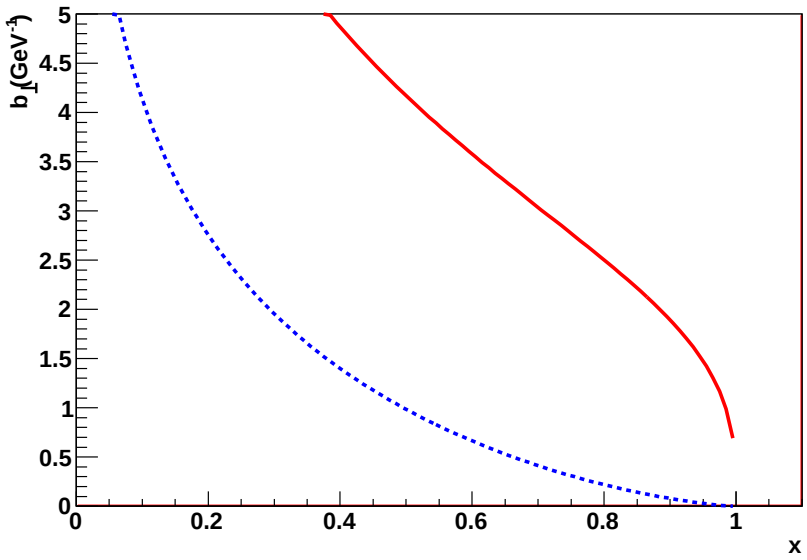

Figure 6.9: Shown are the upper bounds of the value for b. These bounds are determined by applying the condition in equation 6.17 [45]. The solid line is for the Up quark while the dotted is for the down quark.

In Table 6.3 these quantities are tabulated, including the integrals that depend on the GPDs. In this table, the values for the original fit are presented along with values for the new fit.

Quark	Δq	$\int H$	$\int E$	$2J^q$ **	$2J^q$ *	$2L^q$ **	$2L^q$ *
u	0.6	0.37	0.238	0.595	0.583	-0.01	-0.017
d	-0.25	0.20	-0.207	-0.031	-0.059	0.219	0.191
s	-	0.04	0	0.04	0.04	-	-
total	-	0.61	-	0.568	0.524	-	-

Table 6.3: Presented is a calculation of the quark orbital angular momentum using Ji's Sum Rule [54] in the framework of [45]. Compared is this previous work (**), with a new fit (*) using the form factor results presented in this thesis.

6.4.4 Conclusions

With the advent of double polarization measurements, the structure of the nucleon is being probed in fine detail. The neutron electric form factor, presented in this thesis, provides not just a parametrization of the nucleon structure but, with a few assumptions, provides knowledge about the flavor structure and quark orbital angular momentum. The new measurements of this form factor more than double the range of Q^2 covered. These new measurements show agreement with many of the models, but not with pQCD scaling scaled to the previous data.

A fit to G_E^n using these new data shows a decrease in the density of the neutron at small $\vec{b}$ compared to previous work. Using the Sachs form factor data and the dipole approximation of the Sachs magnetic form factor, gives the Pauli and Dirac form factors which shows the expected behavior. Deconvoluting these into the flavor

form factors gives

$$\frac{f_1^d}{f_1^u} \propto Constant \tag{6.26}$$

and

$$\frac{f_2^d}{f_2^u} \propto Q^2 \tag{6.27}$$

behavior. Refitting a model to determine GPDs allows the calculation of quark orbital angular momentum. This shows a slight increase in the contribution to the total angular momentum of the nucleon from the down quark.

New analysis and experiments are needed, both to increase precision at low Q^2 and to show pQCD scaling at higher Q^2. The small effect of FSI and the near 100% neutron polarization seen in polarized helium-3 makes double polarization experiments using polarized helium-3 ideal for future measurements of this form factor.

Appendix A

Neutron Arm Analysis

The neutron arm was developed to detect the outgoing neutron in coincidence with the electron in the interaction $^3\overrightarrow{\text{He}}(e, e'n)$. The neutron arm's position, active area, and sheilding were designed to match the electron spectrometer, Big Bite, at the highest measured value of Q^2 and to provide the highest possible neutron detection efficiency at this value [25]. See Table 4.1 for the kinematics and positioning of Big Bite and the neutron arm.

Building upon the discussion in section 4.6, the neutron detector, known as Big Hand, was a large detector made up of 244 neutron bars totaling 976 ADC and TDC channels and an additional 192 single sided veto bars. In addition, there were four "marker" counters which were placed between the neutron detectors and the veto detectors and used for calibration. Neutrons are identified using the vertical position, horizontal position, time of flight, and the existence of a nearby hit in the veto detectors. The neutron detector was highly segmented to improve the vertical (x) resolution. The horizontal resolution and the time of flight resolution of the neutron arm was improved by a time calibration of all the bars, with the "marker" counters playing a crucial role in the horizontal calibration.

A.1 Simulations

A detailed simulation was undertaken of the neutron arm using Geant 4 [49]. Its goals were to understand the inelastic contribution in the invariant mass and time spectra, to simulate a value for the proton to neutron conversion between the target and neutron bars, and to determine the result of the threshold change for the on this conversion. Additionally, the simulation provides neutron detection efficiency, hadron detection efficiency, and veto efficiency numbers that are needed to understand the neutron arm.

The simulation was designed to include all the material in between the target and the neutron bars in order to properly simulate the events within the neutron detector. This included the iron target box, the target cell, and the material for the target ladder. A document was prepared that shows the components of the target system [57]. On the neutron arm side, all bars, PMT light guides, shielding, cassettes, as well as detector response were included. Details of the geometry were documented by Tim Ngo [73]. The Big Bite acceptance was modeled using Big Bite geometry, a model for the $\vec{B}$ field, and the total shower threshold and resolution, and is in good agreement with observed data.

Quasi-elastic scattering was simulated in the impulse approximation, with ^{3}He momentum distributions from [90]. Parameterizations of the nucleon form factors [59] were used to calculate elastic cross sections and asymmetries. Simple pion production is the dominant inelastic contribution for these kinematics, with cross sections and asymmetries provided by the MAID parameterization [32]. External

radiative effects caused by objects in the vicinity like the beamline were included and internal radiative effects were modeled [1] [82] [50].

The neutron arm response was simulated using the events above on an event-by-event basis with a GEANT4 simulation. Additional software was developed to reproduce PMT signals and electronics responses, and mimic the NA trigger. The simulated data then had the virtual thresholds changed to match the real data, and the virtual data were processed similarly to the real data [82]. This Monte Carlo was developed by Seamus Riordan.

The simulation was used primarily as method to understand the purity factor and the inelastic contribution to the quasi-elastic sample. The purity factor (D_n) is discussed in section 5.5 and the inelastic contribution in section 5.7.2. The simulation also gives proton and neutron detection efficiencies, shown in Table A.1. These are lower than what was predicted.

$Q^2 =$	1.7 GeV^2	2.5 GeV^2	3.5 GeV^2
proton detection efficiency	0.411	0.270	0.210
neutron detection efficiency	0.345	0.250	0.165

Table A.1: A table showing the proton and neutron efficiency as calculated using the Monte Carlo Simulation.

A.2 Calibrations

To achieve the desired resolution needed to identify quasi-elastic events within the neutron arm, all bars within the neutron arm (NA) were calibrated relative to

[1] Model by Mo and Tsai using the peaking approximation.

each other. For the measurement at $Q^2 = 3.5$ GeV^2 the required parallel momentum resolution was 0.250 GeV which corresponds to a time of flight resolution of less than 500 ps [25].

During the commissioning period, the descriminators were set, the cables were emplaced, and the high voltage (HV) for the detector bars was adjusted. The threshold for the NA and the HV for the individual PMTs were adjusted over the course of the experiment. This created a number of different "periods" with different neutron arm detection efficiencies. Changes in high voltage are shown in Table A.2.1. The remainder of this section will be a description of the calibrations necessary to get the desired NA resolution.

The desired situation was that the neutron arm provided a precise time of flight resolution. As explained, this was necessary for quasi-elastic event selection and neutron identification. The time calibration of the neutron arm not only acheived a time resolution of less than 500 ps, but also acheived an accurate and precise horizontal position. The tune of the high voltage, done numerous times over the course of the experiment, provided ADC signals that were the same within 10% for cosmic type events. Differences in the electronics and cables cause the signal read out of the TDC to have a delay unique for each PMT.

The signals used for the HV tune, those from cosmic sources, were similar to each other. However, signals from quasi-elastic events were different from these signals used for HV tune. Due to this, events taken during running conditions created dissimilar signals within the ADC and caused the discriminator to trigger at a different point in the amplitude spectrum compared to events from cosmic sources.

Due to these dissimilar signals, for the best resolution an amplitude correction was required in addition to the time offset calibration. A difficulty with using particles from cosmic events was that the path they travel through the neutron arm was not the same as events caused by interactions in the target. This caused a differently shaped peak which was broader than the peak due to hadron events.

To account for the differences in delay and electronics, a time offset calibration was done for each PMT. An amplitude correction to the mean time and horizontal position within the bar corrected differences caused by differences in signal shape.

A.2.1 High Voltage Tune

The HV for the counters was set so that each neutron counter had similar behavior during operation. The signals should be well behaved, meaning above threshold but below saturation, for hadronic events, and for other events which are expected within the detector during normal operation. This allowed the analysis to treat all bars similarly when calculating time of flight, identifying charged particles, and calculating perpendicular missing momentum (due to the calculated hit position within the neutron arm), and the other quantities needed for quasi-elastic neutron identification. A few detectors stopped being well behaved during the course of the experiment. These were mostly noted and disconnected during the experiment.

The HV tune was done prior to the start of the experiment using cosmic particles. All cosmic rays have similar signatures within the detector, but their signals were not so uniform as those from protons and neutrons from the target.

Because of high voltage (HV) drift and the difficulties in calibrating all photomultiplier tubes (PMTs), a threshold of a 10% difference from the average was used to determine whether the PMT's HV needed adjustment. During the experiment cosmic events continued to be used to adjust the HV when beam was not available, if a PMT drifted outside of this 10% threshold.

A script was developed for online monitoring and adjustment of the high voltage. This allowed for particular HV settings to be saved and for the high voltage of individual bars to be turned on and off as needed. It also allowed the resetting of HV during a trip or other event. Each colored set of bars in figure 4.19 used the same modules for the high voltage, amplifier, discriminator, and other electronics. This high voltage script was written by Eugene Chudakov.

A script was created to realize the HV calibration[2]. The resulting files were fed into the previously described script to change the high voltage. Diagnostic files showing the fitted spectra for the PMTs were produced, with spectra divided into files based on counter type, plane, and side of the counter.

In this HV calibration script, long cosmic events were selected. These were events which were detected in a bar and its vertical neighbors. The amplitudes were tuned towards a common goal (G), which was determined based on the height of the bars relative to each other. This was 1000 channels for the UVA and GLA bars, and 1500 channels for the CMU bars. Two different techniques were used to set

[2]Written by Igor Rachek, and modified by Jonathan Miller, Rob Feuerbach, and Pavel Degtiarenko.

the gain, the first [3] using simply the amplitude of the bars. The peak for minimum ionizing particles was directly compared to the goal to determine the gain to apply.

A second technique [4] used logorithms. This used two pieces of information determined from amplitude, a mean ($A_M = \frac{\ln A_L + \ln A_R}{2}$) and a difference ($A_D = \ln A_R - \ln A_L$). Here L is used for left, R for right, and A is the amplitude while T is the time. In this case the gain was determined by fitting A_D and A_M, and was given by $e^{-\ln G + A_M \pm 0.5 A_D}$ where $+(-)$ was for the right(left) gain. This second technique was used during data collection.

A.2.2 Time Offsets

The resolution of the time of an event in the neutron arm (NA) is a convolution of the alignment of the bars with the internal resolution of the bars. The internal resolution of the bars provides a minimum resolution for the experiment (individual PMT amplitudes can be used to improve the internal resolution of the bars). The time of an event in a neutron bar or counter is just the mean time as determined from the PMTs.

The core concept for the time offset calibration of the neutron arm involved an "alignment" of the times internal to the neutron arm. To call two times aligned, the spectra of two (often neighboring) bars would be shifted to coincide after the relevant corrections were applied. Alignment means that the spectrum in a bar, after corrections for position within the NA and after selecting hadronic events, will

[3] Developed by Igor Rachek.

[4] Developed by Pavel Degtiarenko.

be similair to others bars after such corrections. For example, if a particle passes through two neighboring bars, they are aligned if the time that the particle passed through the bar is the same when corrected for the distance between the two bars that the particle traveled.

Three steps were used to acheive the offset calibration of the PMTs. First, the left times and right times were roughly aligned together. This allowed the left and right times to be associated properly together to form a mean time and time difference of the bar (left time minus right time) which was used to give the horizontal position of the hit. In the second phase of the calibration, the peaks for the mean time and the time difference were aligned for neighboring bars. This allowed clusters of hits to be created (known as clusters in the data), which are hits in neighboring bars with similar mean times and are identified as coming from the same event. In the final calibration, these clusters were used to improve the calibration using charged events (in ^{3}He). This only was used to do the final calibration of the first plane, later planes had their mean time and horizontal position calibration improved using events which travel deep into the neutron detector. The first plane also had its horizontal position calibrated using the known information of the "marker" bars.

The best understood particles that create events within the neutron arm are protons (from H_2), although muons will not deviate noticeably while traveling through the detector. Initially the calibration of the neutron detector was kept entirely internal to the neutron detector. In the final calibration the front plane was calibrated relative to Big Bite using quasi-elastic protons (from ^{3}He), with the later planes calibrated relative to the first plane (N1).

The PMTs in each neutron bar determine two main quantities. These are the mean time of the hit t_{mean} and the horizontal position of the hit y_{pos}. The horizontal position of the hit is determined by the difference in time, t_{diff}, between the measured signals in the two PMTs for a hit. These two quantities, only corrected for offsets, are

$$t_{mean} = A((t_{l,raw} - t_{l,offset}) + (t_{r,raw} - t_{r,offset})) \ , \tag{A.1}$$

$$t_{diff} = B((t_{l,raw} - t_{l,offset}) - (t_{r,raw} - t_{r,offset})) \ . \tag{A.2}$$

In these relationships $t_{l,raw}$ is the left raw time (from the TDC) and $t_{l,offset}$ is the software offset applied to the left TDC value. Here A and B are constants that are about $\frac{1}{2}$ and defined to be so in all calculations.

During the course of the experiment the high voltage was changed many times. Although this was the case, high voltage changes did not change values of the amplitude by much more than 10% and so rough values for the mean time and time difference for a bar will be independent of the high voltage setting. Because of this, the initial calibration was done once, with later calibrations fine tuning the initial calibration after each high voltage change.

The first improvement in calibration was acheived by comparing two bars in neighboring planes and subtracting their mean times [37]. This created a peak for events when there was a hit in both planes at that vertical (x) position. This peak was then adjusted to give the proper time of flight for near c particles and so all later planes were calibrated relative to the first plane (N1). The horizontal position calibration was realized by using the time difference in neighboring bars. This was

done similarly to the mean time calibration. The vertical position within a plane was calibrated using cosmic events.

The central problem with this technique is that cosmic events might not travel through the entire neutron bar; the shower from the cosmic might start or end within the bar. This is different than during running conditions, because the converter layer in front of each neutron scintillator bar results in most detected hadrons beginning interaction directly in front of the scintillator paddle where detection occurs.

The next improvement to the calibration was done by using a better selection of events. These better events were proton and muon events and selected by selecting long events that pass through the neutron arm, where a particle lost little of its momentum prior to being observed in the NA.

The high detection efficiency of protons and muons results in a cleaner spectrum for individual bars, and calibration using these events was better. This improved internal calibration calibrated the later planes relative to the first, by shifting $t_{central}$ to 0:

$$t_{central} = t_{1st} - t_{Nth} - t_{1st \rightarrow Nth} \ . \tag{A.3}$$

Here t_{1st} refers to the mean time of the first plane the particle passed through, and t_{Nth} refers to the mean time of the nth plane the particle passed through (at the same x as the first hit). Subtracted from this difference is the time for the particle to travel between the first and nth planes ($t_{1st \rightarrow Nth}$). The time between planes was calculated using the distance between the planes, and c_n to approximate the speed of a relativistic particle (since the particle is unknown). These well behaved events

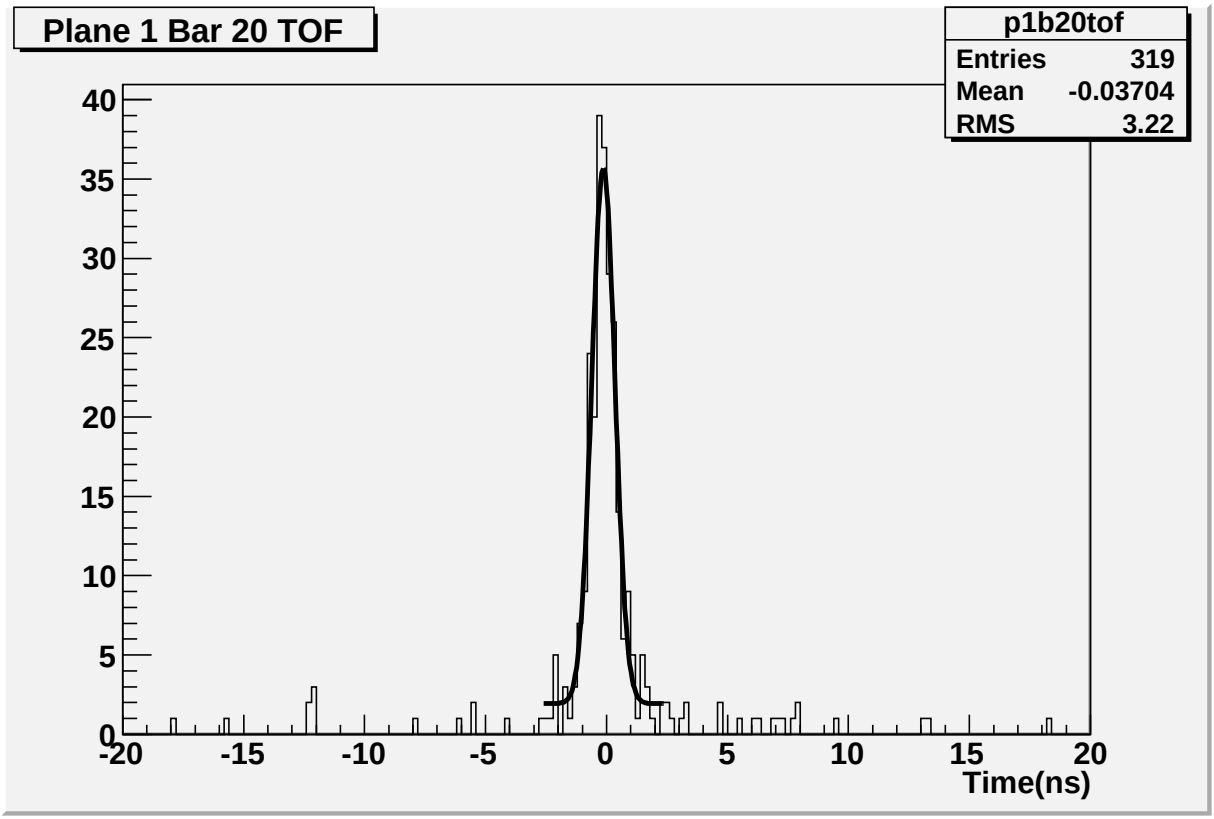

Figure A.1: Calibration of the mean time for plane 1 bar 20. This shows the difference between the time of flight and the expected time of flight peak for quasi-elastic protons between the BigBite scintillators and the front plane of the neutron arm.

were also used to calibrate the horizontal position of the hit within the Neutron Arm, aligning all later planes to the first plane. This completes the internal calibration. Figures A.3 and A.4 demonstrate this relative horizontal position and mean time calibration.

The final improvements to the neutron arm calibration were to achieve an accurate horizontal (y) position and to determine the overall offsets for the vertical position (x) using particles. The best understood particles within the neutron arm (NA) are elastic protons from hydrogen, which form well defined peaks in the mean

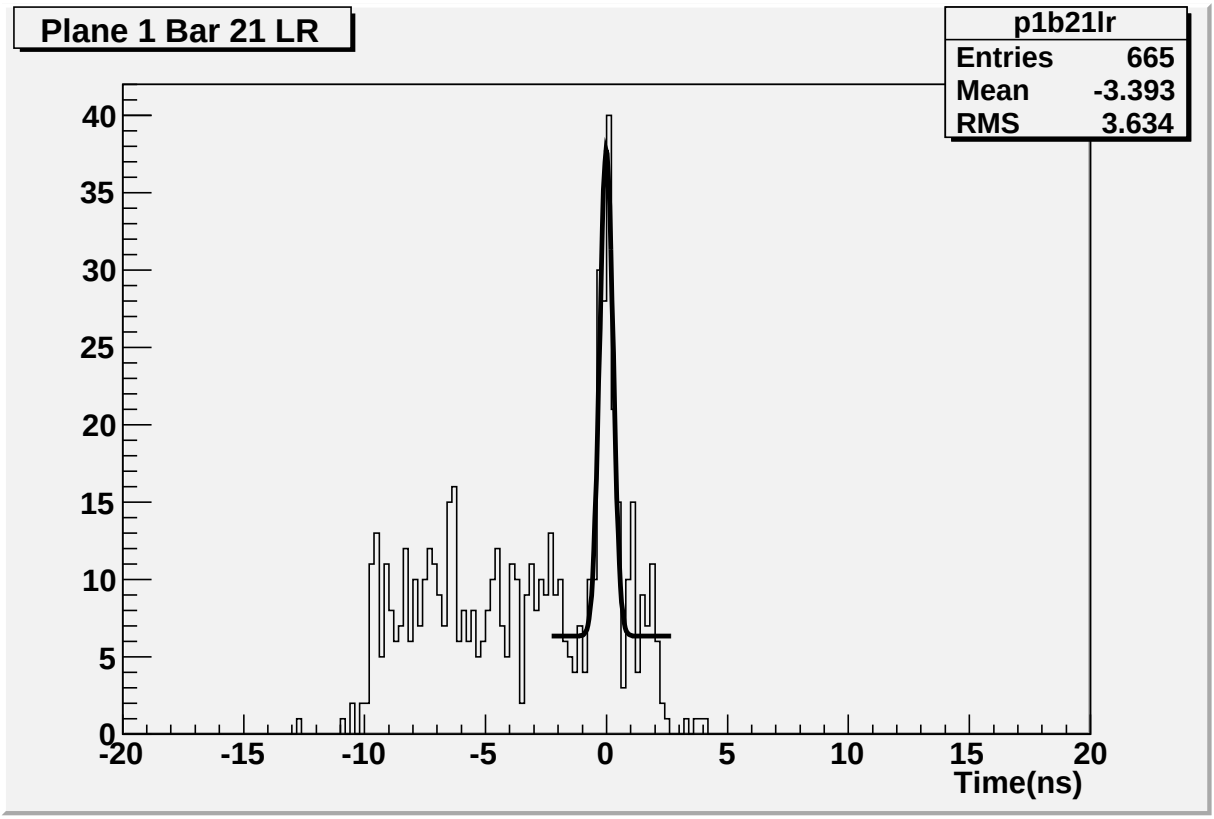

Figure A.2: Calibration of the horizontal position for plane 1 bar 20. This histogram shows the peak in the horizontal bars time difference, with coincidence with a hit in the "marker" counters.

time spectrum of bars in the first plane (N1). After corrections (detailed in equation 5.9) based on the position of the hit within the neutron arm and the time of the event within Big Bite, these spectra were aligned:

$$T_{c,TOF} = t_{1st} + t_{L1A} - t_e - t_h - t_{peak} + t_{rf} \ . \tag{A.4}$$

Here $T_{c,TOF}$ refers to the centered time of flight, t_{1st} refers to the mean time as measured in plane 1 (N1), t_{L1A} refers to the level one accept time (discussed in section 4.7), t_e refers to the time for the electron (discussed in section 5.1), t_h is the expected time for the hadron to travel to the neutron bar (discussed in section 5.3), t_{peak} is the time for the hadron to travel to the neutron bar, and t_{rf} is a correction to the known time of interaction due to RF information about the beam (discussed in section 5.5.3). The spectrum for the time of flight relative to the expected time of flight for protons in ^{3}He is presented in Figure A.2.2.

The neutron arm was placed to measure the maximum number of quasi-elastic events as possible in coincidence with Big Bite, not to measure as many elastics as possible. Because of this, elastic events did not cover the entire face of the neutron arm, but only a portion of it. To calibrate the entire detector, quasi-elastic events were used rather than the cleaner elastic sample. These still gave a tight time of flight peak and have events which pass through the detector.

Four "marker" counters were installed vertically within the neutron detector. These counters had poor resolution and were not meant to be used to determine the vertical position of a hit within the neutron bar. These counters were used to perform an absolute calibration of the horizontal position for all bars in the first

plane. This was done by using the coincidence between a hit in the marker counters and a hit in the neutron arm for a given event. For a single marker PMT the number of counts was small. By using the geometry information for the marker counters [72], the coincident peaks for all four marker counters were combined ($y_{center} = y_{diff} - y_{marker}$), providing the necessary statistics. This y_{center} is the position within the neutron arm for hits where there is a nearby well-timed marker bar hit. Here y_{center} is the peak location, y_{diff} is the original position along the bar, and y_{marker} is the geometric position of the marker counter. In Figure A.2.2 is an example of the resulting spectrum.

The results of the calibration are summarized in Figure A.5 using a single plot showing the main points of calibration: the mean times of planes N2 through N7, the time of flight for N1, and the y_{center} position for the absolute horizontal calibration. In this plot, some of the bars did not have high enough statistics to form a proper peak and are shown as poorly calibrated. These bars have greater uncertainty, and so for these the respective histograms are checked by eye.

A.2.3 Amplitude Correction

The amplitude spectrum was discriminated to provide a clear time for the TDC. However, since there was a threshold for this discrimination, the time measured by the TDC is depended on the shape and size of the amplitude. The mean time and horizontal position for an event were corrected for this amplitude depe-

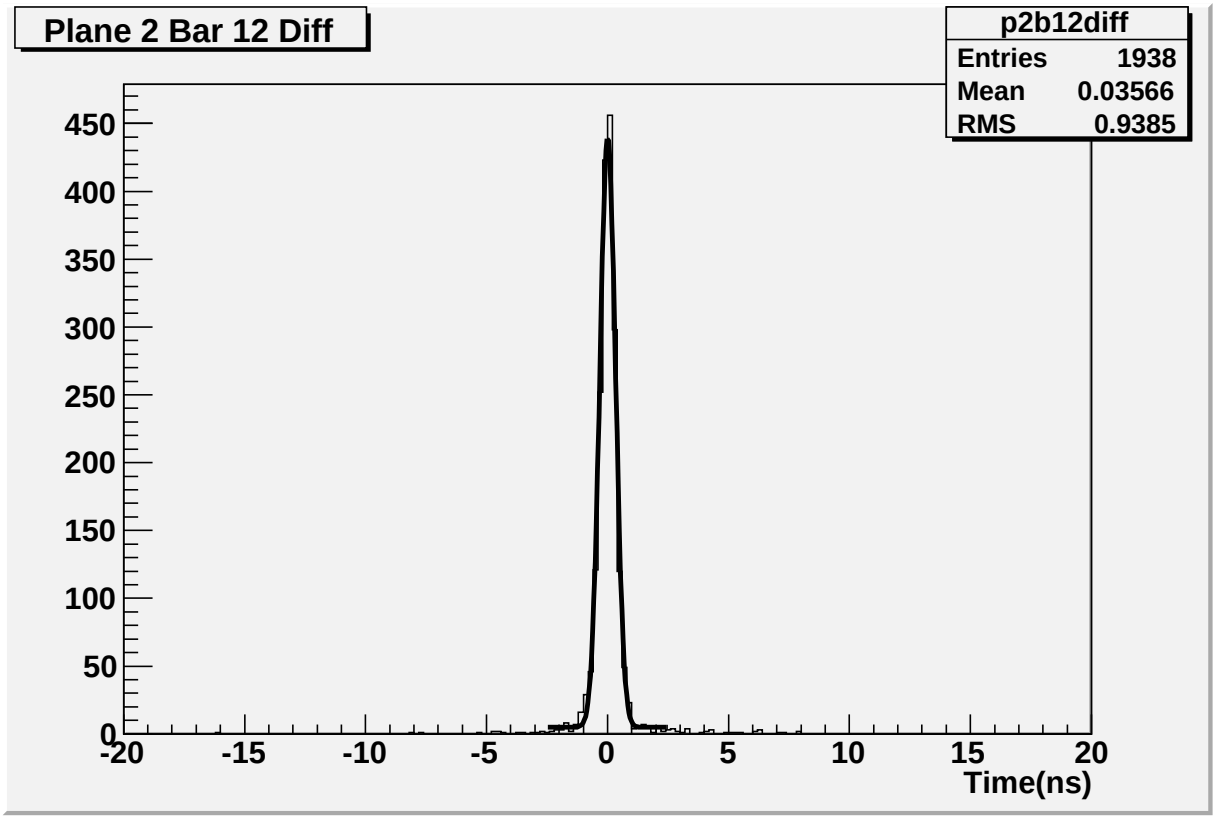

Figure A.3: Calibration of the mean time difference for plane 2 bar 12. This is the difference between neighboring bars in different planes. In particular, this is the difference between plane 1 bar 12 and plane 2 bar 12.

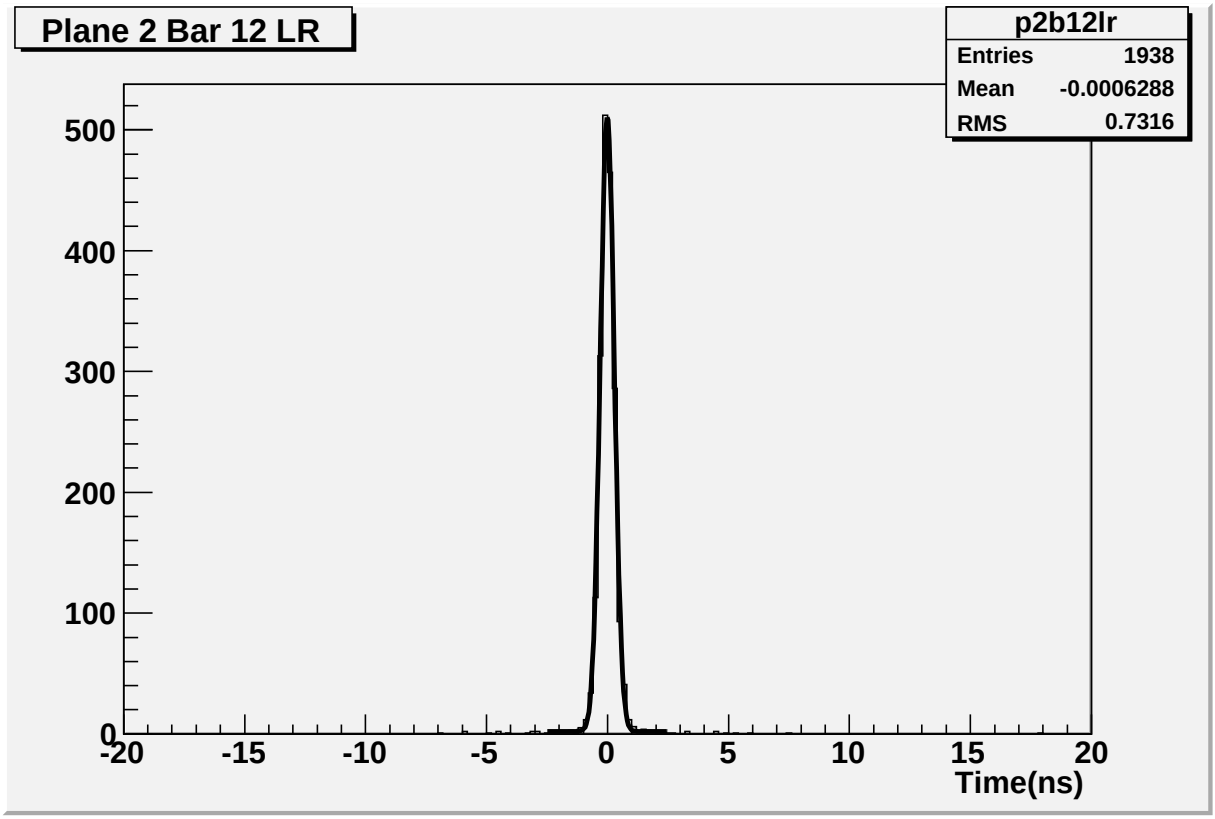

Figure A.4: Calibration of the relative horizontal position for plane 2 bar 12. This is the horizontal position (transformed to time) of the hits in plane 1 bar 12 and plane 2 bar 12 for events with well timed hits within the two bars.

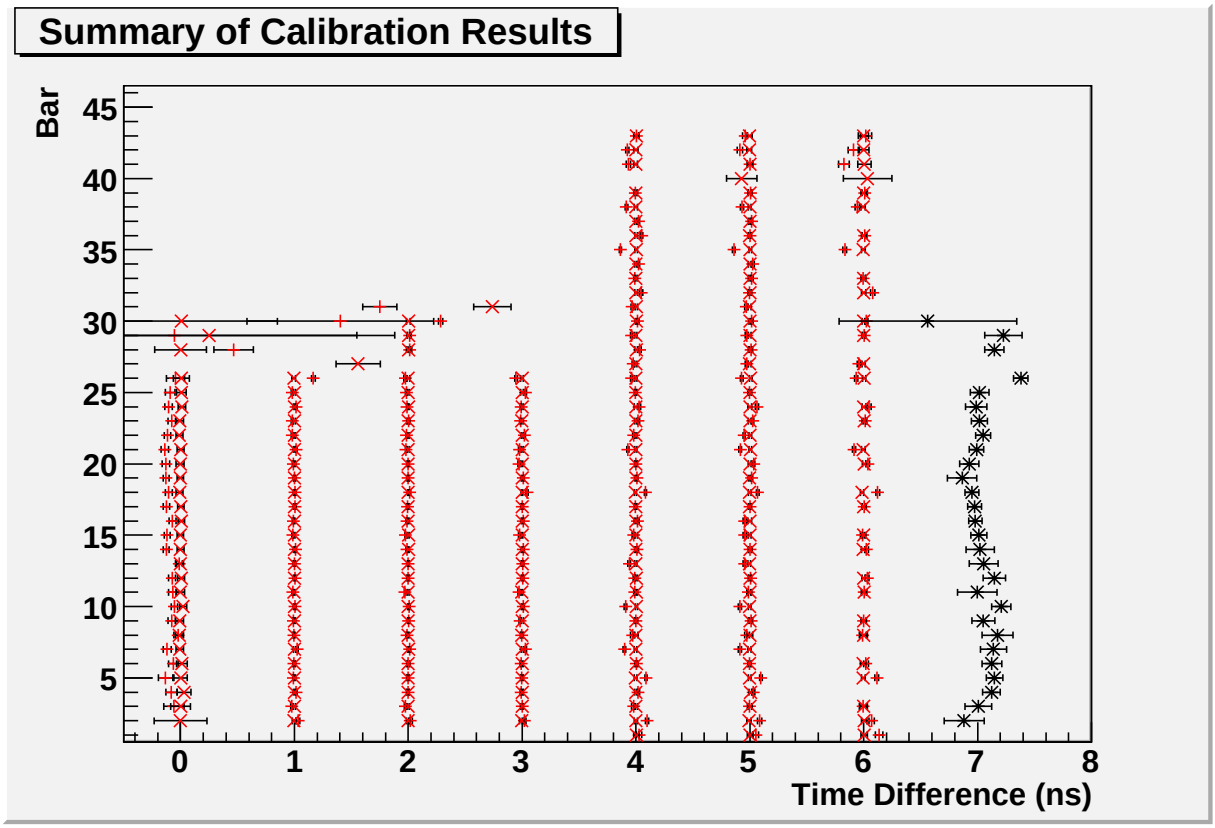

Figure A.5: Calibration summary plot for run 3975 after pass 3 calibration. In this plot, X is the result, + is the before calibration. On the x axis, 0 is for plane 1 and 1-6 show the differences between planes 1 and planes 2-7). At 7 on the x axis is the horizontal absolute position calibration for plane 1.

dence. This relationship for the initial amplitude calibration was

$$t_{corr} = t_i - C_{par}(A_{adc})^{-1} + C_{par}(A_{ref})^{-1} \ . \tag{A.5}$$

In the initial calibration the reference paramters, A_{ref}, were defined to be 0. The values for C_{par} were determined individually for each PMT.

This initial calibration was improved using a model where the amplitude correction was a function of the hit location (ΔY) within the bar. In this model, the amplitude dependent behavior should be the same for both sides of the bar. Additionally, because the threshold was set to be the same for all bars, this behavior should also be independent of which particular bar was hit. The correction can be approximated as (with a A and ΔY dependence as information from the PMT):

$$\frac{(C_1 + D_1\Delta Y)^2}{A} \approx \frac{C_2 + D_2\Delta Y}{A} \ . \tag{A.6}$$

The desire is to determine the constants which make a narrow peak in the time of flight between the Neutron Arm and Big-Bite. To do this Minuit [30] was used to minimize the following:

$$T_{mean} + \frac{C_2}{2}\left(\frac{1}{A_L} + \frac{1}{A_R}\right) + \frac{D_2}{2}\left(\frac{Y + Y_L + \frac{Y_L+Y_R}{2}}{A_L} + \frac{Y + Y_R + \frac{Y_L+Y_R}{2}}{A_R}\right) \tag{A.7}$$

here Y is the horizontal hit location in the neutron bar, Y_R is the position of right PMT, and Y_L is the position of the left PMT. Y is obviously dependent on both C and D but this is ignored as higher order.

While there were many quasi-elastic events in which the interaction was in the first plane, and some where it was in the second plane, the later planes were less often the plane of first interaction. By using quasi-elastic events the first two

planes were corrected for amplitude dependence. These bars were compared to bars in later planes to fit their amplitude dependence. To do this, the following formula was used, where T_{N+2} is the time of flight for a hadron in the desired plane,

$$T_{N+2} = 2T_{N+1} - T_N \ . \tag{A.8}$$

A.2.4 Energy Calibration

The energy calibration of the neutron arm was not used in this analysis. Initial efforts to do this are presented in Tim Ngo's thesis [72].

A.2.5 Veto Calibration

The veto was calibrated relative to the neutron arm first plane (N1). This calibration was acheived by using events with coincident hits in two veto bars with similar x position in both veto planes. For example, a left(right) veto bar was calibrated relative to a left(right) bar in the other plane. Doing this step by step the entire veto was internally calibrated, using the relative shift between the two veto planes. Figure 4.19 shows that each veto bar covers vertical space with two bars on the other veto plane. These planes were also offset horizontally relative to each other, the coincident region allowed left times and right times to be aligned. This provided an overall, intra-veto calibration and alignment. A central veto detector provided an overall offset compared to the neutron plane one (N1) using coincident events between it and a neutron bar, completing the initial veto offset calibration.

This initial calibration was improved by looking at long events and aligning

the resultant peaks in the veto to those in the neutron detectors at corresponding x position. The horizontal position within the bar can be corrected for, but this would provide resolution beyond that needed due to the interactions before the veto in the shielding, and was not included in this analysis.

These long tracks have hits in many planes within the neutron arm and almost always have hits in the veto as well. These charged tracks were used to align the veto peak with the observed peak in plane one (N1). The relationship between veto amplitude and time was used to correct the time in the veto for this alignment. The relationship in equation A.3 was used, except the veto planes were substituted in for the Nth neutron plane. An example histogram used in the calibration is shown in Figure A.6.

A.3 Neutron Software

The neutron arm software takes the raw data encoded in coda files and processes it through the decoding, coarse processing, and fine processing to form clusters with position, corrected times, and a calculated track to the target.

The data is first pulled from raw coda files in the process of decoding and analysis. The reference hit, which was read into a specific channel of the F1 TDC, must exist for the event to be decoded. The decoding process loops through all TDC and ADC channels, and creates independent arrays of hits for raw analysis. These include the corrections to change the PMT values from channels into time, but does not allow the determination of mean time or horizontal position. An offset

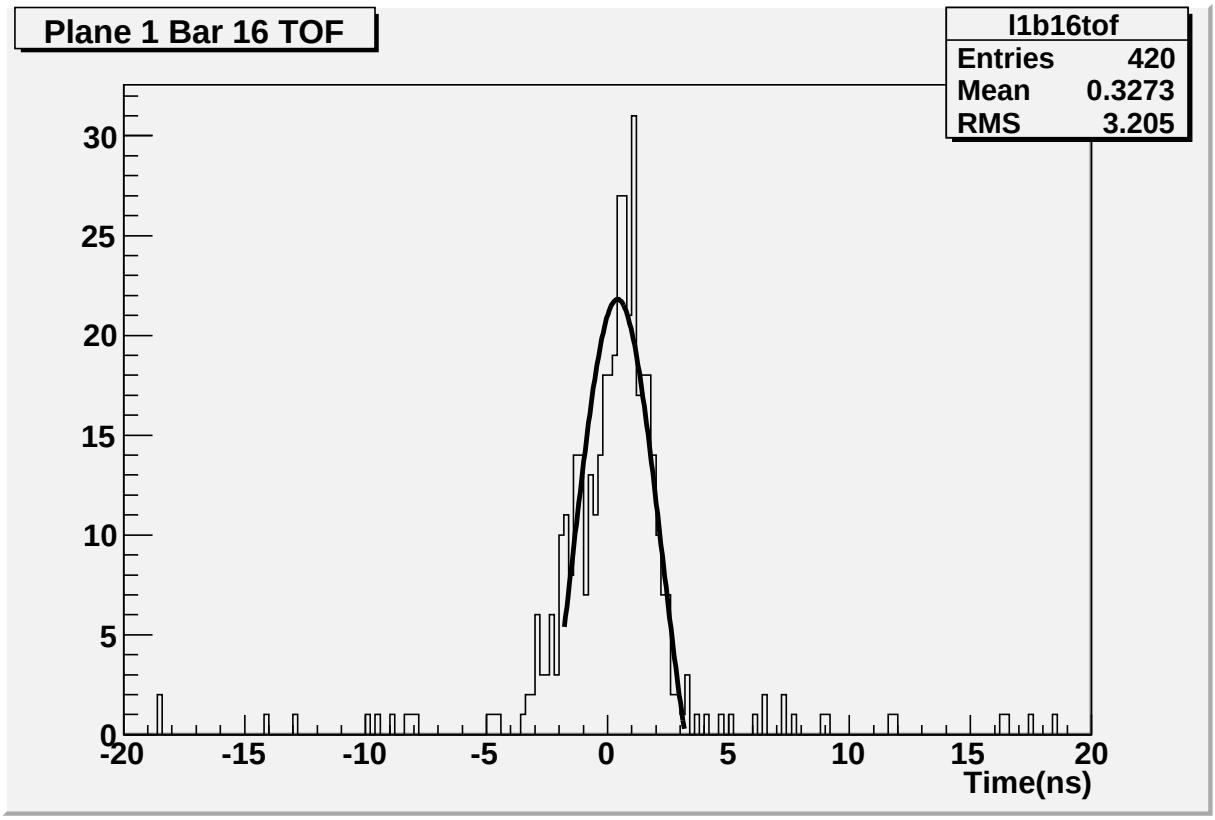

Figure A.6: Calibration of the veto time for the left veto plane 1 bar 16.

is applied to the PMT time (t_{off}) to correct the time relative to the reference time

$$t_{off} = t_{ref} \pm W * t_{res} \ . \tag{A.9}$$

In this formula $+(-)$ is selected when the difference between time and reference time is greater(less) than $+(-)$ half of W, the maximum number of channels in the F1 TDC. The trigger provides a delayed signal to serve as this reference time (t_{ref}). Because of this all neutron arm times are given compared to the trigger time (see NA trigger discussion in section 4.7). t_{res} is the resolution, which was 0.118 ns for the F1 TDC. The F1 TDC was constantly acquiring hits, keeping track of the information in each channel relative to the reference time which was determined by the trigger time. The trigger also determined when the TDC was read. The total number of channels in the F1 TDC (W) is 135558. The PMT time also included the time offsets, read in from the database. All indices are separate at this stage, even for ADC and TDC information for the same PMT.

In the coarse processing, the hits were sorted by bar number and value. The hits were looped through, each PMT time was checked if it was within a limited range, and the existence of ADC and TDC hits for both PMTs for a bar was checked. Hits that pass these checks were considered "complete". At this stage the mean time was corrected for the amplitude correction. This is also where the mean time and the horizontal position of a hit were calculated. The equations for the quantities

calculated during this processing are

$$\begin{aligned} t_{diff} &= \frac{(t_r - t_l)}{2} \\ t_{mean} &= \frac{(t_r + t_l)}{2} \\ y_t &= t_{diff} c_n \\ A_{bar} &= \sqrt{A_l * A_r} \ . \end{aligned} \tag{A.10}$$

Here t_{mean} is the mean time of the hit (and t_l and t_r are corrected left and right times), while t_{diff} is the difference between times of hits in the left and right PMTs. This difference allows the calculation of the horizontal position ($y = y_t + y_{offset}$) of the hit. The constant c_n is the propagation speed of the signal within the bar. Also, A_l and A_r are the left and right amplitudes, respectively, while A_{bar} gives the "energy" for the full bar.

The last step of the neutron arm decoding was the fine processing. The horizontal position of the hit is checked to see if it exists within the neutron arm. After this check, the clusters are created. This is done by sorting the hits and then looping through hits with each hit placed in only one cluster. In this loop, the first hit is put into a cluster, the AddNeigbors method is called (recursively) which collects (and removes from further consideration) neighboring (in time and position) hits. A hit is classified as a neighbor if it is one bar away and within 10 ns. These clusters are then sorted by "energy". A track is created from the cluster (using only the initial hit information) back to the target, and this is used further in analysis. The path length and momentum direction variables (but momentum is not constructed at this stage) are also created. The time window of 10 ns is large relative to the ¡

0.5 ns resolution. Various improvements to the cluster algorithm were investigated, but none of them significantly changed the number of clusters within 20 ns of the expected neutron time of flight, and thus were not included in the analysis.

A.4 Veto Analysis

As previously described (section 4.6.2), the veto was made up of two planes of detectors with 48 detectors per plane. These detectors were segmented into left and right veto counters, providing a total of 192 separate PMTs which form the veto detector. The two veto planes were also shifted vertically and horizontally relative to eachother [72]. This vertical and horizontal segmentation improved the localization of veto detector hits for association with neutron detector hits. Because of the shift between the two planes, the edges of the neutron detector were only covered by a single plane of veto, which reduced the detection efficiency of the veto and hence provided different charge identification efficiency in these edges compared to the central region of the neutron arm. These edges were removed in the analysis presented in this thesis.

The horizontal segmentation of the veto detectors allowed for the identification of charged hits in the neutron detectors based upon horizontal position of the cluster. If the hadron hit was far to one side of the detector, than a charged identification in the veto on the other side of the detector would not identify a charged hadron. Figure A.10 shows this, where the time of the hit relative to the neutron detectors and the horizontal position of the hit within the neutron detector are plotted. Only

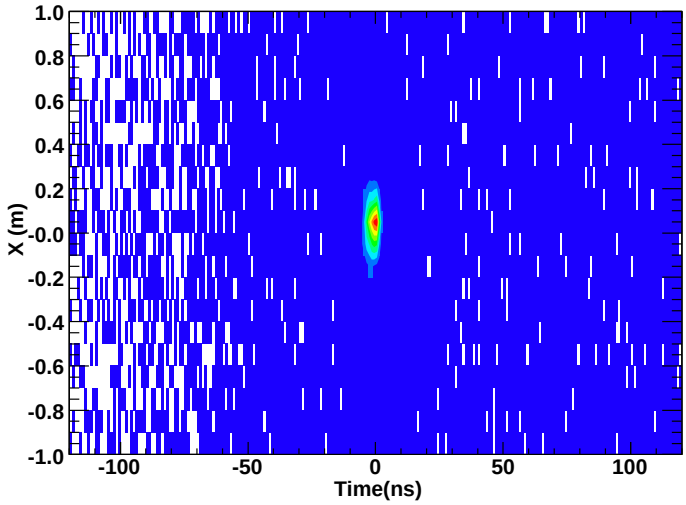

Figure A.7: Plot of X position in the veto subtracted by the X position in the neutron arm versus Δt. These are for quasi-elastic hits in the neutron arm. Plotted on the x axis is the time difference between the neutron arm and the veto arm. This identifies a region of 0.3-0.5 m to consider in the veto detector to identify charge hits.

veto bars within a vertical region were considered as hits to identify a charged hadron (see figure A.7).

The veto dead-time was different for the individual veto counters. This was determined by measuring the least amount of time between sequential hits. For analysis, only a single value was used for a set of bars, this is shown in Table A.4. The deadtime for individual bars could be 40-120 ns.

The veto detection efficiency depended on the horizontal, time, and amplitude cuts used to identify charged particles. Many events in this deadtime region were low amplitude. Since charged particles arrived within the coincidence time region, when the ADC gate was active, these low amplitude events were not events where an earlier event masked the veto hit from the charged particle. Figure A.8 shows the time

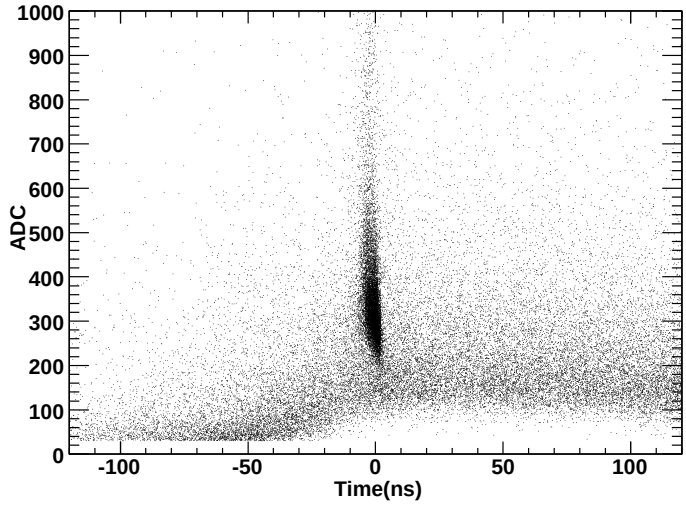

Figure A.8: Plotted is the time difference between the veto hit and the neutron arm hit for a single veto plane versus the amplitude in the veto bar. This figure shows all bars in the plane. The gate is seen to start arround 40 ns before the coincidence hit in the neutron arm. The deadtime of the various veto detectors is between 40 and 110 ns. During this dead time, the hits are identified as charged if the amplitude is above 200. For a region of ± 10 ns around 0, all events are identified as charged.

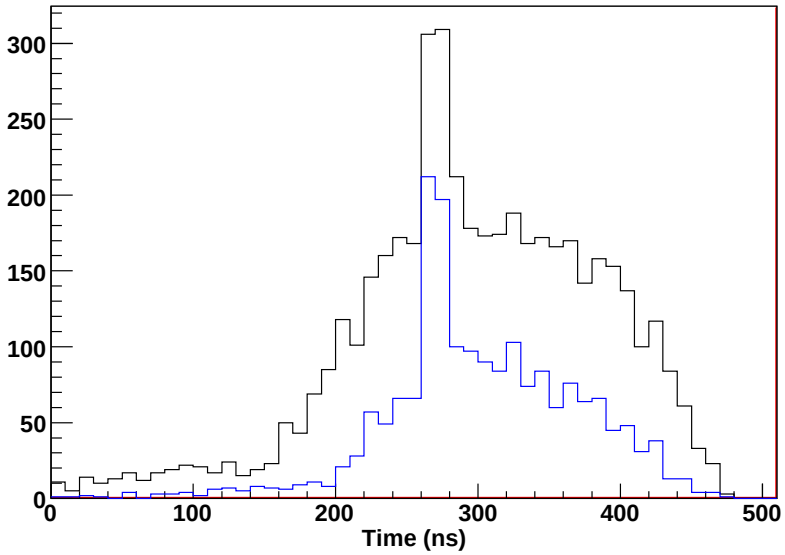

Figure A.9: Plot showing the rate both with and without a 200 channel ADC cut for the veto detector L1-14. The ADC cut rate is in blue. The window between 300 and 350 ns was used to calculate the rate. This rate is in kHz.

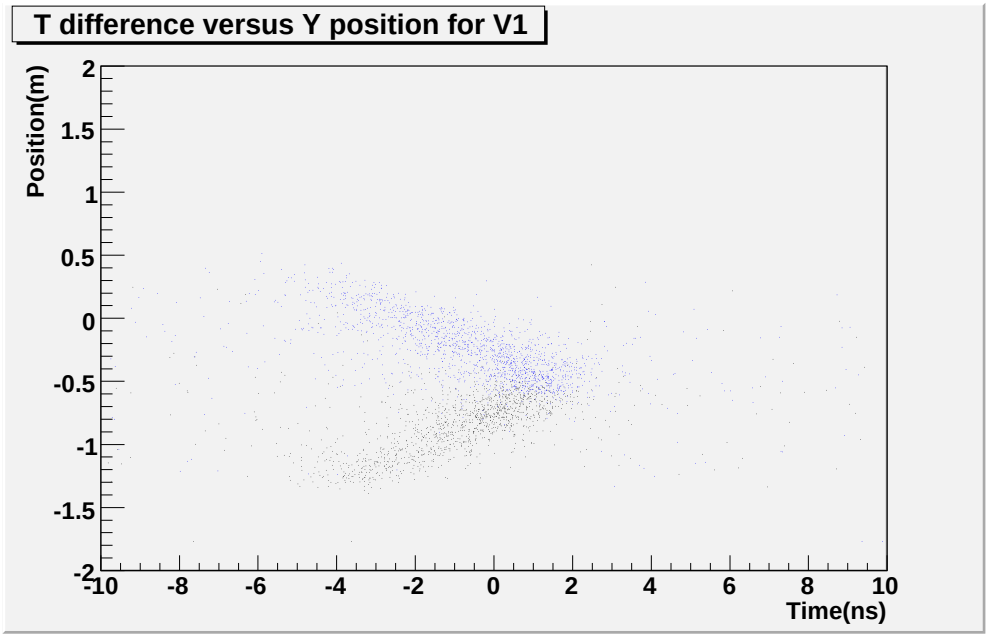

Figure A.10: Plot of hits within the Veto detector. Colors are given to show coincidence between the two separate halves of the V1 veto detector.

versus amplitude, and the charge identification selection mechanism. By requiring an amplitude for the hit, the effective rate in the veto detector was decreased (Figure A.9). Using this technique, the combined veto detector efficiency was measured to be 95%.

Identifier	Date	Comment	Change
new_crate19	May 6		Large, same as 19
new_crate23	May 3		hatsv22:2002 S0
new_crate23	May 3		Same
new_crate22	May 3		Large
new_crate21	May 3		Large
new_crate20	May 3		hatsv22:2002 S0
new_crate19	Apr 29		PS1:2004 S5 + S9 and PS1:2004 S9 + S11
new_crate18	Apr 29	4335-4338	PS1:2004 S5 + S9 + S11 + PS1:2004 S9
new_crate17	Apr 29		No Change
new_crate16	Apr 23	4151	PS1:2002 S9 and PS1:2004 S9
new_crate15	Apr 23		Small?
new_crate14	Apr 19	4068	Large
new_crate13	Apr 19		PS1:2002 S9
new_crate12	Apr 18	4050?	Small
new_crate11	Apr 17	4016	Small
new_crate10	Apr 17		Large
new_crate9	Apr 17		PS1:2004 S11 + S15 + S9 +S10
045.set	Apr 12		PS1:2002 S14 and PS1:2004 S11 + S15
new_crate8	Apr 6	3714	S1:2002 S14 + S11
new_crate7	Apr 4		PS1:2002 S14
new_crate6	Apr 4		Large
new_crate6.set	Apr 4	3665	Same
new_crate5.set	Apr 4		Large
new_crate5	Apr 4		Large
new_crate4	Apr 4		
new_crate4.set	Apr 4		Large
new_crate3.set	Apr 3		Large
044_new.set	Apr 3	3621	Large
006_new.set	Apr 3		Large
006_crate3.set	Apr 3		Large
006.set	Apr 3		Large
044	Apr 1	3570	Same
043	Mar 24	3320s/3330s	Large
042	Mar 23		Large
041	Mar 23	3290/3270	Large
040	Mar 22	3268	Large
039	Mar 22		Only PS1:2002 S14
03-04-2006	Mar 15	3016?	Large
038	Mar 1	2477	Large

Table A.2: Table of the list of high voltage changes (HV) for the neutron arm in the E02-013 experiment.

Bar Number	Veto Plane 1	Veto Plane 2
Right	120 ns	100 ns
Left	65 ns	65 ns

Table A.3: A table showing the deadtime region for a set of veto detectors. This was selected as the maximum for that set of detectors.

Number of Events	V1 only	V1 with > 1 V1	V2 with > 1 V1
0	35.5%	92.7%	08.5%
At least 1	59.7%	06.8%	84.0%
At least 2	04.4%	00.4%	06.8%

Table A.4: A table of the correlation beetween hits in Veto plane 1 and Veto plane 2. The is for all events within a single run in kinematic 2A (3190).

Appendix B

Error Analysis

In the measurement of the electric form factor of the neutron at $Q^2 = 3.5$ GeV^2 statistical uncertainty is the main component of the error. The double polarization technique removes some sources of systematic uncertainty (as described in section 3.3). Due to the small asymmetry, a large statistical sample is required. The primary cause of the small asymmetry is the small size of G_E^n.

The error analysis for E02-013 entails propagation of correlated and uncorrelated systematic and statistical uncertainties for the equations used to calculate G_E^n from the measured quantites. Equation 5.43 gives the factors that contribute to G_E^n. The uncertainty in a few of these factors give the most important contributions to the final precision of the G_E^n measurement.

For the propagation of the uncertainties, standard error techniques are used [94]. Assuming the errors are uncorrelated the expression to determine the uncertainty in a function q which depends on the components $x, ..., z$ is

$$\delta q = \sqrt{\left(\frac{\partial q}{\partial x}\delta x\right)^2 + ... + \left(\frac{\partial q}{\partial z}\delta z\right)^2}\ . \tag{B.1}$$

When q is proportional to the product or quotient of the components,

$$\frac{\delta q}{q} = \sqrt{\left(\frac{\delta x}{x}\right)^2 + ... + \left(\frac{\delta z}{z}\right)^2}\ . \tag{B.2}$$

The correlated systematic errors also contribute to the final uncertainty. As an example, there were not independent measurements of polarization for every run, so

the systematic error was defined to be the same fractional error as the polarization after the summation, rather than being included in the summation error calculation (equation 5.47). Explicit discussion of the error analysis using formula B.1 follows.

For statistical error (with large statistics), assuming a Poisson distribution, the formula

$$\frac{\delta N}{N} = \frac{1}{\sqrt{N}} \tag{B.3}$$

is used, where N is the pertinent statistics. For small asymmetries and large statistics method of determination of the uncertainty is valid [81]

$$\delta A \approx \frac{1}{\sqrt{N}} - \frac{(N^+ - N^-)^2}{N^{\frac{5}{2}}} \approx \frac{1}{\sqrt{N}} \ . \tag{B.4}$$

The formula B.4 is used to determine the statistical error in empirically measured asymmetries like the raw accidental background asymmetry and raw neutron asymmetry. The statistical uncertainty for quasi-elastic event counts, background counts, and other counts is determined using equation B.3.

The following dilution factors, polarizations, and asymmetry corrections are used in the calculation of the physical asymmetry (equation 5.43): D_{back}, D_{N_2}, A_{back}, $D^p_{N_2}$, A_{sum}, D_p, D^p_n, P_n, P_{beam}, $P_{^3He}$ (for description see below). Some of these depend on the same sources of uncertainty. Common sources of uncertainty in these factors and corrections are a systematic uncertainty due to the charge determination in the accidental background technique (see section 5.5.1) and statistical uncertainties due to the raw neutral counts and the raw background counts. While the systematic uncertainty due to the charged to uncharged background ratio is a component of almost all dilutions and corrections, the small number of raw back-

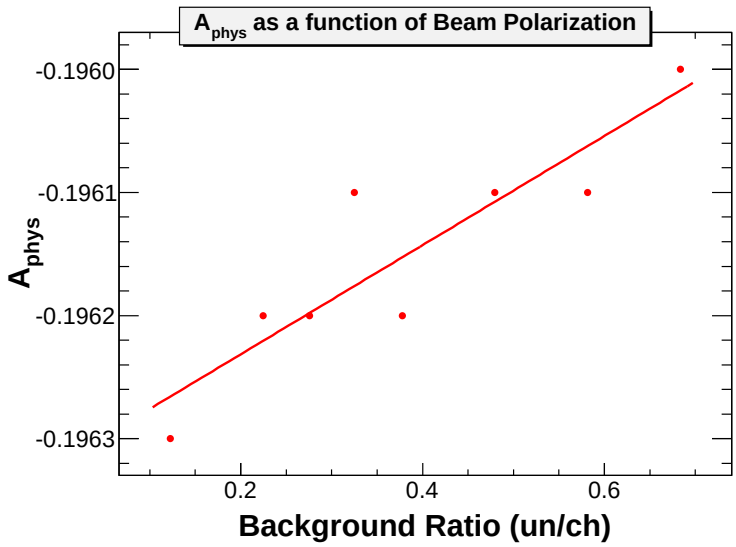

Figure B.1: The physical asymmetry as the accidental background ratio of charged to uncharged used in the calculation is changed. This figure shows that the dependence on this ratio is very small, with an estimated fractional uncertainty on the accidental background charge ratio of 20%. This esimated fractional uncertainty corresponds to a fractional uncertainty of less than 0.2%. Plotted is a linear fit, showing the small dependence. This is for an analysis of Kinematic 2(b).

ground makes it of minimal importance. This is observed in Figure B where the change of neutron physical asymmetry as a function of the charge ratio of the background is plotted for kinematic 2. This ratio will be treated as a constant for the rest of this error analysis. The value for this ratio and accidental background counts is presented in Table B.3.

As described in section 4.4.2 the polarization changes run to run, and a modified asymmetry is calculated on a run per run basis, and then used in a weighted sum for the entire kinematic (as derived in Appendix C). The only components which change significantly on a per run basis are the target polarization and neutron purity factor. The neutron purity factor and the rest of the dilutions are corrected for after

the summation (see equation 5.48)

$$A_{sum} = \frac{\sum_i \frac{A_{raw,i}}{P_{^3He,i}} N_i P^2_{^3He,i}}{\sum_i N_i P^2_{^3He,i}} \ . \tag{B.5}$$

The factor A_{back} can be found by using equation

$$A_{back} = \frac{N^+_{back} - N^-_{back}}{N \langle P_{^3He} \rangle} = A_{back,raw} \frac{N_{neut,back}}{N \langle P_{^3He} \rangle} \ . \tag{B.6}$$

The accidental background asymmetry correction contributes to the statisical uncertainty through the counts in the raw accidental background and quasi-elastic samples and through the accidental background asymmetry. As described in section 5.5.1, the neutral accidental background is related to the raw accidental background by $N_{neut,back} = f_{back} N_{back}$. Additionally, it contributes to the systematic uncertainty through the target polarization.

The polarization of the target and nucleus and beam are presented in sections 4.3 and 4.4.2 and in [39]. The target polarization ($P_{^3He}$) uncertainty is correlated between kinematics 3, 4, and 2(b). As mentioned in 5.7.1, the values for the polarizations of the protons and neutron within the helium nucleus depend on the theoretical model used to calculate the nuclear corrections. Changes in these values will be correlated. The value used for the beam polarization (P_{beam}) and systematic uncertainty is arrived at from inspecting Table 4.2.

The dilution caused by the accidental background (equation 5.38) is written as

$$D_{back} = 1 - \frac{N_{neut,back}}{N} \ . \tag{B.7}$$

The sources of statistical uncertainty are the counts of the raw accidental background and quasi-elastic samples, similar to the accidental background asymmetry

correction.

The dilution from the nitrogen in the neutron sample (equation 5.40 gives the method to properly calculate this) can be written as

$$D_{N_2} = 1 - \frac{N_{N_2}}{N - N_{neut,back}} \ , \tag{B.8}$$

with a dependence on the uncertainties in the constants shown in Table B.1. The dominant sources of systematic uncertainty in this factor are from the densities for N_2 in the ^{3}He target and in the reference cell. The dominant source of statistical uncertainty is due to the nitrogen quasi-elastic events and background. The uncertainties for this dilution were propagated using equation B.1. The results for this error analysis are also presented in Table B.1. This uncertainty is treated as independent from the other uncertainties, although there is a small contribution from the ^{3}He quasi-elastic sample.

The dilution of the protons in the neutron sample (equation 5.32) can be expressed as

$$D_n = 1 - \frac{N_{proton}}{N - N_{neut,back} - N_{N_2}} \ . \tag{B.9}$$

Here the sources of uncertainty are statistical from the background, charged quasi-elastic, neutral quasi-elastic in H_2, N_2 and ^{3}He, and systematic from the technique and model. It is assumed that the statistical uncertainty from Minuit and the systematic uncertainty from the technique dominates all other sources of error. By considering other analyses, a fractional systematic error of 5% was arrived at. The cited statistical uncertainty is that given by Minuit fitting [30].

Finally, the dilution caused by other final state interactions within the neutron

sample can be expressed as

$$D_{FSI} = 1 - \frac{N_{FSI}}{N - N_{neut,back} - N_{N_2} - N_{proton}} \ . \tag{B.10}$$

Because the dilution due to final state interactions is undetermined but guided by theory [42][88], an estimate is determined for the systematic uncertainty that accounts for the likely values of this dilution.

The proton asymmetry has similar dilutions as the neutral asymmetry, with a couple of important differences. This formula 5.54 is

$$A_{proton} = \frac{1 - D_n}{D_{back} D_{N2}} P_{beam} P_{prot} A_{p,phys} \ . \tag{B.11}$$

The polarization of protons within the nucleus, P_{prot} is provided by theory [89]. The proton physical asymmetry is calculated from the proton form factor ratio as described in equation 5.49:

$$A_{p,phys} = \frac{B\lambda_{proton} + C}{\lambda^2_{proton} + D} \ . \tag{B.12}$$

Here the uncertainty in λ_{proton} is determined from the parameterization [59]. The calculation and uncertainties for the quantities used in the determination of A_{proton} are in Table B.2.

A reminder that the expression for the physical asymmetry is (equation 5.43)

$$A_{phys} = \frac{A_{sum} - A_{back} - A_{proton}}{P_n P_{beam} D_{back} D_{N_2} D_p D_{fsi}} \ . \tag{B.13}$$

By applying equation B.1 to equation 5.43, the statistical and systematic uncertainty of the physical asymmetry are calculated. These results, along with the individual contributions to the uncertainties, are presented in Table **??** for kinematic 2a, Table B.5 for kinematic 2b, Table B.6 for kinematic 3, and Table B.7 for kinematic 4.

	D_{N_2}			$D^c_{N_2}$		
$Q^2 =$	2.5 GeV^2	3.5 GeV^2	1.5 GeV^2	2.5 GeV^2	3.5 GeV^2	1.5 GeV^2
$\rho_{^3He}$	0.164	0.164	0.164	0.164	0.164	0.164
ρ_{N_2}	4.4	3.6	9.1	4.4	3.6	9.1
$Q_{^3He}$	184399	228766	167206	184399	228766	167206
Q_{N_2}	14020	37920	5489	14020	37920	5489
$N_{^3He}$	2089.1	252.9	6969.8	19076.7	3044.2	72525
N_{N_2}	220.5	20.3	668.8	1123.2	175.6	3760.3
D_{N_2}	0.9493	0.9781	0.9473	0.9714	0.9843	0.9715
Statistical	0.0036	0.0051	0.0022	0.0009	0.0012	0.0048
Systematic	0.0047	0.0021	0.0051	0.0027	0.0015	0.0028

Table B.1: A table showing the measurements and error calculations for the nitrogen dilution of the uncharged sample, for all three kinematics. $N_{^3He}$ is the number of background corrected counts for the selected ^3He runs, ρ_{N_2} is the nitrogen density, $Q_{^3He}$ is the total charge of the selected ^3He runs. This calculation is as described in section 5.5.2. Densities are determined by target measurements [62][57][81].

parameter	$Q^2 = 2.5$ GeV^2	$Q^2 = 3.5$ GeV^2	$Q^2 = 1.7$ GeV^2
G_E^p	0.0330 ± 0.0051	0.018 ± 0.004	0.077 ± 0.007
G_M^p	0.1378 ± 0.0049	0.089 ± 0.004	0.262 ± 0.006
$A_{p,phys}$	0.177 ± 0.028	0.185 ± 0.030	0.197 ± 0.021
P_{prot}	-0.1 ± 0.004	-0.1 ± 0.004	-0.1 ± 0.004
P_{beam}	0.835 ± 0.03	0.835 ± 0.03	0.835 ± 0.03
D_{N2}	$0.949 \pm 0.004 \pm 0.005$	$0.978 \pm 0.005 \pm 0.002$	$0.947 \pm 0.002 \pm 0.005$
D_{back}	0.9702 ± 0.0003	0.9731 ± 0.0005	0.9697 ± 0.0002
D_n	$0.806 \pm 0.023 \pm 0.04$	$0.885 \pm 0.047 \pm 0.044$	0.697 ± 0.019
A_{proton}	-0.0009 ± 0.0002	-0.0018 ± 0.0003	-0.0054 ± 0.0007

Table B.2: A table of the errors for the calculation of A_{proton}. The calculation is calculated according to equation 5.54. The uncertainty in G_M^p and G_E^p is determined using a parameterization [59] and the propagation of the error is according to equation B.1. Parenthesis is used to identify the systematic uncertainty.

The uncertainty in the ratio of neutron form factors, or λ, is determined using equation B.1 and 5.55. This is a straightforward calculation [38], but the value for λ is only determined for the central value of Q^2. To determine the value for the electric form factor of the neutron, equations B.2 and 5.58 were used. The results are displayed in Table B.4.

parameter	$Q^2 = 2.5$ GeV^2	$Q^2 = 3.5$ GeV^2	$Q^2 = 1.7$ GeV^2
Hadron Ratio	0.325 ± 0.065	0.26 ± 0.04	0.33 ± 0.05
Hadons	2495	4201	2762
Neutral	1883.2	1092.3	911.5
Charged	611.8	3108.7	1850.5

Table B.3: A table for all three kinematics showing the measurements for the charged and uncharged background and the uncertainty in the background ratio.

parameter	$Q^2 = 2.5$ GeV^2	$Q^2 = 3.5$ GeV^2	$Q^2 = 1.7$ GeV^2
GEn/GMn	-0.2219	-0.2434	-0.1991
Error	$\pm 0.0325 \pm 0.0293$	$\pm 0.0457 \pm 0.0202$	$\pm 0.0183 \pm 0.0330$
GMn	-0.0954 ± 0.0019	-0.0556 ± 0.0011	-0.1636 ± 0.0032
GEn	0.0212	0.0135	0.0326
Error	$\pm 0.0031 \pm 0.0028$	$\pm 0.0025 \pm 0.0012$	$\pm 0.0030 \pm 0.0054$

Table B.4: A table of the errors for the calculation of G_E^n. Uncertainty in the ratio of form factors was calculated from the physical asymmetry as expressed in section 5.6 and Table 5.8 and Table 5.7. The uncertainty in G_M^n is determined from a parameterization [59] and propagation of the error is according to equation B.1.

quantity	value	σ_{stat}	contrib. A_{phys}	σ_{syst}	contrib. A_{phys}
A_{meas}	-0.0446	± 0.0055	0.024	–	-
$P_{^3He}$	0.4359	–	-	± 0.02	0.018
$A_{back,raw}$	0.0279	± 0.0004	0.00004	–	-
D_{FSI}	0.95	–	-	± 0.01	0.002
D_n	0.806	± 0.023	0.005	± 0.040	0.008
$A_{p,phys}$	0.177	–	-	± 0.028	0.0004
P_{beam}	0.835	–	-	± 0.03	0.007
N_{total}	33001	± 182	0.0001	–	-
N_{back}	4201	± 65	0.0003	–	-
P_n	0.86	–	-	± 0.02	0.004
P_{prot}	-0.100	–	-	± 0.004	0.0002
D_{N_2}	0.949	± 0.0036	0.0007	± 0.0047	0.0009
A_{phys}	-0.191	-	± 0.024	-	± 0.022

Table B.5: A table of the uncertainties that contribute to the physical asymmetry (A_{phys}). The contributions are calculated and contribute to the physical asymmetry precision as determined by equation B.1. This table shows the errors for $Q^2 = 2.5$ GeV^2.

quantity	value	σ_{stat}	A_{phys} contrib.	σ_{syst}	A_{phys} contrib.
A_{meas}	-0.0358	± 0.0080	0.029	–	-
$P_{^3He}$	0.477	–	-	± 0.02	0.0109
$A_{back,raw}$	-0.0233	± 0.0004	0.00004	–	-
D_{FSI}	0.95	–	-	± 0.01	0.0013
D_n	0.885	± 0.047	0.0054	± 0.044	0.0051
$A_{p,phys}$	0.182	–	-	± 0.030	0.0005
P_{beam}	0.835	–	-	± 0.03	0.0046
N_{total}	15319	± 124	0.0001	–	-
N_{back}	2748	± 52	0.0003	–	-
P_n	0.86	–	-	± 0.02	0.0030
P_{prot}	-0.1	–	-	± 0.004	0.0001
D_{N_2}	0.978	± 0.0051	0.0006	± 0.0021	0.0003
A_{phys}	-0.132	-	± 0.030	-	± 0.013

Table B.6: A table of the uncertainties that contribute to the physical asymmetry (A_{phys}). The contributions are calculated and contribute to the physical asymmetry precision as determined by equation B.1. This table shows the errors for $Q^2 = 3.5$ GeV^2.

quantity	value	σ_{stat}	A_{phys} contrib.	σ_{syst}	A_{phys} contrib.
A_{meas}	-0.0569	± 0.0031	0.0144	–	-
$P_{^3He}$	0.4883	–	-	± 0.02	0.0218
$A_{back,raw}$	0.0007	± 0.00001	0.0000	–	-
D_{FSI}	0.95	–	-	± 0.01	0.0027
D_n	0.696	± 0.018	0.0043	± 0.035	0.0112
$A_{p,phys}$	0.1969	–	-	± 0.0207	0.0013
P_{beam}	0.835	–	-	± 0.03	0.0096
N_{total}	105529	± 325	0.0001	–	-
N_{back}	17834	± 134	0.0003	–	-
P_n	0.86	–	-	± 0.02	0.0059
P_{prot}	-0.1	–	-	± 0.004	0.0005
D_{N_2}	0.9473	± 0.0022	0.0006	± 0.0051	0.0013
A_{phys}	-0.2537	-	± 0.0150	-	± 0.0272

Table B.7: A table of the uncertainties that contribute to the physical asymmetry (A_{phys}). The contributions are calculated and contribute to the physical asymmetry precision as determined by equation B.1. This table shows the errors for $Q^2 = 1.7$ GeV^2.

Appendix C

Calculations

C.1 Asymmetry Best Value

The formula to determine the best value of a set of gaussian measurements is the one presented in undergraduate textbooks, and the method to determine the best value of a distribution is also presented, but the formula for an asymmetry is not. The method used here is the maximum likelihood method. For this asymmetry, there are two Poisson distributions of N_+ and N_-.

A Poisson distribution is decribed by[94]

$$P_\mu(\nu) = e^{-\mu}\frac{\mu^\nu}{\nu!} \ , \tag{C.1}$$

where ν is the number of occurrences and μ is the expected number of occurrences. The asymmetry is completely described by the number of positive counts with positive and negative helicity, N_+^i and N_-^i (i is the ith experiment). This gives the likelihood

$$L = P_{\mu_+}(N_+^i) \times P_{\mu_-}(N_-^i) \times \cdots \ . \tag{C.2}$$

The μ, or expected number of occurrences, for some run, is identified as

$$\mu_\pm = \left(N_+^e + N_-^e\right)\frac{1 \pm A^e}{2} = \frac{N_+^e + N_-^e \pm \left(N_+^e - N_-^e\right)}{2} = N_\pm^e \ . \tag{C.3}$$

Here the index e gives the expected value for that given run period, while i is the

ith measured value. The expected value of counts for + and − give the best value for the asymmetry.

There are many measurements (given by index i), all having their own best value for the counts to give the best asymmetry. This allows us to have

$$\mu_{\pm,i} = \kappa_{\pm,i} = \kappa_i \frac{1 \pm A_i^e}{2} \ , \tag{C.4}$$

where κ is the correct N to get the best asymmetry. Following the previous work for the Poisson distribution

$$\sum \frac{\partial lnL}{\partial A} = (-1 + \frac{N_{\pm i}}{\mu_{\pm i}})(\pm \frac{\kappa_i P_i}{2}) = \sum \frac{N_{i+} P_i}{1 - AP_i} - \frac{N_{i-} P_i}{1 + AP_i} = 0 \ . \tag{C.5}$$

Using the standard expansion

$$(1 \pm AP_i)^{-1} = 1 \pm P_i A \ , \tag{C.6}$$

the relationship

$$\sum P_i (N_{i+} - N_{i-}) = -\sum P_i^2 N_i A \tag{C.7}$$

is arrived at, which gives

$$A = \frac{-\sum P_i (N_{i+} - N_{i-})}{\sum P_i^2 N_i} \ . \tag{C.8}$$

Putting it into a more recognizable form

$$A = \frac{-\sum P_i^2 N_i \frac{A_i}{P_i}}{\sum P_i^2 N_i} \ , \tag{C.9}$$

with the corresponding statistical uncertainty.

Appendix D

Jefferson Laboratory E02-013 Collaboration

The collaboration list for the E02-013 experiment is on the next page.

S. Abrahamyan,[1] B. Craver,[2] A. Kelleher,[3] A. Kolarkar,[4] J. Miller,[5] S. Riordan,[2,6] G. Cates,[2] N. Liyanage,[2] B. Wojtsekhowski,[7] A. Acha,[8] K. Allada,[4] B. Anderson,[9] K. A. Aniol,[10] J.R.M. Annand,[11] J. Arrington,[12] T. Averett,[3] A. Beck,[13] S. Beck,[13] W. Boeglin,[8] H. Breuer,[5] J.R. Calarco,[14] A. Camsonne,[7] J.P. Chen,[7] E. Chudakov,[7] L. Coman,[8] B. Crowe,[15] F. Cusanno,[16] D. Day,[2] P. Degtyarenko,[7] C. Dutta,[4] C. Ferdi,[17] C. Fernandez,[18] R. Feuerbach,[7] L. Fraile,[18] G. Franklin,[6] S. Frullani,[16] S. Fuchs,[3] F. Garibaldi,[16] N. Gevorgyan,[1] R. Gilman,[19] A. Glamazdin,[20] J. Gomez,[7] K. Grimm,[3] J.-O. Hansen,[7] D. Higinbotham,[7] R. Holmes,[21] T. Holmstrom,[3] D. Howell,[22] C.W. de Jager,[7] X. Jiang,[19] M.K. Jones,[7] J. Katich,[3] L. Kaufman,[23] M. Khandaker,[24] J.J. Kelly,[5] W. Korsch,[4] J. LeRose,[7] R. Lindgren,[2] J. Lopez,[18] P. Markowitz,[8] D.J. Margaziotis,[10] S. Mayilyan,[1] K. McCormick,[25] Z.-E. Meziani,[26] R. Michaels,[7] B. Moffit,[3] S. Nanda,[7] V. Nelyubin,[27] T. Ngo,[10] D.M. Nikolenko,[28] B. Norum,[2] L. Pentchev,[3] C.F. Perdrisat,[3] E. Piasetzky,[13] R. Pomatsalyuk,[20] D. Protopopescu,[11] A. Puckett,[29] V.A. Punjabi,[24] X. Qian,[22] Y. Qiang,[29] B. Quinn,[6] I. Rachek,[28] R. Ransome,[19] P. Reimer,[12] B. Reitz,[7] J. Roche,[7] D. Rohe,[30] G. Ron,[13] O. Rondon,[2] G. Rosner,[11] A. Saha,[7] M. Sarsian,[8] B. Sawatzky,[26] J. Segal,[7] A. Semenov,[9] I. Semenova,[9,7] M. Shabestari,[2] A. Shahinyan,[1] Yu. Shestakov,[28] J. Singh,[2] S. Širca,[29] S. Stepanyan,[31] V. Stibunov,[32] V. Sulkosky,[3] S. Tajima,[2] Al Tobias,[2] J. Udias,[18] G. Urciuoli,[16] B. Vlahovic,[15] H. Voskanyan,[1] K. Wang,[2] F. Wesselmann,[24] S. Wood,[7] J. Wright,[25] H. Yao,[22] and X. Zhu[29]

(The Jefferson Lab E02-013 Collaboration)

[1] *Yerevan Physics Institute, Yerevan 375036, Armenia*
[2] *University of Virginia, Charlottesville 22903*
[3] *College of William and Mary, Williamsburg, VA 23187*
[4] *University of Kentucky, Lexington, Kentucky 40506*
[5] *University of Maryland, College Park, Maryland 20742*
[6] *Carnegie Mellon University, Pittsburgh, Pennsylvania 15213*
[7] *Thomas Jefferson National Accelerator Facility, Newport News, Virginia 23606*
[8] *Florida International University, Miami, Florida 33199*
[9] *Kent State University, Kent , Ohio 44242*
[10] *California State University Los Angeles, Los Angeles, CA 90032*
[11] *University of Glasgow, Glasgow G12 8QQ, Scotland, U.K.*
[12] *Argonne National Laboratory, Argonne, Illinois 60439*
[13] *Tel Aviv University, Tel Aviv, 69978 Israel*
[14] *University of New Hampshire, Durham, NH 03824*
[15] *North Carolina Central University, Durham, North Carolina 27707*
[16] *INFN, Sezione di Sanitá and Institute Superiore di Sanitá , I-00161 Rome, Italy*
[17] *Université Blaise Pascal/IN2P3, F-63177 Aubière, France*
[18] *Madrid University, Madrid, Spain*
[19] *Rutgers, The State University of New Jersey, Piscataway, NJ 08854*
[20] *Kharkov Institute of Physics and Technology, Kharkov 61108, Ukraine*
[21] *Syracuse University, Syracuse, New York 13244*
[22] *Duke University and TUNL, Durham, North Carolina 27708*
[23] *University of Massachusetts, Amherst, Massachusetts 01003*
[24] *Norfolk State University, Norfolk, Virginia 23504*
[25] *Old Dominion University, Norfolk, Virginia 23529*
[26] *Temple University, Philadelphia, Pennsylvania 19122*
[27] *St. Petersburg Nuclear Physics Institute, Gatchina, 188350, Russia*
[28] *Budker Institute for Nuclear Physics, Novosibirsk 630090, Russia*
[29] *Massachusetts Institute of Technology, Cambridge, MA 02139*
[30] *Universität Basel, CH-4056 Basel, Switzerland*
[31] *Kyungpook National University, Taegu City, South Korea*
[32] *Institute for Nuclear Physics, Tomsk ???, Russia*

Bibliography

[1] *Techniques for Nuclear and Particle Physics Experiments: A How-to Approach.* Oxford University Press, 2009.

[2] Sergey Abrahamyan. personal communication, 2006-2009.

[3] J. Alcorn et al. Basic Instrumentation for Hall A at Jefferson Lab. *Nucl. Instrum. Meth.*, A522:294–346, 2004. doi: 10.1016/j.nima.2003.11.415.

[4] C. Amsler et al. Review of particle physics. *Phys. Lett.*, B667:1, 2008. doi: 10.1016/j.physletb.2008.07.018.

[5] Hall A analyzer. http://hallaweb.jlab.org/root/index.html.

[6] H. Arenhovel. On Deuteron breakup by electrons and the momentum distribution of nucleons in the deuteron. *Nucl. Phys.*, A384:287–301, 1982. doi: 10.1016/0375-9474(82)90336-0.

[7] H. Arenhovel. On the determination of the electric neutron form-factor in d (e polarized), e-prime (n polarized) p. *Phys. Lett.*, B199:13–16, 1987. doi: 10.1016/0370-2693(87)91454-7.

[8] H. Arenhovel, W. Leidemann, and E. L. Tomusiak. The role of the neutron electric form-factor in d (e, e- prime n) n including polarization observables. *Z. Phys.*, A331:123–138, 1988.

[9] H. Arenhovel, W. Leidemann, and E. L. Tomusiak. General formulae for polarization observables in deuteron electrodisintegration and linear relations. *Few Body Syst.*, 15:109–127, 1993. doi: 10.1007/BF01076428.

[10] R. G. Arnold, Carl E. Carlson, and Franz Gross. Polarization transfer in elastic electron scattering from nucleons and deuterons. *Phys. Rev.*, C23:363, 1981.

[11] J. Becker et al. Determination of the neutron electric form factor from the reaction he-3(e,e' n) at medium momentum transfer. *Eur. Phys. J.*, A6:329–344, 1999.

[12] Andrei V. Belitsky, Xiang-dong Ji, and Feng Yuan. A perturbative qcd analysis of the nucleon's pauli form factor f2(q**2). *Phys. Rev. Lett.*, 91:092003, 2003.

[13] J. Bermuth et al. The neutron charge form factor and target analyzing powers from he-3(pol.)(e(pol.),e' n) scattering. *Phys. Lett.*, B564:199–204, 2003.

[14] M. S. Bhagwat, I. C. Cloet, and C. D. Roberts. Covariance, Dynamics and Symmetries, and Hadron Form Factors. 2007.

[15] R. Bijker and F. Iachello. Re-analysis of the nucleon space- and time-like electromagnetic form factors in a two-component model. *Phys. Rev.*, C69: 068201, 2004.

[16] B. Blankleider and R. M. Woloshyn. Quasielastic scattering of polarized electrons on polarized he-3. *Phys. Rev.*, C29:538, 1984.

[17] P. G. Blunden, W. Melnitchouk, and J. A. Tjon. Two-photon exchange in elastic electron-nucleon scattering. *Phys. Rev. C*, 72(3):034612, Sep 2005. doi: 10.1103/PhysRevC.72.034612.

[18] R. Bradford, A. Bodek, Howard Scott Budd, and J. Arrington. A new parameterization of the nucleon elastic form factors. *Nucl. Phys. Proc. Suppl.*, 159: 127–132, 2006. doi: 10.1016/j.nuclphysbps.2006.08.028.

[19] Stanley J. Brodsky. Light-front QCD. 2004.

[20] Stanley J. Brodsky and Guy F. de Teramond. Light-front hadron dynamics and AdS/CFT correspondence. *Phys. Lett.*, B582:211–221, 2004. doi: 10.1016/j.physletb.2003.12.050.

[21] Stanley J. Brodsky, Susan Gardner, and Dae Sung Hwang. Discrete symmetries on the light front and a general relation connecting nucleon electric dipole and anomalous magnetic moments. *Phys. Rev.*, D73:036007, 2006. doi: 10.1103/PhysRevD.73.036007.

[22] Matthias Burkardt. Generalized parton distributions and distribution of partons in the transverse plane. 2001.

[23] Matthias Burkardt. Impact parameter space interpretation for generalized parton distributions. *Int. J. Mod. Phys.*, A18:173–208, 2003. doi: 10.1142/S0217751X03012370.

[24] Matthias Burkardt. Some inequalities for the generalized parton distribution E(x,0,t). *Phys. Lett.*, B582:151–156, 2004. doi: 10.1016/j.physletb.2003.12.058.

[25] G. Cates, K. McCormick, B. Reitz, and B. Wojtsekhowshi. Jlab proposal 02-013. 2002.

[26] I. C. Cloet and C. D. Roberts. Form Factors and Dyson-Schwinger Equations. *PoS*, LC2008:047, 2008.

[27] T. De Forest. Off-shell electron nucleon cross-sections. the impulse approximation. *Nucl. Phys.*, A392:232–248, 1983.

[28] M. Diehl. Generalized parton distributions: Recent results. *AIP Conf. Proc.*, 842:294–302, 2006. doi: 10.1063/1.2220251.

[29] M. Diehl. Generalized parton distributions from form factors. *Nucl. Phys. Proc. Suppl.*, 161:49–58, 2006. doi: 10.1016/j.nuclphysbps.2006.08.048.

[30] Minuit documentation. http://wwwasdoc.web.cern.ch/wwwasdoc/minuit/minmain.html.

[31] T. W. Donnelly and A. S. Raskin. Considerations of polarization in inclusive electron scattering from nuclei. *Annals Phys.*, 169:247–351, 1986.

[32] D. Drechsel, O. Hanstein, S. S. Kamalov, and L. Tiator. A unitary isobar model for pion photo- and electroproduction on the proton up to 1-GeV. *Nucl. Phys.*, A645:145–174, 1999. doi: 10.1016/S0375-9474(98)00572-7.

[33] S. Kadlecek T. G. Walker E. Babcock, I. A. Nelson. *Phys. Rev. A*, 71:013414, 2005.

[34] T. Eden et al. Electric form-factor of the neutron from the h-2 (e (polarized), e-prime n (polarized)) h-1 reaction at q**2 = 0.255-(gev/c)**2. *Phys. Rev.*, C50:1749–1753, 1994.

[35] S. Eidelman et al. Review of particle physics. *Phys. Lett.*, B592:1, 2004. doi: 10.1016/j.physletb.2004.06.001.

[36] W. Fabian and H. Arenhovel. Electrodisintegration of deuterium including nucleon detection in coincidence. *Nucl. Phys.*, A314:253–286, 1979. doi: 10.1016/0375-9474(79)90599-2.

[37] Robert Feuerbach. personal communication, 2007.

[38] G.B. Franklin. Gen asymmetry corrections for finite angular acceptance., 2006.

[39] J.L. Friar et al. Neutron polarization in polarized ^{3}he targets. *Phys. Rev. C*, 42:2310–2314, 1990.

[40] S. Galster et al. Elastic electron - deuteron scattering and the electric neutron form-factor at four momentum transfers 5-fm**-2 ¡ q**2 ¡ 14-fm**-2. *Nucl. Phys.*, B32:221–237, 1971. doi: 10.1016/0550-3213(71)90068-X.

[41] Alan Gavalya. personal communication, 2006-2009.

[42] R.J. Glauber. Cross sections in deuterium at high energies. *Physical Review*, 100(1):242–248, October 1955.

[43] D. I. Glazier et al. Measurement of the electric form factor of the neutron at q**2 = 0.3-0.8 (gev/c)**2. *Eur. Phys. J.*, A24:101–109, 2005.

[44] J. Golak, G. Ziemer, H. Kamada, H. Witala, and Walter Gloeckle. Extraction of electromagnetic neutron form factors through inclusive and exclusive polarized electron scattering on polarized he-3 target. *Phys. Rev.*, C63:034006, 2001.

[45] M. Guidal, M. V. Polyakov, A. V. Radyushkin, and M. Vanderhaeghen. Nucleon form factors from generalized parton distributions. *Phys. Rev.*, D72:054013, 2005.

[46] F. Halzen and A. Martin. *Quarks and Leptons.* John Wiley and Sons, 1984.

[47] C. Herberg et al. Determination of the neutron electric form factor in the d(e,e' n)p reaction and the influence of nuclear binding. *Eur. Phys. J.*, A5:131–135, 1999.

[48] Coda homepage. http://coda.jlab.org, .

[49] GEANT homepage. http://geant4.web.cern.ch/geant4/, .

[50] MCEEP homepage. http://hallaweb.jlab.org/software/mceep/mceep.html, .

[51] E. S. Hrycyshyn and L. Krause. *Can. J. Phys.*, 48:2761, 1970.

[52] R. Frisch I. Estermann and O. Stern. Magnetic Moment of the Proton. *Nature*, 132:169–170, 1933. doi: 10.1038/132169a0.

[53] Hall A Information. http://hallaweb.jlab.org.

[54] Xiang-Dong Ji. Gauge invariant decomposition of nucleon spin. *Phys. Rev. Lett.*, 78:610–613, 1997. doi: 10.1103/PhysRevLett.78.610.

[55] C. E. Jones-Woodward et al. Determination of the neutron electric form-factor in quasielastic scattering of polarized electrons from polarized he-3. *Phys. Rev.*, C44:571–574, 1991.

[56] A. Kelleher. *A Measurement of the Neutron Electric Form Factor at Very large Momentum Transfer Using Polarized Electrons Scattering from A Polarized Helium-3 Target.* PhD thesis, College of William and Mary, 2009.

[57] Aidan Kelleher. personal communication, 2006-2009.

[58] J. J. Kelly. Nucleon knockout by intermediate-energy electrons. *Adv. Nucl. Phys.*, 23:75–294, 1996.

[59] J. J. Kelly. Simple parametrization of nucleon form factors. *Phys. Rev.*, C70: 068202, 2004. doi: 10.1103/PhysRevC.70.068202.

[60] F. Klein and H. Schmieden. Electromagnetic nucleon form-factors in the space - like region. *Nucl. Phys.*, A623:323c–332c, 1997.

[61] A. Kolarkar. *Precision Measurements of the Neutron Electric Form Factor at High Momentum Transfers.* PhD thesis, University of Kentucky, 2007.

[62] Ameya Kolarkar. personal communication, 2006-2007.

[63] C. W. Leemann, D. R. Douglas, and G. A. Krafft. The Continuous Electron Beam Accelerator Facility: CEBAF at the Jefferson Laboratory. *Ann. Rev. Nucl. Part. Sci.*, 51:413–450, 2001. doi: 10.1146/annurev.nucl.51.101701.132327.

[64] G. Peter Lepage and Stanley J. Brodsky. Exclusive Processes in Perturbative Quantum Chromodynamics. *Phys. Rev.*, D22:2157, 1980. doi: 10.1103/PhysRevD.22.2157.

[65] Earle L. Lomon. Effect of recent R(p) and R(n) measurements on extended Gari-Kruempelmann model fits to nucleon electromagnetic form factors. *Phys. Rev.*, C66:045501, 2002. doi: 10.1103/PhysRevC.66.045501.

[66] R. Madey et al. Measurements of g(e)(n)/g(m)(n) from the h-2(e(pol.),e' n(pol.))h-1 reaction to q**2 = 1.45-(gev/c)**2. *Phys. Rev. Lett.*, 91:122002, 2003.

[67] A. D. Martin, W. J. Stirling, R. S. Thorne, and G. Watt. Parton distributions for the LHC. *Eur. Phys. J.*, C63:189–285, 2009. doi: 10.1140/epjc/s10052-009-1072-5.

[68] M. Meyerhoff et al. First measurement of the electric form-factor of the neutron in the exclusive quasielastic scattering of polarized electrons from polarized he-3. *Phys. Lett.*, B327:201–207, 1994.

[69] Gerald A. Miller. Light front cloudy bag model: Nucleon electromagnetic form factors. *Phys. Rev.*, C66:032201, 2002.

[70] Gerald A. Miller. Charge Density of the Neutron. *Phys. Rev. Lett.*, 99:112001, 2007. doi: 10.1103/PhysRevLett.99.071802.

[71] Gerald A. Miller. Meson Clouds and Nucleon Electromagnetic Form Factors. 2008.

[72] T. Ngo. *Neutron arm study and calibration for the gen experiment at thomas jefferson national laboratory.* PhD thesis, California State University, 2007.

[73] T. Ngo. Geometry document. 2008.

[74] M. Ostrick et al. Measurement of the neutron electric form factor g(e,n) in the quasifree h-2(e(pol.),e' n(pol.))p reaction. *Phys. Rev. Lett.*, 83:276–279, 1999.

[75] I. Passchier et al. The charge form factor of the neutron from the reaction h-2(pol.)(e(pol.),e' n)p. *Phys. Rev. Lett.*, 82:4988–4991, 1999.

[76] C. F. Perdrisat, V. Punjabi, and M. Vanderhaeghen. Nucleon electromagnetic form factors. 2006.

[77] B. Plaster. *The Neutron Electric Form Factor to Q**2 = 1.45-(GeV/c)**2.* PhD thesis, MIT, 2004.

[78] B. Plaster et al. Measurements of the neutron electric to magnetic form factor ratio g(e(n))/g(m(n)) via the h-2(e(pol.),e' n(pol.))h-1 reaction to q**2 = 1.45-(gev/c)**2. *Phys. Rev.*, C73:025205, 2006.

[79] Igor Rachek. personal communication, 2005.

[80] A. S. Raskin and T. W. Donnelly. Polarization in coincidence electron scattering from nuclei. *Ann. Phys.*, 191:78, 1989.

[81] S. Riordan. *Measurements of the Electric Form Factor of the Neutron at Q**2 = 1.7 and 3.5 (GeV/c)**2.* PhD thesis, Carnegie Mellon University, 2008.

[82] Seamus Riordan. personal communication, 2006-2009.

[83] C. D. Roberts. Hadron Properties and Dyson-Schwinger Equations. *Prog. Part. Nucl. Phys.*, 61:50–65, 2008. doi: 10.1016/j.ppnp.2007.12.034.

[84] D. Rohe et al. Measurement of the neutron electric form factor g(en) at 0.67-(gev/c)**2 via he-3(pol.)(e(pol.),e' n). *Phys. Rev. Lett.*, 83:4257–4260, 1999.

[85] M. V. Romalis and G. D. Cates. *Phys. Rev. A*, 58:3004, 1998.

[86] Cern root homepage. http://root.cern.ch.

[87] R. G. Sachs. High-energy behavior of nucleon electromagnetic form factors. *Phys. Rev*, 126(6):2256–2260, jun 1962. doi: 10.1103/PhysRev.126.2256.

[88] Misak M. Sargsian. Selected topics in high energy semi-exclusive electro-nuclear reactions. *Int. J. Mod. Phys.*, E10:405–458, 2001. doi: 10.1142/S0218301301000617.

[89] Misak Sarksian. personal communication, 2009.

[90] Rocco Schaivilla. private communication, 2008.

[91] R. Schiavilla and I. Sick. Neutron charge form factor at large q**2. *Phys. Rev.*, C64:041002, 2001.

[92] H. Schmieden. Double polarization experiments at intermediate energy. *Nucl. Phys.*, A663:21–28, 2000.

[93] Jaideep Singh. personal communication, 2006-2009.

[94] John R. Taylor. *Introduction to Error Analysis: The Stuy of Uncertainties in Physical Measurements.* University Science Books, 1996.

[95] A. K. Thompson et al. Quasielastic scattering of polarized electrons from polarized he-3 and measurement of the neutron's form- factors. *Phys. Rev. Lett.*, 68:2901–2904, 1992.

[96] Javier R. Vignote, M. C. Martinez, J. A. Caballero, E. Moya de Guerra, and J. M. Udias. A$(\vec{e}, e'\vec{p})$B responses from bare nucleons to complex nuclei. *Phys. Rev.*, C70:044608, 2004. doi: 10.1103/PhysRevC.70.044608.

[97] G. Warren et al. Measurement of the electric form factor of the neutron at q**2 = 0.5-gev/c**2 and 1.0-gev/c**2. *Phys. Rev. Lett.*, 92:042301, 2004.

[98] Bogdan Wojtsekhowski. personal communication, 2007-2009.